Studies to develop high activity MoS_2: crystallography, thermal analysis and catalytic activity

A thesis submitted to the

Faculty of Mathematics and Natural Sciences

of the Christian Albrechts University of Kiel

for the degree of

Doctor rer. nat.

presented by

Martha Emilia Poisot Vazquez

Kiel, Feb. 2007

Examiner:	Prof. Dr. Wolfgang Bensch
Co-examiner:	Prof. Dr. Norbert Stock
Date of the oral examination:	02.02.2007
To print approved:	02.03.2007

The Dean

Affirmation

I declare that the work presented here was performed by myself, under the supervision of my scientific tutor, only using the devices, resources and media mentioned in the thesis. The PhD thesis is solely submitted to the University of Kiel.

Martha Emilia Poisot Vazquez

Kiel, February 2007.

a Guillermo

Contents

Contents

1. Introduction

In recent years, the air pollution by nitrogen oxides, sulfur oxides and particulate matters included in diesel exhaust gas in metropolitan areas has become a very serious problem. On the other hand sulfur impurities contained in diesel fuel are irreversible poisons for catalytic converters used for exhaust emission treatment in modern engines. Therefore, the optimization of the hydrodesulfurization (HDS) of middle distillates (diesel and light fuel oil) represents a challenge for refiners and researchers to provide clean transportation fuels to meet increasingly stringent environmental regulations worldwide. In 2005, the sulfur limit of diesel oil was reduced in Europe from 350 to 50 ppm. Diesel oil with even less sulfur is already on the market, e.g. in Germany [1]. In Japan refiners began producing ultra-low sulfur diesel (ULSD, < 10 ppm sulfur) before January 2005. This and many other countries are planning to set the limit to 10 ppm by 2009 [2]. Furthermore, zero-emission levels and consequently zero or ultra-low sulfur content has to be achieved for most of the developed countries in the next 10 years.

The problem of deep removal of sulfur has become more serious due to the higher and higher sulfur contents in the crude oils [3]. To achieve zero or ultra-low sulfur content in fuels the efforts of industrial and academic researchers must improve the reactor concepts and the catalysts at the same time, which is a great challenge.

Changes of the reactor concepts in conventional gas oil hydrotreating units to convert the alkyl substituted (di-)benzothiophenes - especially those substituted at the 4 and 6 positions – make the deep HDS possible applying the following alterations:

- Decrease of the throughput means that either less gas oil can be hydrotreated or additional reactor capacity must be installed.
- The increase of hydrogen partial pressure produces fuels with a lower aromatic level which is advantageous for diesel properties.
- Introduction of more active HDS catalysts, particularly for removing the refractory S-containing molecules.
- Increasing the temperature is the simplest option. But it will increase the catalyst deactivation by coke formation and suppress the hydrogenation of aromatics, which is an equilibrium-limited reaction and very important considering the aromatics level specifications [4].

One should keep in mind that all these changes are costly, and obviously the different companies will only introduce these improvements if it is necessary.

But the new technology of the Nebula catalyst developed jointly by ExxonMobil, AkzoNobel and NipponKetjen demonstrates that such an improved activity for ultra-low sulfur diesel is

possible. With the new approach fuels 5 ppm sulfur level can be produced by a one-stage hydroprocessing under moderate conditions. For units operating at medium to high pressures designed for 350 or 500 ppm sulfur this new technology meets the future specifications with low or moderate investments [5].

Also Cosmo Oil has developed a new CoMo HDS catalyst, C-606A, for production of ultra-low sulfur diesel (ULSD) fuels, enabling less than 10 ppm sulfur content when straight-run light gas oil feedstock was treated under industrial hydrotreating conditions in a commercial hydrotreater designed to produce 500 ppm sulfur diesel fuels [6]. Lately, Haldor Topsoe has developed new supports and new preparation procedures for a new family of high activity hydroprocessing catalysts. This new BRIM^{TM} technology optimizes the rim site hydrogenation (HYD) functionality and increases the rate of the direct desulfurization (DDS) pathway. Recently, a new CoMo catalyst was produced, TK-576 BRIM^{TM}, for ULSD production at a low hydrogen partial pressure of 30 bar with very high conversion rates. The feedstock was a mixture of 25% light cycle oil (LCO) and 75% straight run gas oil (SRGO) diesel, and the feedstock sulfur content was about 1.8 wt% [7].

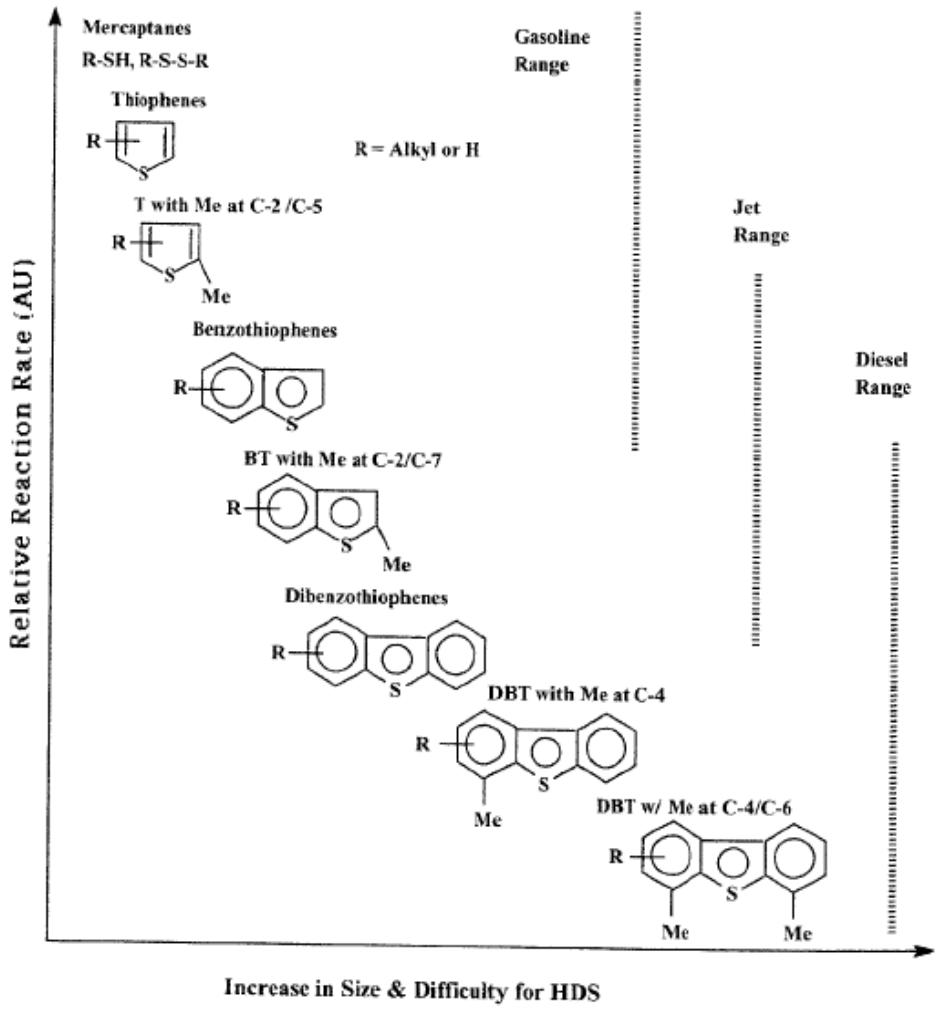

Fig. 1.1 Sulfur containing compounds in petroleum, from reference [3].

1.1 Raw oil components

The individual components in liquid fuels become very important in controlling the catalysis of HDS under deep hydrotreating conditions. Raw fuels are complex mixtures of various compounds. The sulfur compounds found in petroleum or synthetic oils are generally classified into heterocycles or non-heterocycles. The latter comprises thiols, sulfides and disulfides. Heterocycles are mainly composed of thiophenes, with one or several rings and their alkyl substituents. Examples of sulfur containing compounds found in raw oil are shown in Fig. 1.1. There are several components present for which HDS to remove the sulfur atom in the heterocycle is very difficult [3]. It has been observed that methyl groups adjacent to the S atom retard HDS due to steric effects, while those distant from the S atom generally increase HDS activity, an effect attributed to an increased electron density on the S atom (inductive effect).

1.2 Hydrodesulfurization

Hydrotreating or hydroprocessing refers to a variety of catalytic hydrogenation processes which saturate unsaturated hydrocarbons and remove S, N, O and metals from different pretroleum streams in a refinery, see Table 1.

Hydrotreating catalysts are commonly referred to as HDS catalysts. Hydrodesulfurization is a catalytic hydrogenation process which removes sulfur in petroleum. To gain a quantitative understanding of HDS kinetics, a common approach is to carry out HDS of representative model compounds. The HDS reactivity of the compounds may change depending on various reaction conditions and catalysts, but it decreases with the increasing number of rings [8].

Table 1. Main purposes for hydrotreating reactions.

HDS	(Hydrodesulfurization)	Eliminate sulfur in organosulfur compounds
HYD	(Hydrogenation)	Hydrogenation of aromatic compounds
HDN	(Hydrodenitrogenation)	Eliminate nitrogen in N-heterocyclic compounds
HDO	(Hydrodeoxygenation)	Eliminate oxygen of organic-oxygen containing comp.
HDM	(Hydrodemetallation)	Eliminate metals from metal-containing organic impurities
HCR	(Hydrocracking)	Conversion to lighter fractions

In a high pressure experiment, DBT is one of the most non-reactive sulfur compounds in higher boiling fractions of fossil fuels. It is readily available commercially and therefore it is a good model compound for characterizing the HDS chemistry of heterocyclic sulfur compounds. The HDS of DBT proceeds through two independent and parallel pathways (see Fig. 1.2), proposed by the early work of Gates and coworkers [9]:

- the direct desulfurization (DDS) pathway yielding biphenyl (BP) and
- the hydrogenation pathway (HYD) yielding cyclohexylbenzene (CHB) with a

tetrahydrogenated compound as an intermediate.

Several authors [10-13] have proposed that both pathways have a dihydrodibenzothiophene derivative as a common intermediate (see Fig. 1.3). This intermediate can indeed be transformed in two different manners:

i) through further hydrogenation into tetrahydro and hexahydrodibenzothiophene and after C-S bond cleavages eventually into cyclohexylbenzene (representing the HYD pathway);

ii) through a C-S bond cleavage as first step followed by the partial hydrogenation of the benzene ring bearing the S-H group to form a second dihydrointermediate which subsequently will give biphenyl through C-S bond cleavage with rearomatization (representing the DDS pathway). This process [13] involves a series of hydride and proton additions, assuming a heterolytic dissociation of hydrogen [14] and C-S bond cleavages through an elimination mechanism [15].

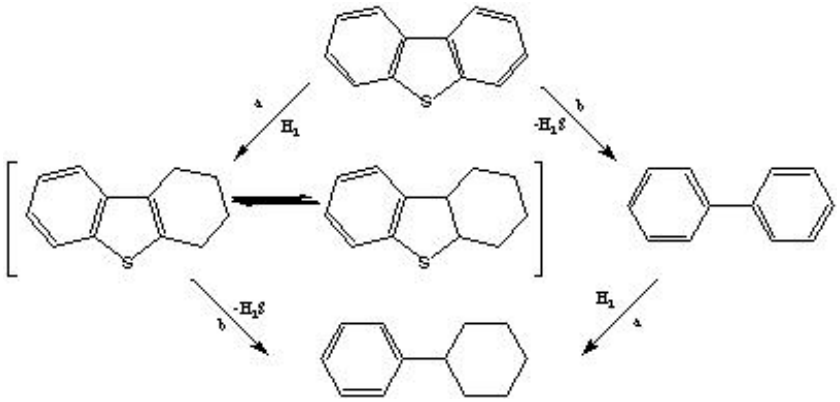

Fig. 1.2 HDS of DBT reaction pathways: a) HYD and b) DDS, from reference [16].

In hydrotreating reactions the relative contribution of each pathway is determined by the reaction conditions, i.e. mainly the hydrogen pressure used, the reactant reactivity and the catalyst chosen are the dominating factors. But it appears that in most hydrotreating reactions pre-hydrogenation of the heteroatom ring occurs prior to C-X (X = S, N or O) bond breaking as a consequence of the relatively strong bonding between the heteroatom and an aromatic-type carbon atom (sp^2 bonding) in contrast to the weaker bonding with an aliphatic-type carbon (sp^3 bonding). A possible exception is in the HDS of thiophene compounds, where the S-C (sp^2) bond is relatively weak, and direct sulfur removal may occur without saturation of the heteroatom ring. It has been proposed that increasing the basic character of the sulfur anions [17-20] the promoter enhances the rate of C-S bond cleavage through the elimination mechanism. Consequently, this step is in the case of DBT rate-limiting for MoS_2/Al_2O_3 catalysts, and it becomes fast on promoted catalysts so that the DDS route is preferred.

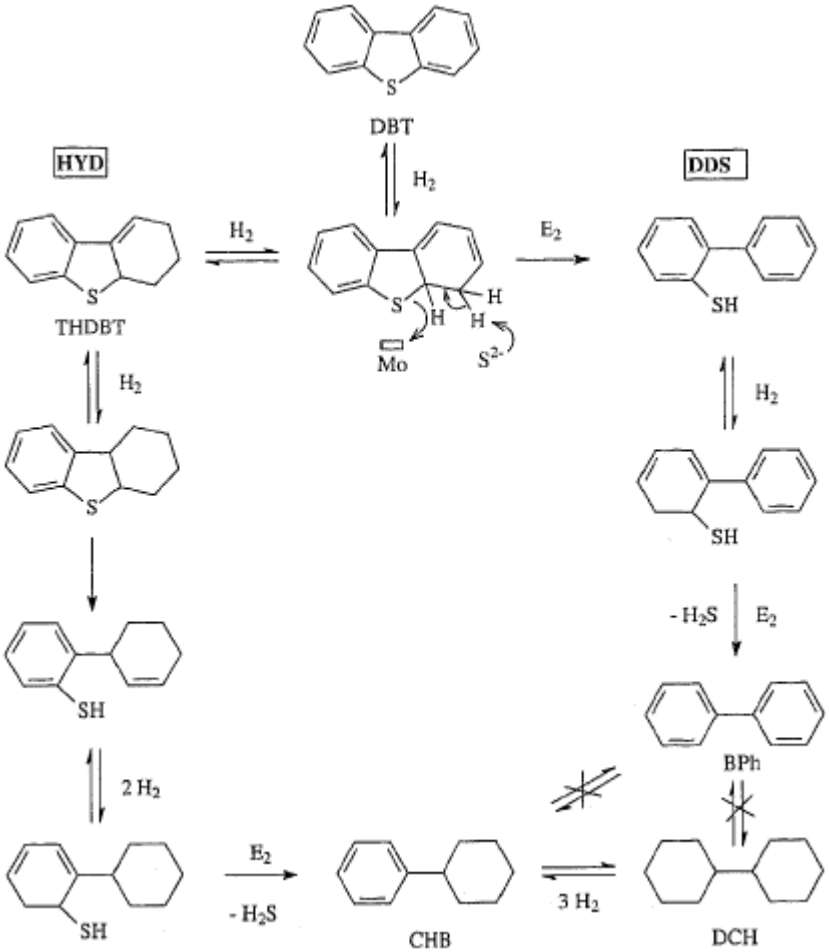

Fig. 1.3 HDS of DBT reaction pathways involving a dihydrodibenzothiophene intermediate, from reference [21].

Several authors have tried to explain the selectivity for the HYD or DDS pathway during catalytic reaction. One suggestion is that the difference between HYD and DDS centers would depend on the way the reactant can adsorb on these reactive centers. DDS active centers adsorb compounds like dibenzothiophene through their sulfur atom as they would do for H_2S [22-23], while centers involved in the HYD pathway adsorb such molecules flat through one of the aromatic rings [24-25]. Daage and Chianelli [26] proposed also an explanation for the existence of different catalytic centers of unsupported MoS_2 as function of the stacking height of the MoS_2 slabs in the so-called **Rim-Edge** model (Fig. 1.4), corresponding to the specific requirements of hydrogenation - flat adsorption of the substrate - and C-S bond cleavage - adsorption through the sulfur atom. Their hypothesis states that the rim-sites are active for hydrogenation reactions and C-S bond cleavage while edge-sites are active only in C-S bond breaking. The proposed model did not include the promotion effect on selectivity.

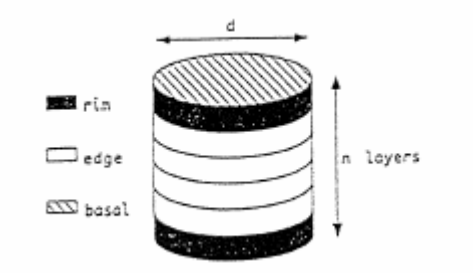

Fig. 1.4 Rim-edge model of a MoS_2 catalyst, from reference [26].

Another explanation which in a way recalls that of the rim-edge model was considered by Egorova and Prins [24]. They supposed that the DDS active sites are located at the edges of the MoS_2 slabs whereas, according to the proposal of Drew et al [27], the HYD active sites are located at the corners, and consequently could allow the π adsorption of the bulky molecules and would be less sensitive to the poisoning effect of H_2S [21]. However, it must be acknowledged that up to day there is no definitive proof of the existence of a common dihydrodibenzothiophene intermediate to both HDS pathways, although this type of intermediate must exist because hydrogenation of at least one of the aromatic rings proceeds.

1.2.1 Reaction sites

In order to understand the properties of hydrotreating catalysts it is important to obtain a complete description of both the structures and the sites where the catalysis takes place, i.e., the active sites. This purpose is particularly difficult to achieve due to the amorphous-like or highly dispersed nature of the active species and the simultaneous presence of many different types of phases. Additionally, the structure of the active species depends on the process conditions during the preparation of the catalyst. For decades, many studies have been produced misleading results on the operating catalysts because they were obtained under conditions far from those applied during catalytic reactions. Therefore, it is not surprising that a large number of results and proposals contradict each other. In-situ studies with different analytic techniques are necessary for a better understanding how such catalysts work under real conditions.

Nowadays, several surface science techniques like atomic force microscopy (AFM), scanning tunneling microscopy (STM) and theoretical studies like density functional theory (DFT) as well as in-situ characterization techniques as extended X-ray absorption fine structure (EXAFS) are available, and it has been established [28-29] that the active Mo is present as small MoS_2-like nanostructures. Structural information on hydrotreating catalysts has been in many cases interpreted in terms of several models like the monolayer model, the intercalation

model, the contact synergy model and the Co-Mo-S model. The last model will be explained below for an interpretation of the promoter effect of nickel and cobalt.

Since the early studies of Lipsch [30] and Kolbe [31] it has been widely accepted that the active sites are sulfur anion vacancies or coordinatively unsaturated sites (CUS) created in a reaction with hydrogen. Recently, the first atom-resolved scanning tunneling microscopy (STM) studies performed on a realistic HDS model catalyst were reported by the Topsoe group [32]. They studied a few nanometers wide gold-supported MoS_2 particles showing that the unpromoted catalyst may exhibit a triangular morphology in contrast to the hexagonal morphology expected for bulk crystals. Later, the same group synthesized single layers of MoS_2 to study the material using STM techniques and modeling by DFT [33]. The studies were performed simulating the HDS conditions with an environment of hydrogen and thiophene. The surprising result is that thiophene is adsorbed through the triangular shaped MoS_2 nanocluster fully saturated with sulfur which forms dimers (Fig. 1.5).

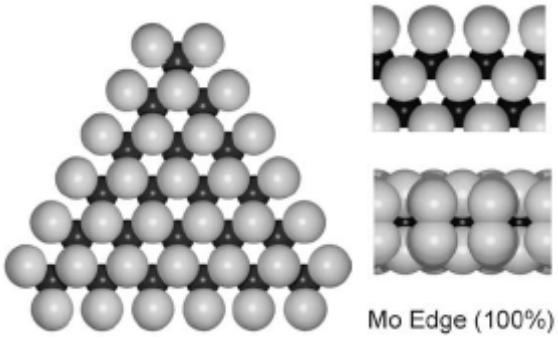

Fig. 1.5 Ball model of MoS_2 triangular single layer (left). Top and side views of the edge structure with the Mo edge with S dimers (S, bright; Mo, dark) (right), from reference [33].

This result is clearly in contrast to the common accepted hypothesis that coordinatively unsaturated sites (CUS) are required for the binding of the molecules. The binding sites are one dimensional metallic brim sites (metallic edge state) as proposed by DFT calculations. Such sites were observed in STM images as a pronounced bright brim located on top of the triangular MoS_2 nanocluster adjacent to the edge itself. The theoretical calculations [34-36] show that the brim sites originate from d-d bonds between the first row of Mo atoms and p-d bonds between the second row of S atoms and the Mo atoms below.

Thiophene was π-bonded to the brim site by a flat η^5-like adsorption geometry. After supplying pre-dissociated hydrogen an adsorption on the sulfur dimers was observed, leading to the formation of SH groups on the edges. In terms of hydrogenation the close vicinity of the reactants may promote the reaction. The SH groups may play an essential role, both in the

creation of vacancies and in providing hydrogen for the hydrogenation reactions. The adsorption on the brim sites facilitated not only the hydrogenation, but also the cleavage of the first C-S bond. In summary, the reactivity can be explained by a two step process in which the thiophene is first hydrogenated and the first C-S bond is cleaved on the brim sites. Then the ring-opened molecule is subsequently transported to a sulfur vacancy on the cluster edge, where the second C-S bond can be broken and the final sulfur extrusion could occur on a vacancy [37]. The STM results indicate that the last reaction of the HYD pathway may take place on the same type of vacancy sites as those involved in the DDS pathway. DFT calculations [38] indicate that the DDS pathway may be even more favored on the S-terminated edges where vacancies are more easily formed, but they are easily quenched with the strong inhibition by H_2S of the direct desulfurization pathway.

In order to conclude about the validity of these studies the catalyst must be studied after it has been stabilized under the commercial operating conditions.

1.2.2 Promoter effect

The Co-Mo-S model was proposed by the Topsoe group [39] by the direct observation of a Co-Mo-S phase, identified mainly by in-situ Mössbauer spectroscopy, extended X-ray absorption spectroscopy (EXAFS), and infrared spectroscopy studies. The Co-Mo-S phase is similar to the MoS_2 structure with the promoter atoms located at the (100) edge planes in five-fold coordinated sites thus replacing a molybdenum atom.

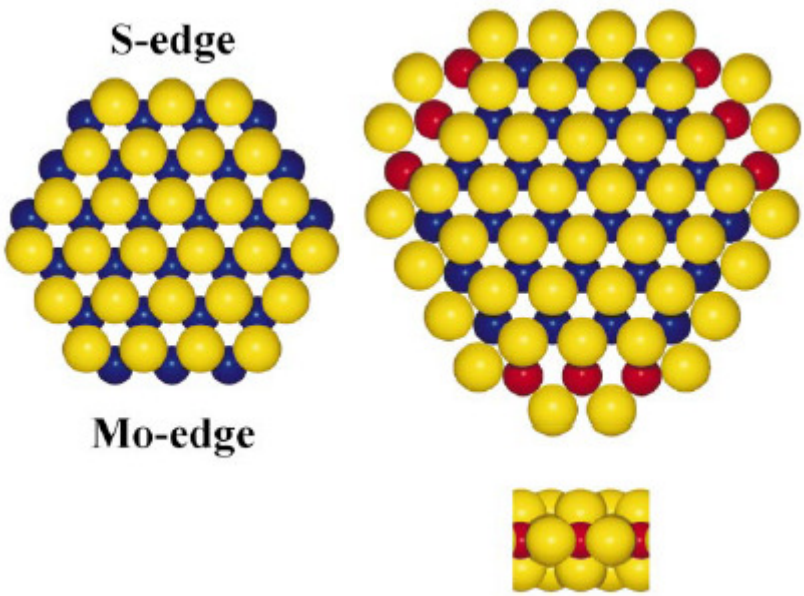

Fig. 1.6 Ball model of the proposed hexagonally truncated Co-Mo-S structure with Co fully substituted at the S-edge (S, yellow; Mo, blue, Co; red), from reference [40].

Recently, the first Co-Mo-S structure was identified with STM imaging techniques [40]. The Co-Mo-S phase has a hexagonally truncated shape (Fig. 1.6) opposed to the triangular shape of the unpromoted MoS_2 nanoclusters.

The hexagonal truncated morphology of this model phase presents both terminations with S and Mo edges. In contrast to the previous model, the STM images showed that the Co promoter atoms have no effect onto the Mo edges, but Co atoms prefer to locate at the S edge. The model proposes that at the S edge the Mo atoms are fully substituted by Co atoms. A tetrahedral environment of the Co atom is suggested enabling the adsorption of sulfur containing reactants. It is also possible that the enhanced electronic density of the sulfur atoms adjacent to cobalt atoms may be a key to understand the increased reactivity of the Co-Mo-S structure. On the other hand, high angular annular dark field scanning transmission electron microscopy (HAADF-STEM) applied to study Ni-Mo-S nanoclusters allowed the observation of the modification of the triangular shaped MoS_2 nanoclusters with an additional truncation leading to the hexagonal truncated morphology [41].

The effect of the promoter onto the Mo-S bond strength is explained by the synergy model [25] and on the basis of ab initio calculations using DFT [20]. The strength of the Mo-S bond is more reduced when Ni substitutes Mo than when Mo is replaced by Co at the edges of the MoS_2 slabs. As a consequence, in a NiMo catalyst the sulfur anions would be more basic than those in the corresponding cobalt catalyst, facilitating the neutralization of the acidic character of H_2S.

1.2.3 Unsupported catalysts

The role of support interactions in HDS catalysts is very important because this is a key parameter used to control the catalyst activity and selectivity. Using alumina as the support Mo-O-Al linkages can be formed depending on the calcination procedure. The support effect has been related to the formation of the Type I Co-Mo-S structure which is the low activity form of the Type II Co-Mo-S catalyst [42, 43]. Therefore, the use of weakly interacting supports such as carbon is nowadays preferred [44, 45].

Typical sulfided hydrotreating catalysts consist of Co or Ni promoted MoS_2 or WS_2 supported on alumina or silica. But it has been stated that the behavior of unsupported catalysts as a function of the chemical composition is similar to that observed for supported catalysts [17]. Unsupported HDS catalysts have been prepared by several methods, including co-maceration [8], homogeneous sulfide precipitation [46], thiosalt decomposition [47], or impregnated thiosalt decomposition [48]. The materials obtained with these preparation methods need to be activated by one of two ways: *ex-situ* activation in a H_2/H_2S mixture before being active in

catalytic reactions or directly by *in-situ* activation which consists in the direct decomposition of the Mo or W containing precursors in the presence of a hydrocarbon solvent during the HDS of DBT [49]. The catalytic properties of MoS_2 and WS_2 prepared by one of these methods depend strongly on the reacting atmosphere and on the heating conditions [8, 46-48].
Thiosalt decomposition is an interesting alternative preparation because it provides a simple and reproducible method for obtaining MoS_2 catalysts with controlled stoichiometry. Some patents have reported the use of tetraalkylammonium thiometalates to generate carbon containing MoS_2 and/or WS_2 catalysts with high surface areas and an improved activity for the HDS of DBT. Such catalysts are described with the general formula $MoS_{2-y}C_z$ [50]. The role of carbon in these HDS catalysts is not completely understood. Recent studies have shown that carbon, at least partially, is included in the arrangement of the active sites by a replacement of sulfur atoms at the reactive edges of MoS_2 platelets. Carbon stabilizes texturally the sulfide particles, keeping crystallites smaller and less stacked. The active transition metal sulfide is called sulfided supported transition metal carbides (SSTMC) [51].
The *in-situ* activation of tetraalkylammonium thiomolybdates (alkyl = propyl, pentyl, hexyl, heptyl and octyl) generates low stacked MoS_2 catalysts with high surface areas and fine dispersed active phases [52]. Applying the *in-situ* activation of bimetallic Co-Mo alkylthiomolybdates, mesoporous catalysts with a high surface area are produced with high contents of carbon (C/Mo = 2.2 - 3.3). Such catalysts show a strong enhancement of the direct desulfurization pathway due to the synergistic effect of the promoter. The use of carbon-containing precursors leads to a strong increase in the HDS activity with a strong favored hydrogenolysis function when longer alkyl chains are used in the precursor material [53].
Nowadays, optimizing the selectivity of a given process is often more important than increasing the overall reaction rate.
In the present work nickel was chosen as promoter for molybdenum disulfide catalysts to favor the selectivity for the DDS pathway. For the synthesis of the catalysts tetraalkylammonium thiomolybdates were used as precursors trying to obtain high HDS activity.

1.3 Literature

[1] W. Wache, L. Datsevich, A. Jess, G. Neumann, Fuel, 86 (2006) 1483.

[2] EP directive 2003/17/EC, J. Off., Eur. Commun. L, 76 (2003) 11.

[3] C. Song, Catal. Today, 86 (2003) 211.

[4] J. W. Gosselink, Cat. Tech., 2 (1998) 127.

[5] F. L. Plantenga, R. G. Leliveld, Appl. Catal. A., 248 (2003) 1.

[6] T. Fujikawa, H. Kimura, K. Kiriyama, K. Hagiwara, Catal. Today 111 (2006) 188.

[7] H. Topsoe, B. Hinnemann, J. S. Norskov, J. V. Lauritsen, F. Besenbacher, P. L. Hansen, G. Hytoft, R. G. Egeberg, K. G. Knudsen, Catal. Today, 107 (2005) 12.

[8] G. Hagenbach, Ph. Courty, B. J. Delmon, J. Catal., 31 (1973) 264.

[9] M. Houalla, D. H. Broderick, B. C. Gates, AIChEJ., 24 (1978) 1015.

[10] V. Meille, E. Schulz, M. Lemaire, M. Vrinat, J. Catal., 170 (1997) 29.

[11] F. Bataille, J. L. Lemberton, P. Michaud, G. Perot, M. Vrinat, M. Lemaire, E. Schulz, M. Breysse, S. Kasztelan, J. Catal., 191 (2000) 409.

[12] G. H. Singhal, R. L. Espino, J. E. Sobel, G. A. Huff, J. Catal., 67 (1981) 457.

[13] J. Mijoin, G. Perot, F. Bataille, J. L. Lemberton, M. Breysee, S. Kasztelan, Catal. Lett., 71 (2001) 139)

[14] C. Thomas, L. Vivier, J. L. Lemberton, S. Kasztelan, G. Perot, J. Catal., 167 (1997) 1.

[15] G. H. Singhal, R. L. Espino, J. E. Sobel, G. A. Huff, J. Catal., 67 (1981) 457.

[16] T. Kabe, A. Ishihara, W. Qian, Hydrodesulfurization and Hydrodenitrogenation, Wiley-VCH, Tokyo (1999).

[17] H. Topsoe, B. S. Clausen and F. E. Massouth in Catalysis Science and Technology, Vol. 11, Eds. J. R. Anderson and M. Boudard, Springer, Berlin (1996).

[18] R. R. Chianelli, Catal. Rev.-Sci. Eng., 26 (1984) 361.

[19] H. Topsoe, B.S. Clausen, N.-Y. Topsoe, E. Pedersen, W. Niemann, A. Müller, H. Bögge, B. Lengeler, J. Chem. Soc., Faraday Trans., I 83 (1987) 2157.

[20] R. R. Chianelli, G. Berhault, P. Raybaud, S. Kasztelan, J. Hafner, H. Toulhoat, Appl. Catal. A, 227 (2002) 83.

[21] V. Rabarihoela-Rakotovao, S. Brunet, G. Perot, F. Diehl, Appl. Catal. A, 306 (2006) 34.

[22] M. Macaud, A. Milenkovic, E. Schulz, M. Lemaire, M. Vrinat, J. Catal., 193 (2000) 255.

[23] T. Kabe, A. Ishihara, Q. Zang, Appl. Catal. A, 97 (1993) 11.

[24] M. Egorova, R. Prins, J. Catal., 225 (2004) 417.

[25] H. Farag, K. Sakanishi, M. Kouzu, A. Matsumura, Y. Sugimoto, I. Saito, Catal. Commun., 4 (2003) 321.

[26] M. Daage, R. R. Chianelli, J. Catal., 149 (1994) 414.

[27] M. G. B. Drew, S. J. Edmonson, G. A. Forsyth, R. J. Hobson, P. C. H. Mitchell, Catal. Today, 2 (1988) 633.

[28] B. S. Clausen, B. Lengeler, R. Candia, J. Als Nielsen, H. Topsoe, Bull. Soc. Chim. Belg., 90 (1981) 1249;

[29] T . G. Parham, R. P. Merril, J. Catal. 85 (1984) 295.

[30] J. M. J. Lipsch, G. C. A. Schuit, J. Catal., 15 (1969) 174.

[31] S. Kolbe, Can. J. Chem. 47 (1969) 352)

[32] S. Helveg, J. V. Lauritsen, E. Laegsgaard, I. Stensgaard, J. K. Norskov, B. S. Clausen, H. Topsoe, F. Besenbacher, Phys. Rev. Lett., 84 (2000) 951.

[33] J. V. Lauritsen, M. Nyberg, J. K. Norskov, B. S. Clausen, H. Topsoe, E. Laegsgaard, F. Besenbacher, J. Catal., 224 (2004) 94.

[34] J. V. Lauritsen, M. V. Bollinger, E. Laegsgaard, K. W. Jacobsen, J. K. Norskov, B. S. Clausen, H. Topsoe, F. Besenbacher, J. Catal., 221 (2004) 510.

[35] M. V. Bollinger, K. W. Jacobsen, J. K. Norskov, Phys. Rev. B67 (2003) 085410.

[36] M. V. Bollinger, J. V. Lauritsen, K. W. Jacobsen, J. K. Norskov, S. Helveg, F. Besenbacher, Phys. Rev. Lett. 87 (2001) 196803.

[37] J. V. Lauritsen, F. Besenbacher, Adv. Catal., 50 (2006) 97.

[38] L. S. Byskov, J. K. Norskov, B. S. Clausen, H. Topsoe, J. Catal., 187 (1999) 109.

[39] N.-Y. Topsoe, H. Topsoe, J. Catal., 84 (1983) 386.

[40] J. V. Lauritsen, S. Helveg, E. Laegsgaard, I. Stensgaard, B. S. Clausen, H. Topsoe, F. Besenbacher, J. Catal., 197 (2001) 1.

[41] A. Carlsson, M. Brorson and H. Topsoe, J. Microscopy, 223 (2006) 179.

[42] H. Topsoe, R. Candia, N.-Y. Topsoe, B. S. Clausen, Bull. Soc. Chim. Belg. 93 (1984) 783.

[43] R. G. Leliveld, A. J. Van Dillen, J. W. Geus, D. C. Konigsberger, J. Catal., 165 (1997) 184.

[44] L. Medici, R. Prins, J. Catal., 163 (1996) 38.

[45] L. Coulier, G. Kishan, J. A. R. Van Veen, J. W. Niemantsverdriet, J. Phys. Chem., B106 (2002) 5897.

[46] R. Candia, B. S. Clausen, H. J. Topsoe, J. Catal., 77 (1982) 564.

[47] M. Zdrazil, Catal. Today, 3 (1988) 269.

[48] S. Fuentes, G. Diaz, F. Pedraza, H. Rojas, N. Rosas, J. Catal., 113 (1988) 535.

[49] J. Espino, L. Alvarez, C. Ornelas, J. L. Rico, S. Fuentes, G. Berhault, G. Alonso, Catal. Lett., 90 (2003) 171.

[50] T. A. Pecoraro, R. R. Chianelli, US Patent 4,528,089 (1985).

[51] G. Berhault, A. Mehta, A. C. Jianhong Yang, L. Rendon, M. J. Yácaman, L. Cota Araiza, A. Duarte Moller, R. R. Chianelli, J. Catal., 198 (2001) 9.

[52] G. Alonso, G. Berhault, A. Aguilar, V. Collins, C. Ornelas, S. Fuentes, R. R. Chianelli, J. Catal., 208 (2002) 359.

[53] H Nava, C. Ornelas, A. Aguilar, G. Berhault, S. Fuentes, G. Alonso, Cat. Lett., 86 (2003) 257.

2. Aim

Aim of the project and some remarks

The main objects of the work were:

- Development of a one-step synthesis of high active promoted molybdenum disulfide catalysts containing carbon to improve the catalytic activity of hydrodesulfurization (HDS) of dibenzothiophene (DBT).
- Promotion of the catalysts with nickel to favor the selectivity for the direct desulfurization (DDS) pathway in the HDS of DBT.
- Preparation of MoS_2 based catalysts for the *cis-trans* isomerization of butene-2 and for the isomerization of 2-methyl-1-butene.
- Synthesis and characterization of appropriate precursors for the preparation of active catalysts based on Mo and W sulfides.
- Study of the thermal decomposition pathways of tetraalkylammonium tetrathiomolybdates and tetrathiotungstates.

The work was started with the intention to synthesize new molybdenum based catalysts for isomerization reactions of selected molecules. The proposal for this work is supported by the Deutsche Forschungsgemeinschaft. Unfortunately, the collaborating group in Bochum (Prof. Dr. W. Grünert) experienced several technical problems which could not be solved within a reasonable time period. After about one and a half year we decided to change the direction of the project towards the synthesis and characterization of new catalysts for the HDS reaction. Therefore, the main results presented in the thesis deal with the materials prepared and characterized for HDS catalytic reactions.

3. Results

The results are organised in three main parts of the thesis:

- Determination of the crystal structures of single crystals of the tetraalkylammonium tetrathiomolybdates and tetrathiotungstates used as precursors for the catalyst syntheses.
- Investigation of the thermal decomposition behavior of the precursors.
- Chemical characterization of the promoted and unpromoted catalysts and investigation of the catalytic activity during hydrodesulfurization (HDS) of dibenzothiophene (DBT).

Most of these results are published and the publications are presented following the above mentioned topics.

3.1 Crystallographic and characterization studies

3.1.1 Diammonium tetrathiotungstate, $(NH_4)_2[WS_4]$ determined at 150 K

The main purpose of this study was a more accurate determination of the H atom positions. With this knowledge interatomic separations are more accurate and the proposed hydrogen-bonding interactions between cations and anions are on a more profound ground. In the present structure several N-H···S bonding interactions are observed connecting the cations and anions into a three-dimensional network. The own work for this publication was the synthesis of the crystal.

3.1.2 Synthesis, Crystal Structures and Properties of Three New Tetrathiomolybdates with Organic Ammonium Cations

The three new thiomolybdates $R[MoS_4]$ (R = $pipH_2$, $trenH_2$, $(prop)_4N$) were synthesised by the base promoted cation exchange method. In the first two compounds anions and cations are joined via S···H bonding interactions. The influence of the number and strengths of these interactions onto the Mo-S bond lengths is obvious: strong S···H bonds yield longer Mo-S bond lengths. In the third compound no S···H bonding interactions are possible and as a consequence the Mo-S bond lengths scatter in a significantly narrower range. The thermal decomposition was studied with DTA-TG experiments. All compounds decompose to form amorphous MoS_x materials. The thiomolybdate with R = $(prop)_4N$ yields a very porous material with large cavities. The reaction mechanism of the decomposition was studied with combined DTA-TG-MS experiments. The results suggest that during the two-step decomposition trialkylamine and dipropyldisulfide molecules are emitted simultaneously. An endothermic event at relatively low temperatures suggests a phase transition prior to the decomposition reaction. When the reaction is stopped after the first decomposition step, a new

compound is formed as is evidenced by X-ray powder diffractometry. The own contribution to this work was the synthesis and thermal characterization of the last compound.

3.1.3 Synthesis, X-ray Structures, Spectroscopic and Thermal Characterisation of Two New Organic Ammonium Tetrathiotungstates

The two new tetrathiotungstates $(pipH_2)[WS_4]$ and $(trenH_2)[WS_4]\cdot H_2O$ were characterised by elemental analysis, IR, Raman, UV-Vis and ^{1}H-NMR spectroscopy, thermoanalysis and single crystal X-ray work. Like in the analogous Mo compounds the structures are characterized by an extended N-H···S/O bonding network. A similar influence of the number and strengths of these interactions onto the W-S bond lengths is found like for the analogous Mo compounds. Raman and IR spectra clearly indicate the distortion of the WS_4 tetrahedra. The thermal decomposition of the compounds under an inert atmosphere yields amorphous products with high C contents which is a characteristic feature of good HDS catalysts. In addition, the decomposition of the materials does not proceed via WS_3 as an intermediate material. The water molecule of the second compound can be reversibly de- and re-hydrated. The own contribution to this work was the extended study of the thermal behavior and the characterisation of the decomposition products.

3.1.4 Bis(diethylenetriamine)cobalt(II) tetrathiomolybdate(VI) oxotrithiamolybdate(IV).

The crystal structure determination of this new complex revealed that it is composed of two superimposed anions, i.e., $MoOS_3^{2-}$ and MoS_4^{2-} coexist in one compound. The Mo-S vibrations in the infrared spectrum show a splitting evidencing the reduced symmetry. The Co^{2+} ion is surrounded by two tri-dentate diethylentriamine ligands in a slightly distorted octahedral environment. Compared to the analogous ethylenediamine compound the distortion of the octahedron is less strong. Efforts to obtain single crystals of the corresponding nickel compound were not successful. But the similarities of the X-ray powder patterns of the two compounds suggest that they are isostructural.

3.1.5 Synthesis, spectroscopic and X-ray structure characterisation of Bis(tetramethylammonium), Bis(tetraethylammonium) and Bis(tetrapropylammonium) Tetrathiotungstates.

Single crystals of the three new tetraalkylammonium tetrathiotungstates were synthesized via the direct salt substitution route. The materials were characterized by single crystal structure determination, IR and Raman spectroscopy. In the compounds no N-H···S interactions are

possible and consequently the WS_4 tetrahedra are only slightly distorted as is evidenced by IR and Raman spectra. In contrast, the positional disorder of the alkylammonium ions decreases with increasing alkyl chain length. The non-hydrogen atomic volume decreases in the same direction suggesting that the interactions between the more bulky alkyls groups is stronger than between the small groups. Crystallographic data for tetramethylammonium tetrathiotungstate were reported in the past. But the present study demonstrates that the correct space group is $P2_12_12_1$. The relation between the two unit cells is a doubling of one of the lattice parameters. An interesting observation is that tetraethylammonium tetrathiotungstate is not isostructural to the analogous molybdenum compound, which crystallises in a triclinic space group. Such examples are rare and until now there are only few tetrathiomolybdates and tetrathiotungstates which do not crystallize in the same space group.

3.1.6 Synthesis, Spectroscopic and X-Ray Structure Characterisation of Bis(tetramethylammonium) and Bis(tetra-n-butylammonium) Tetrathiomolybdates.

Like the analogous tetrathiotungstates the new tetrathiomolybdates were prepared using the direct salt substitution approach starting with $(NH_4)_2MoS_4$ as educt. Both compounds crystallize in non-centrosymmetric orthorhombic space groups. Attempts to determine the crystal structure of tetraethylammonium tetrathiomolybdate failed due to a very pronounced disorder of the tetraethylammonium ions. Nevertheless, the crystal symmetry could be determined as tetragonal with a centred space group being the most probable choice space group. It is notable that the analogous tetrathiotungstate compound was reported to crystallize in the monoclinic space group $P2_1/n$. Hence, this pair of compound is another rare example in the thiotungstate/thiomolybdate chemistry. In the structure of the tetramethylammonium compound the MoS_4 ion is only slightly distorted in accordance with the absence of N-H···S interactions. But the cations show a pronounced positional disorder. Like for the tetrathiotungstates the positional disorder is suppressed for the more bulky butylammonium ion. The IR and Raman spectra of the compounds show a slight shift of the Mo-S main vibrations to lower energy with increasing alkyl chain length, an observation which was also made for the tetrathiotungstates.

3.1.1

inorganic papers

Acta Crystallographica Section E
Structure Reports Online
ISSN 1600-5368

Diammonium tetrathiotungstate(VI), $(NH_4)_2[WS_4]$, at 150 K

Bikshandarkoil R. Srinivasan,[a] Martha Poisot,[b] Christian Näther[b]* and Wolfgang Bensch[b]

[a]Department of Chemistry, Goa University PO, Goa 403 206, India, and [b]Institut für Anorganische Chemie, Christian-Albrechts-Universität Kiel, Olshausenstraße 40, D-24098 Kiel, Germany

Correspondence e-mail: cnaether@ac.uni-kiel.de

Key indicators

Single-crystal X-ray study
T = 150 K
Mean σ(W–S) = 0.001 Å
R factor = 0.018
wR factor = 0.048
Data-to-parameter ratio = 25.7

For details of how these key indicators were automatically derived from the article, see http://journals.iucr.org/e.

A low-temperature structure determination of the title compound, $(NH_4)_2[WS_4]$, indicates several short N—H···S contacts between the two crystallographically independent ammonium cations and the tetrahedral $[WS_4]^{2-}$ anions, which are all located on crystallographic mirror planes.

Received 17 September 2004
Accepted 23 September 2004
Online 9 October 2004

Comment

In recent work, it has been shown that the $(NH_4)^+$ ion significantly influences the chemical behaviour of $[MoS_4]^{2-}$; this has been attributed to hydrogen-bonding interactions between the cations and anions in $(NH_4)_2[MoS_4]$ (Schwarz *et al.*, 2003). In view of our recent interest in the chemistry of tetrathiotungstates (Srinivasan *et al.*, 2003), we have redetermined the structure of diammonium tetrathiotungstate at low temperature. The title compound, (I), is isostructural with $(NH_4)_2[MoS_4]$ (Lapasset *et al.*, 1976), $Cs_2[MoS_4]$ (Raymond *et al.*, 1995), $Rb_2[MoS_4]$ (Ellermeier *et al.*, 1999), $K_2[MoS_4]$ (Emirdag-Eanes & Ibers, 2001) and $Rb_2[WS_4]$ (Yao & Ibers, 2004). The cell constants and space group for (I) are consistent with earlier results determined from oscillation photographs (Sasvári, 1963). In contrast with the older work, we have located the H atoms.

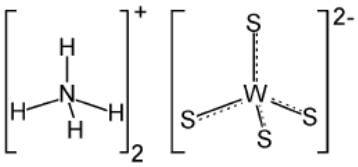

(I)

The asymmetric unit of (I) consists of halves of a tetrahedral $[WS_4]^{2-}$ ion and two crystallographically independent ammonium cations, which are all located on crystallographic mirror planes (Fig. 1). The W—S distances range from 2.1856 (11) to 2.2090 (10) Å (Table 1) and are comparable with those of 2.171 (2)–2.205 (2) Å recently reported for $Rb_2[WS_4]$ (Yao & Ibers, 2004). In the crystal structure, anions and cations are linked *via* N—H···S hydrogen bonding (Fig. 2). No disordering of the H atoms in the NH_4^+ ion is found in (I), unlike in the corresponding Mo analogue, where the H atoms are disordered over two orientations of both NH_4^+ cations (Schwarz *et al.*, 2003). Several short N—H···S contacts, with H···S ranging from 2.57 to 3.03 Å, are observed between the cations and the anions, which are comparable with those of 2.55–3.02 Å reported for the Mo analogue (Table 2). The N···S distances for one of the cations fall in the

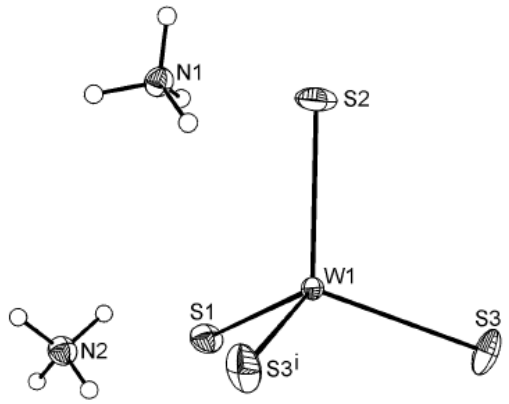

Figure 1
The constituent ions of diammonium tetrathiotungstate, with the atom-labelling scheme. Displacement ellipsoids are drawn at the 50% probability level [symmetry code: (i) $x, \frac{3}{2} - y, z$].

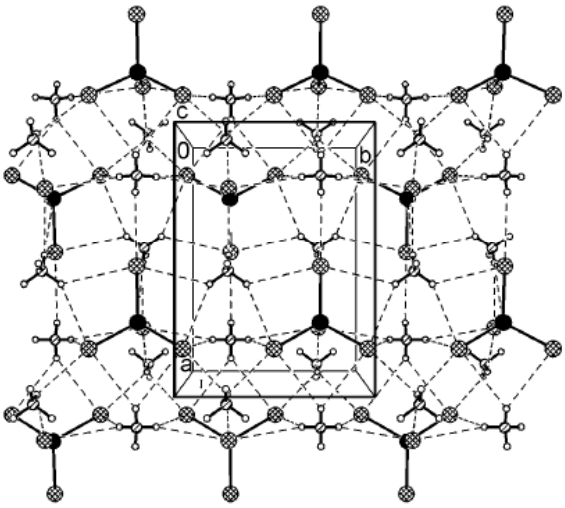

Figure 2
The crystal structure of diammonium tetrathiotungstate, viewed along the c axis (intermolecular hydrogen bonds are shown as dashed lines). Key: W atoms are black circles, S atoms crosshatched circles and N atoms circles shaded bottom left to top right.

range 3.242 (4)–3.5552 (7) Å, while the N···S distances for the second cation are longer, at 3.483 (4)–3.633 (4) Å (Table 2).

Experimental

The title complex was prepared according to the procedure reported by McDonald *et al.* (1983). The product was obtained as orange–yellow crystalline blocks in 60% yield by passing a rapid stream of H_2S gas for 9 h at 333 K into a solution of tungstic acid (5 g) dissolved in concentrated ammonium hydroxide (40 ml) and water (10 ml). At the end of 9 h, the reaction mixture was filtered and the filtrate was set aside for a day, resulting in the formation of crystals of the title complex.

Crystal data

$(NH_4)_2[WS_4]$	Mo $K\alpha$ radiation
M_r = 348.17	Cell parameters from 7250 reflections
Orthorhombic, *Pnma*	θ = 10–25°
a = 9.6054 (6) Å	μ = 14.97 mm^{-1}
b = 6.9863 (5) Å	T = 150 (2) K
c = 12.2557 (10) Å	Block, yellow
V = 822.43 (10) Å^3	0.10 × 0.09 × 0.08 mm
Z = 4	
D_x = 2.812 Mg m^{-3}	

Data collection

Stoe IPDS diffractometer	962 reflections with $I > 2\sigma(I)$
φ scans	R_{int} = 0.032
Absorption correction: numerical (*X-SHAPE*; Stoe & Cie, 1998)	θ_{max} = 27.9°
T_{min} = 0.238, T_{max} = 0.297	$h = -12 \rightarrow 12$
7433 measured reflections	$k = -9 \rightarrow 9$
1054 independent reflections	$l = -16 \rightarrow 16$

Refinement

Refinement on F^2	$w = 1/[\sigma^2(F_o^2) + (0.0285P)^2 + 1.1841P]$ where $P = (F_o^2 + 2F_c^2)/3$
$R[F^2 > 2\sigma(F^2)]$ = 0.018	$(\Delta/\sigma)_{max}$ = 0.001
$wR(F^2)$ = 0.048	$\Delta\rho_{max}$ = 0.74 e Å^{-3}
S = 1.10	$\Delta\rho_{min}$ = −1.36 e Å^{-3}
1054 reflections	Extinction correction: *SHELXL97*
41 parameters	Extinction coefficient: 0.0029 (3)
H-atom parameters constrained	

Table 1
Selected geometric parameters (Å, °).

W1—S2	2.1856 (11)	W1—S1	2.2090 (10)
W1—S3	2.1870 (7)		
S2—W1—S3	109.25 (3)	S2—W1—S1	110.33 (4)
S3^{i}—W1—S3	108.23 (4)	S3—W1—S1	109.87 (2)

Symmetry code: (i) $x, \frac{3}{2} - y, z$.

Table 2
Hydrogen-bonding geometry (Å, °).

D—H···A	D—H	H···A	D···A	D—H···A
N1—H1N1···S2^{ii}	0.86	2.78	3.278 (3)	118
N1—H1N1···S3^{iii}	0.86	2.83	3.489 (3)	135
N1—H1N1···S3^{iv}	0.86	2.83	3.489 (3)	135
N1—H2N1···S2	0.86	2.57	3.242 (4)	136
N1—H2N1···S1	0.86	2.75	3.439 (3)	139
N1—H3N1···S3^{v}	0.86	2.65	3.414 (3)	149
N1—H3N1···S1^{v}	0.86	2.93	3.5552 (7)	131
N2—H1N2···S1	0.86	2.89	3.483 (4)	128
N2—H2N2···S3^{vi}	0.86	2.87	3.513 (3)	133
N2—H2N2···S3^{vii}	0.86	2.87	3.513 (3)	133
N2—H2N2···S1^{viii}	0.86	3.03	3.633 (4)	129
N2—H3N2···S3^{v}	0.86	2.82	3.563 (3)	146
N2—H3N2···S2^{v}	0.86	2.86	3.5289 (6)	136

Symmetry codes: (ii) $x - \frac{1}{2}, y, \frac{1}{2} - z$; (iii) $\frac{3}{2} - x, 1 - y, z - \frac{1}{2}$; (iv) $\frac{3}{2} - x, \frac{1}{2} + y, z - \frac{1}{2}$; (v) $1 - x, 1 - y, 1 - z$; (vi) $x - 1, y, z$; (vii) $x - 1, \frac{3}{2} - y, z$; (viii) $x - \frac{1}{2}, y, \frac{3}{2} - z$.

The H atoms were located in a difference map and were refined with fixed bond lengths (N—H = 0.86 Å) and fixed isotropic displacement parameters [$U_{iso}(H) = 1.5U_{eq}(N)$] using a riding model. The maximum electron-density peak is located 0.98 Å from atom W1.

Data collection: *IPDS* (Stoe & Cie, 1998); cell refinement: *IPDS*; data reduction: *IPDS*; program(s) used to solve structure: *SHELXS97* (Sheldrick, 1997); program(s) used to refine structure: *SHELXL97* (Sheldrick, 1997); molecular graphics: *XP* in *SHELXTL*

(Bruker, 1998); software used to prepare material for publication: *XCIF* in *SHELXTL*.

This work is supported by the state of Schleswig-Holstein and the Deutsche Forschungsgemeinschaft. BRS thanks the Department of Science and Technology (DST), New Delhi, for financial assistance under grant No. SR/S1/IC-41/2003.

References

Bruker (1998). *SHELXTL*. Version 5.10. Bruker AXS Inc., Madison, Wisconsin, USA.
Emirdag-Eanes, M. & Ibers, J. A. (2001). *Z. Kristallogr. New Cryst. Struct.* **216**, 484.
Ellermeier, J., Näther, C. & Bensch, W. (1999). *Acta Cryst.* C**55**, 1748–1751.
Lapasset, P. J., Chezeau, N. & Belougne, P. (1976). *Acta Cryst.* B**32**, 3087–3088.
McDonald, J. W., Friesen, G. D., Rosenhein, L. D. & Newton, W. E. (1983). *Inorg. Chim. Acta*, **72**, 205–210.
Raymond, C. C., Dorhout, P. K. & Miller, S. M. (1995). *Z. Kristallogr.* **210**, 775.
Sasvári, K. (1963). *Acta Cryst.* **16**, 719–724.
Schwarz, D. E., Rauchfuss, T. B. & Wilson, S. R. (2003). *Inorg. Chem.* **42**, 2410–2417.
Sheldrick, G. M. (1997). *SHELXS*97 and *SHELXL*97. University of Göttingen, Germany.
Srinivasan, B. R., Dhuri, S. N., Näther, C. & Bensch, W. (2003). *Acta Cryst.* C**59**, m124–m127.
Stoe & Cie (1998). *IPDS* (Version 2.89) and *X-SHAPE* (Version 1.03). Stoe & Cie, Darmstadt, Germany.
Yao, J. & Ibers, J. A. (2004). *Acta Cryst.* E**60**, i10–i11.

3.1.2

Synthesis, Crystal Structures and Properties of Three New Tetrathiomolybdates with Organic Ammonium Cations

Bikshandarkoil R. Srinivasan[a], Sunder N. Dhuri[a], Martha Poisot, Christian Näther, and Wolfgang Bensch

Institut für Anorganische Chemie, Christian-Albrechts-Universität Kiel, Olshausenstraße 40, D-24098 Kiel, Germany
[a] Department of Chemistry, Goa University PO, Goa 403 206, India

Reprint requests to Prof. Dr. Wolfgang Bensch. Fax: +49-(0)431-880-1520.
E-mail: wbensch@ac.uni-kiel.de

Z. Naturforsch. **59b,** 1083 – 1092 (2004); received June 9, 2004

Dedicated to Prof. Dr. Wilhelm Preetz on the occasion of his 70th birthday

Three new tetrathiomolybdates $(pipH_2)[MoS_4]$ (**1**), $(trenH_2)[MoS_4]\cdot H_2O$ (**2**) and $[(prop)_4N]_2[MoS_4]$ (**3**) (pip = piperazine, tren = tris(2-aminoethyl)amine and prop = *n*-propyl) were synthesized and characterized by elemental analysis, infrared spectroscopy, single crystal X-ray crystallography, and thermoanalysis. All compounds were prepared by the base promoted cation exchange method, *i.e.* by the reaction of the ammonium salt of $[MoS_4]^{2-}$ with the corresponding organic amine or organic ammonium hydroxide. In the compounds **1** and **2** the organic amines pip and tren are diprotonated and they are linked to the tetrahedral $[MoS_4]^{2-}$ dianions through weak hydrogen bonding interactions. The strength and number of these hydrogen bonds affect the Mo-S bond lengths and a relatively long Mo-S bond of 2.2114(8) Å is observed in **1** while the longest Mo-S bond in **2** is 2.1951(5) Å. In compound **3** no S···H-N interactions are possible and the Mo-S bond lengths scatter in a more narrow range compared to those in compounds **1** and **2**. The thermal behavior was investigated using differential thermal analysis and thermogravimetry. On heating compound **1** decomposes in two closely related steps while **2** loses first the crystal water followed by the decomposition of the tetrathiomolybdate. The final products are amorphous molybdenum sulfides. The decomposition of compound **3** yields a very porous material with sponge-like morphology.

Key words: Thiomolybdates, Crystal Structures, Thermal Properties, Optical Properties

Introduction

The chemistry of soluble metal sulfide complexes is emerging as a frontier area of research in view of the relevance of metal sulfide compounds in hydrodesulfurization catalysis (HDS), energy, environmental and material science [1]. In recent years, the use of tetraalkylammonium tetrathiomolybdates as precursor materials for the preparation of MoS_2 catalysts is showing much promise in the field of HDS catalysis [2]. The nature of the alkyl group in the precursors has been shown to affect the surface area, pore size distribution as well as HDS selectivity. Current and future investigations will be focused on the preparation of HDS catalysts, which have a large specific surface and a distinct ratio of rim and edge sites. The field of catalytically active transition metal sulfides has been reviewed [3, 4]. The synthesis and HDS activity of Ni-Mo-S catalysts [5] and Co-Mo-S catalysts [6] both derived from thiomolybdates have been reported recently.

The group VI metal Mo exhibits a wide range of metal to sulfur stoichiometries, metal oxidation states, coordination geometries and bonding modes of the sulfido ligands [7]. A variety of structurally diverse Mo-S compounds like $[MoS(S_4)_2]^{2-}$, $[Mo_2(S)_2(\mu\text{-}S)_2(S_2)_2]^{2-}$, $[Mo_2(S)_2(\mu\text{-}S)_2(S_4)(S_2)]^{2-}$, $[Mo_2(S)_2(\mu\text{-}S)_2(S_4)_2]^{2-}$, $[SMo(MoS_4)_2]^{2-}$ *etc.* have been prepared from tetrathiomolybdates by reacting with the appropriate reagents, which indicates the importance of the $[MoS_4]^{2-}$ moiety as a building block for the synthesis of several novel Mo-S complexes [8 – 12]. In recent years the use of tetrathiomolybdate for the treatment of metastatic cancer has added an entire new dimension to its chemistry [13, 14]. Although $[MoS_4]^{2-}$, one of the simplest soluble Mo-S complexes, has been known from the days of Berzelius

0932–0776 / 04 / 1000–1083 $ 06.00 © 2004 Verlag der Zeitschrift für Naturforschung, Tübingen · http://znaturforsch.com

[15], a systematic chemistry of this complex has been developed only in the last two to three decades primarily by Müller and coworkers [16]. The use of thiomolybdate as a versatile reagent for the preparation of a variety of compounds and also its relevance in bioinorganic chemistry and medicine has been recently reviewed [17]. It has been shown by Bezverkhyy *et al.* that $[MoS_4]^{2-}$ can be used as a precursor for the facile synthesis of highly dispersed MoS_2 [18]. The same group has reported that the chemical properties of $[MoS_4]^{2-}$ can be substantially changed by surrounding it with organic ammonium cations for example cetyltriethyl ammonium [19]. This report gains further credence from the work of Rauchfuss and co-workers wherein the reactivity characteristics of $[MoS_4]^{2-}$ towards PMe_3 (Me is methyl) have been reported [20]. Here it has been shown that acetonitrile solutions of $(Et_4N)_2[MoS_4]$ (Et is ethyl) and PMe_3 are stable, while acetonitrile solutions of $(NH_4)_2[MoS_4]$ and PMe_3 react to form the hexacoordinated Mo(IV) complex $[MoS_2(PMe_3)_4]$ indicating the role of proton sources for S transfer. A possible reason for this differing reactivity of $(NH_4)_2[MoS_4]$ and$(Et_4N)_2[MoS_4]$ has been attributed to the short H-bonding contacts between the cation and anion in $(NH_4)_2[MoS_4]$ [20], a structural feature which is absent in $(Et_4N)_2[MoS_4]$ [21].

In our work we have shown the importance of hydrogen bonding interactions in the lengthening of M-S (M = Mo or W) bond distances in several $[MS_4]^{2-}$ complexes [22–31]. The above observations taken together with our recent results in this area clearly indicate that a rich chemistry of thiomolybdates can be developed by suitably changing the hydrogen bonding interactions between the cation and $[MoS_4]^{2-}$. These studies can then be useful to derive a structure-function correlation in terms of the M-S bond distances. The H-bonding interactions in thiomolybdates can be fine tuned by a proper choice of the amine, which differs in its bulkiness and also the number of potential H-bonding donors attached to the amino nitrogen atoms. In the present work we have employed the cyclic amine piperazine (pip), the polyamine tris(2-aminoethylamine) (tren) and tetra-*n*-propylammonium hydroxide $[(prop)_4N]OH$ generated *in situ* from $[(prop)_4N]Br$ and NaOH, for the cation exchange reaction with ammonium tetrathiomolybdate. From these reactions we have isolated the compounds $(pipH_2)[MoS_4]$ (**1**), $(trenH_2)[MoS_4]\cdot H_2O$ (**2**) and $[(prop)_4N]_2[MoS_4]$ (**3**). In compound **1** both N atoms of pip are protonated resulting in the formation of $(pipH_2)^{2+}$, while only two of the four N atoms are protonated in **2** leading to the formation of $(trenH_2)^{2+}$. The structure of compound **1** which was reported earlier [32] has been redetermined by us at low temperatures, because the quality of the earlier structural data was poor. In compound **3** the N atoms of the cations are fully alkylated and hence S···H-N bonding is not possible. The compounds have been characterized by elemental analysis, infrared spectroscopy, single crystal X-ray crystallography and thermoanalysis. The results of these investigations are described in this paper.

Experimental Section

Materials and methods

The amines pip, tren, tetra-*n*-propylammonium bromide and ammonium heptamolybdate and the solvents were used in this investigation as obtained from commercial sources. $(NH_4)_2[MoS_4]$ was freshly prepared by literature method [33]. Far-IR spectra (range 80 to 500 cm^{-1}) were measured on a Bruker IFS 66 infrared spectrometer in pressed polyethylene disks. MIR spectra of the compounds were recorded in a KBr matrix. The samples were ground with dry KBr into fine powders and pressed into transparent pellets. The spectra were recorded in the IR region of 450 to 3000 cm^{-1}, (resolution 1 cm^{-1}) with a ATI Mattson Genesis infrared spectrometer. Raman spectra were measured in the region from 100 to 3500 cm^{-1} on a Bruker IFS 66 Fourier transform Raman spectrometer. DTA-TG measurements were performed simultaneously using the STA-409CD device (Netzsch). The thermal investigations were performed in Al_2O_3 crucibles using a heating rate of 4 K/min up to 600 °C and purged in a nitrogen stream of approximately 75 ml/min. EDX analysis was performed with a Philips ESEM XL 30 scanning electron microscope equipped with an EDAX analyzer. X-ray powder patterns were recorded in transmission geometry using a STOE STADI P diffractometer (Cu-K_α = 1.54056 Å).

*Preparation of $(pipH_2)[MoS_4]$ (**1**)*

Freshly prepared ammonium tetrathiomolybdate (260 mg, 1 mmol) was dissolved in distilled water (15 ml) and anhydrous piperazine (86 mg, 1 mmol) dissolved in distilled water (5 ml) was added at room temperature. The reaction mixture was stirred for ~ 5 min and then filtered. The clear filtrate was left undisturbed in a refrigerator. After 2 days red blocks of compound **1** were obtained which were filtered, washed with ice-cold water (2 ml) followed by isopropanol (10 ml) and diethylether (10 ml), and dried under vacuum. Yield 65%. – IR data: 3000 (br), 1544, 1440, 1371, 1297, 1186, 1079, 910, 862, 655, 556, 479, 465, 445, 336, 267, 200, 133, and 93 cm^{-1}. – Raman Data: 496, 478, 469, 448, 438,

Table 1. Technical details of data acquisition and selected refinement results for $(pipH_2)[MoS_4]$ **1**, $(trenH_2)[MoS_4]\cdot H_2O$ **2**, and $[(prop)_4N]_2[MoS_4]$ **3**.

Compound	$(pipH_2)$-$[MoS_4]$ (**1**)	$(trenH_2)$-$[MoS_4]\cdot H_2O$ (**2**)	$[(prop)_4N]_2$-$[MoS_4]$ (**3**)
Formula	$C_4H_{12}MoN_2S_4$	$C_6H_{22}N_4OMoS_4$	$C_{24}H_{56}N_2MoS_4$
MW [g/mol]	312.36	390.47	596.93
Space group	$P2_1/c$	$P2_1/c$	$C2/c$
a [Å]	8.2520(9)	11.470(2)	32.334(4)
b [Å]	11.238(1)	11.793(2)	13.812(2)
c [Å]	11.929(2)	12.483(2)	15.017(3)
β [°]	95.20(2)	111.63(1)	109.24(2)
Volume [Å^3]	1101.7(2)	1569.5(4)	6331.7(2)
Z	4	4	8
Temperature / K	293	293	293
μ [mm^{-1}]	1.90	1.356	0.69
$F(000)$	624	800	2560
$d_{calc.}$ [g· cm^{-3}]	1.883	1.652	1.252
2θ Range [°]	3 – 60	3 – 60	3 – 60
hkl Range	0/11;−14/4; −16/16	−16/1;−16/16; −16/17	−42/40;−18/12; 0/19
Refls collected	5058	9614	14726
Refls unique	3217	4588	7657
Data [$F_o>4\sigma(F_o)$]	2258	3990	5001
$R_{int.}$	0.0535	0.0229	0.0395
min./max transm.	–	0.7867 / 0.8513	–
$\delta\rho$ [e/Å^3]	−0.69 /0.670	−0.80 /0.46	0.28 / −0.47
Parameters	101	146	511
R_1 [$F_o>4\sigma(F_o)$][a]	0.0290	0.0209	0.0305
$wR2$ for all data	0.0730	0.0560	0.0758
Goodness of fit	1.017	1.042	0.977

[a] $R_1 = \Sigma||Fo| - |Fc||/\Sigma|Fo|$.

Table 2. Atomic coordinates [$\times 10^4$] and equivalent isotropic displacement parameters [Å$^2 \times 10^3$] for $(pipH_2)[MoS_4]$ **1**.

Atom	x	y	z	U_{eq}
Mo(1)	7927(1)	2790(1)	5944(1)	22(1)
S(1)	7930(1)	3920(1)	7418(1)	30(1)
S(2)	5739(1)	1646(1)	5854(1)	29(1)
S(3)	10115(1)	1663(1)	6118(1)	29(1)
S(4)	7924(1)	3860(1)	4431(1)	33(1)
N(1)	4594(3)	2698(2)	8239(2)	29(1)
C(1)	3680(3)	1576(3)	8328(2)	29(1)
C(2)	2314(3)	1739(3)	9079(2)	28(1)
N(2)	1242(3)	2737(2)	8668(2)	28(1)
C(3)	2168(4)	3864(3)	8582(3)	34(1)
C(4)	3525(4)	3693(3)	7823(3)	32(1)

U_{eq} is calculated as one third of the trace of the orthogonalised U_{ij} tensor.

199, 184 and 175 cm^{-1}. – Analysis found (calcd): C 15.04 (15.38), H 3.83 (3.88), N 8.71 (8.97), S 40.95 (41.06).

*Preparation of $(trenH_2)[MoS_4]\cdot H_2O$ (**2**)*

Freshly prepared ammonium tetrathiomolybdate (520 mg, 2 mmol) was dissolved in distilled water (50 ml) containing 5 drops of ammonia solution. An aqueous tren solution

Table 3. Atomic coordinates [$\times 10^4$] and equivalent isotropic displacement parameters [Å$^2 \times 10^3$] for $(trenH_2)[MoS_4]\cdot H_2O$ **2**.

Atom	x	y	z	U_{eq}
Mo(1)	1787(1)	3575(1)	2323(1)	26(1)
S(1)	53(1)	3020(1)	2509(1)	41(1)
S(2)	1543(1)	3576(1)	498(1)	35(1)
S(3)	3266(1)	2420(1)	3299(1)	40(1)
S(4)	2250(1)	5303(1)	3001(1)	39(1)
N(1)	6392(1)	3908(1)	3075(1)	29(1)
C(1)	6714(1)	2725(1)	3417(1)	33(1)
C(2)	8024(1)	2645(1)	4327(1)	34(1)
N(2)	8369(1)	1440(1)	4636(1)	34(1)
C(3)	5928(2)	4490(1)	3883(1)	34(1)
C(4)	6272(2)	5731(2)	4004(1)	43(1)
N(3)	7644(2)	5876(1)	4469(1)	46(1)
C(5)	5477(2)	4004(2)	1886(1)	36(1)
C(6)	6023(2)	3710(2)	981(1)	39(1)
N(4)	7069(2)	4412(1)	976(1)	43(1)
O(1)	9395(2)	5453(2)	3441(2)	86(1)

Table 4. Atomic coordinates [$\times 10^4$] and equivalent isotropic displacement parameters [Å$^2 \times 10^3$] for $[(prop)_4N]_2$-$[MoS_4]$ **3**.

Atom	x	y	z	U_{eq}
Mo(1)	3732(1)	7430(1)	4146(1)	36(1)
S(1)	4195(1)	6680(1)	3596(1)	51(1)
S(2)	3165(1)	7934(1)	2983(1)	56(1)
S(3)	3504(1)	6435(1)	5006(1)	61(1)
S(4)	4056(1)	8660(1)	5010(1)	60(1)
N(1)	2550(1)	4890(1)	6034(1)	34(1)
C(1)	2485(1)	5318(2)	5058(1)	35(1)
C(2)	2197(1)	6197(2)	4787(2)	45(1)
C(3)	2179(1)	6536(2)	3813(2)	49(1)
C(4)	2112(1)	4630(2)	6138(2)	42(1)
C(5)	1830(1)	3937(2)	5409(2)	56(1)
C(6)	1418(1)	3706(2)	5627(2)	64(1)
C(7)	2770(1)	5639(2)	6777(1)	41(1)
C(8)	2876(1)	5297(2)	7791(2)	65(1)
C(9)	3095(1)	6085(3)	8459(2)	96(1)
C(10)	2829(1)	3983(2)	6141(2)	42(1)
C(11)	3310(1)	4137(2)	6277(2)	47(1)
C(12)	3515(1)	3196(2)	6119(2)	52(1)
N(2)	5000	9109(2)	2500	36(1)
C(21)	5070(1)	8454(2)	3351(2)	40(1)
C(22)	5116(1)	8970(2)	4275(2)	53(1)
C(23)	5205(1)	8250(2)	5075(2)	58(1)
C(24)	5397(1)	9758(2)	2640(2)	44(1)
C(25)	5823(1)	9242(2)	2777(2)	58(1)
C(26)	6180(1)	9970(2)	2792(2)	75(1)
N(3)	5000	4220(2)	2500	44(1)
C(31)	5224(2)	5056(5)	3192(4)	53(1)
C(32)	5424(2)	4808(5)	4222(4)	72(2)
C(31')	5124(2)	4575(4)	3469(4)	47(1)
C(32')	5486(2)	5321(5)	3731(5)	63(2)
C(33)	5594(1)	5632(2)	4786(2)	83(1)
C(34)	5338(2)	3395(4)	2648(4)	48(1)
C(35)	5771(2)	3621(5)	2500(4)	64(2)
C(34')	5366(2)	3842(4)	2179(4)	56(1)
C(35')	5606(2)	3028(5)	2733(5)	73(2)
C(36)	6025(1)	2754(3)	2540(2)	95(1)

Table 5. Selected interatomic distances (Å) and angles (°) for $(pipH_2)[MoS_4]$ **1**, $(trenH_2)[MoS_4]\cdot H_2O$ **2** and $[(prop)_4N]_2[MoS_4]$ **3**.

$(pipH_2)[MoS_4]$ **1**:			
Mo(1)−S(4)	2.1683(8)	Mo(1)−S(1)	2.1687(8)
Mo(1)−S(3)	2.2004(7)	Mo(1)−S(2)	2.2114(8)
S(4)−Mo(1)−S(1)	110.48(3)	S(4)−Mo(1)−S(3)	109.71(3)
S(1)−Mo(1)−S(3)	108.66(3)	S(4)−Mo(1)−S(2)	110.04(3)
S(1)−Mo(1)−S(2)	108.71(3)	S(3)−Mo(1)−S(2)	109.21(3)
$(trenH_2)[MoS_4]\cdot H_2O$ **2**:			
Mo(1)−S(3)	2.1670(5)	Mo(1)−S(1)	2.1856(5)
Mo(1)−S(2)	2.1905(5)	Mo(1)−S(4)	2.1951(5)
S(3)−Mo(1)−S(1)	107.89(2)	S(3)−Mo(1)−S(2)	110.97(2)
S(1)−Mo(1)−S(2)	109.79(2)	S(3)−Mo(1)−S(4)	109.79(2)
S(1)−Mo(1)−S(4)	109.71(2)	S(2)−Mo(1)−S(4)	108.68(2)
$[(prop)_4N]_2[MoS_4]$ **3**:			
Mo(1)−S(3)	2.1749(7)	Mo(1)−S(4)	2.1837(7)
Mo(1)−S(2)	2.1885(8)	Mo(1)−S(1)	2.1928(7)
S(3)−Mo(1)−S(4)	109.19(3)	S(3)−Mo(1)−S(2)	108.34(3)
S(4)−Mo(1)−S(2)	109.76(3)	S(3)−Mo(1)−S(1)	109.48(3)
S(4)−Mo(1)−S(1)	109.79(3)	S(2)−Mo(1)−S(1)	110.25(3)

(0.5 ml in 10 ml water) was added at room temperature. The reaction mixture was filtered and the clear filtrate was left undisturbed. After a day red blocks of compound **2** were obtained, which were filtered, washed with ice-cold water (2 ml), followed by isopropanol (15 ml) and diethylether (20 ml), and dried under vacuum. Yield 70%. – IR data: 3462 (br), 3328(w), 3277(w), 3072, 3004, 2924, 2829, 1601, 1569, 1513, 1464, 1345, 1295, 1115, 1071, 1007, 963, 857, 755, 487, 467, 450, 357, 344, 248, 215, 203, 185, 132, and 101 cm^{-1}. – Analysis found (calcd): C 18.34 (18.45), H 5.71 (5.64), N 14.23 (14.35), S 32.63 (32.85).

*Preparation of $[(prop)_4N]_2[MoS_4]$ (**3**)*

Freshly prepared $(NH_4)_2MoS_4$ (2 g, 7.7 mmol) was dissolved in distilled water (60 ml). This solution was added to a mixture of tetra-*n*-propylammonium bromide (4 g, 15.4 mmol) and NaOH (0.6 g, 15.5 mmol) in distilled water (10 ml). The resulting solution was stirred at room temperature for 10 min and then kept undisturbed overnight, precipitating red crystals of $[(prop)_4N]_2MoS_4$. The crystalline compound was filtered, washed with ice-cold water (2 ml), followed by isopropanol (15 ml) and diethylether (20 ml), and dried under vacuum. Yield 80%. – IR data: 2965 (br), 2931, 2871, 1470 (s), 1376 (w), 1325 (w), 970 (s), 759 (w), 475 (sh), 465 (s), 448 (w), cm^{-1}. – Analysis found (calcd): C 47.95 (48.3), H 9.5 (9.4), N 4.6 (4.7), S 20.8 (21.5).

Single crystal X-ray diffractometry

Intensity data for compounds **1**–**3** were collected on a AED2 four circle diffractometer at room temperature using graphite monochromated Mo-K_α radiation. For **2** a numerical absorption correction was applied. All structures were solved with direct methods using SHELXS-97 [34] and refinement was carried out against F^2 using SHELXL-97 [35]. All non-hydrogen atoms were refined using anisotropic displacement parameters. The hydrogen atoms were positioned with idealized geometry and refined using the riding model with fixed isotropic displacement parameters. Four carbon atoms of one of the three crystallographically independent tetra-*n*-propylammonium cations were disordered in two positions and were refined using a split model. The technical details of data acquisition and some selected refinement results are summarized in Table 1. The atomic coordinates and equivalent isotropic displacement parameters for compounds **1**–**3** are presented in Tables 2–4. Selected bond lengths, and bond angles for compounds **1** to **3** and hydrogen bonding parameters are listed in Tables 5–7.

Table 6. Hydrogen-bonding geometry (Å, °) for $(pipH_2)[MoS_4]$ **1**.

D-H···A	d(D-H)	d(H···A)	d(D···A)	∠DHA	Symmetry code
N1-H1A···S2	0.900	2.561	3.298	139.62	
N1-H1A···S1	0.900	2.648	3.303	130.33	
N1-H1B···S2	0.900	2.379	3.260	166.21	$x, -y+\frac{1}{2}, z+\frac{1}{2}$
N2-H2C···S3	0.900	2.465	3.219	141.50	$x-1, -y+\frac{1}{2}, z+\frac{1}{2}$
N2-H2C···S4	0.900	2.884	3.465	123.65	$x-1, -y+\frac{1}{2}, z+\frac{1}{2}$
N2-H2D···S3	0.900	2.454	3.255	162.91	$x-1, y, z$
N2-H2D···S1	0.900	2.819	3.274	112.72	$x-1, y, z$

Table 7. Hydrogen-bonding geometry (Å, °) for $(trenH_2)[MoS_4]\cdot H_2O$ **2**.

D-H…A	d D-H	d H…A	d D…A	∠ DHA	Symmetry code
N1-H1···S2	0.860	2.583	3.396	158.03	$x+1, -y+\frac{1}{2}, z+\frac{1}{2}$
N1-H1···S1	0.860	2.936	3.448	120.06	$x+1, -y+\frac{1}{2}, z+\frac{1}{2}$
N2-H2···S4	0.860	2.530	3.379	169.34	$-x+1, y-\frac{1}{2}, -z+\frac{1}{2}$
N2-H2···S2	0.860	2.992	3.386	110.12	$-x+1, y-\frac{1}{2}, -z+\frac{1}{2}$
N2-H3···N4	0.860	1.946	2.805	177.06	$x, -y+\frac{1}{2}, z+\frac{1}{2}$
N3-H1···S4	0.860	2.623	3.413	153.12	$-x+1, -y+1, -z+1$
N3-H2···O1	0.860	1.985	2.797	157.11	
N3-H3···S2	0.860	2.458	3.313	172.51	$-x+1, y+\frac{1}{2}, -z+\frac{1}{2}$
N4-H1···S3	0.890	2.929	3.715	148.18	$-x+1, y+\frac{1}{2}, -z+\frac{1}{2}$
N4-H2···S1	0.890	3.019	3.638	128.29	$x+1, y, z$
O1-H1···S1	0.820	2.499	3.286	161.38	$x+1, y, z$
O1-H2···S1	0.820	2.586	3.395	169.33	$-x+1, y+\frac{1}{2}, -z+\frac{1}{2}$

Crystallographic data (excluding structure factors) have been deposited with the Cambridge Crystallographic Data Centre as supplementary publication no. CCDC 241130 (**1**), CCDC 241131 (**2**) and CCDC 241132 (**3**). Copies of the data can be obtained, free of charge, on application to CCDC, 12 Union Road, Cambridge CB2 1 EZ, UK. (fax: +44-(0)1223-336033 or email: deposit@ccdc.cam.ac.uk).

Results and Discussion

Synthetic aspects

The synthesis of the title compounds has been readily accomplished in good yields by reacting $(NH_4)_2[MoS_4]$ with the corresponding organic amines. In the synthesis of **3**, tetra-*n*-propylammonium hydroxide is generated *in situ* by the reaction of tetra-n-propylammonium bromide with NaOH, which then functions as the organic base. The formation of the title complexes from ammonium tetrathiomolybdate on treatment with the organic amines can be explained as a base promoted cation exchange reaction, wherein the stronger organic base replaces the weak ammonia of $(NH_4)_2[MoS_4]$ as shown below. We have used a similar methodology for the isolation of tetrathiomolybdates as well as tetrathiotungstates $[MS_4]^{2-}$ (M = Mo, W) with ethylenediammonium, 1,3-propanediammonium, N,N,N',N'-tetramethylethylenediammonium and 1,4-dimethylpiperazinium cations indicating the generality of this reaction [26–30].

$$(NH_4)_2[MoS_4] + amine/ammoniumhydroxide \rightarrow \mathbf{1}-\mathbf{3} + 2NH_3$$

The compounds are quite stable in air and less soluble in water unlike ammonium tetrathiomolybdate.

Crystal structures

In the structures of the title compounds tetrahedral $[MoS_4]^{2-}$ anions and the counter cations $(pipH_2)^{2+}$ (in **1**), $(trenH_2)^{2+}$ (in **2**), and $[(prop)_4N]^+$ (in **3**) are found. In **1** and **2** all unique atoms are on general positions whereas in **3** N(2) and N(3) are located on special positions. In compound **1** piperazinium cations and tetrahedral $[MoS_4]^{2-}$ anions are connected *via* weak hydrogen bonds. In **1** the cyclic organic cation adopts the chair form and the C-C and C-N bond lengths and bond angles are in good agreement with those reported for other complexes containing the same cation [36,37]. The MoS_4 tetrahedron is distorted with S-Mo-S angles between 108.66(3) and 110.04(3)°. The Mo-S bond distances vary from 2.1683(8) to 2.2114(8) Å, with a mean Mo-S bond length of 2.1872 Å (Table 5). Although the geometric parameters of **1** are in agreement with those in other thiomolybdates like $(enH_2)[MoS_4]$ (en = ethylenediamine) [26] or $[Co_2(tren)_3][MoS_4]_2$ [24], two of the Mo-S bond distances are longer,

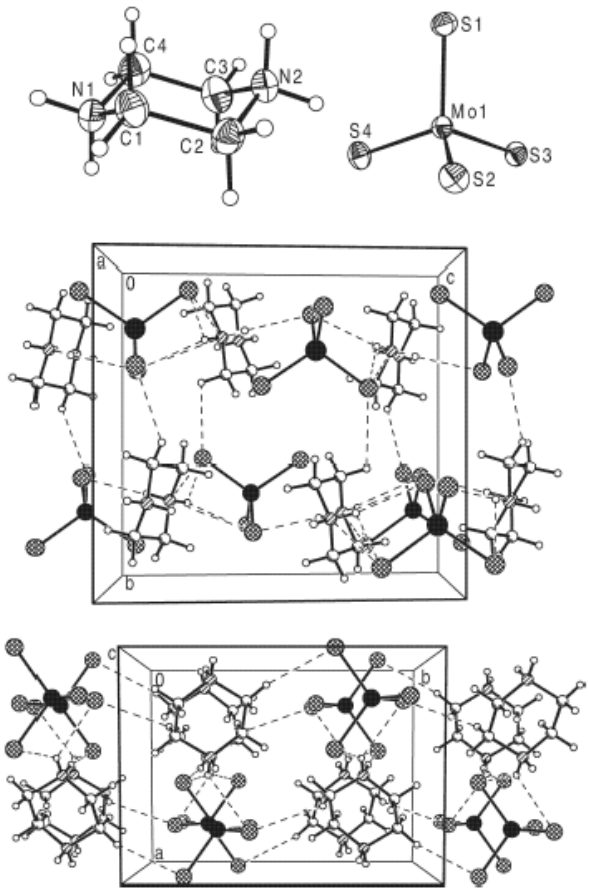

Fig. 1. Crystal structure of $(pipH_2)[MoS_4]$ **1** with labeling and displacement ellipsoids drawn at the 50% probability level (top), with view in the direction of the crystallographic *a*-axis (middle) and *c*-axis (bottom) (hydrogen bonding is shown as dashed lines).

while the other two distances are shorter than the average Mo-S bond length of 2.177(6) Å reported for $(Et_4N)_2[MoS_4]$ [21]. The elongation of Mo-S bond distances in **1** can be attributed to the observed short hydrogen bonding contacts (2.379 to 2.884 Å) between the cation and anion (Table 6). This results in an extended three-dimensional network as shown in Fig. 1. The S···H distances in **1** are shorter than the S···H distances of 2.55 to 3.02 Å reported for $(NH_4)_2[MoS_4]$ [20]. The atoms S(1,2,3) have two S···H contacts and S(4) has one such interaction. This feature is responsible for the very short Mo-S(4) distance of 2.1683 Å. The small D-H···A bond angle of 123.65° together with the longest S···H distance of 2.884 Å observed for S(4) indicates a very weak interaction. The shortest S···H distance of 2.379 Å is accompanied by the

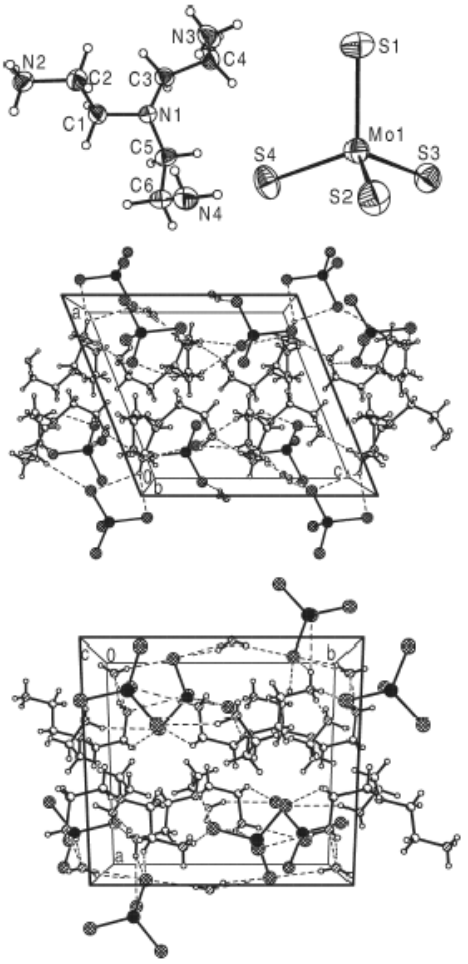

Fig. 2. Crystal structure of $(trenH_2)[MoS_4]\cdot H_2O$ **2** with labeling and displacement ellipsoids drawn at the 50% probability level (top), with view in the direction of the crystallographic *a*-axis (middle) and *c*-axis (bottom) (hydrogen bonding is shown as dashed lines).

largest D-H···A angle which can explain the long Mo-S(2) bond of 2.2114(8) Å. The intermediate Mo-S bond lengths can be similarly explained based on the strengths of the H-bonding interactions. To the best of our knowledge the Mo-S(2) distance of 2.2114(8) Å in **1** is one of the longest Mo-S bond lengths reported so far for tetrathiomolybdate complexes. It is also noted that the difference between the longest and the shortest Mo-S bond distances of 0.0431 Å in **1** is very large. This is probably responsible for the appearance of a split Mo-S vibration in the IR spectrum.

In the structure of **2** diprotonated tren cations, tetrathiomolybdate anions and crystal water are present (Fig. 2). Only two of the four N atoms in tren are protonated while the tertiary atom N(1) as well as one of the primary amino group N(4) are not protonated. A similar feature has been observed in $(trienH_2)[MoS_4]$ (trien = triethylenetetramine) which is derived from the isomeric amine trien [38]. All interatomic distances and angles in the tren cation are in agreement with the data reported for complexes containing the tren moiety like $[Co_2(tren)_3][MoS_4]_2$ [24]. As in **1** the $[MoS_4]$ tetrahedron is distorted with S-Mo-S angles between 107.89(2) and 110.97(2)° and Mo-S bond lengths from 2.1670(5) to 2.1951(5) Å, with a mean Mo-S distances of 2.1846 Å (Table 5). In **2** three of the Mo-S bonds are longer than the average Mo-S distance of 2.177 Å reported for $(Et_4N)_2[MoS_4]$ [21]. In **2** short S···H contacts are observed between the organic cation and the anion (Table 7), and the crystal water is also involved in two H···S(1) interactions. The resulting H bonding network is shown in Fig. 2. The S···H contacts range from 2.458 to 3.019 Å and are shorter than those (2.55 to 3.02 Å) reported for $(NH_4)_2[MoS_4]$ [20]. The shortest Mo-S bond length of 2.1670(5) Å is observed for S(3), which has only one contact to a H atom at a distance of 2.929 Å (Table 7). The analysis of the situation for S(1) and S(4) shows some interesting trends. The atom S(4) has two H atoms at distances 2.623 and 2.530 Å with corresponding angles of 153.12 and 169.34° and the longest Mo-S bond length of 2.1951(5) Å. On the other hand, S(1) has four interactions with H atoms, two with H atoms of the ammonium groups and two with H atoms of the water molecule. The two former are very weak (2.936 Å, angle: 120.06°; 3.019 Å, 128.29°) while the latter two interactions are significantly stronger (2.499 Å, 161.38°; 2.586 Å, 169.33°). The resulting Mo-S(1) bond of 2.1856(5) Å is surprisingly short as one would expect that this bond is at least as long as the Mo-S(4) bond. One possible explanation may be that despite the short S(1)···H distances to the H atoms of the water molecule the interactions are weaker than with H atoms bound to N with S···H separations of comparable lengths. Finally, S(2) has two short contacts (Table 7), and the Mo-S(2) bond amounts to 2.1905(5) Å. The difference between the longest and the shortest Mo-S bond distances in **2** of 0.0281 Å is slightly smaller than that observed in **1**.

In compound **3** three crystallographically independent $[(prop)_4N]^+$ cations are observed with two of them located in special positions (see Fig. 3). The C-C and C-N bond lengths as well as the angles observed

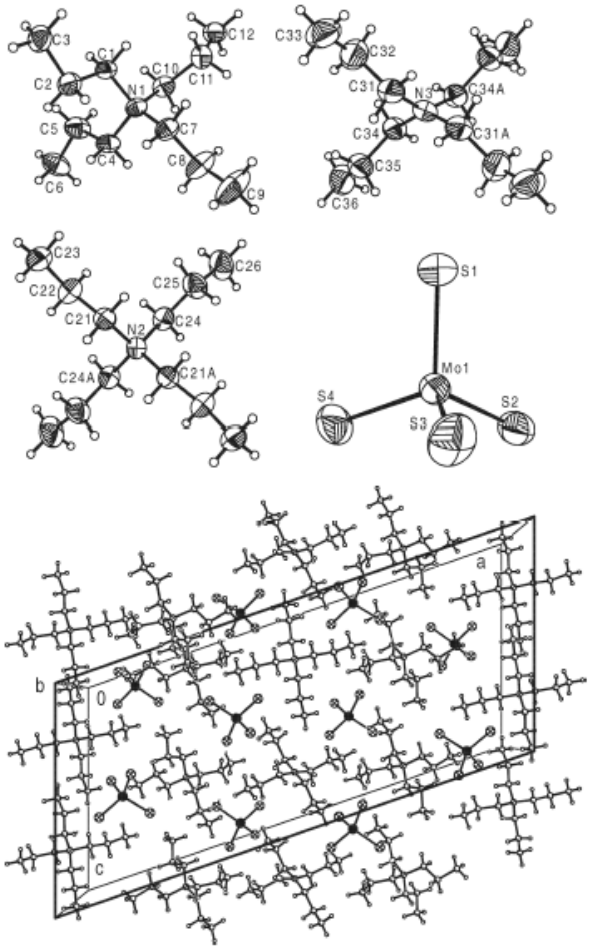

Fig. 3. Crystal structure of $[(prop)_4N]_2[MoS_4]$ **3** with labeling and displacement ellipsoids drawn at the 50% probability level (top), with view in the direction of the crystallographic *c*-axis (bottom).

for the cation are in the normal range. The S-Mo-S angles between 108.34(1)° and 110.25(1)° (Table 5) demonstrate the distortion of the $[MoS_4]^{2-}$ tetrahedron. The Mo-S bond lengths scatter in a more narrow range than in **1** and **2** with values from 2.1749(7) to 2.1928(7) Å and a mean Mo-S bond distance of 2.1850 Å. The difference between the longest and shortest bond amounts to 0.0179 Å and is the lowest value for all three compounds. It is interesting to note that the average Mo-S distance in **3** is significantly longer than in $(Et_4N)_2[MoS_4]$ of 2.177(6) Å.

Spectral studies

Several bands in the central part of the IR spectra observed for compounds **1**, **2** and **3** can be attributed to absorptions of the cations. The infrared spectrum of **2** exhibits a broad and strong band at around 3462 cm^{-1} that is assignable to the O-H stretching vibration of the crystal water. In contrast, the anhydrous compounds **1** or **3** are devoid of any bands above 3100 cm^{-1}. The N-H stretching vibrations appear at around 3000 cm^{-1} in **1** and at 3072 and 3004 cm^{-1} in **2**. Since complex **2** contains protonated amine as well as free amine more bands are observed for **2** in the N-H region. The shift to lower wave numbers compared to the free amine in **1** or **2** can be attributed to the H-bonding interactions (N-H···S) between the organic cation and the tetrathiomolybdate anion. For the free tetrahedral $[MoS_4]^{2-}$ anion four characteristic bands $\nu_1(A_1)$, $\nu_2(E)$, $\nu_3(F_2)$, and $\nu_4(F_2)$ are expected [16, 39]. All four bands are Raman active while only ν_3 and ν_4 are infrared active. Many tetrathiomolybdates exhibit a single strong band at around 475 cm^{-1} assignable to the triply degenerate asymmetric stretching vibration (ν_3) of the Mo=S bond [16, 26, 33]. Interestingly, for **1** this vibration is split up and appears as a doublet at 479 and 465 cm^{-1} with a further band around 445 cm^{-1}. The observed extra signals cannot be assigned to vibrations of the organic cation in view of the fact that no strong signals are observed for $(pipH_2)Cl_2$ below 500 cm^{-1}. Hence these features indicate considerable distortion of the $[MoS_4]$ tetrahedron and can be explained by the lowering in symmetry [16], which is probably responsible for the symmetric stretching vibration (ν_1) of the Mo=S bond at 445 cm^{-1} to appear as a medium intensity band. The IR inactive (ν_1) vibration is seldom observed for undistorted tetrahedral compounds. The assignment of the 445 cm^{-1} band for the symmetric stretching vibration gains credence form the observation of an intense signal in the Raman spectrum of **1** at 448 cm^{-1}. For **2** the IR absorptions are located at around 487 and 467 cm^{-1} with a very weak shoulder at 450 cm^{-1}. The same arguments can be used to explain the occurrence of three bands instead of one when the $[MoS_4]$ tetrahedron is not distorted. The reduced symmetry of the anion in **3** is also obvious from its IR spectrum. A broad asymmetric and intense band with the maximum located at 464 cm^{-1} is seen with a shoulder at 474 cm^{-1}. A third signal occurs at 448 cm^{-1}.

Thermal studies

The thermal stability of all three compounds was investigated using DTA-TG measurements. On heating

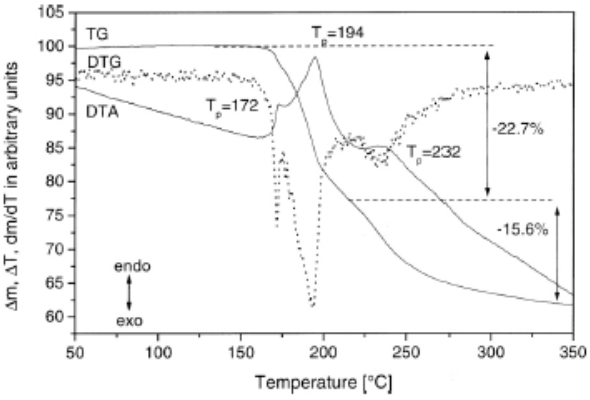

Fig. 4. DTA, TG and DTG curves for $(pipH_2)[MoS_4]$ **1** (heating rate 4 K/min; N_2 atmosphere; given are the peak temperatures (T_p) in °C and the mass loss in %).

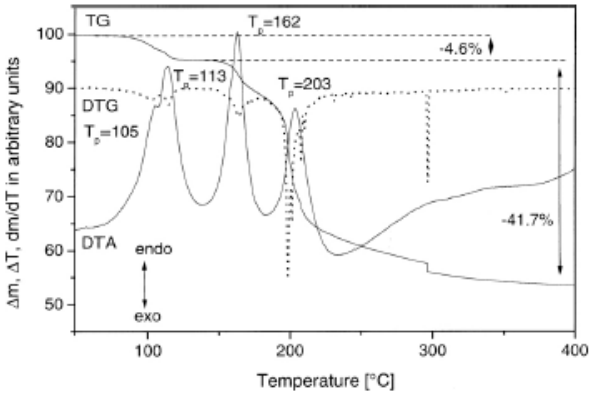

Fig. 5. DTA, TG and DTG curves for $(trenH_2)[MoS_4]\cdot H_2O$ **2** (heating rate 4 K/min; N_2 atmosphere; given are the peak temperatures (T_p) in °C and the mass loss in %).

compound **1**, the decomposition starts at about 170 °C, which is accompanied by endothermic events in the DTA at 172 and 194 °C (Fig. 4). From the DTG curve it is obvious that this reaction occurs in several steps, which cannot be fully resolved. The complete mass loss up to 330 °C where the DTG curve shows a minimum is about 38.3%, which is in good agreement with the emission of hydrogen sulfide and piperazine (Δm_{theo}(-piperazine/-H_2S) = 38.5%) resulting in the formation of MoS_3 according to the following equation (1):

$$(pipH_2)[MoS_4] \rightarrow pip + H_2S + MoS_3 \qquad (1)$$

The simultaneous emission of amine and H_2S has been observed by us earlier during a thermal decomposition study of $(1,3\text{-}pnH_2)[MoS_4]$ (1,3-pn is 1,3-propanediamine) [27]. On further heating of the sample, a slow mass decrease was observed and the residual mass of 60.6% at about 800 °C (not shown in the DTA-TG curve) shows that the intermediately formed MoS_3 is transformed into MoS_2. The elemental analysis of the black residue indicates that a small amount of C and N remained in the product, the X-ray powder pattern of which showed no sharp reflections but only broad humps indicating that an amorphous product was formed.

When compound **2** is heated a single mass step of 4.6% occurs at about 80 °C, which can be attributed to the loss of the water incorporated in the crystals (Δm_{theo}(-H_2O) = 4.6%) (Fig. 5). From the DTA and the DTG curve it is obvious that this reaction consists of two endothermic events, which occur at 105 and 113 °C. The loss of water is complete at about 140 °C. On further heating the sample mass decreases strongly and two endothermic events are observed at 162 and 203 °C. The DTG curve shows that the decomposition reaction proceeds in three different steps, which cannot fully be resolved. The experimental mass loss up to about 290 °C where the DTG curve shows a minimum is about 37.4% which is in good agreement with the loss of the amine ligands (Δm_{theo}(-tris(2-aminoethyl)amine)) = 37.4%). However, the C, H, N analysis of the final black residue revealed the presence of large amounts of organic matter and therefore, it can be assumed that as in the decomposition of compound **1** the amine and H_2S are emitted simultaneously. Upon a further increase of the temperature the sample mass decreases slowly. The C, H and N analytical data of the residue indicate the formation of a contaminated MoS_{3-x} sulfide. An X-ray examination of the residue showed it to be amorphous. Therefore, the decomposition of compound **2** follows predominantly the following equation (2):

$$(trenH_2)[MoS_4]\cdot H_2O \rightarrow tren + H_2S + MoS_3 + H_2O \qquad (2)$$

For **3**, DTA-TG measurements showed a strong endothermic event at 99 °C (Fig. 6). Because the sample mass remains constant it can be inferred that a phase transition occurs. With an increase in temperature, a mass loss is observed in two steps. The DTG curve shows that the first mass loss consists of several different successive steps, which cannot be fully resolved. The complete mass loss up to 360 °C is 69.6% which is slightly more than expected for the loss of the organic components and sulfur leading to the formation

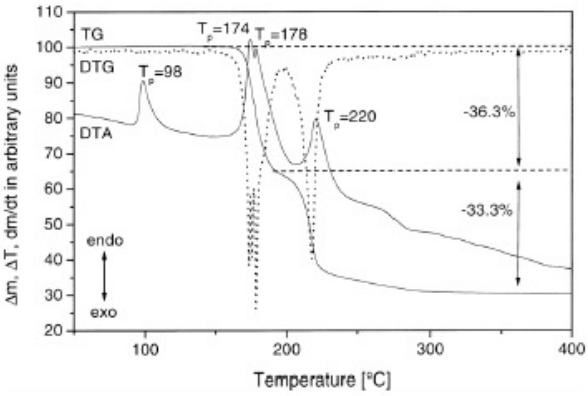

Fig. 6. DTA, TG and DTG curves for $[(prop)_4N]_2[MoS_4]$ **3** (heating rate 4 K/min; N_2 atmosphere; given are the peak temperatures (T_p) in °C and the mass loss in %).

of MoS_3 ($\Delta m_{theo}(-C_{24}H_{56}N_2S)$) = 67.8%). However, elemental analysis shows residual carbon in the product (composition: $MoS_2C_{0.7}$) suggesting that MoS_2 is formed.

The thermal properties of compound **3** were also investigated in the past [2, 40]. The authors proposed the following sequence of decomposition steps (3, 4):

$$\mathbf{3} \rightarrow (CH_3CH_2CH_2)_3N + CH_3CH_2CH_2NS + (CH_3CH_2CH_2)_4MoS_3 \quad (3)$$

$$(CH_3CH_2CH_2)_4MoS_3 \rightarrow (CH_3CH_2CH_2)_2S + CH_3(CH_2)_4CH_3 + MoS_2 \quad (4)$$

These reaction steps were obviously assigned based on the mass changes alone during the decomposition. In the earlier work an initial mass loss of 2% was also reported and attributed to elimination of impurities like trace amounts of water [40]. To shed further light onto this complex behavior we investigated the thermal reactions with DTA-TG measurements coupled with mass spectroscopy. In contrast to the previous investigations we find that the mass spectra in both steps are identical which show that in both steps the same compounds are emitted. An analysis of the pattern shows clearly that tripropylamine (m/z = 143) is emitted in both steps. The remaining peaks can be assigned to the formation of dipropyldisulfide ($CH_3CH_2CH_2SSCH_2CH_2CH_3$; m/z = 150). There are no hints for the formation of $CH_3CH_2CH_2NS$, $(CH_3CH_2CH_2)_2S$ or $CH_3(CH_2)_4CH_3$ as proposed from the results obtained in previous investigations

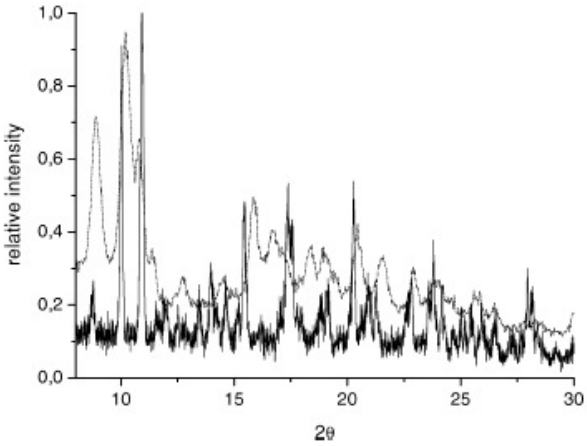

Fig. 7. X-ray powder pattern of compound **3** (full line) and of the product obtained when the thermal decomposition is stopped at 200 °C (dotted line).

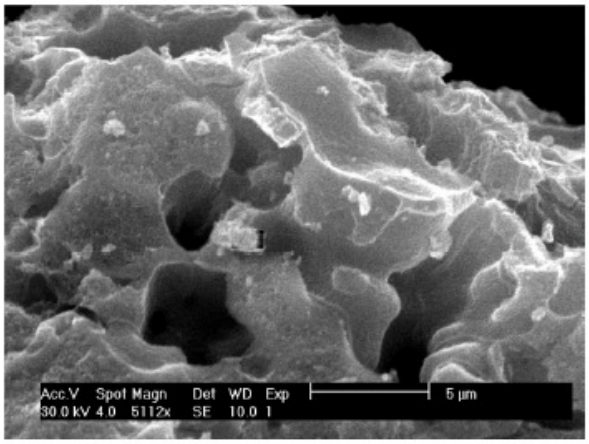

Fig. 8. SEM micrograph of the decomposition product of compound **3**.

[40]. The following equation may account for our observations (5):

$$\mathbf{3} \rightarrow 2\,(CH_3CH_2CH_2)_3N + (CH_3CH_2CH_2SSCH_2CH_2CH_3) + 2\,MoS_2 \quad (5)$$

However, if the reaction is stopped after the first TG step at about 200 °C, the X-ray powder pattern is completely different from that of the starting compound and does not correspond to that of MoS_3 or MoS_2 (Fig. 7). The relatively low modulation shows also that practically no amorphous molybdenum sulfides are present. This experiment is indicative of the fact that some unknown intermediate compound is formed and that the overall reaction must be more complicated.

The decomposition products were also examined with Scanning Electron Microscopy. The products of **1** and **2** are composed of fine particles with a plate-like morphology. In contrast the product of **3** shows pores with diameters in the μm range and a sponge-like morphology (Fig. 8). This observation is in accordance with literature results [2] where the mesoporosity was explained due to the accumulation of gases during the thermal decomposition process, the formation of channels being caused upon the escape of the gases to the surface of the material.

Acknowledgements

Financial support by the State of Schleswig-Holstein and the Deutsche Forschungsgemeinschaft (DFG) is gratefully acknowledged. Work done at Goa University is supported by the University Grants Commission (UGC) New Delhi under the Special Assistance Program.

[1] T. Rauchfuss, Inorg. Chem. **43**, 14 (2004) and references cited therein.
[2] G. Alonso, G. Berhault, A. Aguilar, V. Collins, C. Ornelas, S. Fuentes, R. R. Chianelli, J. Catal. **208**, 359 (2002).
[3] M. Breysse, E. Furimsky, S. Kasztelan, M. Lacroix, G. Perot, Catal. Rev. **44**, 651 (2002).
[4] D. D. Whitehurst, T. Isoda, I. Mochida, Adv. Catal. **42**, 345 (1988).
[5] F. Pedraza, S. Fuentes, Catal. Lett. **65**, 107 (2000).
[6] H. Nava, C. Ornelas, A. Aguilar, G. Berhault, S. Fuentes, G. Alonso, Catal. Lett. **86**, 257 (2003).
[7] D. Coucouvanis, Adv. Inorg. Chem. **45**, 1 (1998).
[8] E. D. Simhon, N. C. Baenziger, M. G. Kanatzidis, D. Coucouvanis, J. Am. Chem. Soc. **103**, 1218 (1981).
[9] W. H. Pan, M. A. Harmer, T. R. Halbert, E. I. Stiefel, J. Am. Chem. Soc. **106**, 459 (1984).
[10] M. Draganjac, E. Simhon, L. T. Chan, M. G. Kanatzidis, N. C. Baenziger, D. Coucouvanis, Inorg. Chem. **21**, 3321 (1982).
[11] S. A. Cohen, E. I. Stiefel Inorg. Chem. **24**, 4657 (1984).
[12] W. H. Pan, M. E. Leonowicz, E. I. Stiefel, Inorg. Chem. **22**, 672 (1983).
[13] G. J. Brewer, R. D. Dick, D. K. Grover, V. LeClaire, M. Tseng, M. Wicha, K. Pienta, B. D. Redman, T. Jahan, V. K. Sondak, M. Strawderman, G. Lecarpentier, S. D. Merajver, Clinical Cancer Res. **6**, 1 (2000).
[14] G. N. George, I. J. Pickering, H. H. Harris, J. Galler, D. Klein, J. Lichtmannegger, K. H. Summer, J. Am. Chem. Soc. **125**, 1704 (2003).
[15] J. J. Berzelius, Poggendorffs Ann. Phys. Chem. **7**, 262 (1826).
[16] A. Müller, E. Diemann, R. Jostes, H. Bögge, Angew. Chem. **93**, 957 (1981); Angew. Chem. Int. Ed. Engl. **20**, 934 (1981) and references therein.
[17] S. H. Laurie, Eur. J. Inorg. Chem. 2443, (2000).
[18] I. Bezverkhyy, P. Afanasiev, M. Lacroix, Inorg. Chem. **39**, 5416 (2000).
[19] I. Bezverkhyy, P. Afanasiev, M. Lacroix, Mater. Res. Bull. **37**, 161 (2002).
[20] D. E. Schwarz, T. B. Rauchfuss, S. R. Wilson, Inorg. Chem. **42**, 2410 (2003).
[21] M. G. Kanatzidis, D. Coucouvanis, Acta Crystallogr. **C39**, 835 (1983).
[22] J. Ellermeier, C. Näther, W. Bensch, Acta Crystallogr. **C55**, 501 (1999).
[23] J. Ellermeier, C. Näther, W. Bensch, Acta Crystayllogr. **C55**, 1748 (1999).
[24] J. Ellermeier, W. Bensch, Z. Naturforsch. **56b**, 611 (2001).
[25] J. Ellermeier, W. Bensch, Monatsh. Chem. **133**, 945 (2002).
[26] B. R. Srinivasan, B. K. Vernekar, K. Nagarajan, Indian J. Chem. **40A**, 563 (2001).
[27] B. R. Srinivasan, S. N. Dhuri, C. Näther, W. Bensch, Inorg. Chim. Acta, in press.
[28] B. R. Srinivasan, S. N. Dhuri, C. Näther, W. Bensch, Acta Crystallogr. **C59**, m124 (2003).
[29] B. R. Srinivasan, S. N. Dhuri, C. Näther, W. Bensch, Acta Crystallogr. **E58**, m622 (2002).
[30] B. R. Srinivasan, S. N. Dhuri, C. Näther, W. Bensch, Acta Crystallogr. **E59**, m681 (2003).
[31] J. Ellermeier, R. Stähler, W. Bensch, Acta Crystallogr. **C58**, m70 (2002).
[32] P. A. Koz'min, Z. V. Popova, Zh. Strukt. Khim. (Russ.) **12**, 99 (1971).
[33] J. W. McDonald, G. D. Friesen, L. D. Rosenhein, W. E. Newton, Inorg. Chim. Acta **72**, 205 (1983).
[34] G. M. Sheldrick, SHELXS-97: Program for the solution of crystal structures, University of Göttingen, Germany (1994).
[35] G. M. Sheldrick, SHELXL-97: Program for the refinement of crystal structures, University of Göttingen (1997).
[36] B. R. Srinivasan, C. Näther, W. Bensch, Acta Crystallogr. **E59**, m639 (2003).
[37] J. Tyrselova, L. Kuchta, F. Pavelcik, Acta Crystallogr. **C52**, 17 (1996).
[38] S. Pokhrel, K. S. Nagaraja, B. Varghese, J. Struc. Chem. **44**, 689 (2003).
[39] K. Nakamoto, Infrared and Raman Spectra of Inorganic and Coordination Compounds 4th Edition, John Wiley, New York (1986) 130.
[40] G. Alonso, G. Berhault, R. R. Chianelli, Inorg. Chim. Acta **316**, 105 (2001).

3.1.3

Synthesis, X-ray Structures, Spectroscopic and Thermal Characterization of Two New Organic Ammonium Tetrathiotungstates

Bikshandarkoil R. Srinivasan[a], Sunder N. Dhuri[a], Martha Poisot[b], Christian Näther[b], and Wolfgang Bensch [b,*]

[a] Goa/India, Department of Chemistry, Goa University
[b] Kiel, Institut für Anorganische Chemie der Christian-Albrechts Universität

Received December 6th, 2004.

Dedicated to Professor Rüdiger Kniep on the Occasion of his 60th Birthday

Abstract. Two new tetrathiotungstates $(pipH_2)[WS_4]$ (**1**) and $(trenH_2)[WS_4] \cdot H_2O$ (**2**) (pip = piperazine and tren = tris(2-aminoethyl)amine) were synthesized and characterized by elemental analysis, infrared, Raman, UV-Visible and ^{1}H NMR spectroscopy, single crystal X-ray crystallography, and thermoanalysis. In **1** and **2** the amines pip and tren are diprotonated and they are linked to the $[WS_4]^{2-}$ tetrahedra via weak N-H···S (**1**, **2**) and N-H···O (**2**) hydrogen bonds. In **2** the H atoms of the H_2O molecule have also contacts to S atoms. The strength and number of the S···H interactions affect the W-S bond lengths and a relatively long W-S bond of 2.2147(7) Å is observed in **1** while the longest W-S bond in **2** is 2.1997(6) Å. The different degree of distortion of the $[WS_4]^{2-}$ anions is reflected in the IR and Raman spectra. The compounds decompose upon heating in an inert atmosphere to form amorphous $WS_{2.1}C_{1.2}N_{0.3}$ and $WS_{2.1}C_3N_{0.8}$ respectively, and the C and N content of the decomposition products is determined by the C and N content of the amines. In contrast to other tetrathiotungstates, the thermal reaction of both compounds do not proceed via amorphous WS_3 as an intermediate phase. Compound **2** can be reversibly de- and re-hydrated, and the process of re-hydration proceeds presumably via dissolution-re-crystallization mechanism.

Keywords: Tetrathiotungstates; Crystal structures; Spectral and Thermal Properties

Introduction

The chemistry of soluble metal sulfide complexes is still an attractive field of research due to its importance in hydrodesulfurization catalysis (HDS), environment and material science [1]. The soluble sulfides of the group VI metals W and Mo [2, 3] are unique as they exhibit a wide range of metal to sulfur stoichiometries, metal oxidation states, coordination and bonding modes of the sulfido ligands. Interestingly, many of the known W-S complexes have been synthesized using the simple mononuclear tetrathiotungstate indicating that $[WS_4]^{2-}$ is an useful starting material in W-S chemistry. The ammonium salt of tetrathiotungstate was first prepared a long time ago by *Berzelius* [4], but much of its chemistry has been developed only in the last three decades [5] since the first reported synthesis of $[Ni(WS_4)_2]^{2-}$ complex [6].

In recent years, the use of organic ammonium tetrathiotungstates as precursors for the preparation of WS_2 catalysts has shown much promise in the field of hydrodesulfurization (HDS) catalysis [7]. The nature of the organic moiety in the precursors has been shown to affect the surface area, pore size distribution, the carbon content as well as HDS selectivity. Interestingly, only few of these tetrathiotungstates have been structurally characterized. In addition, a systematic study how the organic ammonium species influences and determines the final carbon content has not been undertaken until now. The tetrahedral $[MS_4]^{2-}$ (M = W, Mo) unit is an important building block, which can be used to generate a great variety of fascinating structures [2, 3]. This structural diversity can be attributed to the flexibility of the tetrahedral motif as evidenced by the structural characterization of several $[WS_4]^{2-}$ and also the corresponding $[MoS_4]^{2-}$ complexes with several counter ions in our recent work [8–19]. In almost all these complexes, the $[MS_4]$ tetrahedron is slightly distorted with one or two of the M-S bonds elongated, which we have explained on the basis of the strength and numbers of S···H interactions between $[MS_4]^{2-}$ and the organic cation. It has also been reported in the literature for Mo-S compounds that the chemical properties of $[MoS_4]^{2-}$ can be substantially changed by surrounding it with bulky organic ammonium cations [20]. The role of hydrogen bonding interactions between the cation and anion to influence the reactivity characteristics has also been reported [21]. In view of this we are investigating the synthesis, structural and thermal characterization of organic ammonium tetrathiometalates of the group VI metals and have already shown that a rich chemistry of tetrathiomolybdates can be developed by suitably changing the hydrogen bonding interactions between the cation and $[MoS_4]^{2-}$ [22]. In continuation of this work, we describe herein the synthesis, spectroscopic, thermal and X-ray structural characterization of two new

* Prof. Dr. Wolfgang Bensch
Inst. f. Anorg. Chemie der Universität
Olshausenstr. 40
D-24098 Kiel
Fax: +49-(0)431-880-1520
E-mail: wbensch@ac.uni-kiel.de

Table 2 Hydrogen-bonding (in Å, °) for $(pipH_2)[WS_4]$ (**1**).

D-H···A	d(D-H)	d(H···A)	<DHA	d(D···A)	Symmetry code
N2-H1···S1	0.900	2.486	140.83	3.234	x−1, y, z
N2-H2···S1	0.900	2.458	163.71	3.331	x−1, −y+1/2, z−1/2
N1-H1···S2	0.900	2.389	166.67	3.272	
N1-H1···S2	0.900	2.587	138.85	3.318	x, −y+1/2, z−1/2
N2-H1···S3	0.900	2.881	124.33	3.470	x−1, y, z
N1-H2···S4	0.900	2.638	130.95	3.299	x, −y+1/2, z−1/2
N2-H2···S4	0.900	2.841	112.07	3.287	x−1, −y+1/2, z−1/2

tetrathiotungstates obtained by the reaction of $[WS_4]^{2-}$ with the cyclic diamine piperazine (pip) and the polyamine tris(2-aminoethylamine) (tren).

Results and Discussion

Crystal Structures

The synthesis of the two new tetrathiotungstates was readily accomplished in good yields by the base promoted cation exchange reaction. The details of this synthetic route have already been described in our recent report [22]. The compounds **1** and **2** are quite stable in air and less soluble in water unlike ammonium tetrathiotungstate. However, both are freely soluble in aqueous ammonia. In the structures of the title compounds tetrahedral $[WS_4]^{2-}$ anions and the counter cations $(pipH_2)^{2+}$ (in **1**), and $(trenH_2)^{2+}$ (in **2**) are found. In **1** and **2** all unique atoms are located on general positions. Compound **1** is isostructural to $(pipH_2)[MoS_4]$ recently reported by us [22]. In (**1**) the $(pipH_2)^{2+}$ cations and $[WS_4]^{2-}$ anions are connected via weak hydrogen bonds. The organic cation adopts the chair form with C-C and C-N bond lengths and bond angles being in good agreement with those for other complexes containing the same cation [22−24]. The $[WS_4]^{2-}$ tetrahedron is slightly distorted (S-W-S angles: 108.57(3)−110.49(3)°, Table 1). The W-S bonds vary from 2.1762(7) to 2.2147(7) Å, with a mean W-S bond length of 2.1937 Å (Table 1). These parameters agree well with those in other compounds like $[Ni(tren)_2][WS_4]$ [8] or $(enH_2)[WS_4]$ (en = ethylenediamine) [9]. Two W-S bonds are longer, while the other two are shorter at around 2.1762(7) Å. The elongation of W-S bond distances can be attributed to short S···H contacts (2.389 to 2.881 Å) (Table 2), which results in an extended three-dimensional hydrogen-bonded network (Fig. 1). The S···H distances in **1** are shorter than in $(enH_2)[WS_4]$ (2.432−3.003 Å). In **1** S(1), S(2), and S(4) have two S···H contacts while S(3) has only one (Table 3). This feature is responsible for the very short W-S(3) distance of 2.1762 (7) Å. The D-H···A bond angle of 124.33° together with the longest S···H distance of 2.881 Å observed for S(3) indicates a very weak interaction. The shortest S···H separation of 2.389 Å is accompanied by the largest D-H···A

Table 1 Selected bond lengths and angles (in Å, degree) for $(pipH_2)[WS_4]$ (**1**).

W(1)-S(3)	2.1762(7)	N(1)-C(4)	1.492(4)
W(1)-S(4)	2.1797(7)	C(1)-C(2)	1.510(4)
W(1)-S(1)	2.2042(7)	C(2)-N(2)	1.502(4)
W(1)-S(2)	2.2147(7)	N(2)-C(3)	1.479(4)
N(1)-C(1)	1.485(4)	C(3)-C(4)	1.510(3)
S(3)-W(1)-S(4)	110.49(3)	C(1)-N(1)-C(4)	111.6(2)
S(3)-W(1)-S(1)	109.67(3)	N(1)-C(1)-C(2)	110.7(2)
S(4)-W(1)-S(1)	108.57(3)	N(2)-C(2)-C(1)	110.0(2)
S(3)-W(1)-S(2)	110.12(3)	C(3)-N(2)-C(2)	112.1(2)
S(4)-W(1)-S(2)	108.75(3)	N(2)-C(3)-C(4)	110.3(2)
S(1)-W(1)-S(2)	109.20(3)	N(1)-C(4)-C(3)	110.3(2)

Table 3 Selected bond lengths and angles (in Å, degree) for $(trenH_2)[WS_4]\cdot H_2O$ (**2**).

W(1)-S(3)	2.1739(6)	C(1)-C(2)	1.512(3)
W(1)-S(1)	2.1925(7)	C(2)-N(2)	1.489(3)
W(1)-S(2)	2.1954(6)	C(3)-C(4)	1.505(3)
W(1)-S(4)	2.1997(6)	C(4)-N(3)	1.477(4)
N(1)-C(1)	1.470(3)	C(5)-C(6)	1.521(3)
N(1)-C(5)	1.471(3)	C(6)-N(4)	1.458(3)
N(1)-C(3)	1.475(3)		
S(3)-W(1)-S(1)	108.09(3)	C(5)-N(1)-C(3)	110.58(18)
S(3)-W(1)-S(2)	110.90(3)	N(1)-C(1)-C(2)	110.60(17)
S(1)-W(1)-S(2)	109.68(3)	N(2)-C(2)-C(1)	110.52(18)
S(3)-W(1)-S(4)	109.80(3)	N(1)-C(3)-C(4)	111.97(19)
S(1)-W(1)-S(4)	109.63(3)	N(3)-C(4)-C(3)	110.6(2)
S(2)-W(1)-S(4)	108.73(2)	N(1)-C(5)-C(6)	113.7(2)
C(1)-N(1)-C(5)	111.93(18)	N(4)-C(6)-C(5)	116.0(2)
C(1)-N(1)−C(3)	110.98(17)		

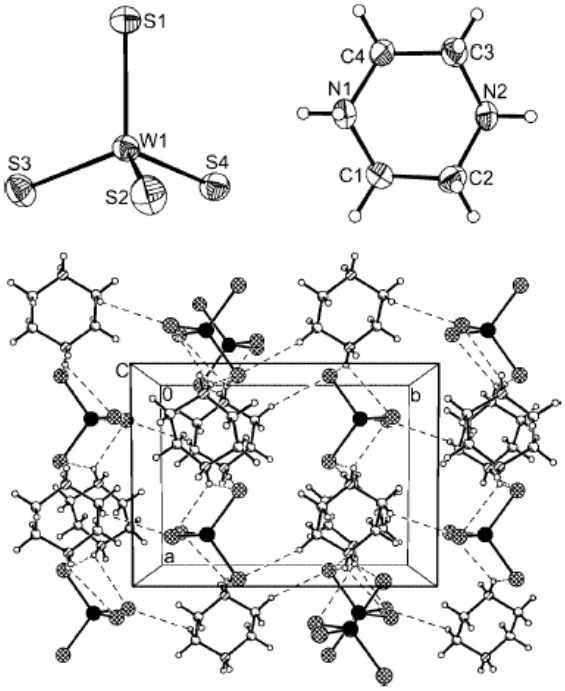

Fig. 1 Crystal structure of $(pipH_2)[WS_4]$ (**1**) with view of the $[WS_4]^{2-}$ anion (top: left) and the $(pipH_2)^{2+}$ cation (top: right) with labeling and displacement ellipsoids drawn at the 50 % probability level. The packing along the c-axis is shown in the lower part (hydrogen bonding is shown as dashed lines).

angle which can explain the long W-S(2) bond of 2.2147(7) Å. The intermediate W-S bond lengths can be similarly explained based on the strengths of the H-bonding interactions. To our knowledge, the W-S(2) distance of 2.2147(7) Å in **1** is one of the longest W-S bonds in tetrathiotungstates and is comparable with that in (1,4-dmpH$_2$)[WS$_4$] (1,4-dmpH$_2$: 1,4-dimethylpiperazinium) of 2.2136(8) Å [11]. In addition, in **1** the difference between the longest and the shortest W-S bonds of 0.0385 Å is large, and this probably is responsible for the appearance of a split W-S vibration in the IR spectrum.

Compound **2** is isostructural with (trenH$_2$)[MoS$_4$] · H$_2$O [22] containing the diprotonated (trenH$_2$)$^{2+}$ ion. In **2** (trenH$_2$)$^{2+}$cations, [WS$_4$]$^{2-}$ anions and H$_2$O molecules are present (Fig. 2). We note that **2** is the first example of a structurally characterized hydrated tetrathiotungstate. Interatomic distances and angles in (trenH$_2$)$^{2+}$ are in excellent agreement with those in [Co$_2$(tren)$_3$][MoS$_4$]$_2$ and (trenH$_2$)[MoS$_4$] · H$_2$O [15, 22]. The [WS$_4$]$^{2-}$ tetrahedron is slightly distorted with W-S bond lengths in the range of 2.1739(6) to 2.1997(6) Å (mean W-S distance: 2.1904 Å) (Table 3). Three of the W-S bonds are longer than the average W-S distance of 2.1893 Å reported for (enH$_2$)[WS$_4$] [9]. In **2** short S···H-N contacts are observed which are slightly longer than in **1** (Table 4 and Fig. 2). The shortest W-S bond of 2.1739(6) Å is observed for S(3), which has only

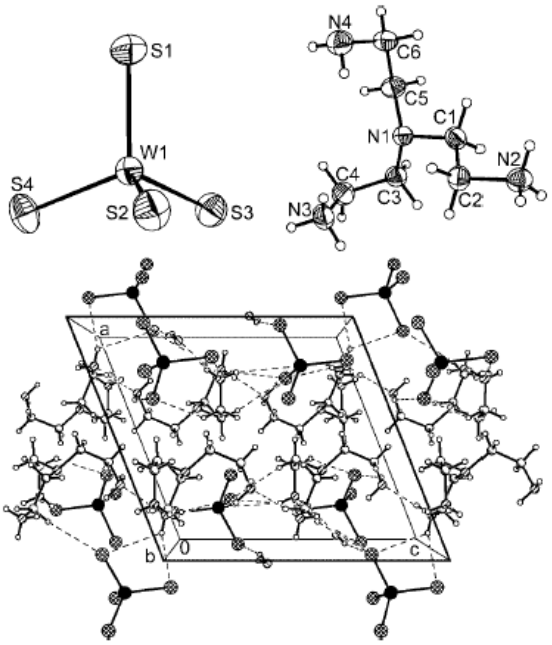

Fig. 2 Crystal structure of (trenH$_2$)[WS$_4$] · H$_2$O (**2**) with view of the WS$_4$ anion (top: left) and the (trenH$_2$)$^{2+}$ cation (top: right) with labeling and displacement ellipsoids drawn at the 50 % probability level and of the packing in the direction of the c-axis (bottom) (hydrogen bonding is shown as dashed lines).

Table 4 Hydrogen-bonding (in Å, °) for (trenH$_2$)[WS$_4$]·H$_2$O (**2**).

D-H···A	d(D-H)	d(H···A)	<DHA	d(D···A)	Symmetry code
N2-H1···S1	0.861	2.946	119.97	3.457	x+1, −y+1/2, z+1/2
N4-H2···S1	0.892	3.015	128.32	3.636	x+1, y, z
O1-H1···S1	0.822	2.500	161.20	3.289	x+1, y, z
O1-H2···S1	0.822	2.596	169.28	3.407	−x+1, y+1/2, −z+1/2
N2-H1···S2	0.861	2.590	158.17	3.405	x+1, −y+1/2, z+1/2
N2-H2···S2	0.862	2.994	110.07	3.388	−x+1, y−1/2, −z+1/2
N3-H3···S2	0.861	2.462	172.65	3.318	−x+1, y+1/2, −z+1/2
N4-H1···S3	0.891	2.939	148.28	3.727	−x+1, y+1/2, −z+1/2
N2-H2···S4	0.862	2.536	169.24	3.387	−x+1, y−1/2, −z+1/2
N3-H1···S4	0.862	2.634	152.95	3.424	−x+1, −y+1, −z+1
N2-H3···N4	0.862	1.946	176.84	2.807	x, −y+1/2, z+1/2
N3-H2···O1	0.862	1.983	156.99	2.797	

one contact to a H atom at a distance of 2.939 Å (Table 4). The analysis of the situation for S(1) and S(4) shows some interesting trends. S(4) has two contacts to H atoms of 2.536 and 2.634 Å, N-H···S(4) angles of 169.24 and 152.95° and the longest W-S bond length of 2.1997(6) Å. S(1) has two contacts to H atoms of the ammonium groups and two to H atoms of H$_2$O (Table 4). The two former are long (2.946 Å, 119.97°; 3.015 Å, 128.32°) while the latter two interactions are significantly shorter (2.500 Å, 161.20°; 2.596 Å, 169.28°). The W-S(1) bond of 2.1925(5) Å is surprisingly short as one would expect that this bond is at least as long as the W-S(4) bond. One possible explanation may be that despite the short S(1)···H distances to the H atoms of H$_2$O the interactions are weaker than those to H atoms bound to N. This explanation gains more credence as a similar behavior was observed in the isostructural Mo complex [22]. Finally, S(2) has two short contacts, and the W-S(2) bond amounts to 2.1954(6) Å. The difference between the longest and the shortest W-S bond distances in **2** of 0.0158 Å is smaller than that observed in **1**.

Spectral studies

The UV-Visible spectra of **1** and **2** in dilute aqueous ammonia exhibit bands at around 393, 277 and 221 nm. The peak positions are almost identical to that in the corresponding ammonium or tetraethylammonium salts [5, 25] and can be assigned to the charge transfer transitions of the tetrahedral [WS$_4$]$^{2-}$ moiety. The ^{1}H NMR spectrum of **1** in DMSO-d_6 exhibits a sharp singlet at δ = 3.25 ppm assignable to the magnetically equivalent methylene protons. Two triplets at δ = 2.55 (J = 6 Hz) and δ = 2.82 (J = 5.5 Hz) one each for the equivalent -CH$_2$ groups (C1, C3 and C5) directly bonded to N1 and the other for the remaining three -CH$_2$ groups (C2, C4 and C6) are observed in the ^{1}H NMR spectrum of **2**. Because only these signals are observed a very rapid exchange of the N-H protons with the trace amounts of water in DMSO-d_6 can be assumed.

The bands in the central part of the IR spectra of **1** (Fig. 3), and **2** (Fig. 4) are due to absorptions of the organic cations. The IR of **2** exhibits a broad and strong band at around 3471 cm^{-1} due to the O-H stretching vibration of H$_2$O. The N-H stretching modes appear at around

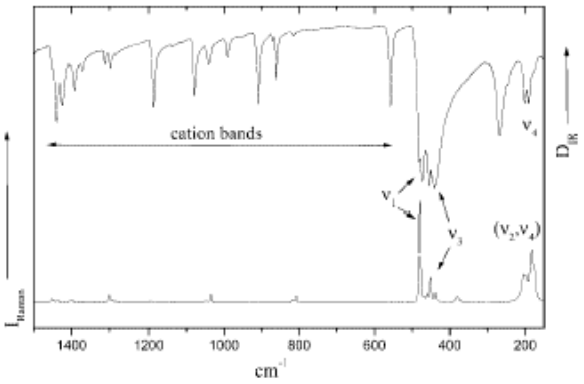

Fig. 3 Raman and IR spectra of $(pipH_2)[WS_4]$ (**1**).

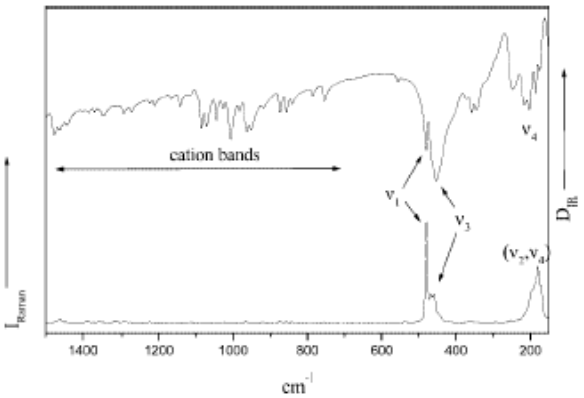

Fig. 4 Raman and IR spectra of $(trenH_2)[WS_4]\cdot H_2O$ (**2**).

3000 cm^{-1} in **1** and at 3084 and 3009 cm^{-1} in **2**. The shift to lower wave numbers compared to the free amines in **1** or **2** can be attributed to the H-bonding interactions (N-H···S). For free tetrahedral $[WS_4]^{2-}$ anions four characteristic bands $\nu_1(A_1)$, $\nu_2(E)$, $\nu_3(F_2)$, and $\nu_4(F_2)$ are expected [26]. All four bands are Raman active while only ν_3 and ν_4 are infrared active. Many tetrathiotungstates exhibit a single strong band at around 455 cm^{-1} assignable to the triply degenerate asymmetric stretching vibration (ν_3) of the W=S bond [5, 26]. Interestingly, for **1** ν_3 is split and appears as a doublet at 454 and 441 cm^{-1} with a further band around 473 cm^{-1} (Fig. 3). The observed extra signals cannot be caused by the $(pipH_2)^{2+}$ cations as no strong signals are observed for $(pipH_2)Cl_2$ below 500 cm^{-1}. Hence these features indicate considerable distortion of the $[WS_4]$ tetrahedron and can be explained by the lowering of symmetry [5], which is probably responsible for the symmetric stretching vibration (ν_1) of the W=S bond at 473 cm^{-1} to appear in the spectrum. The IR inactive (ν_1) vibration is normally not observed for undistorted tetrahedral compounds. The assignment of the 473 cm^{-1} band for the symmetric stretching vibration gains credence from the observation of an intense signal in the Raman spectrum at 480 cm^{-1}. The IR active (ν_4) vibration is also observed as a doublet at 191 and 201 cm^{-1}. The weak signal at 451 cm^{-1} in the Raman spectrum can be assigned to the (ν_3) vibration while the signal at 183 cm^{-1} is due to the degenerate (ν_2) and (ν_4) modes. For **2** the IR absorptions are observed at 481 and 454 cm^{-1}. Unlike in **1** the signal at 454 cm^{-1} is not clearly split even though it appears quite broad (Fig. 4), i. e. the distortion of the anion is less pronounced in accordance with the smaller difference in bond distances between the longest and the shortest W-S bonds. The IR spectrum of complex **2** can be explained similarly as for **1**.

Thermal studies

The thermal decomposition behavior of $(NH_4)_2[WS_4]$ is well documented and is represented by the equation (1)

$$(NH_4)_2[WS_4] \rightarrow 2\ NH_3 + H_2S + WS_3 \qquad (1)$$

The compound is stable up to 180 °C and decomposes with an endothermic peak at 280 °C [5, 27]. The intermediate formed WS_3 has been reported to be stable between 310 and 340 °C followed by decomposition into S and WS_2. The formation of WS_2 is accompanied by a sharp exothermic event at 339 °C. Compound **1** is found to be thermally more stable and decomposition starts at 208 °C accompanied by a strong endothermic signal at T_{peak} = 289 °C (Fig. 5). We note that **1** is also thermally more stable than the corresponding isostructural Mo analog ($T_{decomp.}$ = 140 °C) [22]. Until 400 °C a mass loss of about 30 % is observed. Above 400 °C the weight change is small and the total loss till 600 °C is 32.14 %. For the formation of WS_3 the expected value is 30.04 % and for WS_2 38.04 %. Interestingly, after the heat treatment the residue contains 1.87 % N and 5.54 % C leading to a composition $WS_{2.1}C_{1.2}N_{0.3}$ (EDX:

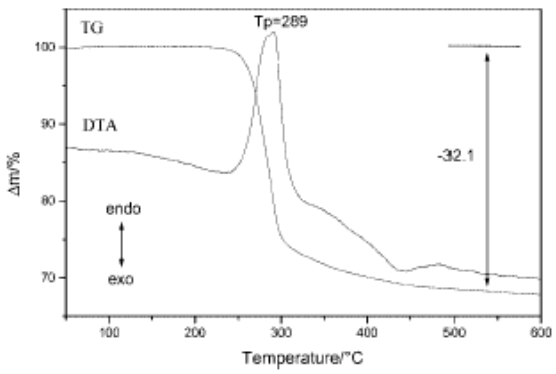

Fig. 5 DTA and TG curves for $(pipH_2)[WS_4]$ (**1**) (heating rate 4 K/min; N_2 atmosphere; given are the peak temperatures (T_p) in °C and the mass loss in %).

W:S = 1:1.94). In the X-ray powder pattern of the black decomposition product only broad modulations are observed, indicating that the material is amorphous. The formation of a predominantly disulfide residue by the thermal decomposition of **1** in a single endothermic step at a relatively low temperature indicates that in contrast to other tetrathiotungstates no WS_3 is formed as an intermediate.

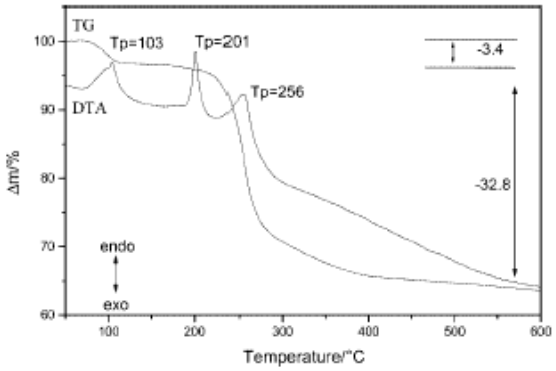

Fig. 6 DTA and TG curves for $(trenH_2)[WS_4]\cdot H_2O$ (**2**) (heating rate 4 K/min; N_2 atmosphere; given are the peak temperatures (T_p) in °C and the mass loss in %).

Compound **2** loses the water starting at about 70 °C ($-H_2O$ Δm_{exp} = 3.43 %; H_2O Δm_{theo} = 3.76 %) with T_{peak} = 103 °C (Fig. 6). Increasing the temperature two more endothermic events are observed with T_{peak} = 201 and 256 °C and a mass loss of 32.8 % is obtained. In another experiment the decomposition was stopped at about 110 °C and the anhydrous product thus obtained exhibited a significantly different X-ray powder pattern compared to that of the starting material. The second endothermic peak is not accompanied with a significant mass loss and therefore decomposition of the material was stopped at 210 °C in another experiment. Interestingly, in the crucible a black melt was formed and the X-ray powder pattern showed only a strong modulated background.

The thermal behavior of **2** is quite similar to that of $(trenH_2)[MoS_4]\cdot H_2O$ [22] with a slightly lower value for the dehydration process, while the decomposition of the anhydrous tetrathiotungstate thus formed is observed at elevated temperatures as compared to the Mo analogue. This observation is similar to that observed for complex **1** and indicates that $[WS_4]^{2-}$ complexes are thermally more stable than the corresponding $[MoS_4]^{2-}$ analogues. However, as for compound **1** the final black residue shows appreciable amounts of C (12.01 %) and N (3.67 %) yielding a composition $WS_{2.1}C_3N_{0.8}$. The presence of more C and N in the residue of **2** than in **1** is presumably due to the larger C and N content of tren compared to pip in **1**, indicating that a larger C content of the staring material yields a product containing more C. This observation is of special interest because for active HDS catalysts the actual C content is important. As for **1** the amorphous nature of the residue is evident in the X-ray powder diagram (not shown). In view of the emerging importance of disulfide materials as well as carbon contaminated metal sulfides in catalysis, additional experiments involving different heating rates and characterization of the intermediates formed are underway.

Re-hydration studies

Compound **2** emits water at a relatively low temperature. In further experiments the re-hydration behavior of the dehydrated sample was studied with X-ray diffractometry and electron microscopy. The dehydrated sample was stored in a desiccator over water atmosphere and powder patterns were collected after distinct times. The reaction is slow as can be seen in Fig. 7, and the dehydrated and re-hydrated phases coexist over a long time. After 6 days the pattern is very similar to that of the pristine compound. To gain further insight how the reaction takes place selected crystals were investigated after dehydration and after re-hydration (Fig. 8). As can be seen in Fig. 8 (top) the surface of the crystal after the heat treatment is relatively smooth with some small holes. After re-hydration the surface is rough with a large number of small cavities (Fig. 8, bottom). One possible explanation is that the dehydrated material partially dissolves in the water vapor and re-crystallizes forming the H_2O containing starting material, i.e. it is a dissolution-re-crystallization reaction. The process is slow explaining the long time until full re-hydration is observed.

Conclusions

Two new tetrathiotungstates $(pipH_2)[WS_4]$ (**1**) and $(trenH_2)[WS_4]\cdot H_2O$ (**2**) are obtained in good yields by the base promoted cation exchange method. Compound **2** is the first example of a structurally characterized hydrated tetrathiotungstate. In both compounds the $[WS_4]^{2-}$ tetra-

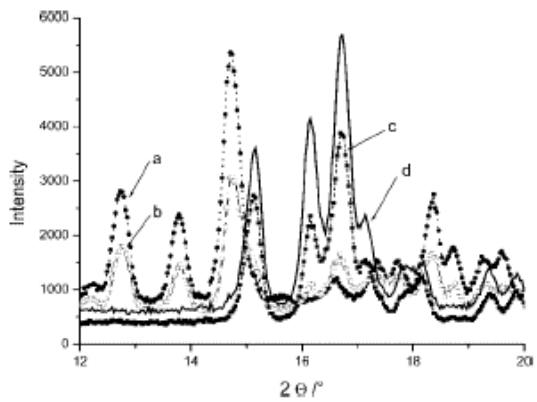

Fig. 7 X-ray powder patterns of dehydrated compound **2** (trace a), re-hydrated for 2 d (trace b), re-hydrated for 6 d (trace c), and the pristine material (trace d).

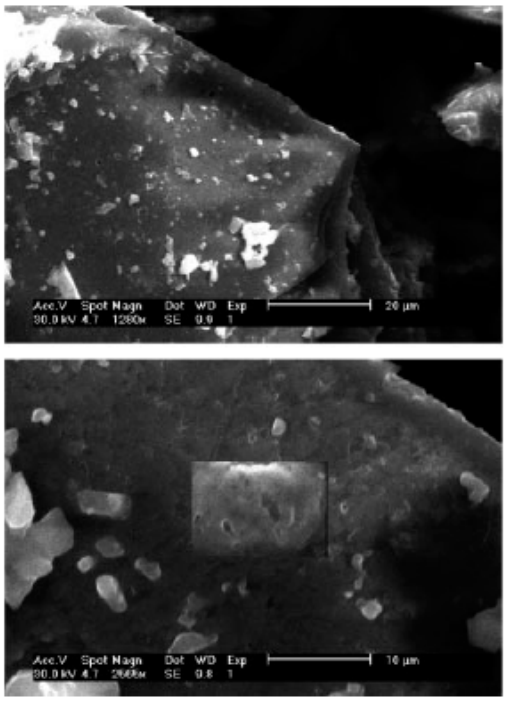

Fig. 8 SEM micrographs of **2** after dehydration (top) and after re-hydration (bottom).

hedra are distorted which can be explained on the basis of the strength and number of N-H···S interactions. In **2** N-H···S as well as O-H···S interactions are observed. The rigorous analysis of the geometric parameters in **2** suggests that the O-H···S interactions are weaker compared to the N-H···S interactions in terms of their ability to elongate W-S bonds. Our future work in this field is directed to the synthesis of new tetrathiotungstates which exhibit both types of such interactions. In addition, the results of the thermal decomposition reactions are of special interest for the preparation of C containing amorphous WS_2 materials as HDS catalysts which are obtained without the formation of a WS_3 intermediate, i.e. in the final amorphous products the W:S ratio is close to 1 : 2. Systematic experiments are also under way to correlate the residual C and N content in the WS_2 phases with the available C and N content in the starting tetrathiotungstates. The directed thermal decomposition of suitable $R[WS_4]$ precursors (R = organic cation) can be a promising and easy route for the preparation of WS_2 based HDS catalysts.

Experimental Section

Materials and methods

The amines pip, tren, tungstic acid and the solvents were used in this investigation as obtained from commercial sources with analytical purity. $(NH_4)_2[WS_4]$ was prepared by literature method [25]. Far-IR spectra (range 80 to 500 cm^{-1}) were measured on a Bruker IFS 66 infrared spectrometer in pressed polyethylene disks. MIR spectra of the compounds were recorded in a KBr matrix. The samples were ground with dry KBr into fine powders and pressed into transparent pellets. The spectra were recorded in the IR region of 450-3000 cm^{-1}, (resolution 1 cm^{-1}) by an ATI Mattson Genesis infrared spectrometer. Raman spectra were measured in the region 100-3500 cm^{-1} on a Bruker FRA106 Fourier transform Raman spectrometer. ^1H NMR spectra were recorded on a Bruker 300 MHz FT-NMR instrument. UV-Visible spectra were recorded in dilute ammonia using matched quartz cuvettes on a Varian Cary 5 UV-VIS-NIR equipment. C, H, N and S analyses were performed on a HEKA Tech Euro EA elemental analyzer. DTA-TG measurements were performed simultaneously using a Netzsch STA-409CD device. The thermal investigations were performed in Al_2O_3 crucibles using a heating rate of 4 K/min up to 600 °C and purged in a nitrogen stream of 75 mL/min. EDX analysis was performed with a Philips ESEM XL 30 scanning electron microscope equipped with an EDAX analyzer. X-ray powder patterns were recorded in transmission geometry using a STOE STADI P diffractometer (CuK_α = 1.54056 Å).

Syntheses of the complexes

$(pipH_2)[WS_4]$ (1). Ammonium tetrathiotungstate (348 mg, 1 mmol) was dissolved in distilled water (20 ml) and anhydrous piperazine (86 mg, 1 mmol) dissolved in distilled water (5 ml) was added at room temperature. The reaction mixture was stirred for ~ 5 min and then filtered. The clear filtrate was left undisturbed in a refrigerator. After 2 days yellow blocks of compound **1** were obtained. These were filtered, washed with ice-cold water (2 ml) followed by isopropanol (10 ml) and diethylether (10 ml), and dried under vacuum. Yield 80 %.

Elemental analysis found: C 12.18 (calc. 12.00), H 3.00 (3.03), N 7.03 (7.00), S 32.84 (32.04) %.

IR data: 2989, 2928, 2752, 2668, 1510, 1425, 1400, 1371, 1298, 1186, 1079, 909, 862, 556, 473 (ν_1), 454 (ν_3), 441, 267, 201, 191 (ν_4), 125, and 92 cm^{-1}.
Raman Data: 480 (ν_1), 460, 451 (ν_3), 438, 380, 203 (ν_2), and 183 (ν_4) cm^{-1}.
UV-Vis data in nm (ε_{max} in $mol^{-1}.l.cm^{-1}$) 393 (14800), 277 (18900), 221 (18600)

$(trenH_2)[WS_4]\cdot H_2O$ (2). The reaction of ammonium tetrathiotungstate (348 mg, 1 mmol) with tren (0.35 ml) in water (10 ml) instead of anhydrous piperazine in the earlier reaction resulted in the formation of compound **2** in 70 % yield.

Elemental analysis found: C 15.11 (calc. 15.06), H 4.72 (4.60), N 11.31 (11.63), S 26.23 (26.81) %.

IR data: 3471, 3330, 3278, 3084, 3009, 2886, 2829, 1601, 1569, 1513, 1478, 1345, 1295, 1142, 1086, 1007, 963, 857, 754, 481 (ν_1), 454 (ν_3), 357, 344, 247, 218, 203, 185 (ν_4), 133, and 101 cm^{-1}.
Raman data: 480, 467, 459 and 179 cm^{-1}.
UV-Vis data in nm (ε_{max} in $mol^{-1}.l.cm^{-1}$) 393 (16360), 277 (22460), 221 (23800).

Single crystal X-ray diffractometry

Intensity data were collected on a Philips PW1100-four circle diffractometer for **1** and AED2 four circle diffractometer for **2** at room temperature using graphite monochromated Mo-K_α radiation. For both compounds a numerical absorption correction was applied. The structures were solved with direct methods using

Table 5 Technical details of data acquisition and selected refinement results for $(pipH_2)[WS_4]$ (**1**) and $(trenH_2)[WS_4]\cdot H_2O$ (**2**).

Compound	$(pipH_2)[WS_4]$ **1**	$(trenH_2)[WS_4]\cdot H_2O$ **2**
Formula	$C_4H_{12}WN_2S_4$	$C_6H_{22}N_4OWS_4$
MW /g/mol	400.25	478.37
Space group	$P2_1/c$	$P2_1/c$
a /Å	8.2534(7)	11.495(1)
b /Å	11.271(1)	11.810(1)
c /Å	11.996(1)	12.519(1)
β /°	95.11(1)	111.70(1)
Volume /Å^3	1111.6(2)	1579.2(2)
Z	4	4
Temperature / K	293	293
μ / mm^{-1}	11.09	7.83
$F(000)$	752	928
$D_{calc.}$ / g·cm^{-3}	2.392	2.012
2θ Range / °	3 − 60	3 − 60
hkl Range	0/11; −15/5; −16/16	−16/1; −16/16; −16/17
Refls. collected	4913	10399
Refls. unique	3241	4600
Data ($Fo>4\sigma(Fo)$)	2632	3961
$R_{int.}$	0.0162	0.0193
Min./max. transm.	0.1631 0.3001	0.2413 / 0.3650
$\delta\rho$ /(e/Å^3)	−0.57 /0.58	−0.99 / 0.72
Parameters	101	146
$R1$ [$Fo>4\sigma(Fo)$]	0.0176	0.0170
$wR2$ for all data	0.0399	0.0401
Goodness of fit	0.990	1.062

Table 6 Atomic coordinates [·10^4] and equivalent isotropic displacement parameters [Å^2·10^3] for compounds **1** and **2**.

Atom	x	y	z	U_{eq}
$(pipH_2)[WS_4]$ (1)				
W(1)	7906(1)	2207(1)	5940(1)	22(1)
S(1)	10103(1)	3328(1)	6112(1)	30(1)
S(2)	5721(1)	3355(1)	5853(1)	30(1)
S(3)	7901(1)	1134(1)	4432(1)	34(1)
S(4)	7908(1)	1077(1)	7415(1)	30(1)
N(1)	4583(3)	2706(2)	3242(2)	28(1)
C(1)	3508(4)	3698(3)	2829(3)	32(1)
C(2)	2140(4)	3867(3)	3570(3)	34(1)
N(2)	1221(3)	2725(2)	3659(2)	28(1)
C(3)	2297(3)	1740(3)	4071(2)	30(1)
C(4)	3655(3)	1577(3)	3320(3)	30(1)
$(trenH_2)[WS_4]\cdot H_2O$ (2)				
W(1)	1790(1)	3573(1)	2326(1)	26(1)
S(1)	51(1)	3022(1)	2507(1)	41(1)
S(2)	1546(1)	3574(1)	502(1)	35(1)
S(3)	3272(1)	2415(1)	3301(1)	41(1)
S(4)	2255(1)	5302(1)	3006(1)	40(1)
N(1)	6402(2)	3910(2)	3076(2)	30(1)
C(1)	6720(2)	2725(2)	3419(2)	33(1)
C(2)	8027(2)	2642(2)	4321(2)	34(1)
N(2)	8368(2)	1437(2)	4633(2)	35(1)
C(3)	5935(2)	4492(2)	3881(2)	34(1)
C(4)	6274(3)	5729(2)	4001(2)	43(1)
N(3)	7648(2)	5873(2)	4462(2)	48(1)
C(5)	5490(2)	4003(2)	1890(2)	37(1)
C(6)	6027(3)	3708(2)	982(2)	39(1)
N(4)	7071(2)	4404(2)	974(2)	44(1)
O(1)	9402(3)	5450(2)	3447(3)	85(1)

Equivalent isotropic U calculated as a third of the trace of the orthogonalised U_{ij} tensors

SHELXS-97 [28] and refinement was carried out against F^2 using SHELXL-97 [29]. All non-hydrogen atoms were refined using anisotropic displacement parameters. The hydrogen atoms were located in difference maps but positioned with idealized geometry and refined using the riding model with fixed isotropic displacement parameters. The technical details of data acquisition and some selected refinement results are summarized in Table 5. The atomic coordinates and equivalent isotropic displacement parameters for compounds **1** and **2** are presented in Table 6.

Crystallographic data (excluding structure factors) have been deposited with the Cambridge Crystallographic Data Centre as supplementary publication no. CCDC 249579 (**1**) and CCDC 249578 (**2**). Copies of the data can be obtained, free of charge, on application to CCDC, 12 Union Road, Cambridge CB2 1 EZ, UK. (fax: +44-(0)1223-336033 or email: deposit@ccdc.cam.ac.uk).

Acknowledgements. Financial support by the State of Schleswig-Holstein and the Deutsche Forschungsgemeinschaft (DFG) is gratefully acknowledged. B.R.S. thanks the Department of Science and Technology (DST), New Delhi for financial support (SR/S1/IC-41/2003). W.B. and B.R.S. acknowledge the DST, New Delhi and Deutscher Akademischer Austauschdienst (DAAD) Bonn, for the sanction of a DST-DAAD (PPP) project.

References

[1] T. Rauchfuss, *Inorg. Chem.* **2004**, *43*, 14 and references cited therein.
[2] T. Shibhahara, *Coord. Chem. Rev.* **1993**, *123*, 73.
[3] D. Coucouvanis, *Adv. Inorg. Chem.* **1998**, *45*, 1.
[4] J. J. Berzelius, *Poggendorffs Ann. Phys. Lpz.* **1826**, *8*, 277.
[5] A. Müller, E. Diemann, R. Jostes, H. Bögge, *Angew. Chem.* **1981**, *93*, 957; *Angew. Chem. Int. Ed. Engl.* **1981**, *20*, 934 and references cited therein.
[6] A. Müller, E. Diemann, *Chem. Commun.* **1971**, 65.
[7] G. Alonso, G. Berhault, A. Aguilar, V. Collins, C. Ornelas, S. Fuentes, R. R. Chianelli, *J. Catal.* **2002**, *208*, 359.
[8] J. Ellermeier, R. Stähler, W. Bensch, *Acta Crystallogr.* **2002**, *C58*, m70.
[9] B. R. Srinivasan, S. N. Dhuri, C. Näther, W. Bensch, *Acta Crystallogr.* **2002**, *E58*, m622.
[10] B. R. Srinivasan, S. N. Dhuri, C. Näther, W. Bensch, *Acta Crystallogr.* **2003**, *C59*, m124.
[11] B. R. Srinivasan, S. N. Dhuri, C. Näther, W. Bensch, *Acta Crystallogr.* **2003**, *E59*, m681.
[12] B. R. Srinivasan, M. Poisot, C. Näther, W. Bensch, *Acta Crystallogr.* **2004**, *E60*, i136.
[13] J. Ellermeier, C. Näther, W. Bensch, *Acta Crystallogr.* **1999**, *C55*, 501.
[14] J. Ellermeier, C. Näther, W. Bensch, *Acta Crystallogr.* **1999**, *C55*, 1748.
[15] J. Ellermeier, W. Bensch, *Z. Naturforsch.* **2001**, *56b*, 611.
[16] J. Ellermeier, W. Bensch, *Monatsh. Chem.* **2002**, *133*, 945.
[17] B. R. Srinivasan, B. K. Vernekar, K. Nagarajan, *Indian J. Chem.* **2001**, *40A*, 563.
[18] B. R. Srinivasan, S. N. Dhuri, C. Näther, W. Bensch, *Inorg. Chim. Acta* **2005**, *358*, 279.
[19] J. Ellermeier, *Ph.D. thesis*, Christian-Albrecht Universität-Kiel, March 2002.
[20] I. Bezverkhyy, P. Afanasiev, M. Lacroix, *Mat. Res. Bull.* **2002**, *37*, 161.

[21] D. E. Schwarz, T. B. Rauchfuss, S. R. Wilson, *Inorg. Chem.* **2003**, *42*, 2410.
[22] B. R. Srinivasan, S. N. Dhuri, M. Poisot, C. Näther, W. Bensch, *Z. Naturforsch.* **2004**, *59b*, 1083.
[23] B. R. Srinivasan, C. Näther, W. Bensch, *Acta Crystallogr.* **2003**, *E59*, m639.
[24] B. R. Srinivasan, A. R. Naik, C. Näther, W. Bensch, *Acta Crystallogr.* **2004**, *E60*, m1384.
[25] J. W. McDonald, G. D. Friesen, L. D. Rosenhein, W. E. Newton, *Inorg. Chim. Acta* **1983**, *72*, 205.
[26] K. Nakamoto, *Infrared and Raman Spectra of Inorganic and Coordination Compounds*, 4th. Ed., John Wiley, New York, 1986, p. 130.
[27] T. P. Prasad, E. Diemann and A. Müller, *J. Inorg. Nucl. Chem.* **1973**, *35*, 1895.
[28] G. M. Sheldrick, *SHELXS-97, Program for the solution of crystal structures*, Univ. of Göttingen, Germany 1994.
[29] G. M. Sheldrick, *SHELXL-97, Program for the refinement of crystal structures*, Univ. of Göttingen 1997.

3.1.4

metal-organic papers

Acta Crystallographica Section E
Structure Reports
Online
ISSN 1600-5368

Bis(diethylenetriamine)cobalt(II) tetrathiomolybdate(VI) oxotrithiamolybdate(VI)

Martha Poisot, Christian Näther* and Wolfgang Bensch

Institut für Anorganische Chemie, Christian-Albrechts-Universität Kiel, Olshausenstrasse 40, D-24098 Kiel, Germany

Correspondence e-mail: cnaether@ac.uni-kiel.de

Received 10 May 2006
Accepted 15 May 2006

Key indicators

Single-crystal X-ray study
T = 293 K
Mean σ(C–C) = 0.009 Å
Disorder in main residue
R factor = 0.041
wR factor = 0.098
Data-to-parameter ratio = 17.1

For details of how these key indicators were automatically derived from the article, see http://journals.iucr.org/e.

In the crystal structure of the title compound, $[Co(C_4H_{13}N_3)_2]_2[MoS_4][MoS_3O]$, discrete $[MoS_4]^{2-}$ and $[MoS_3O]^{2-}$ anions, as well as $[Co(C_4H_{13}N_3)_2]^{2+}$ cations are found. Both anions occupy the same crystallographic position and are therefore disordered. The Co atom is octahedrally coordinated by six N atoms of the diethylenetriamine ligand whereas the Mo atom shows a distorted tetrahedral geometry.

Comment

During the past few years, a large number of tetrathiomolybdates have been prepared in the presence of an organic cation. Compared to the number of such compounds, those containing a transition metal complex cation are rare and some examples are $[Ni(en)_3]MoS_4$ (en is ethylenediamine; Ellermeier *et al.*, 1999), $[Ni(en)_3]_3(MoS_4)Br_4{\cdot}2en$ (Ellermeier, 2002), $[Mn(dien)_2]MoS_4$ (dien is diethylenetriamine; Ellermeier & Bensch, 2002), $[Ni(dien)_2]_2(MoS_4)Br_2$ (Ellermeier, 2002), $[Co_2(tren)_3]$-$(MoS_4)_2$ (tren is triethylenetetramine; Ellermeier & Bensch, 2001), $[(C_6H_5)_4P]_2[M(MoS_4)_2]$ (M = Ni, Fe, Zn) (Müller *et al.*, 1971), and $(Pr_4N)_2[Ni(MoS_4)_2]$ (Callahan & Piliero, 1980).

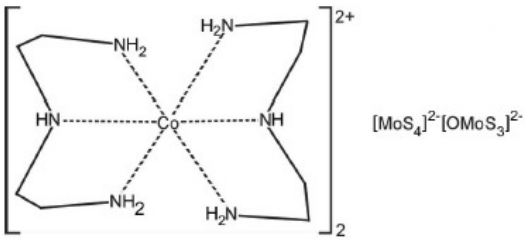

(I)

The structure of the title compound consists of isolated $[Co(dien)_2]^{2+}$ cations and $[MoS_4]^{2-}$ as well as $[MoS_3O]^{2-}$ anions, which are connected *via* N—H···S hydrogen bonding (Fig. 1 and Table 2). Each Co^{2+} ion is sixfold coordinated by the six N atoms of two tridentate dien ligands within a distorted octahedron. The Co—N distances (Table 1) are between 2.152 (4) and 2.197 (4) Å. The *trans* N—Co—N angles in the title compound are in the range 177.54 (16)–178.61 (17)°. The geometric parameters indicate that the CoN_6 octahedron in the title compound is less distorted than in the analogous en compound. The anion was first refined assuming that only S is bound to Mo. In this case, the Mo—S bonds were between 1.977 (3) and 2.2045 (17) Å with a difference of 0.2275 Å between the longest and the shortest bond. This is a rather large difference; in most tetrathiomolybdates the difference lies between 0.02 and 0.05 Å (Srinivasan *et al.*,

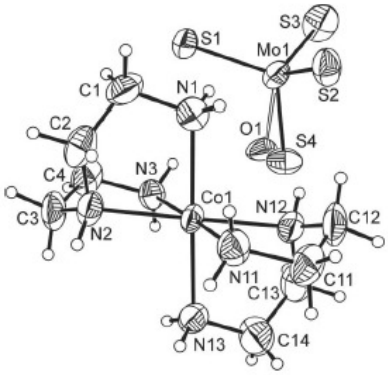

Figure 1
The asymmetric unit of the title compound, with the atom labellling and displacement ellipsoids drawn at the 50% probability level. The Mo—O bond in the disordered anion is shown as an open bond.

2004). Furthermore, the symmetry of the anion would be significantly reduced and the IR spectrum should then show a split Mo—S vibration. The relatively high anisotropic displacement parameters of S4 suggested a slight contamination with oxygen. The refinement of S4 with a split model finally yielded an $[MoS_4]^{2-}$ and an $[MoS_3O]^{2-}$anion which are superimposed in the crystal structure (Table 1). The presence of oxygen was proved with IR spectroscopy. The partial occupancy of the S4 position by oxygen leads to a much more realistic Mo—S bond length and a reasonable Mo—O distance.

Experimental

Cobalt(II) chloride (0.5 mmol) and $(NH_4)_2MoS_4$ (0.5 mmol) were heated for 5 d at 373 K in a mixture of 3 ml diethylenetriamine and 3 ml water in a Teflon-lined steel autoclave. The resulting red–orange crystals (70% yield) were dried under vacuum.

Crystal data

$[Co(C_4H_{13}N_3)_2]_2[MoS_4][MoOS_3]$
M_r = 962.86
Monoclinic, $P2_1/n$
a = 7.4164 (5) Å
b = 15.9171 (11) Å
c = 15.4070 (12) Å
β = 93.063 (9)°
V = 1816.2 (2) Å^3
Z = 2
D_x = 1.761 Mg m^{-3}
Mo $K\alpha$ radiation
μ = 2.01 mm^{-1}
T = 293 (2) K
Block, red–orange
0.09 × 0.09 × 0.08 mm

Data collection

Stoe IPDS-1 diffractometer
φ scans
Absorption correction: none
11766 measured reflections
3269 independent reflections
2455 reflections with $I > 2\sigma(I)$
R_{int} = 0.048
θ_{max} = 25.7°

Refinement

Refinement on F^2
$R[F^2 > 2\sigma(F^2)]$ = 0.041
$wR(F^2)$ = 0.099
S = 1.02
3269 reflections
191 parameters
H-atom parameters constrained
$w = 1/[\sigma^2(F_o^2) + (0.0458P)^2 + 2.2351P]$
where $P = (F_o^2 + 2F_c^2)/3$
$(\Delta/\sigma)_{max}$ < 0.001
$\Delta\rho_{max}$ = 0.55 e Å^{-3}
$\Delta\rho_{min}$ = −0.60 e Å^{-3}
Extinction correction: *SHELXL97*
Extinction coefficient: 0.0022 (6)

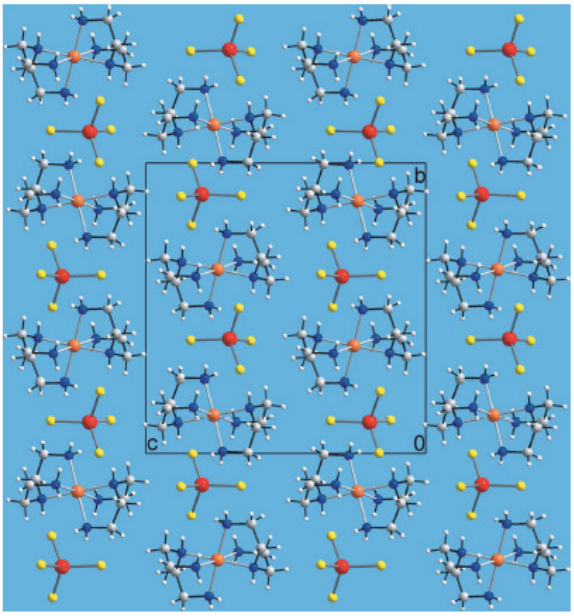

Figure 2
The crystal structure of the title compound, viewed along the *a* axis. The O atoms have been omitted for clarity.

Table 1
Selected geometric parameters (Å, °).

Mo1—O1	1.796 (17)	Co1—N2	2.164 (4)
Mo1—S4	2.050 (6)	Co1—N11	2.182 (4)
Mo1—S2	2.1826 (16)	Co1—N1	2.191 (4)
Mo1—S3	2.1908 (16)	Co1—N13	2.196 (4)
Mo1—S1	2.2041 (14)	Co1—N3	2.197 (4)
Co1—N12	2.152 (4)		
O1—Mo1—S4	14.0 (5)	N12—Co1—N1	98.35 (16)
O1—Mo1—S2	114.5 (5)	N2—Co1—N1	80.64 (16)
S4—Mo1—S2	103.84 (19)	N11—Co1—N1	89.79 (18)
O1—Mo1—S3	112.0 (7)	N12—Co1—N13	80.48 (16)
S4—Mo1—S3	109.2 (2)	N2—Co1—N13	100.55 (16)
S2—Mo1—S3	108.11 (7)	N11—Co1—N13	90.77 (18)
O1—Mo1—S1	102.3 (5)	N1—Co1—N13	178.61 (17)
S4—Mo1—S1	115.37 (18)	N12—Co1—N3	100.80 (17)
S2—Mo1—S1	108.71 (6)	N2—Co1—N3	80.43 (16)
S3—Mo1—S1	111.11 (6)	N11—Co1—N3	177.54 (16)
N12—Co1—N2	178.43 (18)	N1—Co1—N3	90.75 (16)
N12—Co1—N11	81.49 (17)	N13—Co1—N3	88.74 (16)
N2—Co1—N11	97.29 (17)		

Table 2
Hydrogen-bond geometry (Å, °).

D—H···A	D—H	H···A	D···A	D—H···A
N1—H1N···S4^{i}	0.90	2.53	3.396 (8)	161
N1—H2N···S2	0.90	2.79	3.497 (5)	136
N2—H3N···S3^{ii}	0.91	2.82	3.613 (5)	147
N3—H4N···S1	0.90	2.76	3.567 (4)	150
N3—H5N···S3^{iii}	0.90	2.58	3.409 (4)	154
N11—H6N···S4^{i}	0.90	2.30	3.133 (8)	153
N11—H7N···S1^{ii}	0.90	2.84	3.635 (5)	149
N12—H8N···S2	0.91	2.73	3.525 (4)	146
N12—H8N···S4	0.91	2.76	3.491 (8)	138
N13—H9N···S1^{ii}	0.90	2.73	3.574 (5)	157

D—H···A	D—H	H···A	D···A	D—H···A
N13—H10N···S3^{iii}	0.90	2.61	3.493 (5)	166
N1—H1N···O1^{i}	0.90	2.34	3.18 (2)	155
N11—H6N···O1^{i}	0.90	2.43	3.290 (18)	161

Symmetry codes: (i) $x-1, y, z$; (ii) $-x+\frac{1}{2}, y+\frac{1}{2}, -z+\frac{3}{2}$; (iii) $-x+\frac{3}{2}, y+\frac{1}{2}, -z+\frac{3}{2}$.

All H atoms were positioned with idealized geometry and were refined with fixed isotropic displacement parameters [U_{iso}(H) = 1.2U_{eq}(C,N)] using a riding model, with C—H = 0.97 Å, C—H = 0.90 Å or N—H = 0.91 Å. The disordered S and O atoms were refined using a split model and anisotropic displacement parameters. Refinement of their site occupation factors proves that they are occupied 50:50, and this was assumed in the final refinement.

Data collection: *IPDS Software* (Stoe & Cie, 1998); cell refinement: *IPDS Software*; data reduction: *IPDS Software*; program(s) used to solve structure: *SHELXS97* (Sheldrick, 1997; program(s) used to refine structure: *SHELXL97* (Sheldrick, 1997); molecular graphics: *XP* in *SHELXTL* (Bruker, 1998) and *DIAMOND* (Brandenburg, 1999); software used to prepare material for publication: *CIFTAB* in *SHELXTL*.

This work is supported by the State of Schleswig-Holstein and by the Deutsche Forschungsgemeinschaft DFG (project: BE 1653/11–2).

References

Brandenburg, K. (1999). *DIAMOND*. Version 2.1c. Crystal Impact GbR, Bonn, Germany.

Bruker (1998). *SHELXTL*. Version 5.1. Bruker AXS Inc., Madison, Wisconsin, USA.

Callahan, K. P. & Piliero, P. A. (1980). *Inorg. Chem.* **19**, 2619–2626.

Ellermeier, J. (2002). PhD thesis, Kiel University, Germany.

Ellermeier, J. & Bensch, W. (2001). *Z. Naturforsch. Teil B*, **56**, 611–619.

Ellermeier, J. & Bensch, W. (2002). *Monatsh. Chem.* **133**, 945–957.

Ellermeier, J., Näther, C. & Bensch, W. (1999). *Acta Cryst.* C**55**, 501–503.

Müller, A., Ahlhorn, E. & Heinsen, H. H. (1971). *Z. Anorg. Allg. Chem.* **386**, 102–106.

Sheldrick, G. M. (1997). *SHELXS97* and *SHELXL97*. University of Göttingen, Germany.

Srinivasan, B. R., Dhuri, S. N., Poisot, M., Näther, C. & Bensch, W. (2004). *Z. Naturforsch. Teil B*, **59**, 1082–1092.

Stoe & Cie (1998). *IPDS Software*. Version 2.89. Stoe & Cie, Darmstadt, Germany.

3.1.5

Synthesis, Spectroscopic and X-Ray Structure Characterisation of Bis(tetramethylammonium), Bis(tetraethylammonium) and Bis(tetrapropylammonium) Tetrathiotungstates

Martha Poisot, Christian Näther, and Wolfgang Bensch

Institut für Anorganische Chemie, Christian-Albrechts-Universität Kiel, Olshausenstr. 40, D-24098 Kiel, Germany

Reprint requests to Prof. Dr. Bensch. Fax: +49(0)431 880 1520. E-mail: wbensch@ac.uni-kiel.de

Z. Naturforsch. **61b**, 1061 – 1066 (2006); received May 2, 2006

The three new tetraalkylammonium tetrathiotungstates $((Me)_4N)_2[WS_4]$ (**1**), $((Et)_4N)_2[WS_4]$ (**2**) and $((nPr)_4N)_2[WS_4]$ (**3**) were prepared *via* a direct salt substitution using $(NH_4)_2[WS_4]$ as starting material. Compound **1** crystallises in the chiral orthorhombic space group $P2_12_12_1$ with $a = 8.9433(4)$, $b = 15.5658(9)$ and $c = 37.279(2)$ Å. Compound **2** crystallises in space group $P2_1/n$ with lattice parameters $a = 16.6695(12)$, $b = 9.3415(6)$, $c = 16.9965(13)$ Å and $\beta = 117.185(15)°$. The third compound **3** crystallises in space group $C2/c$ with the lattice parameters $a = 32.440(2)$, $b = 13.8453(6)$, $c = 15.0563(10)$ Å and $\beta = 109.19(7)°$. The structures of all compounds consist of slightly distorted $[WS_4]^{2-}$ tetrahedra and tetraalkylammonium cations which are packed in different ways. One interesting observation is that the disorder of parts of the alkyl groups decreases with increasing chain length. The IR and Raman spectra show the vibrations of the $[WS_4]^{2-}$ tetrahedron with a slight shift with increasing alkyl chain length. The most prominent IR-band of the $[WS_4]^{2-}$ tetrahedra is broad but not split, indicating that the distortion of the tetrahedra is small.

Key words: Crystal Structure, Tetrathiotungstates, IR and Raman Spectroscopy

Introduction

The production of clean transport fuels by hydrotreating and specially deep hydrodesulfurization (HDS) has recently gained attention due to the introduction of new environmental legislation regarding fuel specifications [1, 2]. In order to meet the specifications there is an increased need to understand and consequently improve HDS catalysts. Alumina is the most widely used support material for preparing HDS catalysts due to its good mechanical and textural properties. However, one of its disadvantages is the strong interaction with metal precursors in the catalysts preparation step, which makes the complete sulfidisation of supported metal oxides difficult [3 – 5]. On the other hand, carbon has been probed as alumina replacement, and several studies [3 – 10] have demonstrated that carbon supported MoS_2, (Co/Ni)Mo(W) sulphide catalysts show a HDS activity superior to that of the alumina supported counterparts. This high activity can be attributed to an enhanced dispersion of catalytically active species.

Recently, Alonso *et al.* have reported that very efficient carbon containing MoS_2 and WS_2 catalysts are produced by the *in situ* decomposition of precursors during HDS of DBT [11]. In a previous report results of the synthesis of MoS_2 catalysts by the thermal decomposition of tetraalkyl tetrathiomolybdates were presented [12]. Moreover, the role of structural carbon for the activity of HDS catalysts was investigated and the results of a profound study gave evidences that a critical C content is essential for a high performance of such catalysts [13]. For MoS_2 based catalysts we demonstrated that the C content of the active material can be determined by the C content of the $(R)MoS_4$ precursors (R = organic ammonium ions) [12]. With respect to W-S chemistry it was demonstrated recently that the well known ammonium tetrathiotungstate is a useful precursor for the soft synthesis of WS_2 nanotubes [14, 15]. In another report the suitability of bis(cetyltrimethyammonium) tetrathiotungstate as a precursor for the formation of bulk quantities of uniform WS_2 nanotubes was reported [16]. In the meantime about 20 different tetrathiotungstates with different cations as charge balancing ions were reported in the literature [17 – 26]. The present contribution is part of our ongoing investigations aimed to the synthesis of active and efficient MoS_2 and

Table 1. Technical details of data acquisition and selected refinement results for **1–3**.

Compound	1	2	3
Formula	$C_8N_2H_{24}WS_4$	$C_{16}N_2H_{40}WS_4$	$C_{24}N_2H_{56}WS_4$
MG [g/mol]	460.38	572.59	684.80
Space group	$P2_12_12_1$	$P2_1/n$	$C2/c$
Temperature [K]	293	293	293
Wavelength [Å]	0.71073	0.71073	0.71073
a [Å]	8.9433(4)	16.6695(12)	32.440(2)
b [Å]	15.5658(9)	9.3415(6)	13.8453(6)
c [Å]	37.279(2)	16.9965(13)	15.0563(10)
β [°]	90	117.185(15)	109.19(7)
V [Å^3]	5189.7(5)	2354.3(3)	6386.7(7)
Z	12	4	8
μ [mm^{-1}]	7.139	5.26	3.89
$F(000)$	2688	1152	2816
D_{calc} [g cm^{-3}]	1.768	1.615	1.424
Crystal size [mm]	0.14, 0.09, 0.05	0.15, 0.11, 0.06	0.16, 0.12, 0.08
2θ Range [°]	2–22	5–56	5–56
Collected refls	26540	22976	31153
Unique reflections	6609	5644	7615
Data [$Fo > 4\sigma(Fo)$]	5191	4265	5779
$R_{int.}$	0.0884	0.0410	0.0534
$\Delta\rho$ [e/Å^3]	−2.224/1.664	−1.047/1.067	−0.708/0.526
Parameters refined	364	225	318
$R1$ [$Fo>4\sigma(Fo)$][a]	0.0567	0.0294	0.0300
$wR2$ for all unique data	0.1483	0.0744	0.0664
Goodness of fit	1.169	1.034	1.034
BASF parameter	0.43(4)	–	–

[a] $R1 = \Sigma||Fo| - |Fc||/\Sigma|Fo|$.

Table 2. Selected geometric parameters (Å, °) for $((Me)_4N)_2$-$[WS_4]$ (**1**).

W(1)-S(1)	2.187(8)	W(2)-S(7)	2.079(7)
W(1)-S(2)	2.162(8)	W(2)-S(8)	2.176(7)
W(1)-S(3)	2.196(8)	W(3)-S(9)	2.219(10)
W(1)-S(4)	2.192(10)	W(3)-S(10)	2.202(9)
W(2)-S(5)	2.165(9)	W(3)-S(11)	2.199(8)
W(2)-S(6)	2.155(8)	W(3)-S(12)	2.182(8)
S(2)-W(1)-S(1)	109.0(4)	S(7)-W(2)-S(8)	108.5(4)
S(2)-W(1)-S(4)	108.0(4)	S(6)-W(2)-S(8)	109.5(4)
S(1)-W(1)-S(4)	112.5(4)	S(5)-W(2)-S(8)	110.7(4)
S(2)-W(1)-S(3)	109.6(4)	S(12)-W(3)-S(11)	109.8(4)
S(1)-W(1)-S(3)	109.1(3)	S(12)-W(3)-S(10)	108.1(3)
S(4)-W(1)-S(3)	108.6(4)	S(11)-W(3)-S(10)	108.4(4)
S(7)-W(2)-S(6)	109.5(4)	S(12)-W(3)-S(9)	111.0(3)
S(7)-W(2)-S(5)	108.6(4)	S(11)-W(3)-S(9)	110.2(4)
S(6)-W(2)-S(5)	110.1(4)	S(10)-W(3)-S(9)	109.3(4)

WS_2 catalysts, and its Ni/Co promoted versions. For a full characterisation of the precursor materials and an understanding of the chemical reactivity the crystal structures of the compounds should be known. One interesting observation in the tetrathiotungstate chemistry with organic cations as charge balancing ions is the fact that no structural data are available with fully alkylated amines. In this contribution the syntheses, crystal structures and spectroscopic data of three new tetraalkylammonium tetrathiotungstates $(R_4N)_2WS_4$ (R = methyl, ethyl, propyl) are presented.

Experimental Section

Synthesis

The synthesis of the tetralkylammonium salts $(R_4N)_2MoS_4$ has been reported by McDonald [27]. Later this method was improved by Alonso [28]. In the present work, a modified version of the last method was used and crystals were grown from a very dilute solution. The amines and the solvents were used as obtained from commercial sources. $(NH_4)_2WS_4$ was prepared as reported in the literature [27]. Freshly prepared $(NH_4)_2WS_4$ (5 mmol) was dissolved in water (30 ml) and stirred. $(R_4N)Br$ (10 mmol) was dissolved in a solution of NaOH (10 mmol) in 30 ml water and stirred. The first solution was added to the second and the mixture was stirred for 30 min. Afterwards, the solution was kept undisturbed over ice to obtain the red crystalline products. The solid was filtered off and was washed with cold water and ethanol. 80% Yield. These compounds are stable on air.

Characterisation

A CHN-O RAPID combustion analyser from Heraeus was used to determine the content of C, H, N and S, using zinc sample holders with 2–3 mg per sample, heated up to 1000 °C under oxygen atmosphere. Compound **1**: calcd. C 20.9, H 5.21, N 6.08; found C 20.7, H 5.15, N 5.90; compound **2**: calcd. C 33.57, H 6.98, N 4.89; found C 33.42, H 6.93, N 4.89; compound **3**: calcd. C 42.13, H 8.18, N 4.09; found C 42.08, H 8.25, N 4.04.

Far IR spectra (80–500 cm^{-1}) were measured on a Bruker IFS 66 spectrometer in pressed polyethylene disks. MIR spectra (450–3000 cm^{-1}) were recorded in a ATI Mattson Genesis spectrometer. The samples were ground with dry KBr into fine powders and pressed into transparent pellets. Raman spectra were measured from 100 to 3500 cm^{-1} in a Bruker IFS 66 Fourier Transform Raman spectrometer.

Structure refinement details

Single crystal investigation of compounds **1–3** was performed using an Imaging Plate Diffraction System (*IPDS*) [29] with monochromated Mo-K_α-radiation (λ = 0.71073 Å). All structures were solved by direct methods using SHELXS-97 [30] and the refinement was done against F^2 using SHELXL-97 [31]. The data were corrected for Lorentz, polarisation and absorption effects. The crystal of compound 1 was racemically twinned, and a TWIN refinement was performed using SHELXL-97 (BASF parameter:

Table 3. Selected geometric parameters (Å, °) of $((Et)_4N)_2$-$[WS_4]$ (**2**).

W(1)-S(1)	2.2030(12)	W(1)-S(3)	2.1933(12)
W(1)-S(2)	2.1867(12)	W(1)-S(4)	2.1846(12)
S(2)-W(1)-S(1)	109.40(5)	S(3)-W(1)-S(1)	110.59(5)
S(2)-W(1)-S(3)	108.12(5)	S(4)-W(1)-S(1)	109.00(5)
S(4)-W(1)-S(2)	110.21(6)	S(4)-W(1)-S(3)	109.52(6)

Table 4. Selected geometric parameters (Å, °) of $((nPr)_4N)_2$-$[WS_4]$ (**3**).

W(1)-S(1)	2.1978(11)	W(1)-S(3)	2.1834(11)
W(1)-S(2)	2.2009(14)	W(1)-S(4)	2.1919(12)
S(1)-W(1)-S(2)	110.24(4)	S(4)-W(1)-S(1)	109.78(5)
S(3)-W(1)-S(4)	109.16(5)	S(3)-W(1)-S(2)	108.30(5)
S(3)-W(1)-S(1)	109.49(5)	S(4)-W(1)-S(2)	109.84(6)

0.43(4)). All non-hydrogen atoms were refined anisotropically except most of the C and N atoms in compound **1** in which three of the six crystallographically independent cations were disordered. All hydrogen atoms were placed in ideal geometry and were refined using a riding model. In compounds **2** and **3** also some of the cations were disordered and were refined using a split model.

Technical details of the data acquisitions and some refinement results are summarised in Table 1. Lists of selected bond lengths are given in Tables 2, 3 and 4. Crystallographic data (excluding structure factors) for the structures reported in this paper have been deposited with the Cambridge Crystallographic Data Centre as supplementary publication no. CCDC 608050 (**1**), CCDC 608051 (**2**) and CCDC 608052 (**3**). Copies of the data can be obtained, free of charge, on application to CCDC, 12 Union Road, Cambridge CB2 1EZ, UK. (fax: +44-(0)1223-336033 or email: deposit@ccdc.cam.ac.uk).

Results and Discussion

For compound **1** some crystallographic data can be found in literature [32]. It was reported that this compound crystallises in the orthorhombic space group *P*nam with $a = 12.48(1)$, $b = 15.37(2)$ and $c = 8.94(1)$ Å. However, no atomic coordinates and no R-values can be found in the CCDC data base [33]. In addition, the similarity of the unit cell parameters indicates that the authors have overlooked reflections which are leading to a triplication of one unit cell axis.

Complex **1** crystallises in the orthorhombic chiral space group $P2_12_12_1$. There are three crystallographically independent anions per asymmetric unit with no imposed symmetry (Table 2). The W(1)-S distances in the first anion range from 2.162(8) to 2.196(8) Å with an average of 2.184(2) Å. The coordination environment around W(1) is nearly a perfect tetrahedron with minimum and maximum S-W(1)-S angles of 108.0(4) and 112.5(4)° and an average of 109.5(7)°. The W(2)-S bonds are different with values ranging from 2.079(7) to 2.176(7) Å with a mean value of 2.143(7) Å and S-W(2)-S angles between 108.5(4) and 110.7(4)° (average: 109.48(4)°). In the third anion, W(3)-S distances range from 2.182(8) to 2.219(10) Å (average: 2.20(5) Å) and the S-W(3)-S angles are between 108.1(3) and 111.0(3)° (average: 109.46(7)°). At a first glance the W-S bond lengths seem to scatter over a wide range which is unusual for thiotungstates where no S···H bonding interactions can be formed. For instance, the W-S distances with such H bonding interactions range from 2.1856(11) to 2.2090(10) Å in $(NH_4)_2WS_4$ [20]. The difference between the longest and shortest W-S bond distance Δ is a good measure for the distortion of the WS_4 tetrahedron, and the values are 0.034, 0.097, and 0.037 Å for the three independent tetrahedra. Analysing the anisotropic displacement parameters of the S atoms it is obvious that there is some positional disorder in the $W(2)S_4$ tetrahedron which is not pronounced enough to refine the S positions with a split model. Hence it can be assumed that the very short W-S bonds are due to an artefact. A libration correction was also performed but without a significant effect onto the W(2)-S bond lengths. One should keep in mind that libration only shortens the bond lengths if the vibration of the atom is perpendicular to the bond axis. In the present tetrahedron this is not the case, explaining the very small difference of the bond lengths with and without the correction. The spectroscopic results (see below) support the assumption that the true $W(2)S_4$ tetrahedron must be more regular. An appreciable contamination with oxygen can be excluded because no bands are seen in the IR or Raman spectra accounting for W-O stretching vibrations. Furthermore, some of the displacement parameters of the S atoms of $W(1)S_4$ and $W(3)S_4$ are larger than those for the S atoms in compounds **2** and **3**. This may be the reason that the values for Δ of these two tetrahedra are larger than in the other two compounds.

Three methyl groups of the cations show a positional disorder with 50% occupancies for two positions in cations N(1) and N(6), while for cation N(2) the three CH_3 groups exhibit occupancies 60% : 40%. Fig. 1 shows two different views of the arrangement of the cations and anions.

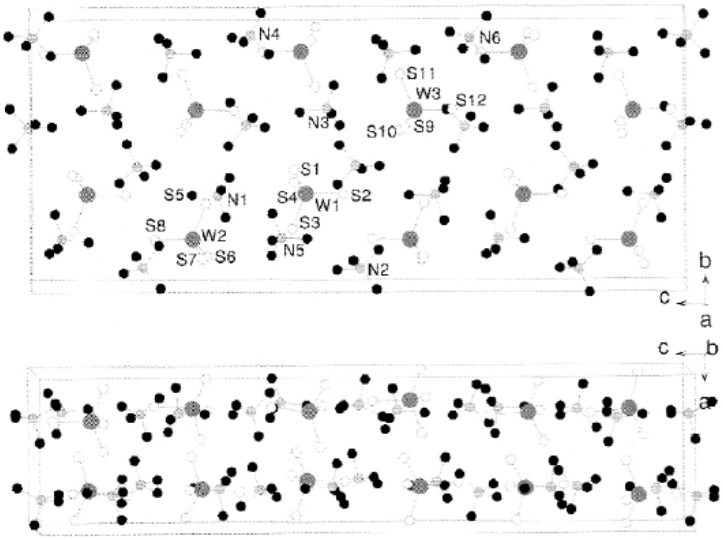

Fig. 1. View of the arrangement of cations and anions in compound **1** along [100] with labelling (top) and along [010] (bottom). Note: H atoms and disordered C atoms are not displayed for clarity.

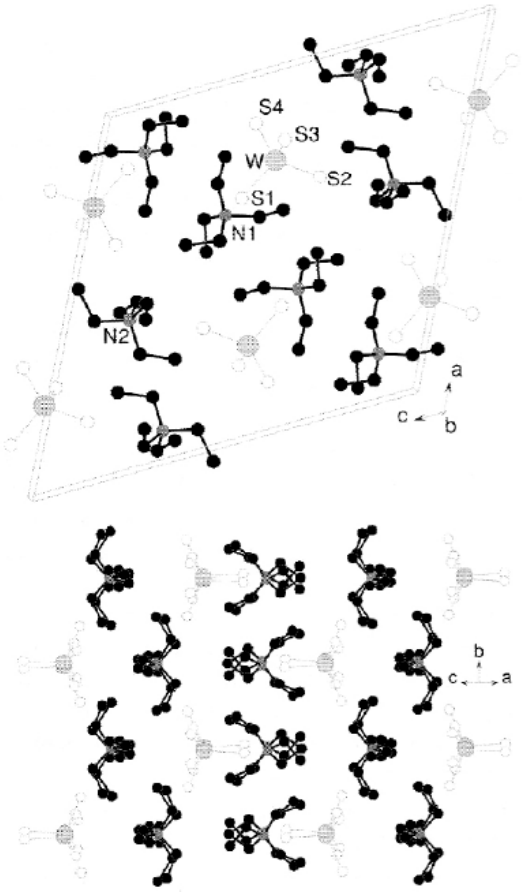

Fig. 2. View of the crystal structure of compound **2** along [010] with labelling (top) and onto the (101) plane (bottom). H atoms and disordered C atoms are not displayed for clarity.

Along [001] there are different types of rods. One is composed only of NMe_4^+ cations (I) and the other contains cations and anions in an alternating fashion (II). These rods show the order (I)-(II)-(II)-(I)-(I)··· along [010] leading to a layer-like arrangement in the (010) plane.

Compound **2** crystallises in the monoclinic space group $P2_1/n$ and is different compared to the analogous Mo compound which crystallises in the triclinic space group P-1 [34]. The crystal structure consists of a discrete tetrathiotungstate anion and two independent tetraethylammonium cations with all atoms located on general positions. The tetrahedral geometry of the WS_4^{2-} anion is only slightly distorted with S-W-S angles between 108.12(5) and 110.59(5)° (Table 2). The W-S bond lengths are between 2.1846(12) and 2.2030(12) Å giving a Δ value of 0.0184 Å. In one of the two cations a positional disorder occurs for the CH_2 group of one C_2H_5 unit (occupancies: 80 : 20). In Fig. 2 the arrangement of the constituents of **2** are displayed. Along [010] the anions and cations form individual rods, and a view onto the (101) plane reveals that within adjacent stacks the cations are arranged in a different way.

Compound **3** crystallises in the monoclinic space group $C2/c$ with all atoms except two N atoms being located on general positions. The structure contains an unique anion and three independent cations with two of them located in special positions. The WS_4 tetrahedron shows only a moderate distortion (S-W-S angles: 108.30(5) – 110.24(4)°, Table 3) and W-S bond

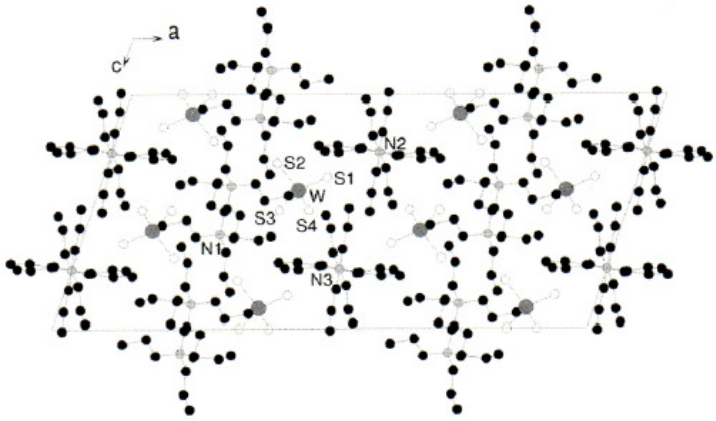

Fig. 3. Packing diagram of the constituents in compound **3** with view along [010] and labelling. Note that H atoms and disordered C atoms are not shown for clarity.

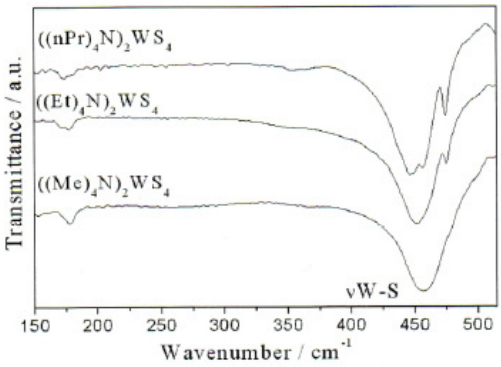

Fig. 4. IR spectra of compounds **1**–**3**.

lengths from 2.1834(11) to 2.2009(14) Å with a corresponding value for Δ of 0.0174 Å. In one of the three cations (N(3)) a positional disorder is observed with the C atoms involved showing a 50 : 50 occupancy. A packing diagram of the anions and cations in $((nPr)_4N)_2WS_4$ is displayed in Fig. 3.

The cations with the N(1) atom are arranged in columns along [001] whereas the remaining two cations alternate along this direction and the WS_4 tetrahedra are located between the rods of cations.

The compounds have been further characterised by IR and Raman spectroscopy. In the middle of the IR spectra several bands are observed which are caused by the organic cation vibrations. The absorptions around 3000 cm^{-1} are assigned to the C-H stretching vibrations with a shift to lower wave numbers with increasing chain length. Between 900 and 1500 cm^{-1} further vibrations of the aliphatic chains and the C-N vibrations are seen [35,36]. For a free tetrahedral WS_4 anion one can expect four characteristic bands $\nu_1(A_1)$, $\nu_2(E)$, $\nu_3(F_2)$, $\nu_4(F_2)$. The bands are Raman active and only ν_3 and ν_4 are IR active [37]. The strong band observed in the 458–478 cm^{-1} region of the IR spectra (Fig. 4) is assigned to the triply degenerated asymmetric vibration ν_3 of the WS_4 tetrahedron [24,26,38]. A slight shift of the maximum of the absorption is observed with increasing alkyl chain length. A similar observation was reported earlier for R = Me and nBu [28] and was explained on the basis of decreasing electropositivity with increasing chain length. But such an effect was not found when R was pentyl or hexyl [39]. Note that the sharp bands at about 480 cm^{-1} in the spectra of the ethyl and propyl compound are due to the organic part of the compounds. The weak absorption at around 175 cm^{-1} can be explained with the ν_4 vibration of the anion. This assignment is supported by strong lines in the Raman spectra located at the same energy [24,26].

The difference between the longest and shortest W-S distances is an important factor which may be considered as a measure for the distortion of the $[WS_4]^{2-}$ tetrahedron. In a recent report [24] we analysed the structural and spectroscopic properties of 14 tetrathiotungstate complexes. One interesting result of the analysis is that a critical value for Δ of about 0.03 Å is required to see a splitting of the bands of the W-S vibrations in the IR spectra. In many tetrathiotungstates the large Δ values are caused by N-H···S interactions and the number as well as the strengths of these determine the distortion of the tetrahedron. In the present compounds no such hydrogen bonding interactions are possible and consequently the values for Δ are small and below the above mentioned limit. The large Δ values for the anions in compound **1** are caused by structural disorder and consequently no splitting of the W-S vibrations occurs in the spectra. For the other two com-

pounds Δ is less than 0.03 Å and as expected only broad absorptions are seen in the IR spectra.

The methyl compound shows the strongest structural disorder of all three samples. The calculation of the space available for a non-hydrogen atom yields 28.8 $Å^3$ for compound **1** and about 25.7 $Å^3$ for the other two compounds. The larger space for the atoms in **1** suggests a less dense packing of the constituents and consequently less strong interactions.

Acknowledgements

The financial support by the Deutsche Forschungsgemeinschaft DFG (project: BE 1653/11-2) and by the State of Schleswig-Holstein is gratefully acknowledged.

[1] K.G. Knudsen, B.H. Cooper, H. Topsoe, Appl. Catal. A. **189**, 205 (1999).
[2] J.W. Grosselink, CaTTech. **4**, 127 (1998).
[3] J.C. Duchet, E.M. van Oers, V.H.J. de Beer, R. Prins, J. Catal. **80**, 386 (1983).
[4] J.P.R. Vissers, B. Scheffer, V.H.J. de Beer, J.A. Mouljin, R. Prins, J. Catal. **105**, 277 (1987).
[5] B. Scheffer, P. Arnoldy, J.A. Mouljin, J. Catal. **112**, 516 (1988).
[6] H. Farag, I. Mochida, K. Sakanishi, Appl. Catal. A. **194**, 147 (2000).
[7] E. Hillerova, Z. Vit, M. Zdrazil, Appl. Catal. **67**, 231 (1991).
[8] H. Farag, D.D. Whitehurst, K. Sakanishi, I. Mochida, Catal. Today **50**, 9 (1999).
[9] G. Kishan, L. Coulier, V.H.J. de Beer, J.A.R. van Veen, J.W. Niemantsverdriet, J. Catal. **19**, 180 (2000).
[10] G. Kishan, L. Coulier, J.A.R van Veen, J.W. Niemantsverdriet, J. Catal. **200**, 194 (2001).
[11] G. Alonso, M. del Valle, J. Cruz, V. Petranovskii, A. Licea-Claverie, S. Fuentes, Catal. Lett. **52**, 55 (1998).
[12] M. Poisot, W. Bensch, S. Fuentes, G. Alonso, Thermochim. Acta **444**, 35 (2006).
[13] G. Berhault, A. Mehta, A.C. Pavel, J. Yang, L. Rendon, M.J. Yacaman, L.C. Araiza, A.D. Moller, R.R. Chianelli, J. Catal. **198**, 9 (2001).
[14] M. Nath, A. Goviondaraj, C.N.R. Rao, Adv. Mater. **13**, 283 (2001).
[15] J. Chen, S.L. Li, F. Gao, Z.L. Tao, Chem. Mater. **15**, 1012 (2003).
[16] Y.D. Li, X.L. Li, R.R. He, J. Zhu, Z.X. Deng, J. Am. Chem. Soc. **124**, 1411 (2002).
[17] J. Ellermeier, R. Stähler, W. Bensch, Acta Crystallogr. **C58**, m70 (2002).
[18] J. Ellermeier, Ph. D. thesis, University of Kiel, Germany (2002).
[19] J. Yao, J.A. Ibers, Acta Crystallogr. **E60**, i10 (2004).
[20] B.R. Srinivasan, M. Poisot, C. Näther, W. Bensch, Acta Crystallogr. **E60**, i136 (2004).
[21] B.R. Srinivasan, S.N. Dhuri, C. Näther, W. Bensch, Acta Crystallogr. **E58**, m622 (2002).
[22] B.R. Srinivasan, S.N. Dhuri, C. Näther, W. Bensch, Acta Crystallogr. **C59**, m124 (2003).
[23] B.R. Srinivasan, S.N. Dhuri, M. Poisot, C. Näther, W. Bensch, Z. Anorg. Allg. Chem. **631**, 1087 (2005).
[24] B.R. Srinivasan, C. Näther, S.N. Dhuri, W. Bensch, Monatsh. Chem. **137**, 397 (2006).
[25] B.R. Srinivasan, S.N. Dhuri, C. Näther, W. Bensch, Acta Crystallogr. **E59**, m681 (2003).
[26] B.R. Srinivasan, C. Näther, S.N. Dhuri, W. Bensch, Polyhedron, 2006, in press.
[27] J.W. McDonald, G.D. Friesen, L.D. Rosenhein, W.E. Newton, Inorg. Chim. Acta **72**, 205 (1983).
[28] G. Alonso, A. Aguirre, I.A. Rivero, S. Fuentes, Inorg. Chim. Acta **274**, 108 (1998).
[29] Stoe & Cie, IPDS (Version 2.89), X-SHAPE (Version 1.03) and REDU4 (Version 7.03), Stoe & Cie, Darmstadt, Germany (1998).
[30] G.M. Sheldrick, SHELXS-97, Program for the solution of crystal structures, University of Göttingen, Germany (1994).
[31] G.M. Sheldrick, SHELXL-97, Program for the refinement of crystal structures, University of Göttingen (1997).
[32] V.N. Serezhkin, Zh. Neorg. Khim. (Russ) Russ. J. Inorg. Chem. **22**, 1554 (1977).
[33] ConQuest Version 1.8; Refcode ZZZBNS (2006).
[34] M.G. Kanatzidis, D. Coucouvanis, Acta Crystallogr. **C39**, 835 (1983).
[35] G. Berhault, L.C. Araiza, A.D. Moller, A. Mehta, R.R. Chianelli, Catal. Lett. **78**, 81 (2002).
[36] M. Hesse, H. Meier, B. Zeeh, Spektroskopische Methoden in der organischen Chemie, 5th Edition, G. Thieme, Würzburg (1995).
[37] A. Müller, N. Weinstock, H. Schulze, Spectrochim. Acta **28A**, 1075 (1972).
[38] K. Nakamoto, Infrared and Raman Spectra of Inorganic and Coordination Compounds, 5th Edition, John Wiley, New York (1997).
[39] G. Alonso, J. Yang, M.H. Siadat, R.R. Chianelli, Inorg. Chim. Acta **325**, 193 (2001).

3.1.6

Synthesis, Spectroscopic and X-Ray Structure Characterisation of Bis(tetramethylammonium) and Bis(tetra-*n*-butylammonium) Tetrathiomolybdates

Martha Poisot, Christian Näther, and Wolfgang Bensch

Institut für Anorganische Chemie, Christian-Albrechts-Universität Kiel, Olshausenstr. 40, 24098 Kiel, Germany

Reprint requests to Prof. Dr. W. Bensch. Fax: +49(0)431 880 1520. E-mail: wbensch@ac.uni-kiel.de

Z. Naturforsch. **2007**, *62b*, 209 – 214; received October 19, 2006

The new tetraalkylammonium tetrathiomolybdates $(Me_4N)_2[MoS_4]$ (1) and $(nBu_4N)_2[MoS_4]$ (2) were prepared *via* a direct salt substitution using $(NH_4)_2[MoS_4]$ as starting material. Compound 1 crystallises in the non-centrosymmetric orthorhombic space group $P2_12_12_1$ with $a = 8.9233(4)$, $b = 15.5210(9)$ and $c = 37.255(3)$ Å. Compound 2 crystallises in the orthorhombic space group $Fdd2$ with $a = 28.9142(18)$, $b = 35.7811(10)$ and $c = 15.6774(17)$ Å. The structures of both compounds consist of slightly distorted $[MoS_4]^{2-}$ tetrahedra and tetraalkylammonium cations which are packed in different ways. Single crystals of $(Et_4N)_2[MoS_4]$ (3) were also investigated giving the lattice parameters $a = 14.0346(7)$ and $c = 12.5143(8)$ Å. A very strong disorder prevented a successful structure refinement and only the anion and one cation could be located. It is remarkable that the disorder of parts of the alkyl groups decreases with increasing chain length, in correlation with the IR and Raman vibrations of the $[MoS_4]^{2-}$ tetrahedron showing a slight shift to lower energy with increasing alkyl chain length. The most prominent IR band of $[MoS_4]^{2-}$ is broad but not split, indicating that the distortion of the tetrahedra is small.

Key words: Crystal Structure, Tetrathiomolybdates, IR and Raman Spectroscopy

Introduction

The synthesis of molybdenum(IV) disulfide has been performed by a wide variety of methods leading to diverse particle sizes ranging from well developed crystals, powders, meso- or microporous materials to nanoparticles for a broad spectrum of purposes: solid lubricants for fireproof products [1], space technologies [2], base materials for semiconductor nanoclusters [3], electrode materials for photoelectrochemical solar cells [4], catalysts for electrochemical hydrogen evolution reactions [5], and the deep hydrodesulfurisation (HDS) of refinery streams [6]. Several research groups have observed that molybdenum sulphide compounds containing carbon (MoS_2-C) show enhanced properties with respect to electrical conductivity [7], tribology [8], morphology [9, 10], and improved catalytic activity for hydrotreating reactions [11]. The role of structurally incorporated carbon for the activity of a HDS catalyst was investigated and the results of a profound study gave evidences that a critical carbon content is essential for a high performance of such catalysts [12].

In a previous report we presented results of the synthesis of MoS_2 catalysts by the thermal decomposition of tetraalkylammonium tetrathiomolybdates, and we demonstrated that for MoS_2-based catalysts the carbon content of the active material can be determined by the carbon content of the $(R_4N)_2MoS_4$ (R = organic substituents) precursors [13]. In the meantime, nine thiomolybdates have been synthesised by our group: piperazinium, tris(2-aminoethyl)aminium, tetrapropylammonium [14], 1,3-propanediammonium, tetramethylethylenediammonium [15], 1,4-butanediammonium [16], bis[(±)-*trans*-2-aminocyclohexylammonium], *trans*-cyclohexane-1,4-diammonium [17], and bis(methylammonium) tetrathiomolybdate [18]. Only one of these compounds contains a tetraalkylammonium ion for charge balancing [14]. The present contribution is part of our ongoing investigations aimed at the synthesis of active and efficient MoS_2 and WS_2 catalysts, and its Ni/Co

promoted versions. The full characterisation of the precursor materials and the understanding of the chemical reactivity require the knowledge of the crystal structures. The syntheses, crystal structures and spectroscopic data of two new tetraalkylammonium tetrathiomolybdates $(R_4N)_2MoS_4$ (R = methyl and n-butyl) are presented. For R = ethyl some preliminary results are also reported.

Experimental Section

Synthesis

The synthesis of tetraalkylammonium salts $(R_4N)_2[MoS_4]$ by different preparative strategies was reported by several groups [19, 20]. In the present work, a slightly modified version was used and crystals were grown from very dilute solutions. The amines and the solvents were used as obtained from commercial sources. $(NH_4)_2[MoS_4]$ was prepared as reported by McDonald [19]. For the synthesis of the tetramethyl and tetraethyl thiomolybdates freshly prepared $(NH_4)_2[MoS_4]$ (1.4 mmol) was dissolved in water (30 mL) and stirred. $(R_4N)Br$ (2.8 mmol) was dissolved in a solution of NaOH (2.8 mmol) in 10 mL of water and stirred. The two solutions were mixed and stirred for 30 min. The solutions were kept undisturbed over ice, and red crystals precipitated overnight. The solids were filtered and washed with cold water and ethanol. The yield was about 80 % for both compounds. The compounds are stable in air for a long time period. The tetra-n-butylammonium thiomolybdate was synthesised using freshly prepared $(NH_4)_2[MoS_4]$ (0.7 mmol) which was dissolved in water (10 mL). An aqueous solution of $(nBu_4N)Br$ (1.4 mmol, 20 mL water) was added and the mixture was stirred for 30 min. Red crystals precipitated overnight which were stored under static vacuum over P_2O_5 (yield 80 %).

Characterisation

A CHN-O RAPID combustion analyser from Heraeus was used to determine the content of C, H, N, and S, using zinc sample holders with 2 – 3 mg samples, heated up to 1000 °C under oxygen atmosphere. Compound **1**: calcd. C 25.8, H 6.5, N 7.5, S 34.5; found C 25.9, H 6.5, N 7.5, S 34.5; compound **2**: calcd. C 54.2, H 10.2, N 3.9, S 18.1; found C 53.2, H 9.9, N 3.9, S 18.4; compound **3**: calcd. C 39.6, H 8.2, N 5.8, S 26.5; found C 39.1, H 8.1, N 5.7, S 26.1. Far IR spectra (80 – 500 cm^{-1}) were measured on a Bruker IFS 66 spectrometer in pressed polyethylene disks. MIR spectra (450 – 3000 cm^{-1}) were recorded with an ATI Mattson Genesis spectrometer. The samples were ground with dry KBr into fine powders and pressed into transparent pellets. Raman spectra were measured from 100 to 3500 cm^{-1} with a Bruker IFS 66 Fourier Transform Raman spectrometer.

Table 1. Technical details of data acquisition and selected refinement results for **1** – **2**.

Compound	**1**	**2**
Formula	$C_8N_2H_{24}MoS_4$	$C_{32}N_2H_{72}MoS_4$
Formula weight, g mol^{-1}	372.47	709.10
Space group	$P2_12_12_1$	$Fdd2$
Temperature, K	293	293
Wavelength, Å	0.71073	0.71073
a, Å	8.9233(4)	28.9142(18)
b, Å	15.5210(9)	35.7811(10)
c, Å	37.255(3)	15.6774(17)
V, $Å^3$	5159.8(5)	16220(2)
Z	12	16
μ, mm^{-1}	1.23	0.55
$F(000)$, e	2304	6144
D_{calc}, g cm^{-3}	1.438	1.162
Crystal size, mm^3	$0.15 \times 0.12 \times 0.12$	$0.6 \times 0.8 \times 0.6$
2θ range, deg	3 – 45	5 – 56
Collected reflections	32907	31396
Unique reflections	6589	9645
Data ($F_o \geq 4\sigma(F_o)$)	5482	6615
R_{int}	0.0436	0.0987
Parameters refined	398	353
Goodness of fit	1.083	0.994
Flack parameter x	0.0751(4)	
BASF parameter	0.455(1)	
$R1$ ($F_o \geq 4\sigma(F_o)$)[a]	0.0328	0.0502
$wR2$ (all unique data)	0.0865	0.1064
$\Delta\rho$, e $Å^{-3}$	−0.455/0.414	−0.4544/0.414

[a] $R1 = \sum ||F_o| - |F_c|| / \sum |F_o|$.

Structure refinement details

Single crystal investigations of the compounds were performed using an Imaging Plate Diffraction System (IPDS-1) [21] with monochromated MoK_α radiation (λ = 0.71073 Å). All structures were solved by Direct Methods using SHELXS-97 [22] and the refinements were carried out against F^2 using SHELXL-97 [23]. The data were corrected for Lorentz polarisation, and absorption effects. The crystal of compound **1** was racemically twinned, and therefore a twin refinement was performed (BASF parameter: 0.45(4)). All non-hydrogen atoms were refined anisotropically except for the methyl groups of two of the six tetramethylammonium cations which exhibit a positional disorder. All hydrogen atoms were placed in ideal geometry and were refined using a riding model. Fore compound **3** the absolute structure was determined be to in agreement with the selected setting (Flack parameter $x = -0.07(4)$). The structure of compound **3** was solved in the space group $P4/n$ and the anion as well as one cation could be located easily, but the second cation was heavily disordered and no reliable structural model could be found.

Technical details of the data acquisitions and some refinement results are summarised in Table 1. Lists of selected bond lengths are given in Tables 2 and 3. Crystallographic data (excluding structure factors) for the structures reported

Table 2. Selected geometric parameters (Å, deg) for $(Me_4N)_2[MoS_4]$ (**1**).

Mo(1)–S(1)	2.175(2)	Mo(2)–S(7)	2.177(3)
Mo(1)–S(2)	2.166(3)	Mo(2)–S(8)	2.172(2)
Mo(1)–S(3)	2.182(2)	Mo(3)–S(12)	2.177(3)
Mo(1)–S(4)	2.178(3)	Mo(3)–S(9)	2.182(2)
Mo(2)–S(5)	2.177(3)	Mo(3)–S(10)	2.183(2)
Mo(2)–S(6)	2.159(3)	Mo(3)–S(11)	2.186(2)
S(1)–Mo(1)–S(4)	110.87(12)	S(6)–Mo(2)–S(5)	109.41(15)
S(2)–Mo(1)–S(3)	109.86(13)	S(8)–Mo(2)–S(5)	110.29(13)
S(1)–Mo(1)–S(3)	109.64(10)	S(7)–Mo(2)–S(5)	109.32(15)
S(4)–Mo(1)–S(3)	108.84(11)	S(9)–Mo(3)–S(10)	110.12(12)
S(2)–Mo(1)–S(1)	108.96(12)	S(9)–Mo(3)–S(11)	109.22(10)
S(2)–Mo(1)–S(4)	108.65(12)	S(10)–Mo(3)–S(11)	108.90(11)
S(6)–Mo(2)–S(8)	109.44(11)	S(12)–Mo(3)–S(9)	110.06(9)
S(6)–Mo(2)–S(7)	109.53(12)	S(12)–Mo(3)–S(10)	108.18(10)
S(8)–Mo(2)–S(7)	108.85(11)	S(12)–Mo(3)–S(11)	110.34(11)

Table 3. Selected geometric parameters (Å, deg) of $(nBu_4N)_2[MoS_4]$ (**2**).

Mo(1)–S(1)	2.1792(14)	Mo(1)–S(3)	2.1898(15)
Mo(1)–S(2)	2.2047(13)	Mo(1)–S(4)	2.1950(13)
S(1)–Mo(1)–S(2)	110.58(6)	S(3)–Mo(1)–S(4)	108.62(6)
S(1)–Mo(1)–S(3)	109.58(8)	S(3)–Mo(1)–S(2)	110.05(5)
S(1)–Mo(1)–S(4)	107.85(6)	S(4)–Mo(1)–S(2)	110.12(5)

in this paper were deposited with the Cambridge Crystallographic Data Centre as supplementary publication no. CCDC 626635 (**1**), CCDC 626636 (**2**). Copies of the data can be obtained, free of charge, from The Cambridge Crystallographic Data Centre *via* www.ccdc.cam.ac.uk/data_request/cif.

Results and Discussion

For $(Me_4N)_2[MoS_4]$ (**1**) some crystallographic data have been published previously [24], and it was claimed that the material crystallises in space group *Pnam*. Unfortunately, no atomic coordinates and no *R* values have been deposited in the CCDC data base [25]. Furthermore, a comparison of the lattice parameters with that of **1** shows that there is a strong indication that the authors have overlooked reflections which lead to tripling of one unit cell axis. According to the present study, compound **1** crystallises in the orthorhombic space group $P2_12_12_1$, which was also observed for the analogous tungsten compound [27]. The unit cell parameters of the analogous tungsten compound are slightly larger than those of the present material which is caused by the differences of the ionic radii of W(VI) and Mo(VI). There are three crystallographically independent anions per asymmetric unit with no imposed symmetry (Table 2). The Mo(1)–S distances in the first anion

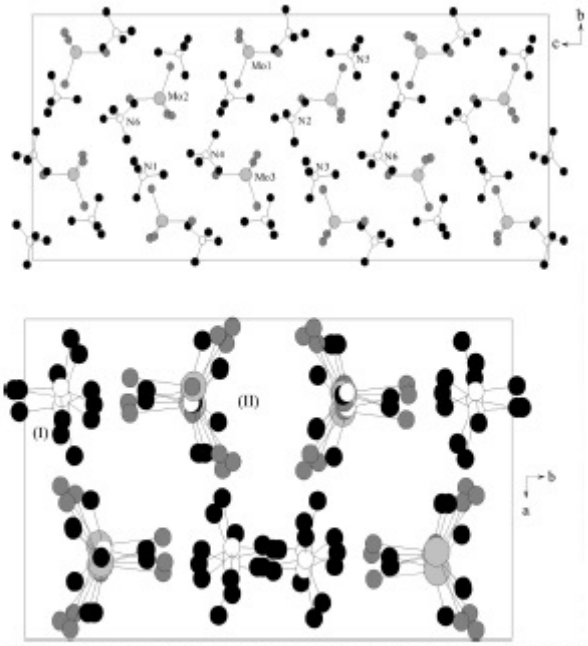

Fig. 1. Arrangement of cations and anions in the crystal of compound **1** viewed along the [100] (top) and along the [001] direction (bottom). The numbers (I) and (II) denote the two different rods formed either by cations alone (I) or by alternating cations and anions (II).

range from 2.165(3) to 2.182(2) Å with an average of 2.173(2) Å. The $Mo(1)S_4$ tetrahedron is slightly distorted with S–Mo(1)–S angles between 108.66(12) and 110.85(12)° (average: 109.75(12)°). The Mo(2)–S bonds are between 2.178(3) and 2.186(2) Å (mean value: 2.182(2) Å) with S–Mo(2)–S angles from 108.24(11) to 110.33(12)° (average: 109.28(12)°). In the third anion, the Mo(3)–S bond lengths range from 2.158(3) to 2.178(3) Å (average: 2.168(3) Å) and the S–Mo(3)–S angles are between 108.86(12) and 110.27(13)° (average: 109.56(12)°) (see also Table 2). The differences Δ between the longest and shortest Mo–S bond lengths amount to 0.016, 0.018, and 0.009 Å for Mo(1), Mo(2), and Mo(3), respectively. These small values as well as the S–Mo–S angles indicate that the tetrahedral geometry is only moderately distorted.

Three methyl groups of the cations show a positional disorder with 50 % occupancies for two positions in cation N(1), while for cation N(2) these groups exhibit occupancies of 60 % : 40 %. Fig. 1 shows two different views of the arrangement of cations and anions. Looking along [001] two different types of rods are seen. Type (I) is composed solely of cations, and

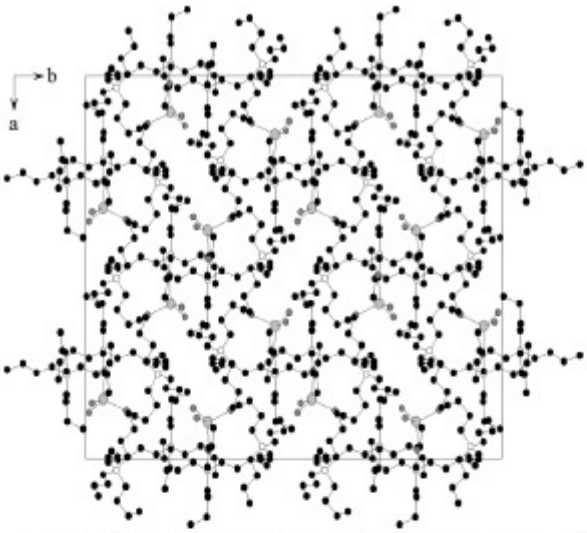

Fig. 2. Arrangement of the cations and anions in the structure of compound 2.

in type (II) cations and anions alternate. Along [010] these rods are arranged with the sequence ... (II)–(II)–(I)–(I).... The view along [010] reveals a layer-like arrangement of cations an anions.

$(n\mathrm{Bu}_4\mathrm{N})_2[\mathrm{MoS}_4]$ (**2**) crystallises in the orthorhombic space group *Fdd*2 with a = 28.9142(18), b = 35.7811(10), and c = 15.6774(17) Å. The asymmetric unit contains one crystallographically independent anion and two independent cations. The MoS_4 tetrahedron shows a moderate distortion which is slightly more pronounced than that for compound **1** (S–Mo–S angles: 107.85(6)–110.58(6)°, Table 1, Mo–S bond lengths: 2.1792(14)–2.2047(13) Å, Table 3) with a corresponding value for Δ of 0.0255 Å. No positional disorder was observed in this structure. In Fig. 2 the arrangement of anions and cations viewed along [001] is displayed. Eight cations are grouped to form pockets which host the anions.

Compound **3** crystallises in a primitive tetragonal space group with cell parameters a = 14.0346(7) and c = 12.5143(8) Å. It is a polymorph of the compound which was obtained by crystallisation in acetonitrile and ether [28]. Normally, thiotungstates and thiomolybdates with the same cation are isostructural. In the present case the Mo compound is not isostructural with the W analogue because the latter was reported to crystallise in space group $P2_1/n$ [27].

The compounds were further characterised by IR and Raman spectroscopy. In addition IR and Raman spectra were also recorded for the propyl compound [14]. The absorptions around 3000 cm^{-1} are assigned to the C–H stretching vibrations with a shift to lower wave numbers with increasing chain length. Between 900 and 1500 cm^{-1} further bands of the aliphatic chains and the C–N vibrations are seen [29,30]. For a free tetrahedral MoS_4 anion four characteristic bands $\nu_1(\mathrm{A}_1)$, $\nu_2(\mathrm{E})$, $\nu_3(\mathrm{F}_2)$, and $\nu_4(\mathrm{F}_2)$ are expected [31,32] of which ν_3 and ν_4 are IR active and all others are Raman active [33]. The strong bands observed in the 400–510 cm^{-1} region of the IR spectra (Fig. 3) are assigned to the triply degenerated asymmetric vibrations ν_3 of the MoS_4 tetrahedra.

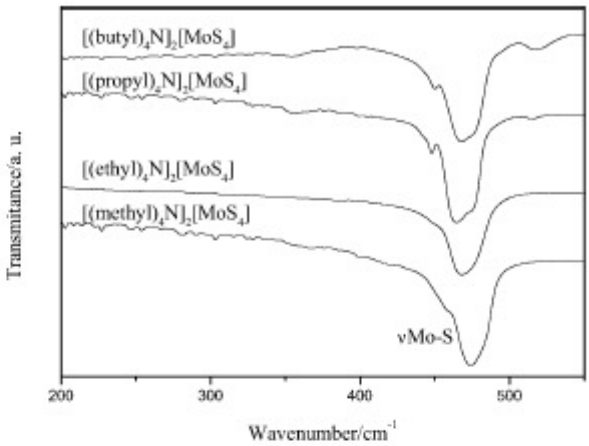

Fig. 3. Infrared spectra of tetraalkylammonium thiomolybdates in the region of Mo–S vibrations.

In the same way as observed for the tungsten analogues a slight shift of the absorption maximum to lower wave numbers with increasing alkyl chain length is observed: Me (474 cm^{-1}) > Et (467 cm^{-1}) > *n*Pr (464 cm^{-1}) < *n*Bu (467.8 cm^{-1}). A similar observation was reported earlier for R = Me and *n*Bu [20] and was explained on the basis of decreasing electropositivity with increasing chain length, but such an effect was not found when R was pentyl or hexyl [34]. However the tendency in the present series of compounds is not regular because for R = *n*Bu the band maximum is comparable with that for R = Et. It therefore appears that the positional disorder affects the absorption maximum leading to the observed trend. The sharp bands at about 450 cm^{-1} in the spectra of the *n*Pr and *n*Bu compounds are due to the organic part of the compounds. As expected the peak maxima of the asymmetric vibrations of the molybdenum compounds occur at higher wave numbers as compared to the tungsten samples.

The difference between the longest and shortest Mo–S distance is an important factor which may be considered as a measure for the distortion of the $[MoS_4]^{2-}$ tetrahedron. In a recent report [35] the structural and spectroscopic properties of 14 tetrathiotungstate complexes were analysed. One interesting result of the analysis is that a critical value for Δ of about 0.03 Å is required to see a splitting of W–S vibrations in the IR spectra. In many tetrathiotungstates and tetrathiomolybdates large Δ values are caused by N–H···S interactions. The analysis also revealed that the number and strength of these interactions determine the distortion of the WS_4 tetrahedron. For the fully alkylated ammonium ions no such hydrogen bonding interactions are possible and consequently the Δ values lie below the above mentioned limit, and only broad absorptions are seen in the IR spectra. A short comment should be made concerning the decrease of the positional disorder of the alkyl groups with increasing size of these molecules. The atomic volume for the non-H atoms decreases from 28.7 $Å^3$ for R = methyl to 25.5 $Å^3$ for $R = n$-butyl, *i. e.*, larger alkyl chains support a more dense packing which reduces the positional disorder.

Acknowledgement

The financial support by the Deutsche Forschungsgemeinschaft DFG (project: BE 1653/11-2) and by the State of Schleswig-Holstein is gratefully acknowledged.

[1] B. Eisenbach, PCT Int. Appl. **2002**, Application: WO 2002-EP1291 20020207.
[2] E. W. Roberts, W. B. Price, Sixth European Space Mechanism & Tribology Symposium, **1995**, ESA SP-374, 273.
[3] B. Abrahams, J. Wilcoxon, *Crit. Rev. Solid State Mater. Sci.* **2005**, *30*, 153.
[4] D. Ostermann, M. Depenbrock, Patent Ger. **2005**, Application: DE 2004-102004012303 20040311.
[5] B. Hinnemann, P. G. Moses, J. Bonde, K. P. Jorgensen, J. H. Nielsen, S. Horch, I. Chorkendorff, J. K. Norskov, *J. Am. Chem. Soc.* **2005**, *127*, 5308.
[6] T. C. Ho, *Catal. Today* **2004**, *98*, 3.
[7] C. Reza-San German, P. Santiago, J. A. Ascencio, U. Pal, M. Perez-Alvarez, L. Rendon, D. Mendoza, *J. Phys. Chem. B* **2005**, *109*, 17488.
[8] H. Kroto, W. K. Hsu, D. Walton, R. Whitby, PCT Int. Appl. **2002**, Application: WO 2002-GB1963 20020430.
[9] X. C. Song, Y. F. Zheng, G. Han, H. Y. Yin, G. S. Cao, *Gaodeng Xuexiao Huaxue Xuebao* **2005**, *26*, 617.
[10] G. Alonso, G. Berhault, F. Paraguay, E. Rivera, S. Fuentes, R. R. Chianelli, *Mater. Res. Bull.* **2003**, *38*, 1045.
[11] G. Alonso, S. Fuentes, R. R. Chianelli, PCT Int. Appl. **2005**, Application: WO 2004-US10677 20040407.
[12] G. Berhault, A. Mehta, A. C. Pavel, J. Yang, L. Rendon, M. J. Yacaman, L. C. Araiza, A. D. Moller, R. R. Chianelli, *J. Catal.* **2001**, *198*, 9.
[13] M. Poisot, W. Bensch, S. Fuentes, G. Alonso, *Thermochim. Acta* **2006**, *444*, 35.
[14] B. R. Srinivasan, S. N. Dhuri, M. Poisot, C. Näther, W. Bensch, *Z. Naturforsch.* **2004**, *59b*, 1083.
[15] B. R. Srinivasan, S. N. Dhuri, C. Näther, W. Bensch, *Inorg. Chim. Acta* **2005**, *358*, 279.
[16] B. R. Srinivasan, C. Näther, W. Bensch, *Acta Crystallogr.* **2005**, *E61*, m2454.
[17] B. R. Srinivasan, C. Näther, W. Bensch, *Acta Crystallogr.* **2006**, *C62*, m98.
[18] B. R. Srinivasan, C. Näther, A. R. Naik, W. Bensch, *Acta Crystallogr.* **2006**, *E62*, m1635.
[19] J. W. McDonald, G. D. Friesen, L. D. Rosenhein, W. E. Newton, *Inorg. Chim. Acta* **1983**, *72*, 205.
[20] G. Alonso, A. Aguirre, I. A. Rivero, S. Fuentes, *Inorg. Chim. Acta* **1998**, *274*, 108.
[21] Stoe & Cie. IPDS (Version 2.89), X-SHAPE (Version 1.03) and REDU4 (Version 7.03, Stoe & Cie, Darmstadt (Germany) **1998**.
[22] G. M. Sheldrick, SHELXS-97: Program for Crystal Structure Solution, University of Göttingen, Göttingen (Germany) **1997**.
[23] G. M. Sheldrick, SHELXL-97: Program for Crystal Structures Refinement, University of Göttingen, Göttingen (Germany) **1997**.
[24] V. N. Serezhkin, *Zh. Neorg. Khim. (Russ); Russ. J. Inorg. Chem.* **1977**, *22*, 1554.
[25] ConQuest Version 1.8; Refcode ZZZBNS, **2006**.
[26] D. E. Schwarz, T. B. Rauchfuss, S. R. Wilson, *Inorg. Chem.* **2006**, *42*, 2410.
[27] M. Poisot, C. Näther, W. Bensch, *Z. Naturforsch.* **2006**, *61b*, 1.
[28] M. G. Kanatzidis, D. Coucouvanis, *Acta Crystallogr.* **1983**, *C39*, 835.
[29] G. Berhault, L. C. Araiza, A. D. Moller, A. Mehta, R. R. Chianelli, *Catal. Lett.* **2002**, *78*, 81.
[30] M. Hesse, H. Meier, B. Zeeh, *Spektroskopische Methoden in der Organischen Chemie*, 5th Ed., G. Thieme, Würzburg, **1995**.
[31] A. Müller, E. Diemann, R. Jostes, H. Bögge, *Angew. Chem.* **1981**, *93*, 957; *Angew. Chem. Int. Ed.* **1981**, *20*, 934.

[32] K. Nakamoto, *Infrared and Raman Spectra of Inorganic and Coordination Compounds*, 5th Ed., John Wiley, New York, **1997**.
[33] A. Müller, N. Weinstock, H. Schulze, *Spectrochim. Acta* **1972**, *28A*, 1075.
[34] G. Alonso, J. Yang, M. H. Siadati, R. R. Chianelli, *Inorg. Chim. Acta* **2001**, *325*, 193.
[35] B. R. Srinivasan, C. Näther, S. N. Dhuri, W. Bensch, *Monatsh. Chem.* **2006**, *137*, 397.

3.2 Thermal studies

3.2.1 Decomposition of Tetraalkylammonium Thiomolybdates characterised by Thermoanalysis and Mass Spectrometry

The thermal behavior of the tetraalkylammonium tetrathiomolybdates $(R_4N)_2MoS_4$ with R ranging from methyl to heptyl was studied with differential thermal analysis (DTA), thermogravimetry (TG), DTA-TG coupled with mass spectrometry (DTA-G-MS), differential scanning calorimetry (DSC), scanning electron microscopy (SEM), X-ray powder diffractometry (XRD) and in-situ thermodiffractometry. The compounds with R = methyl and ethyl show a simple single step decomposition. With increasing alkyl size the decomposition mechanisms become gradually more complex. The onset temperature for the decomposition of the materials is a function of the precursor and a tendency to lower temperatures is observed with increasing size of the amine. During decomposition no S rich intermediates are formed. It is remarkable that only the precursors with R = methyl to pentyl produce nearly stoichiometric molybdenum disulfide with moderate contents of carbon and hydrogen, while for R = hexyl and heptyl sulphur deficient MoS_{2-x} materials with high C and H contents are formed. These materials can be better described as carbosulfides than as contaminated sulfides. With increasing size of the alkylammonium ion the final products contain more and more cavities as can be seen in the SEM images. DSC studies combined with thermodiffractometry experiments were performed for compounds with R = ethyl, propyl, butyl, pentyl and heptyl to further elucidate the nature of some low temperature endothermic events. For R = ethyl a partially reversible phase transition occurs, while for R = propyl three different structural modifications can be identified. The butyl compound undergoes an irreversible phase transition, while the event observed for the heptyl compound is associated with the melting point. The results of the MS experiments suggest a common decomposition mechanism for the compounds. During the thermal reaction trialkylamine and dialkyldisulfide molecules are emitted simultaneously.

3.2.2 Decomposition of Tetraalkylammonium Thiotungstates characterized by Thermoanalysis, Mass Spectrometry, X-ray diffractometry and Scanning Electron Microscopy

The tetraalkylammonium tetrathiotungstate compounds $(R_4N)_2WS_4$ with R ranging from methyl to heptyl present similar decomposition mechanisms as the analogous molybdenum materials. All compounds decompose without forming sulfur rich intermediates. Similarly to the molybdenum analogues, the compounds from methyl to pentyl yield disulfides which are

slightly contaminated with residual C and H. The residual carbon and hydrogen contents increase in the final decomposition products in the same order as the number of C atoms in R_4N increases for compounds with R = hexyl and heptyl carbon rich tungsten disulfides are obtained which are called carbon supported tungsten sulfides. The W/S ratio in the products is about 1.5. A general thermal decomposition mechanism is suggested which follows a bimolecular nucleophilic substitution reaction. In contrast to the findings for the analogous molybdenum samples, the morphology of the final decomposition products shows no tendency to develop porous materials. In the SEM images only for R = heptyl the formation of macro-pores with a sponge-like morphology is seen. X-ray diffraction analysis of the final products shows the formation of amorphous WS_2 up to R = pentyl. But the patterns of the products for R = hexyl and heptyl are different and it can be assumed that carbosulfide phases are formed by a mixed C–W–S sandwich layered structure. DSC studies combined with thermodiffractometry show that tetraethyl and tetrapropyl samples undergo structural phase transitions at low temperatures, which may be due to conformational motion and/or disorder of the alkyl chains. The results of the study indicate that the two tetraalkylammonium thiotungstates obtained by the solvent route are metastable forms that transform into the thermodynamically more stable materials upon heating. The tetrapentyl compound shows an irreversible phase transition while the tetraheptyl sample exhibits a glass-like transition and melting prior to decomposition.

3.2.1

Available online at www.sciencedirect.com
SCIENCE DIRECT®
Thermochimica Acta 444 (2006) 35–45
thermochimica acta
www.elsevier.com/locate/tca

Decomposition of tetra-alkylammonium thiomolybdates characterised by thermoanalysis and mass spectrometry

M. Poisot [a], W. Bensch [a,*], S. Fuentes [b], G. Alonso [c]

[a] *Institut fitr Anorganische Chemie, University of Kiel, Olshausenstr. 40-60, 24118 Kiel, Germany*
[b] *Centro de Ciencias de la Materia Condensada, Universidad Nacional Autonoma de, Mexico, Apdo. Postal 2681, Ensenada, Baja California, CP 22800, Mexico*
[c] *Centro de Investigación en Materiales Avanzados, Miguel de Cervantes No. 120, Chihuahua, Chih., CP 31110, Mexico*

Received 22 November 2005; received in revised form 24 January 2006; accepted 21 February 2006
Available online 28 February 2006

Abstract

The decomposition pattern of tetraalkyl-tetrathiomolybdates with general formula $(R_4N)_2MoS_4$ (with R increasing from methyl to heptyl) was determined by means of differential thermal analysis (DTA), thermogravimetric analysis (TGA) and mass spectroscopy (MS) techniques. The complexity of thermal decomposition reactions increases with the size of the R_4N group. Prior to decomposition at least one phase transition seems to occur in all complexes. The onset of thermal reactions was also a function of the tetra-alkylammonium precursor. All compounds decompose without forming sulfur rich MoS_{2+x} intermediates. For R = methyl to pentyl precursors the MoS_2 produced was nearly stoichiometric, however for R = hexyl and heptyl the S content was significantly reduced with a Mo:S ratio of about 1.5. The carbon and hydrogen residual contents in the product increased with the number of C atoms in R_4N; for N contamination no clear trend was obvious. SEM images show that the formation of macro-pores was also a function of the alkyl group in R_4N. The MoS_2 materials obtained show a sponge-like morphology. Results of DSC experiments in combination with in situ X-ray diffraction also revealed the complex thermal behavior of $(R_4N)_2MoS_4$ materials; reversible and irreversible phase transitions and glass-like transformations were identified in the low temperature range (35–140 °C), before the onset of decomposition.

Keywords: Thiometallates; Tetraalkyl-thiomolybdates; MoS_2 preparation; Thermal decomposition; Thermoanalysis

1. Introduction

Transition metal thiometallate complexes are useful for applications in several processes as biological [1], enzymatic [2] and as catalyst precursors [1,3–9]. Preparation of catalysts with better catalytic activity and stability than the present ones represents a great challenge for the industry and implies the search of new routes of preparation. During the last few years a number of contributions appeared in the literature dealing with different approaches to synthesize MoS_2 catalysts under different synthetic conditions and also the use of alkylthiometallates as catalysts precursors have been reported [10–21]. Transition metal sulfides (TMS), particularly molybdenum and tungsten sulfides, promoted with Co or Ni and supported on alumina are typically used in hydrotreating reactions [22]. The use of bis-thiometallates containing Co, Ni and Mo as precursors of hydrotreating catalysts has been reported [23–26].

The decomposition of ammonium thiomolybdate (ATM) and ammonium thiotungstate (ATT) has been studied by several authors [27,28].

More recently it has been studied by X-ray absorption fine structure spectroscopy (EXAFS) and powder X-ray diffraction (XRD) [29–31]. These compounds form trisulfide compounds $Mo(W)S_3$ as intermediates prior to be transformed to the poorly crystalline (pc) form of MoS_2. The decomposition of tetra-alkylammonium thiometallates has been used for preparation of MoS_2 catalysts for hydrodesulfurization and has been analyzed by means of DTA and TG [32] however a clear mechanism of the process has not yet been reported.

In this work, a further study of tetra-alkylammonium thiomolybdates decomposition patterns by means of combined techniques DTA–TG–DTG and MS is performed. The main goal in this work is to provide a general picture of the decom-

* Corresponding author. Tel.: +49 431 880 2091.
E-mail address: wbensch@ac.uni-kiel.de (W. Bensch).

0040-6031/$ – see front matter © 2006 Elsevier B.V. All rights reserved.
doi:10.1016/j.tca.2006.02.025

position process of tetra-alkyl thiomolybdates $(R_4N)_2MoS_4$, where R changes from C1 (methyl) up to C7 (heptyl).

2. Experimental

2.1. Preparation of $(R_4N)_2MoS_4$ precursors

The synthesis of the tetra-alkylammonium salts $(R_4N)_2MoS_4$ has been reported by McDonald et al. [33]. Later this method was improved by Alonso et al. [34]. In the present work, a modified version of the last method was used.

2.1.1. Synthesis of tetramethyl-, tetraethyl-, tetrapropyl-ammonium thiomolybdate

Fresh prepared $(NH_4)_2MoS_4$ (5 mmol) was dissolved in water (30 ml) and stirred. $(R)_4NBr$ (10 mmol) was dissolved in a solution of NaOH (10 mmol) in 30 ml water and stirred. The first solution was added to the second and the mixture was stirred for 30 min. The solution was kept undisturbed over ice and after one night red crystals precipitated. The solid was filtered and washed with cold water and ethanol, the yield was 80%. These compounds are stable in air for a long time.

2.1.2. Synthesis of tetrabutyl-, tetrapentyl-, tetrahexyl-, and tetraheptyl-ammonium thiomolybdates

Fresh synthesized $(NH_4)_2MoS_4$ (1.9 mmol) was dissolved in water (10 ml) and stirred until a clear solution was obtained. To this solution an aqueous solution of $(R)_4NBr$, R = butyl, pentyl, (3.8 mmol, 20–25 ml water) was added and the mixture was stirred for 30 min. For R = hexyl and heptyl the synthesis was performed in methanol. First a gel-like solid was formed and after ethanol was added dark red crystals precipitated. The solid was filtered and washed with cold water, and the yield was 90%. These compounds are unstable in air and they were stored under nitrogen atmosphere.

2.2. Methods and materials

A CHN-O RAPID combustion analyzer from Heraeus was used to determine the chemical composition of the materials. The samples were heated up to 1000 °C under an oxygen atmosphere in zinc sample holders and the gases were then detected by gas chromatography.

A Philips ESEM XL 30 microscope equipped with an EDAX analyzer was used to perform morphological and elemental analysis. Pictures were taken at different areas of the samples applying different magnifications.

DTA–TG–MS measurements were undertaken simultaneously using a STA-409CD with Skimmer coupling from Netzsch, which is equipped with a quadrupole mass spectrometer QMA 400 (maximum 512 amu) from Balzers. The MS measurements were performed in analog and trend scans modes. All TG curves were corrected for buoyancy and current effects. The heating rate was 4 K/min up to 350 °C. For DTA–TG experiments the samples were placed in Al_2O_3 crucibles under a dynamic nitrogen atmosphere (flow rate: 75 ml/min, purity 5.0). DTA–TG–MS measurements were performed under a dynamic helium atmosphere (flow rate: 50 ml/min, purity 5.6). The MS spectra recorded were compared with data from the National Institute of Standards and Technology, NIST (http://webbook.nist.gov/chemistry). DSC experiments (heating rate: 3 K/min; final temperature: 150 °C) were performed with

Table 1
Data of chemical analysis, weight loss and thermal events for $(R_4N)_2MoS_4$

R	Weight loss (%)	C (%)	H (%)	N (%)	S (%)	Composition	T_p (°C)	T_{onset} (°C)
Methyl	−56.5	25.9	6.5	7.5	34.5	$MoS_{1.96}C_{0.2}N_{0.02}$	246	239
		25.8	6.49	7.52	34.43			
		1.5	0.0	0.2	39			
Ethyl	−64	39.3	8.2	5.7	26.1	$MoS_{1.96}C_{0.79}N_{0.04}H_{0.5}$	43, 224	40, 217
		39.65	8.32	5.78	26.46			
		5.6	0.3	0.4	37.1			
Propyl	−71.4	47.9	9.4	4.6	20.9	$MoS_{1.97}C_{0.73}N_{0.04}H_{0.5}$	108, 176, 222	102, 169, 216
		48.29	9.46	4.69	21.49			
		5.2	0.3	0.4	37.4			
Butyl	−74	54.0	10.1	3.9	18.1	$MoS_{2.03}C_{1.13}N_{0.04}H_{0.8}$	117, 142, 167, 194	115, 139, 157, 189
		54.2	10.23	3.95	18.09			
		7.7	0.5	0.4	37			
Pentyl	−76	58.2	10.6	3.3	15.4	$MoS_{1.99}C_{1.18}N_{0.07}H_{1.14}$	218	205
		58.49	10.8	3.41	15.62			
		8.1	0.6	0.5	36.3			
Hexyl	−79.6	61.5	11.1	3.0	13.4	$MoS_{1.5}C_{1.53}N_{0.09}H_{2.14}$	167, 239, 292	162, 212
		61.76	11.23	3.0	13.74			
		11.1	1.3	0.8	29.1			
Heptyl	−81	64.2	11.7	2.7	11.9	$MoS_{1.3}C_{2.6}N_{0.13}H_{3.33}$	76, 178, 275	72, 158, 244
		64.32	11.57	2.68	12.26			
		18.1	1.9	1.1	24.3			

Chemical composition: first line, experimental values; second line, theoretical values; third line, after decomposition.

a Netzsch DSC 204 Phoenix instrument using aluminum crucibles covered with aluminum lid. Sealed glass ampoules filled with argon were also used as sample carriers to prevent a reaction of the samples with Al. The ampoules were mounted in an aluminum shoe to ensure a good thermal contact with the thermocouple. An empty sealed glass ampoule with an Al shoe was used as reference. For these experiments just the temperature was calibrated measuring mercury, indium, tin and bismuth provided by Netzsch.

3. Results

3.1. Elemental analysis

The results of chemical analysis of the MoS_2 catalysts before and after the thermal decomposition of tetra-alkyl thiomolybdate precursors are shown in Table 1. The content of carbon in the decomposed products increases gradually with the size of the alkyl group, from 1.5 wt.% for tetramethylammonium up to 18.1 wt.% for tetraheptylammonium. The amount of hydrogen and nitrogen also increase from tetramethylammonium to tetraheptylammonium tetrathiomolybdate (from 0 to 1.9 wt.% for H and from 0.2 to 1.1 wt.% for N). According to the chemical analyses the atomic ratio S/Mo is about 2 for the precursors with R = methyl until R = pentyl. But for the hexyl and heptyl samples the S concentration is significantly lower. The atomic composition of the catalysts in Table 1 shows that carbon and hydrogen coexist with MoS_2 in about the same proportion for catalysts derived from C1 to C5 alkyl groups suggesting that they may exist combined as CH groups which remain trapped between the MoS_2 layers or adsorbed on its surface. Otherwise, the amount of N is much lower than that of C and H and are considered as residual trace. The composition of catalysts formed from C6 and C7 alkyl precursors show an important reduction of S concentration as well as a significant augment of C and H, suggesting that these elements substituted partially S in the structure of MoS_2.

These results clearly indicate that the size of alkyl precursor influence the final composition of the decomposition products and that carbon and hydrogen can be an important part of the final MoS_2 catalyst.

3.2. DTA–TG–DTG–MS characterization

3.2.1. Tetramethylammonium thiomolybdate $((CH_3)_4N)_2MoS_4$

The thermal decomposition reaction of $((CH_3)_4N)_2MoS_4$ occurred in one step starting at about 240 °C, accompanied by a strong endothermic peak at T_{onset} = 239 °C (Fig. 1). During this event a mass loss of 56.5% was detected. The weight loss process ended at 350 °C. The thermal decomposition reaction can be represented as

$$((CH_3)_4N)_2MoS_4 \rightarrow 2(CH_3)_3N + (CH_3)_2S_2 + MoS_{1.96}C_{0.2}N_{0.02} \quad (1)$$

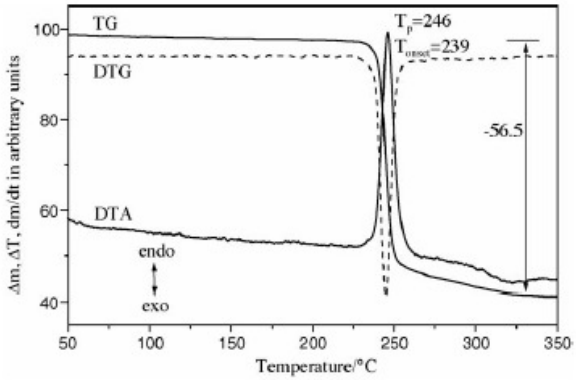

Fig. 1. DTA, TG and DTG plot of $[(methyl)_4N]_2[MoS_4]$ decomposition. Temperature in °C and weight loss in %.

The theoretical mass loss expected for the formation of MoS_2 is 57%, and therefore it can be assumed that some amount of carbon remained trapped or adsorbed in MoS_2. The mass spectrum (Fig. 2) shows that trimethylamine (m/z = 59) and dimethyldisulfide (m/z = 94) were emitted at 240 °C, it is related to the endothermic peak detected. The TG–MS results indicate that tetramethylammonium thiomolybdate decomposes at lower temperature than ammonium thiomolybdate (ATM) and also as shown in Eq. (1) it does not form MoS_3 as an intermediate which further decomposes to MoS_2 as ATM typically does [28,35–38].

3.2.2. Tetraethylammonium thiomolybdate $((CH_3CH_2)_4N)_2MoS_4$

The thermal decomposition reaction of $((CH_3CH_2)_4N)_2MoS_4$ also took place in one step starting at 200 °C, however it was accompanied by at least two endothermic peaks (Fig. 3). The nature of the event at low temperature (T_{onset} = 40 °C) was analyzed by DSC and XRD and will be discussed below. The second peak (T_{onset} = 217 °C) can be assigned to the amine fragmentation and elimination. Similarly to the methyl precursor endothermic peaks may be attributed to molecule rearrangement and formation of diethyldisulfide (DEDS).

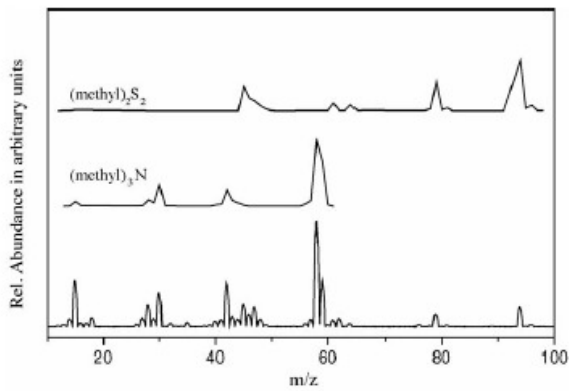

Fig. 2. Mass spectrum of $[(methyl)_4N]_2[MoS_4]$ decomposition at 240 °C. *Note*: the top two traces were taken from http://webbook.nist.gov/chemistry.

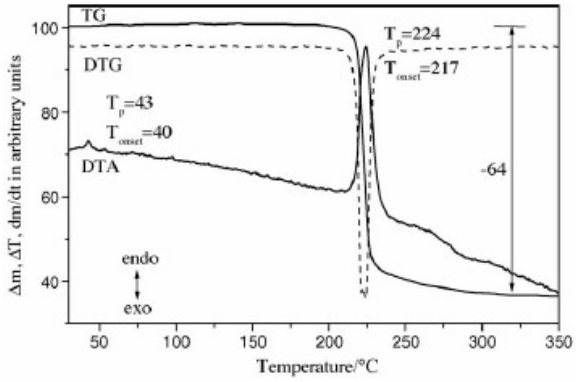

Fig. 3. DTA, TG and DTG plot of $[(ethyl)_4N]_2[MoS_4]$ decomposition. Temperature in °C and weight loss in %.

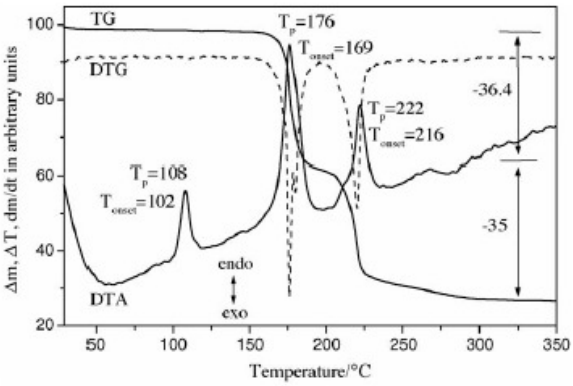

Fig. 5. DTA, TG and DTG plot of $[(propyl)_4N]_2[MoS_4]$ decomposition. Temperature in °C and weight loss in %.

The experimental weight loss of 64.2% is lower than the theoretical value of 66.95% for the formation of MoS_2, in agreement with the larger amount of residual carbon than in the methyl precursor (see Table 1). The weight loss also ended at 350 °C. The corresponding equation is

$$((CH_3CH_2)_4N)_2MoS_4 \rightarrow 2(CH_3CH_2)_3N + (CH_3CH_2)_2S_2 + MoS_{1.96}C_{0.79}N_{0.04}H_{0.5} \quad (2)$$

The MS spectrum (Fig. 4) shows the emission of triethylamine ($m/z = 101$) and DEDS ($m/z = 122.16$) which indicates that a similar pattern of fragmentation as in the methyl precursor occurred, indeed the onset of decomposition decreased to 200 °C. Again, there are no hints for the formation of MoS_3 as an intermediate.

3.2.3. Tetrapropylammonium thiomolybdate $((CH_3(CH_2)_2)_4N)_2MoS_4$

The thermal decomposition reaction of this precursor is more complex than in the previous cases and a two-step decomposition mechanism starting at about 155 and 210 °C is observed (Fig. 5). The first strong endothermic peak at $T_{onset} = 102$ °C corresponds to a phase transition of the crystal structure, whereas the other endothermic events at $T_{onset} = 169$ and 216 °C may be due to molecular redistribution and fragmentation. In the first decomposition step the weight loss amounts to 36.4% while during the next thermal process the weight loss is 35%. The experimental weight change is again lower than the expected value of 73.1% for the formation of MoS_2, and the thermal reaction path may be formulated as

$$((CH_3(CH_2)_2)_4N)_2MoS_4 \rightarrow 2(CH_3(CH_2)_2)_3N + (CH_3(CH_2)_2)_2S_2 + MoS_{1.97}C_{0.73}N_{0.04}H_{0.5} \quad (3)$$

From this equation a substantial increase in retained carbon is observed, but the S content remains very close to stoichiometric values. The weight loss ends at 300 °C, lower than for the two previous samples.

In the mass spectrum (Fig. 6) tripropylamine ($m/z = 143$) and dipropyldisulfide ($m/z = 150$) are identified in both decomposition steps. Both compounds are released at temperatures where the endothermic peak occurs in the DTA trace.

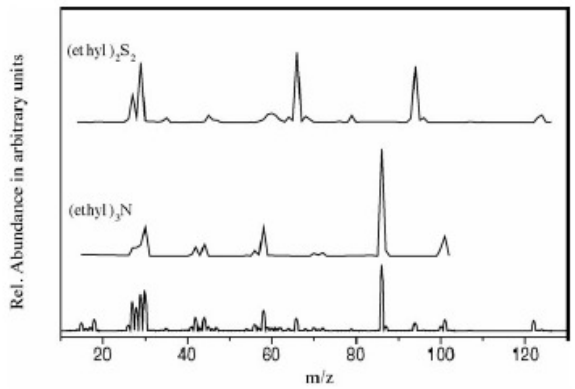

Fig. 4. Mass spectrum of $[(ethyl)_4N]_2[MoS_4]$ decomposition at 222 °C. *Note*: the top two traces were taken from http://webbook.nist.gov/chemistry.

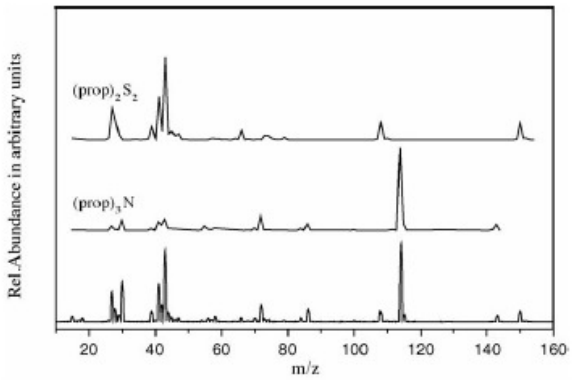

Fig. 6. Mass spectrum of $[(propyl)_4N]_2[MoS_4]$ decomposition at 175 °C. *Note*: the top two traces were taken from http://webbook.nist.gov/chemistry.

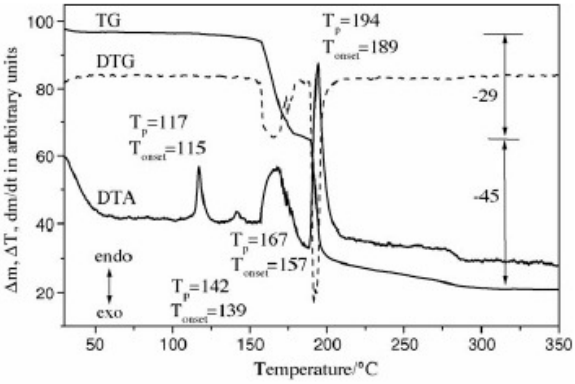

Fig. 7. DTA, TG and DTG plot of $[(butyl)_4N]_2[MoS_4]$ decomposition. Temperature in °C and weight loss in %.

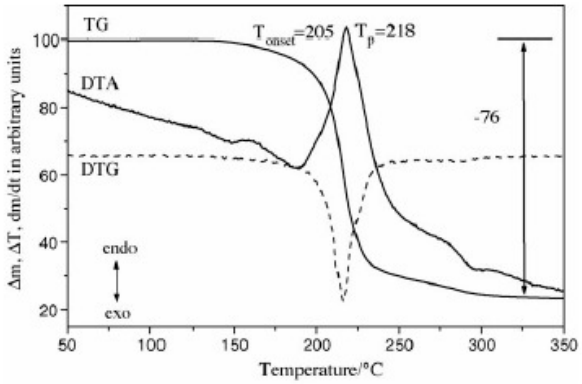

Fig. 9. DTA, TG and DTG plot of $[(pentyl)_4N]_2[MoS_4]$ decomposition. Temperature in °C and weight loss in %.

3.2.4. Tetrabutylammonium thiomolybdate $((CH_3(CH_2)_3)_4N)_2MoS_4$

The thermal decomposition reaction of tetrabutylammonium thiomolybdate is also complex (Fig. 7). First a phase transition (endothermic) occurs at $T_{onset} = 115\,°C$. The second ($T_{onset} = 139\,°C$) and third events ($T_{onset} = 157\,°C$) are accompanied by a weight loss of 29%. During the fourth endothermic peak at $T_{onset} = 189\,°C$ a mass change of 45% is observed. The total weight loss (74%) is again lower than the theoretical value for MoS_2 formation (77.2%), and the thermal decomposition reaction may be formulated as

$$((CH_3(CH_2)_3)_4N)_2MoS_4 \rightarrow 2(CH_3(CH_2)_3)_3N + (CH_3(CH_2)_3)_2S_2 + MoS_{2.03}C_{1.13}N_{0.04}H_{0.8} \quad (4)$$

The large amount of residual carbon in this sample indicates that the elimination of organic fractions from MoS_2 was not very efficient. The two decomposition steps starting at 160 and 190 °C took place at temperatures slightly lower than those in the tetrapropylammonium sample. Similar to the previous case the weight loss ended at 300 °C. Analysis of MS data (Fig. 8) suggests that tributylamine ($m/z = 185$) and dibutyldisulfide ($m/z = 178$) were released during both weight loss steps.

3.2.5. Tetrapentylammonium thiomolybdate $((CH_3(CH_2)_4)_4N)_2MoS_4$

In the DTA curve of the thermal decomposition of $((CH_3(CH_2)_4)_4N)_2MoS_4$ no events indicative for a phase transition are seen. A continuous decay with a broad and strong signal at $T_{onset} = 205\,°C$ occurs in the DTA curve. The TG trace (Fig. 9) shows that degradation of the sample starts at about 150 °C and is accompanied by a total mass loss of 76%, significantly lower than the calculated value (80.3%) for MoS_2 formation. The weight loss ended at 300 °C.

According to the mass spectrometry results (emission of tripentylamine ($m/z = 227$) and dipentyldisulfide ($m/z = 206$) (Fig. 10)) and the chemical analysis of the final product the thermal decomposition reaction of the material may be represented by the equation:

$$((CH_3(CH_2)_4)_4N)_2MoS_4 \rightarrow 2(CH_3(CH_2)_4)_3N + (CH_3(CH_2)_4)_2S_2 + MoS_{1.99}C_{1.18}N_{0.07}H_{1.14} \quad (5)$$

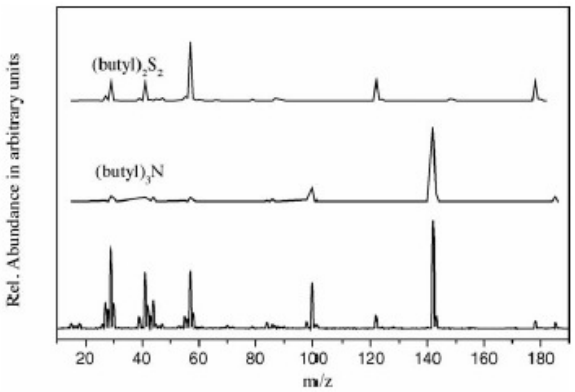

Fig. 8. Mass spectrum of $[(butyl)_4N]_2[MoS_4]$ decomposition at 196 °C. *Note*: the top two traces were taken from http://webbook.nist.gov/chemistry.

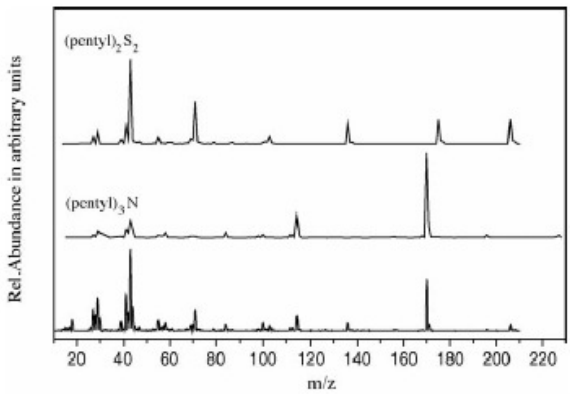

Fig. 10. Mass spectrum of $[(pentyl)_4N]_2[MoS_4]$ decomposition at 218 °C. *Note*: the top two traces were taken from http://webbook.nist.gov/chemistry.

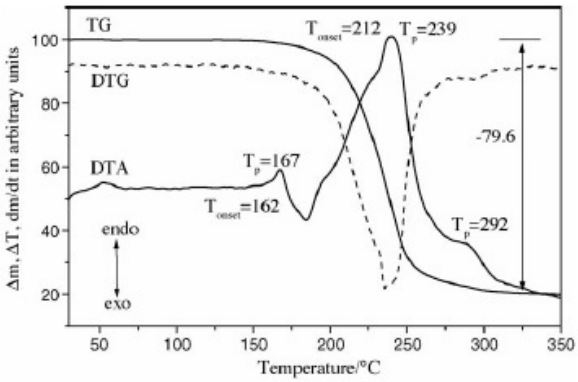

Fig. 11. DTA, TG and DTG plot of $[(hexyl)_4N]_2[MoS_4]$ decomposition. Temperature in °C and weight loss in %.

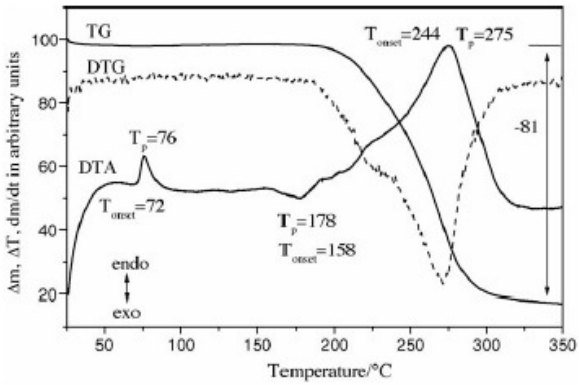

Fig. 13. DTA, TG and DTG plot of $[(heptyl)_4N]_2[MoS_4]$ decomposition. Temperature in °C and weight loss in %.

3.2.6. Tetrahexylammonium thiomolybdate $((CH_3(CH_2)_5)_4N)_2MoS_4$

This compound decomposed in a broad single step from about 180 to 330 °C. The DTA signal shows three peaks at $T_{onset} = 162$, 212 °C, and at $T_p = 292$ °C (Fig. 11). The origin of the first peak is not clear, but the signal may be due to melting of the material. In the DSC experiments (see below) a glass-like transition is seen and the product was more compact after a heat treatment up to 150 °C. Directly after the endothermic signal at $T_{onset} = 162$ °C an exothermic event occurs and the thermal degradation started immediately after this event. The rest of the broad and more or less featureless endothermic peaks correspond to the single weight loss of 79.6%. The difference to the theoretical value for MoS_2 formation of 82.6% is explained by the chemical analysis giving as composition $MoS_{1.5}C_{1.53}N_{0.09}H_{2.14}$. Obviously, during the thermal reaction a large fraction of S is emitted whereas C, H and N are retained in the sample. In the MS curves (Fig. 12) signals of trihexylamine ($m/z = 269$) and dihexyldisulfide ($m/z = 234.2$) are detected. According to these results the thermal decomposition reaction may be formulated as for the other precursors.

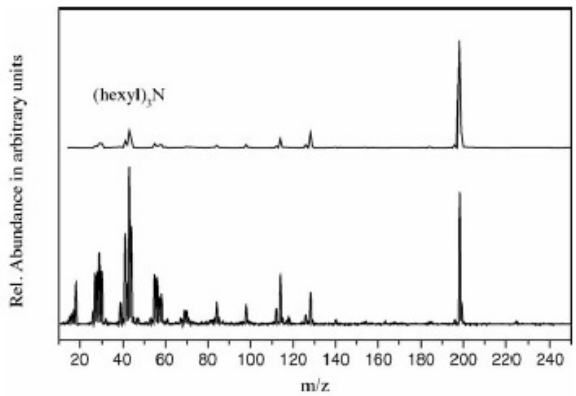

Fig. 12. Mass spectrum of $[(hexyl)_4N]_2[MoS_4]$ decomposition at 241 °C. *Note*: the top trace was taken from http://webbook.nist.gov/chemistry.

3.2.7. Tetraheptylammonium thiomolybdate $((CH_3(CH_2)_6)_4N)_2MoS_4$

The thermal decomposition reaction of tetraheptylammonium thiomolybdate is displayed in Fig. 13. The TG and DTG curves show that the decomposition covers a large temperature range from 180 to 350 °C. In the DTA trace one event occurs at $T_{onset} = 72$ °C that may be associated with a phase transition. This phenomenon will be further discussed below in the DSC and in situ X-ray scattering section. The small exothermic event at $T_{onset} = 158$ °C may be due to a rearrangement of the structure immediately before the decomposition starts; and the stronger endothermic peak at 244 °C is associated with the weight loss of 81%. The DTA signal is very broad indicating a complex fragmentation and reorganization of the constituents in the compound. The theoretical value for MoS_2 formation is 84.5%, and the difference is explained on the basis of chemical analysis of the final product yielding as composition $MoS_{1.3}C_{2.6}N_{0.13}H_{3.3}$. Like for $((CH_3(CH_2)_5)_4N)_2MoS_4$ a large amount of S is emitted during the thermal reaction. Mass spectrometry data (Fig. 14) can be interpreted as emission of triheptylamine ($m/z = 311$) and diheptyldisulfide ($m/z = 262$), which suggest that the thermal decomposition reaction can be formulated as for the previous precursors.

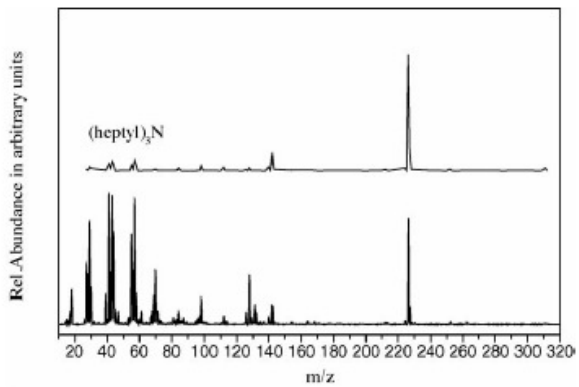

Fig. 14. Mass spectrum of $[(heptyl)_4N]_2[MoS_4]$ decomposition at 265 °C. *Note*: the top trace was taken from http://webbook.nist.gov/chemistry.

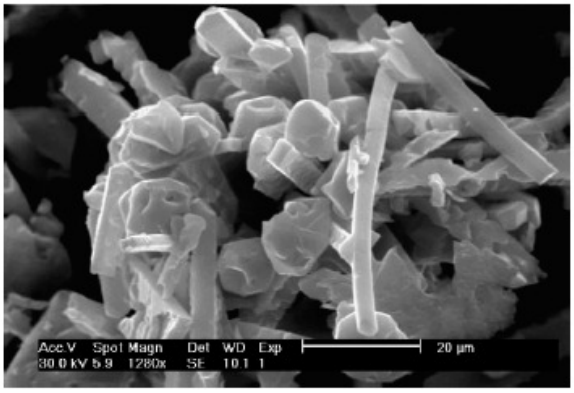

Fig. 15. SEM image of the thermal decomposition product from $[(methyl)_4N]_2[MoS_4]$.

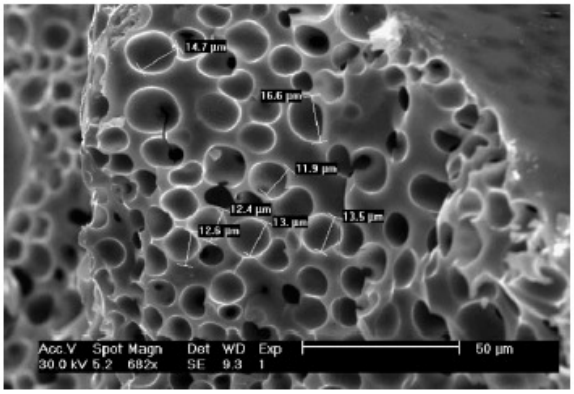

Fig. 17. SEM image of thermal decomposition product from $[(hexyl)_4N]_2[MoS_4]$.

3.3. Scanning electron microscopy

The morphology of the MoS_2 catalysts obtained by the thermal decomposition reactions of tetra-alkyl thiomolybdates was studied with SEM and images of selected materials are shown in Figs. 15–17. In general, formation of cavities (macropores) was observed for all samples and the morphology of the products changed gradually as a function of the alkyl precursor. The size of the cavities increases with the size of the alkyl group in the precursors. All samples exhibit a glassy appearance in SEM micrographs although they contained a high volume of micropores, as it was previously shown by nitrogen adsorption [8]. Such appearance is attributed to the presence of carbon in MoS_2, which is very good for transmission of electrons producing very high contrast images. The SEM micrograph of the tetramethylammonium precursor (Fig. 15) shows long faceted particles, similar to those observed for MoS_2 derived from ATM. Hence, the decomposition process of C1ATM is suggested to be topotactic (same morphology of precursor is maintained) as the process reported for ATM decomposition [39].

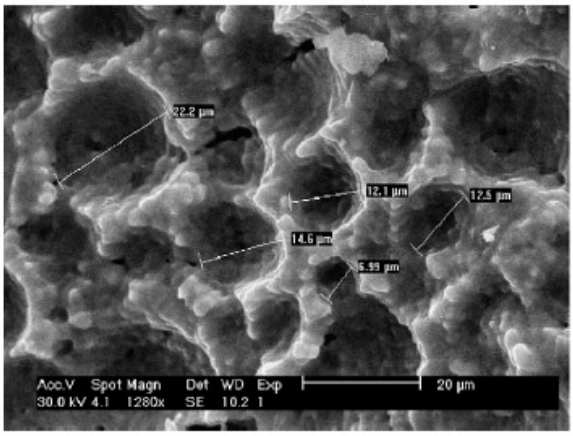

Fig. 16. SEM image of the thermal decomposition product from $[(propyl)_4N]_2[MoS_4]$.

In the SEM micrograph of the tetraethylammonium sample small cavities (about 2 and 6 µm) and large tunnels in the bulk of MoS_2 are seen. The process leading to the formation of cavities was suggested to be associated with the elimination of alkyl groups from the precursor [8]. In the SEM micrograph of tetrapropylammonium precursor (Fig. 16) an increased amount of cavities with a spherical form is observed. The size of these voids is in the range from about 6 up to 22 µm. The MoS_2 material surrounding the holes looks as agglomerated particles. In the SEM micrograph of the tetrabutylammonium thiomolybdate precursor a high density of cavities with a wide range of diameters (2–50 µm) are seen forming a spongy material. Small holes formed inside large cavities indicate that connectivity was developed in this MoS_2 catalyst. Using higher magnifications it is obvious that spherical bubbles have been formed during the decomposition process being responsible for this spongy morphology. The SEM pictures of the tetrapentylammonium and the tetrahexylammonium precursor (Fig. 20) show that the density of cavities is much larger compared to other precursors. In addition, the size distribution looks more homogeneous for these samples than for the others, particularly for the hexyl material. The SEM pictures of the tetraheptylammonium precursor reveal that it contains the largest cavities of all samples indicating that the size of alkyl group is responsible for cavity formation.

The (R_4N) compounds are well known for their applications as template molecules during the synthesis of zeolites and mesoporous materials [40]. The templates stabilise voids inside the solid structure of the precursor and these voids are proportional to the size of the alkyl group in the molecule. The MoS_2 materials generated from the tetra-alkylthiomolybdate precursors have been considered as amorphous mesoporous materials [41] or amorphous zeolites [42].

3.4. DSC experiments and X-ray powder diffraction

As pointed out above several compounds exhibit thermal events at relatively low temperatures that were not accompanied by weight changes. For a better understanding of the thermal properties DSC measurements were performed (Fig. 18) and

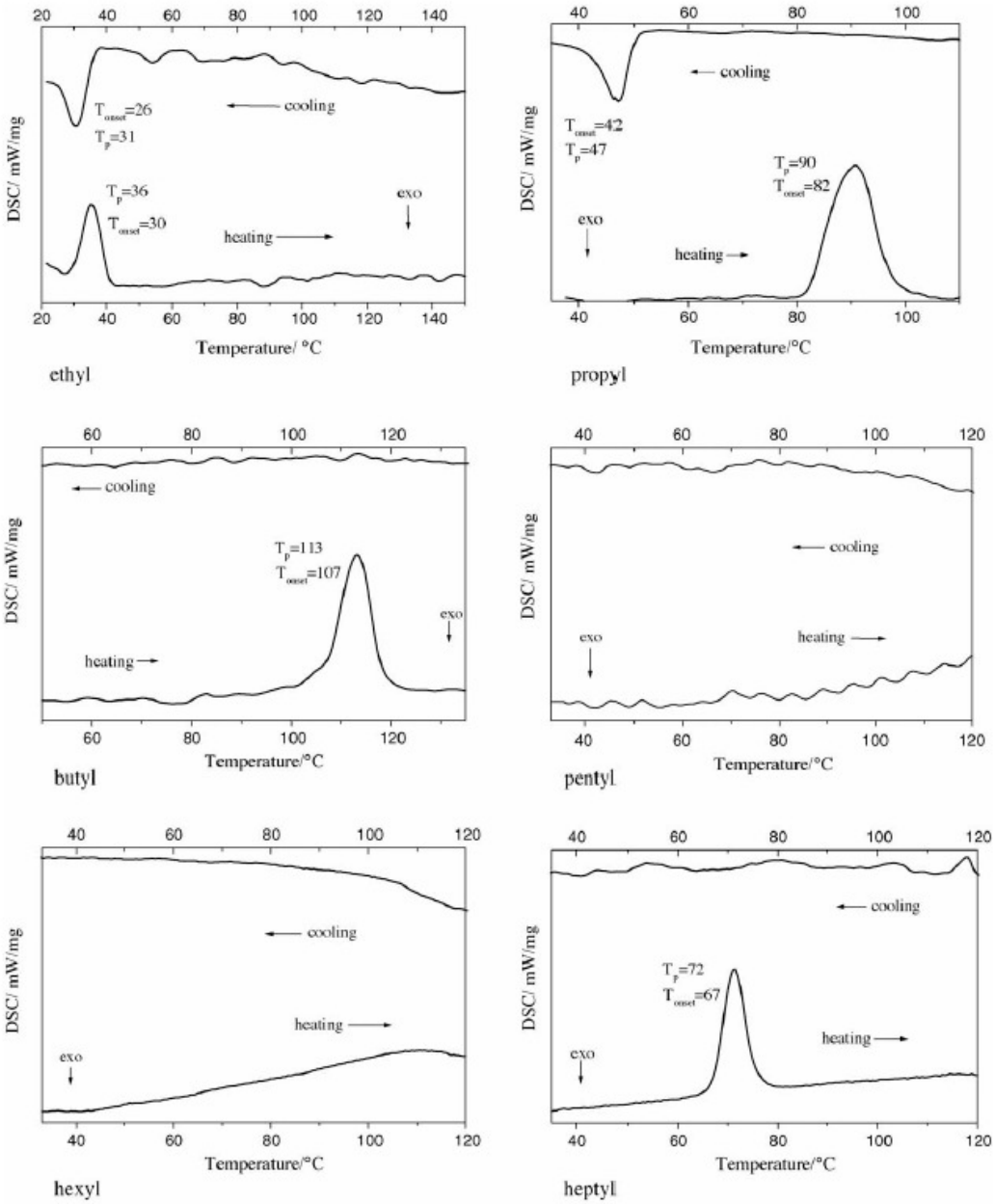

Fig. 18. DSC curves for the tetra-alkylammonium tetrathiomolybdate compounds.

the products were characterised with X-ray powder diffractometry (XPD). For several compounds in situ X-ray diffraction experiments were also performed.

For R = ethyl, events occur at very low temperatures, an endothermic event at $T_{onset} = 30\,°C$ in the heating curve and an exothermic peak at $T_{onset} = 26\,°C$ in the cooling curve. The XPD pattern taken after cycling through these thermal events reveals that the reflections are at the same positions as for the genuine material, but the profiles indicate a poorer crystallinity. The in situ X-ray experiment clearly show the occurrence of a new phase (Fig. 19) indicating that the phase transition was at least partially reversible. The signal in the DSC curve is intense suggesting that the transition may be first order however the exact order cannot be determined with this experiment.

The DSC trace of R = propyl displays an intense endothermic signal at $T_{onset} = 82\,°C$ in the heating curve and an exothermic peak at $T_{onset} = 42\,°C$ during the cooling ramp. The powder pattern after the heat treatment is different compared to the starting material indicating a structural phase transition. The in situ X-ray experiments (Fig. 20) clearly demonstrate that the

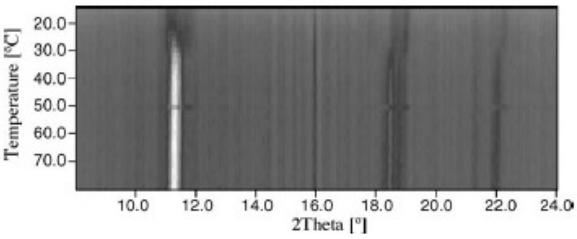

Fig. 19. Powder pattern of the in situ X-ray diffraction experiments for $((CH_3CH_2)_4N)_2MoS_4$.

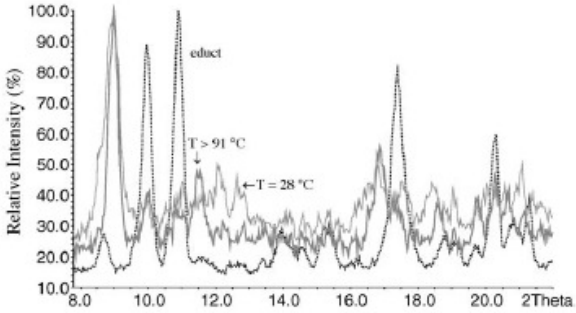

Fig. 20. Selected X-ray powder patterns of the in situ experiments performed for the tetrapropyl compound. Traces are: starting material, data collected at $T > 91$ °C and after cooling to 28 °C.

starting material is first converted to a phase II, which in turn is transformed into a phase III during the cooling process. The reflections of phase II appear again heating phase III above 100 °C. A process of five cycles was performed with DSC, and in the heating cycles an endothermic event occurs always at about 90 °C and an exothermic peak was seen at about 40 °C in the cooling ramp. The structures of the three phases are closely related as evidenced by the similar X-ray powder patterns.

The R = butyl compound shows only one event during the heating cycle ($T_{onset} = 107$ °C), but no signal occurs during the cooling cycle. The X-ray powder pattern (Fig. 21) show strong reflections at positions different from that of the pristine material indicating that a new compound was formed with no reversibility to the original phase. The DSC curves of the tetrapentyl and tetrahexyl compounds display no pronounced signals up to

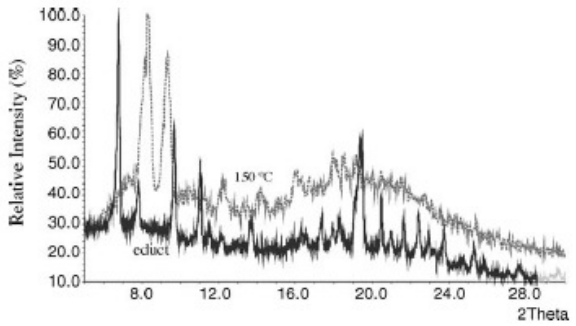

Fig. 21. Powder patterns of tetrabutylammonium tetrathiomolybdate before and after the DSC experiment. *Note*: the sample was heated to 150 °C.

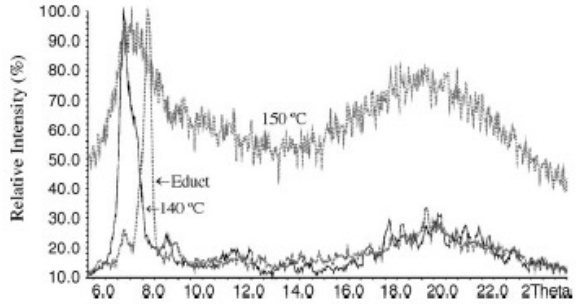

Fig. 22. Powder patterns for tetrapentyl tetrathiomolybdate. The displayed patterns are the starting material, after heating to 140 °C and after a treatment at 150 °C.

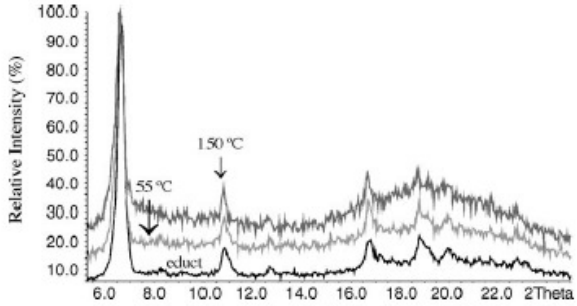

Fig. 23. Experiments of X-ray diffraction for tetrahexyl tetrathiomolybdate. Patterns were recorded from the starting material, after heating to 55 °C and after a treatment at 150 °C.

150 °C, but the traces are typical for glass-like transitions. When the experiment with R = pentyl was stopped at 140 °C the resulting material look like a melt and in the resulting powder pattern (Fig. 22) a strong and broad reflection is located at a different position compared with the starting material. When the compound is heated up to 150 °C the powder pattern of the product show only broad modulations of the background suggesting that the sample was destroyed. For the tetrahexyl sample no signal up to 150 °C is detected in the DSC curve and only a drift of the base line occurs. In the powder patterns (Fig. 23) taken after heating the material to 55 and 150 °C no differences are seen compared with the pristine material suggesting that the compound is stable up to 150 °C, being quite remarkable for this type of materials.

A different behavior is observed for R = heptyl. In the DSC curve an intense signal is seen at $T_{onset} = 67$ °C in the heating curve, but no peak occurs in the cooling curve. The powder pattern of a sample heated to 80 °C (Fig. 24) shows only minor differences compared with the original sample. When the temperature is increased to 150 °C the sample decomposes and the powder diagram indicates the presence of a new compound. In situ X-ray diffraction experiments demonstrate that the sample melts at above 70 °C.

4. Discussion

The decomposition of tetra-alkyl thiomolybdates (methyl up to heptyl) shows different steps of weight loss involving differ-

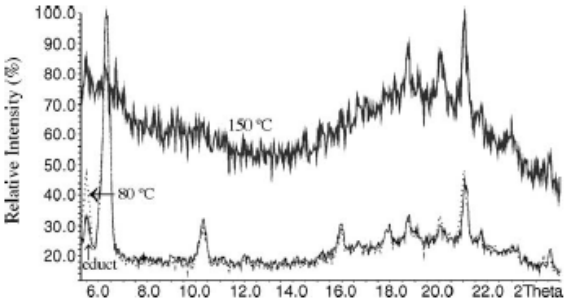

Fig. 24. Results of X-ray diffraction experiments for tetraheptyl tetrathiomolybdate. Patterns were recorded from the starting material, after heating to 80 °C and after a treatment at 150 °C.

ent energy processes as phase transitions, bond breaking and product elimination. Nevertheless, all precursors emit the same type of products during the thermal reaction, trialkylamines and dialkyldisulfides, indicating that besides the increasing complexity of the structure and composition of the precursors the reaction steps may be similar. The transformation of the tetralkylammonium cation R_4N^+ into two trialkylamine molecules and two alkyl radicals which react with two sulfur atoms of the MoS_4^{2-} anion seems to be the best scheme for the decomposition process. As shown above, the reaction process for all precursors can be represented with the general formula:

$$(R_4N)_2MoS_4 \rightarrow 2R_3N + R_2S_2 + MoS_2C_xN_yH_z$$

One possible explanation for the decomposition reaction may base on a concerted S_{N2} mechanism where the nucleophilic attack from one sulfur atom of the thiomolybdate anion to the α-carbon atom of R_4N^+ ions gives the trialkylamines as a product and also the dialkyldisulfides. With this mechanism there is only one transition state, i.e. a pentavalent C atom, usual in S_{N2} mechanisms.

For the two precursors with the largest tetraalkyl groups the sulfur content in the decomposition product is low indicating that the thermal reaction is more complex.

The composition of MoS_2 formed from the alkylthiomolybdates is a function of the precursor, the residual quantities of hydrogen and carbon in the final solid increase with the size of the alkyl group in the starting material, and for R = hexyl and heptyl the contamination with C and H is larger than the sulfur content. The materials formed from educts with R = methyl to pentyl contain sulfur in a Mo:S ratio of 1:2, i.e. they are stoichiometric. However, for the hexyl and heptyl groups the final materials contain less than the stoichiometric sulfur suggesting that carbon and hydrogen may be incorporated into the solid.

The low temperature thermal events were studied with DSC experiments in combination with in situ X-ray diffraction and the results highlight the complex thermal behavior of the materials. The sample with R = ethyl shows a partially reversible phase transition at a very low temperature of about 30 °C as evidenced by in situ XPD experiments. For R = propyl three different structural phases are identified with the in situ XPD investigations. The original material is first transformed to a phase II at about 90 °C. Obviously, such a low temperature indicates that only very small structural rearrangements can occur. Cooling the material down to room temperature an exothermic signal at T_{onset} = 42 °C indicates another structural rearrangement. The X-ray powder patterns recorded under in situ conditions clearly show the formation of a phase III, and all three structures must be very similar due to the similar X-ray powder patterns. The butyl compound irreversibly transforms at about 113 °C into a new phase. The DSC traces for R = pentyl and hexyl suggest a glass-like phase transformation with no pronounced signal in the curves up to 150 °C. The X-ray powder patterns give evidences that the sample with R = pentyl is transformed into a new compound at $T < 150$ °C, and at $T = 150$ °C it is destroyed yielding a featureless powder diagram. Interestingly, the tetrahexyl containing material could be heated up to 150 °C without any significant changes of the X-ray powder patterns. It is quite remarkable that this is the most stable precursor of the whole series of tetra-alkylammonium thiomolybdates. Surprisingly, the DSC curve for the tetraheptyl compound shows an intense endothermic event at T_{onset} = 67 °C but no signal occurs in the cooling cycle. The X-ray powder pattern is very similar to that of the genuine material. Heating the material to 150 °C leads to a decomposition of the sample and X-ray scattering experiments indicate the formation of a new compound.

5. Summary

The decomposition pattern of tetra-alkylammonium thiomolybdates presents several common features as:

- Phase transitions prior to decomposition, either reversible or irreversible, depending on the tetra-alkylammonium thiomolybdate precursor.
- Endothermic peaks during decomposition attributable to structural rearrangements and elimination reactions.
- Formation of trialkylamine and dialkyldisulfide products following a very similar mechanism.
- Increase of carbon and nitrogen contamination in MoS_2 residuals after decomposition with increasing size of R_4N. Decrease of S content below the stoichiometric value for the hexyl and heptyl precursors.
- Formation of cavities in MoS_2 materials obtained by thermal decomposition of tetra-alkyl thiometallates. The size of cavities increases with the size of the alkyl group in the precursor.

The thermal stability and decomposition of all compounds is complex with no simple relation between the number of events, its temperature and its composition. The materials with R = methyl and ethyl decompose in one sharp step, meanwhile a two-step decomposition occur for R = propyl and butyl. For R = pentyl, hexyl and heptyl the strong endothermic signal associated with the decomposition process become gradually broader with increasing size of the tetraalkyl chain covering a large temperature range. The temperature for phase transitions increase with increasing number of C atoms for R = ethyl, propyl and butyl. The remaining three materials show a different behavior with a glass-like transition for R = pentyl and hexyl.

Acknowledgments

The authors thank C. Teske for fruitful discussions and appreciate the technical attendance of C. Ornelas from CIMAV, and the financial support from DGAPA, project No. IN1 19602-3. The financial support by the Deutsche Forschungsgemeinschaft DFG (project: BE 1653/11-2) is also gratefully acknowledged.

References

[1] A. Müller, Transition Metal Chemistry—Current Problems of General, Biological and Catalytical Relevances, Verlag Chemie, Weinheim, 1981.
[2] K.S. Liang, J. Bernholc, W.H. Pan, G.J. Hughes, E.I. Stiefel, Inorg. Chem. 26 (1987) 1422.
[3] A.W. Naumann, A.S. Behan, US Patent 4,243,554 (1981).
[4] T.A. Pecoraro, R.R. Chianelli, US Patent 4,528,089 (1985).
[5] R.R. Chianelli, J. Jacobson, US Patent 4,650,563 (1987).
[6] G. Alonso, M. Del Valle, J. Cruz, V. Petranovskii, A. Licea-Claverie, S. Fuentes, Catal. Today 43 (1998) 117.
[7] G. Alonso, V. Petranovskii, M. Del Valle, J. Cruz-Reyes, A. Licea-Claverie, S. Fuentes, Appl. Catal. A: Gen. 197 (2000) 87.
[8] G. Alonso, G. Berhault, A. Aguilar, V. Collins, C. Ornelas, S. Fuentes, R.R. Chianelli, J. Catal. 208 (2002) 359.
[9] G. Alonso, M.H. Siadati, G. Berhault, A. Aguilar, S. Fuentes, R.R. Chianelli, Appl. Catal. A: Gen. 263 (2004) 109.
[10] G. An, Y. Chai, H. Zhong, C. Zhang, C. Liu, Prepr. Am. Chem. Soc.: Div. Pet. Chem. 50 (3) (2005) 344.
[11] H. Farag, K. Sakanishi, M. Kouzu, A. Matsumura, Y. Sugimoto, I. Saito, Prepr. Am. Chem. Soc., Div. Fuel Chem. 48 (2) (2003) 504.
[12] B.R. Srinivasan, S.N. Dhuri, M. Poisot, C. Näther, W. Bensch, Z. Naturforsch. B 59 (2004) 1083.
[13] B.R. Srinivasan, S.N. Dhuri, M. Poisot, C. Näther, W. Bensch, Z. Anorg. Allg. Chem. 631 (2005) 1087.
[14] D. Liu, Y. Li, R. Zhao, C. Liu, Prepr. Am. Chem. Soc., Div. Pet. Chem. 50 (1) (2005) 128.
[15] I. Bezverkhy, P. Afanasiev, M. Lacroix, Inorg. Chem. 39 (2000) 5416.
[16] A. Leist, S. Stauf, S. Löken, E.W. Finckh, S. Lüdtke, K.K. Unger, W. Assenmacher, W. Mader, W. Tremel, J. Mater. Chem. 8 (1998) 241.
[17] J.H. Zhan, Z.D. Zhang, X.F. Qian, C. Wang, Y. Xie, Y.T. Qian, J. Solid State Chem. 141 (1998) 270.
[18] Ch. Calais, N. Matsubayashi, Ch. Geantet, Y. Yoshimura, H. Shimada, A. Nishijima, J. Catal. 174 (1998) 130.
[19] X. Che, R. Fan, Chem. Mater. 13 (2001) 802.
[20] H. Liao, Y. Wang, S. Zhang, Y. Qian, Chem. Mater. 13 (2001) 6.
[21] M.M. Mdleleni, T. Hyeon, K.S. Suslick, J. Am. Chem. Soc. 120 (1998) 6189.
[22] R.R. Chianelli, Catal. Rev. Sci. Eng. 26 (1984) 361.
[23] A. Müller, A. Diemann, H.H. Heinsen, Chem. Ber. 104 (1971) 975.
[24] A. Müller, W. Hellmann, J. Schneider, U. Schimanski, U. Demmer, A. Trautwein, U. Bender, Inorg. Chim. Acta 65 (1982) L41.
[25] W. Eltzner, M. Breysse, M. Lacroix, M. Vrinat, Polyhedron 5 (1985) 203.
[26] F. Pedraza, S. Fuentes, Catal. Lett. 65 (2000) 107.
[27] T.P. Prasad, E. Diemann, A. Müller, J. Inorg. Nucl. Chem. 35 (1973) 1895.
[28] J. Brito, M. Ilija, P. Hernandez, Thermochim. Acta 256 (1995) 325.
[29] R.I. Walton, A.J. Dent, S.J. Hibble, Chem. Mater. 10 (1998) 3737.
[30] H.W. Wang, P. Skeldon, G.E. Thompson, G.C. Wood, J. Mater. Sci. 32 (1997) 497.
[31] R.I. Walton, S.J. Hibble, J. Mater. Chem. 9 (1999) 1347.
[32] G. Alonso, M. del Valle, J. Cruz, V. Petranovskii, A. Licea-Claverie, S. Fuentes, Catal. Today 43 (1998) 117.
[33] J.W. McDonald, G. Delbert Friesen, L.D. Rosenhein, W.E. Newton, Inorg. Chim. Acta 72 (1983) 205.
[34] G. Alonso, G. Aguirre, I.A. Rivero, S. Fuentes, Inorg. Chim. Acta 274 (1998) 108.
[35] O. Weisser, S. Landa, Sulfide Catalysts: Their Properties and Applications, Pergamon Press, Oxford, 1973.
[36] E. Rode, B. Lebedev, Zh. Neorg. Khim. 6 (1961) 1189.
[37] E. Diemman, A. Müller, Coord. Chem. Rev. 10 (1973) 79.
[38] G. Alonso, M. Del Valle, J. Cruz, A. Licea-Claverie, V. Petranovskii, S. Fuentes, Catal. Lett. 52 (1998) 55.
[39] E. Frommel, J. Diehl, J. Tamiglia, S. Pollack, Proceedings of the 12th North American Meeting of the Catalysis Society, Lexington, KY, 1991, p. PD-38.
[40] K. Holmberg, J. Colloid. Interf. Sci. 274 (2004) 355.
[41] G. Alonso, G. Berhault, F. Paraguay, E. Rivera, S. Fuentes, R.R. Chianelli, Mater. Res. Bull. 38 (2003) 1045.
[42] G. Alonso, M.H. Siadati, R.R. Chianelli, US patent 20050032636 (2005).

3.2.2

Available online at www.sciencedirect.com
ScienceDirect
Thermochimica Acta 453 (2007) 42–51
thermochimica acta
www.elsevier.com/locate/tca

Decomposition of tetraalkylammonium thiotungstates characterized by thermoanalysis, mass spectrometry, X-ray diffractometry and scanning electron microscopy

M. Poisot, W. Bensch *

Institut für Anorganische Chemie, University of Kiel, Olshausenstr. 40-60, 24118 Kiel, Germany

Received 9 August 2006; received in revised form 9 November 2006; accepted 9 November 2006
Available online 17 November 2006

Abstract

Thermal decomposition reactions of tetraalkylammonium thiotungstates, $(R_4N)_2WS_4$ (R = methyl to heptyl), were investigated with DSC and DTA–TG coupled with mass spectroscopy (MS). The results demonstrate that the complexity of thermal decomposition reactions is significantly influenced by the alkyl group, i.e., more complex steps are observed for the materials with longer alkyl chain lengths. Tetraethyl and tetrapropyl complexes show reversible and irreversible phase transitions detected by DSC experiments combined with thermodiffractometry. The tetrapentyl compound undergoes an irreversible phase transition while the tetraheptyl sample exhibits a glass-like transition and melting prior to decomposition. The whole series of compounds decompose without forming sulfur rich WS_n ($n = 3$ or 4) intermediates. The final WS_2 products are nearly stoichiometric for R = methyl to pentyl but for hexyl and heptyl samples the sulfur content is significantly reduced with a W/S ratio of about 1.5. The residual carbon and hydrogen contents increase in the final decomposition products in the same order as the number of C atoms in R_4N increase. For the N content no clear trend is obvious. A general thermal decomposition mechanism is suggested which follows a bimolecular nucleophilic substitution reaction. In the SEM images only for R = heptyl the formation of macro-pores with a sponge-like morphology is seen, but for the other precursors compact materials are formed which in part display a well developed morphology. X-ray diffraction analysis of the final products shows the formation of amorphous WS_2 up to the tetrapentyl precursor. But for the tetrahexyl and tetraheptyl materials the W:S ratio is significantly smaller than 1:2 and large amounts of C and H are determined by chemical analyses. In accordance with previously reported results it can be assumed that a carbosulfide phase is formed by a mixed C–W–S sandwich layered structure.

Keywords: Tetraalkylammonium thiotungstates; WS_2 preparation; Thermal decomposition; Thermoanalysis; Thermodiffractometry

1. Introduction

The increasing restrictions of environmental regulations on sulfur, nitrogen and aromatic contents of vehicle transportation fuels and by the decreasing availability of high quality crude oil deliver a lot of reports about high efficient hydrotreating catalysts. Transition metal sulfides, mainly molybdenum and tungsten disulfide, promoted with cobalt or nickel, are widely used to remove heteroelements [1–3]. Alumina is commercially used as a support because of its high surface area and its strong interaction with MoS_2, which allows good dispersion and stabilization of the active phase [1]. The current research focuses on the support material for the active sulfides. Activated carbon, TiO_2, ZrO_2, zeolites, MgO and various mixed oxides have been studied as potential alternatives for the conventional support [4–7]. Unsupported molybdenum and tungsten sulfide catalysts with high surface areas have been synthesized using thiosalts as precursors [8–12]. Cobalt promoted unsupported catalysts prepared from the decomposition of thiosalts show higher activities than the catalysts obtained by common preparation methods [13]. Some alumina supported tungsten catalysts promoted with nickel were obtained from oxy and thiosalts using fluorine as additive [14–17]. The decomposition of tetraalkylammonium thiometallates has been used to prepare WS_2 catalysts for hydrodesulfurization and the reactions were followed by DTA and TG methods [18]; however a clear mechanism of the processes has not yet been established. During the last few years the number of structurally characterized thiotungstates increased

* Corresponding author. Tel.: +49 431 880 2091.
E-mail address: wbensch@ac.uni-kiel.de (W. Bensch).

0040-6031/$ – see front matter © 2006 Elsevier B.V. All rights reserved.
doi:10.1016/j.tca.2006.11.006

steadily delivering a wide variety of compounds with the following cations: diammonium [19], ethylenediammonium [20], *N*-methylethylenediammonium, monoisopropylammonium, *N*, *N*-dimethyl-1,3-propane-diammonium, 1,4-butanediammonium [21], 1,3-propanediammonium, and *N,N,N′,N′*-tetramethylethylenediammonium [22], piperazine, tris(2-aminoethyl)amine [23], 1,4-dimethylpiperazinium [24]. The main objective of the investigations of these samples was to characterize the crystal arrangement and the influence of N–H···S interactions onto the geometry and bonding properties in the WS_4 moiety.

In a previous contribution the thermal decomposition pathways of tetraalkylammonium tetrathiomolybdates were reported [25]. In our ongoing work we investigated the analogous tetraalkylammonium tetrathiotungstates, $(R_4N)_2WS_4$ (R changes from methyl to heptyl) and the results of the experiments are presented here.

2. Experimental details

2.1. Preparation of $(R_4N)_2WS_4$ starting materials

The synthesis of the tetralkylammonium salts $(R_4N)_2WS_4$ has been reported by McDonald et al. [26] and by Alonso et al. [27]. The last method was used here in a modified version.

2.2. Synthesis of tetramethyl, tetraethyl and tetrapropylammonium thiotungstates

Fresh prepared $(NH_4)_2WS_4$ (1.4 mmol) was dissolved in water (30 mL) with stirring. 2.8 mmol of $(R)_4NBr$ (R = C1 = tetramethyl, C2 = tetraethyl, and C3 = tetrapropyl) was dissolved in NaOH (2.8 mmol) and 10 mL water with stirring. Both solutions were mixed and stirred for 30 min, then kept undisturbed over ice. Yellow crystals precipitated overnight with 80% yield. Cold water and ethanol were used for washing. These compounds are air stable for a long time.

2.3. Synthesis of tetrabutyl, tetrapentyl, tetrahexyl, and tetraheptylammonium thiotungstates

An aqueous solution of fresh $(NH_4)_2WS_4$ (0.7 mmol, 10 mL) was added to an aqueous solution of $(R)_4NBr$ (for R = C4 = tetrabutyl, C5 = tetrapentyl) (1.4 mmol, 20 mL), then stirred for 30 min. For R = C6 = tetrahexyl and C7 = tetraheptyl the solution was obtained in 10 mL water and 10 mL ethanol. Yellow powders precipitated with 80% yield and were stored under static vacuum over P_2O_5.

2.4. Methods and materials

DTA–TG and measurements coupled with mass spectrometry (MS) were performed using a NETZSCH STA-409CD device with Skimmer coupling, equipped with a BALZERS quadrupole mass spectrometer QMA 400 (max. 512 amu). For DTA–TG experiments alumina crucibles were used under a dynamic nitrogen atmosphere (flow rate: 75 mL/min, purity 5.0). In some cases the first derivative of the TG curve was used to confirm a thermal event. The TG curve of an empty crucible was measured under the same experimental conditions and the effects of gas flow and buoyancy were corrected automatically with the evaluation software. DTA–TG–MS measurements were performed under a dynamic helium atmosphere (flow rate: 50 mL/min, purity 5.6) in the analog scan mode. Heating rate of 4 K/min was applied in DTA–TG and MS coupled experiments up to 350 °C. The National Institute of Standards and Technology (NIST) (http://webbook.nist.gov/chemistry) data were used for comparison with the spectra obtained. Note that only one example is presented in the manuscript but all spectra are available as supplementary materials. DSC experiments were performed with a NETZSCH DSC 204 Phoenix device using aluminium crucibles pressed with an aluminium lid and also in sealed glass ampoules filled with argon. Protective atmosphere of nitrogen (30 mL/min) was applied. X-ray powder diffraction (XRPD) and in situ thermodiffractometry was performed on a STOE STADI-P instrument equipped with a graphite-high-temperature oven. The collected data were processed with the STOE WIN "X^{POW}" software. Chemical elemental analyses were performed on a HERAEUS CHN-O RAPID combustion analyzer, using zinc sample holders with 2–3 mg pro sample, heated up to 1000 °C under oxygen atmosphere. Scanning electron microscopy (SEM) and energy dispersive X-ray analysis (EDX) were performed with a Philips ESEM XL 30 scanning electron microscope.

3. Results

3.1. Elemental analysis

The data of the chemical analyses agree well with the chemical composition of the starting materials. These data are summarized together with the composition of the final decomposition products in Table 1. The carbon content increases gradually with the size of the alkyl group (2.02 wt% for C1 up to 11 wt% for C6). The hydrogen and nitrogen contents also increase from C1 to C7 alkyl precursors (0–1.1 wt% for H, 0.46 to 0.73 wt% for N). It is remarkable that the C/H ratio in the decomposition products for C1 to C5 educts remains more or less identical suggesting that these elements may exist combined as CH groups which remain trapped between the WS_2 layers or adsorbed on its surface. The W/S ratio is about 2 for C1–C5 in contrast to the C6 and C7 derived materials containing significantly less sulfur. However, in the last two materials the carbon and hydrogen content is very large and the nature of the incorporated C and H is not fully understood. But according to results presented in the literature one can assume that C partially substitutes S in WS_2 (see also below). In general, the size of the tetraalkylammonium cation influences the composition of the final decomposition product.

3.2. DTA–TG–DTG–MS characterization

3.2.1. Tetramethylammonium and tetraethylammonium thiotungstate $((CH_3)_4N)_2WS_4$ and $((CH_3CH_2)_4N)_2WS_4$

The thermal decomposition of $((CH_3)_4N)_2WS_4$ and $((CH_3CH_2)_4N)_2WS_4$ (Fig. 1) occurs in one step with 43.2%

Table 1
Data of chemical analysis, weight loss and thermal events for $(R_4N)_2WS_4$

R	Weight (%)	C (%)	H (%)	N (%)	S (%)	Composition	T_p (°C); T_e (°C)
Methyl		20.73	5.10	5.80	27.84		
	−43.2	20.87	5.21	6.08	27.86	$WS_{2.09}C_{0.43}N_{0.08}$	285; 265
		2.02	0.0	0.46	26.05		
Ethyl		32.96	6.93	4.89	22.10		
		33.57	6.98	4.89	22.4		
	−52	4.63	0.27	0.41	23.56	$WS_{1.9}C_{0.99}N_{0.07}H_{0.69}$	61, 245; 235
Propyl		42.08	8.25	4.04	18.86		
	−60.4	42.13	8.18	4.09	18.74	$WS_{2.01}C_{1.24}N_{0.11}H_{1.16}$	101, 178, 282; 170, 273
		5.64	0.44	0.59	24.25		
Butyl		42.88	8.14	3.11	14.13		
		48.25	9.04	3.51	16.10		
	−65.2	5.77	0.43	0.39	24.0	$WS_2C_{1.28}N_{0.07}H_{1.14}$	165, 205, 264, 326; 159, 256, 309
Pentyl		51.01	9.30	2.93	13.01		
	−69.3	52.85	9.68	3.08	14.10	$WS_{2.08}C_{1.22}N_{0.04}H_{1.13}$	117, 173.5, 227, 236, 258, 300; 168
		5.51	0.42	0.24	25.0		
Hexyl		55.83	10.23	2.69	10.5		
		56.48	10.19	2.74	12.56		
	−73.2	9.1	0.96	0.47	17.93	$WS_{1.43}C_{1.94}N_{0.08}H_{2.48}$	169, 253; 160, 247
Heptyl		59.2	11.03	2.53	10.86		
	−73.8	58.55	11.83	2.43	11.16	$WS_{1.61}C_{2.49}N_{0.14}H_{2.97}$	156, 250, 288; 146, 264
		11	1.1	0.73	19		

Chemical composition: first line, experimental values; second line, calculated values, third line, after decomposition.

mass loss for the first and 52% for the second compound. The experimental weight changes are less than expected for the formation of WS_2 (theo: 46% for C1 and 56.6% for C2). The differences between the values can be explained on the basis of chemical analysis (Table 1). The thermal degradations are accompanied by strong endothermic peaks ($T_p = 285$ °C, $T_e = 265$ °C for C1 and $T_p = 245$ °C, $T_e = 235$ °C for C2). Interestingly, the onset of thermal decomposition of $((CH_3)_4N)_2WS_4$ occurs at a significantly higher temperature (240 °C) than that of the second compound (150 °C). A thermal event at 61 °C observed for $((CH_3CH_2)_4N)_2WS_4$ was studied with DSC and

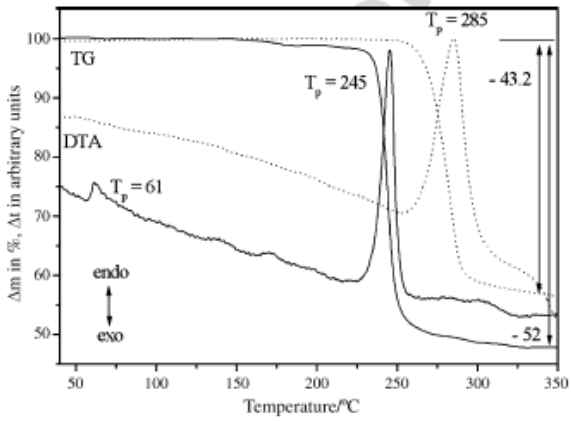

Fig. 1. DTA, TG plot of $[(methyl)_4N]_2[WS_4]$ = dash line and $[(ethyl)_4N]_2[WS_4]$ = solid line. Temperature in °C, mass loss in %.

XRD and the results are discussed below. $((CH_3)_4N)_2WS_4$ decomposes at slightly higher temperature than $(NH_4)_2WS_4$ ($T_p = 252$ °C [28]). In contrast to the ammonium compound no WS_3 is formed as an intermediate during the decomposition of C1 [29,30]. We note that for organic ammonium thiotungstates like $(pipH_2)WS_4$ and $(trenH_2)WS_4$ also a one step decomposition was reported [23]. According to the chemical analysis the C content in the decomposition product of C2 is larger than for C1.

In the mass spectrum recorded at 290 °C during decomposition of $((CH_3)_4N)_2WS_4$ the most intense signals are from the intact ions of tri-methylamine ($m/z = 59$) and dimethyldisulfide ($m/z = 94$). In the MS spectrum of C2 recorded at 244 °C again the intact ions of tri-ethylamine ($m/z = 101$) and diethyldisulfide ($m/z = 122.1$) molecules yield the most intense peaks. In both MS spectra the fragmentation patterns of the molecules matches well with the patterns seen in the NIST database for these molecules.

3.3. Tetrapropylammonium thiotungstate, $((CH_3(CH_2)_2)_4N)_2WS_4$

The DTA–TG curves show two decomposition steps and three endothermic events (Fig. 2). The first peak ($T_p = 101$ °C) represents a phase transition (see below). Thermal decomposition starts at 147 °C showing a strongest endothermic peak at 176 °C ($T_e = 178$ °C) and a second at 282 °C ($T_e = 273$ °C). The total mass loss (41.3% and 19.1% for the two steps) is less than expected for the formation of WS_2. Compared to the C1 and C2 compounds the residual C content is larger (Table 1). The results of the MS experiments clearly show the emission of

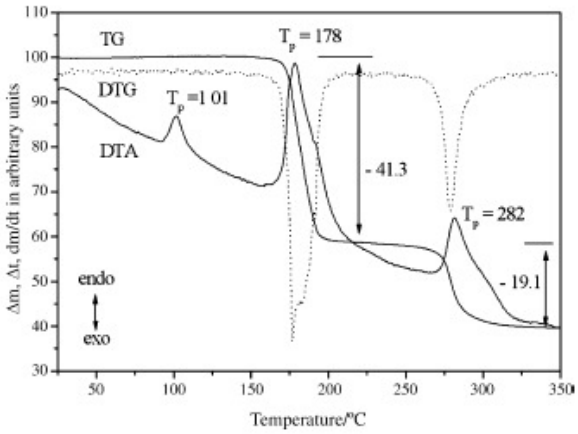

Fig. 2. DTA, TG and DTG plot of $[(propyl)_4N]_2[WS_4]$. Temperature in °C, mass loss in %.

ions of intact tri-propylamine ($m/z = 143$) and dipropyldisulfide ($m/z = 150$) as the main masses, and the fragmentation patterns of these to molecules.

3.3.1. Tetrabutylammonium thiotungstate, $((CH_3(CH_2)_3)_4N)_2WS_4$

The thermal degradation occurs in a wide temperature range (130–330 °C) with two mass losses, which are accompanied by four endothermic peaks (Fig. 3). In the first step the mass is reduced by 44.6% joined to two endothermic peaks, $T_p = 165$ °C ($T_e = 159$ °C) and $T_p = 205$ °C. In the second step the mass is reduced by 20.6% with one endothermic peak ($T_p = 264$ °C, $T_e = 256$ °C). Interestingly, an exothermic event at $T_p = 326$ °C ($T_e = 309$ °C) occurs which may be caused by structural rearrangements within the decomposition product. Like for the other compounds a remarkable difference between experimental (65.2%) and theoretical values for WS_2 formation (68.8%) is observed, and the difference can be explained on the basis of C, H, and N in the final product. MS data show the emission

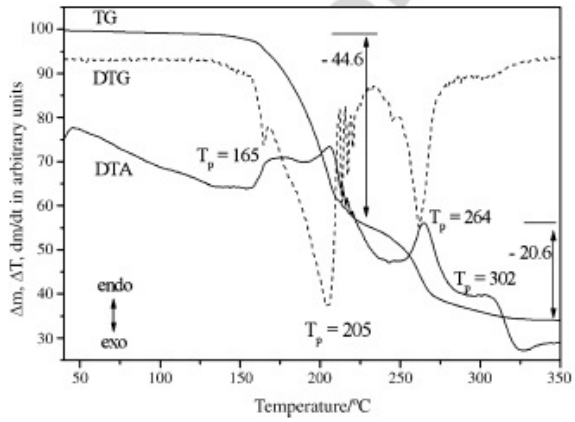

Fig. 3. DTA, TG and DTG plot of $[(butyl)_4N]_2[WS_4]$. Temperature in °C, mass loss in %.

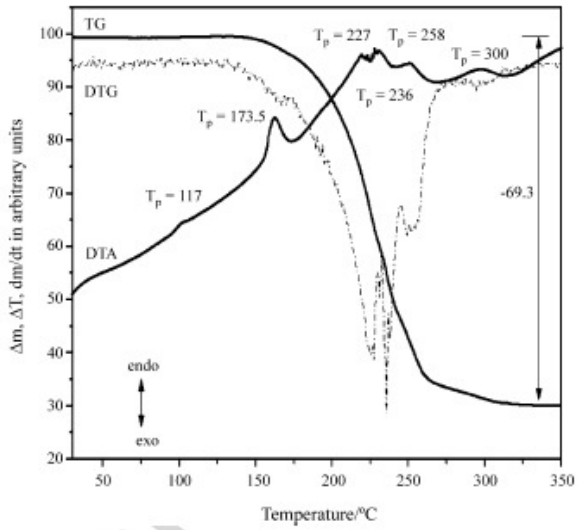

Fig. 4. DTA, TG and DTG plot of $[(pentyl)_4N]_2[WS_4]$. Temperature in °C, mass loss in %.

of tri-butylamine ($m/z = 185$) and dibutyldisulfide ($m/z = 178$) molecule during both weight change steps.

3.3.2. Tetrapentylammonium thiotungstate, $((CH_3(CH_2)_4)_4N)_2WS_4$

Several thermal events are observed in the DTA curve (Fig. 4). The first peak ($T_p = 117$ °C) corresponds to a phase transition (see below). The decomposition step extends from 135 to 330 °C containing four endothermic peaks ($T_p = 173.5, 227, 236$, and 258 °C). In the MS curves in this temperature range tri-pentylamine ($m/z = 227$), dipentyldisulfide ($m/z = 206$) and the fragmentation products of the two molecules are detected. A weak endothermic event at 300 °C in the DTA curve may be due to structural rearrangements of the degraded product. The calculated mass loss for WS_2 formation (72.6%) is larger than the experimental value of 69.3%. Again, the difference is due to C, H, N in the residue (Table 1).

3.3.3. Tetrahexylammonium and tetraheptylammonium thiotungstate $(CH_3(CH_2)_5)_4N)_2WS_4$ and $((CH_3(CH_2)_6)_4N)_2WS_4$

Both compounds decompose within a broad single step (Fig. 5) in the temperature ranges 140–337 °C (C6) and 160–343 °C (C7). In the DTA curve of C6 a very weak endothermal peak is located at $T_p = 169$ °C and an intense signal at $T_p = 253$ °C. The DTA trace of C7 shows a weak endothermic peak ($T_p = 156$ °C) which is discussed below and a complex endothermic event with two maxima at $T_p = 250$ °C and $T_p = 288$ °C. It is remarkable that in the decomposition products the S contents are significantly reduced and the amount of C increased. This observation suggests that S could be replaced by C as already reported by Berhault *et al.* from studies of the interaction of carbon with transition metal sulfides in the activation process of catalysts [31]. The total mass loss for C6

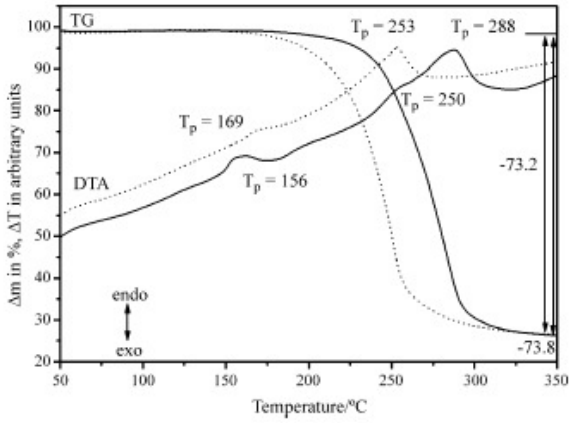

Fig. 5. DTA, TG plot of: $[(hexyl)_4N]_2[WS_4]$ = dash line and $[(heptyl)_4N]_2[WS_4]$ = solid line. Temperature in °C, mass loss in %.

(73.2%) is low compared to 76.6% calculated for WS_2 formation. The same tendency is seen for C7 with total mass loss of 73.8% versus 76.98% calculated. The MS experiments clearly indicate that intact tri-hexylamine (m/z = 269) and dihexyldisulfide (m/z = 234.2) ions are emitted (C6) while the elimination of tri-heptylamine (m/z = 311) and diheptyldisulfide (m/z = 262) is detected for C7. We note that like in the former cases the fragmentation patterns of the tri-alkylamine and diaminsulfide molecules are in agreement with data reported in the NIST database.

3.4. Scanning electron microscopy

In the SEM micrograph of the C1 decomposition product long faceted particles with a rough surface are seen, similar to the WS_2 particles obtained from ammonium thiotungstate (ATT). Therefore, the decomposition process is suggested to be topotactic, i.e. the morphology of the precursor material is maintained [25,32]. The morphology of the C2 decomposition material shows no cavities in contrast to the analogous Mo sample morphology [25]. An interesting morphology occurs in the decomposition product of the C3 precursor (Fig. 6). Needle like particles with size between 30 and 45 μm are observed which are amorphous according to the XRPD pattern. It is documented in the literature that decomposition products of thiotungstates yield products with a more pronounced morphology than the thiomolybdates analogues [33]. For the C4 precursor a partially molten surface is observed while C5 and C6 decomposition materials (Fig. 7) yield solid pieces. Only for the heptyl sample (Fig. 8) the decomposition product shows cavities like those obtained for the Mo analogue [25]. The R_4N molecules are widely used as 'templates' for zeolites and mesoporous material syntheses [34]. The 'templates' stabilize voids inside the solid structure that are proportional to the size of the alkyl group in the molecule. The WS_2 material generated from the heptyl precursor may be considered as an amorphous mesoporous material like that reported before for Mo compounds [25,35], or it may be called amorphous zeolite as claimed by Alonso et al. [36]. Every member of the Mo analogues family developed surface porosity showing a gradual increase of pore sizes according to the alkyl precursor chain length, whereas the W educts produced more compact decomposition products.

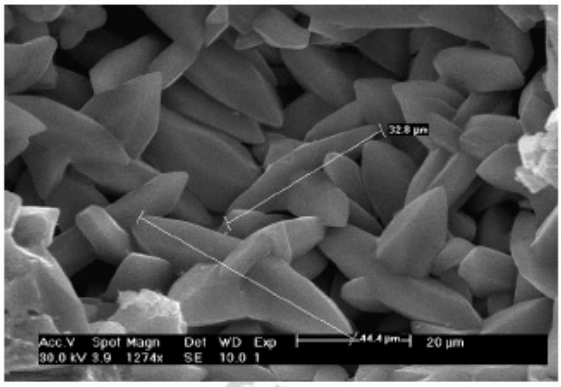

Fig. 6. SEM image of the thermal decomposition product of $[(propyl)_4N]_2[WS_4]$.

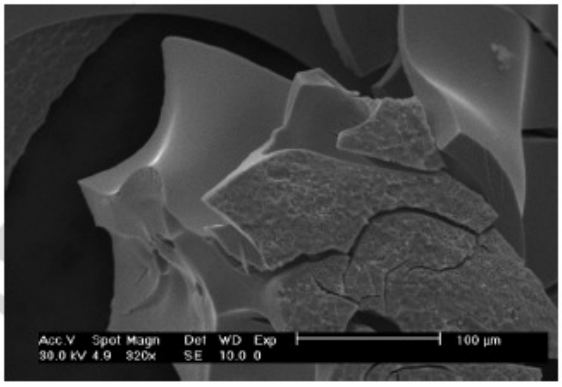

Fig. 7. SEM image of the thermal decomposition product of $[(hexyl)_4N]_2[WS_4]$.

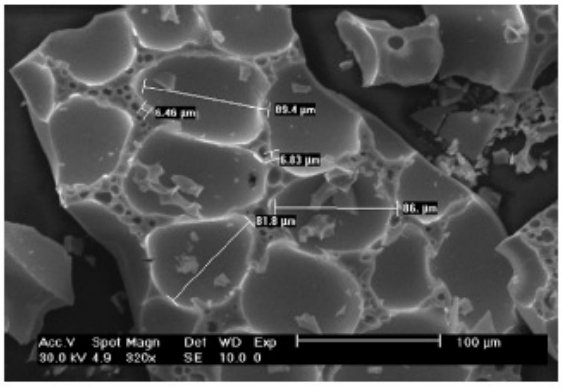

Fig. 8. SEM image of the thermal decomposition product of $[(heptyl)_4N]_2[WS_4]$.

3.5. DSC experiments and X-ray powder diffraction

The DSC trace of the tetraethyl sample exhibits an endothermic event ($T_p = 64\,°C$) in the heating curve and an exothermic peak ($T_p = 29\,°C$) in the cooling curve (Fig. 9). After this treatment the XRPD shows reflections of a new crystalline phase (Fig. 10), which was further supported by thermodiffractometry experiments (Fig. 11). In order to follow the reversibility of this structural phase transition another DSC experiment was undertaken. In the DSC curves an endothermic event occurs ($T_p = 34\,°C$, $T_e = 29\,°C$) which matches not with the event seen during the first heating experiment, meanwhile the second cooling curve shows an exothermic peak ($T_p = 29\,°C$, $T_e = 23\,°C$) identical to that registered in the first cooling curve. Obviously, the pristine material (I) undergoes an irreversible structural phase transition to a new phase (II), and this second phase shows a reversible structural phase transition to phase (III). Transition temperatures of compounds R_4NBF_4 (R = C1–C4) have been observed at 63 °C for C2 [37]. The C3 sample shows a similar behaviour with that of the tetraethyl compound with a broad and intense endothermic signal ($T_p = 88\,°C$, $T_e = 78\,°C$) in the heating curve and an exothermic peak ($T_p = 53\,°C$, $T_e = 45\,°C$) in the cooling curve (Fig. 9). The XRPD pattern of the material after the DSC experiment exhibits reflections of a new crystalline phase (Fig. 12). Again, the structural phase transition is confirmed by thermodiffractometry measurements (Fig. 13). The reversibility of the phase transition was probed by a second DSC measurement, which displays an endothermic event ($T_p = 91\,°C$, $T_e = 74\,°C$) during heating and an exothermic peak ($T_p = 51\,°C$, $T_e = 44\,°C$) during cooling. Like in the previous case this material (I) transforms to a new phase (II), which reversibly undergoes a phase transition into a third phase (III). Interestingly

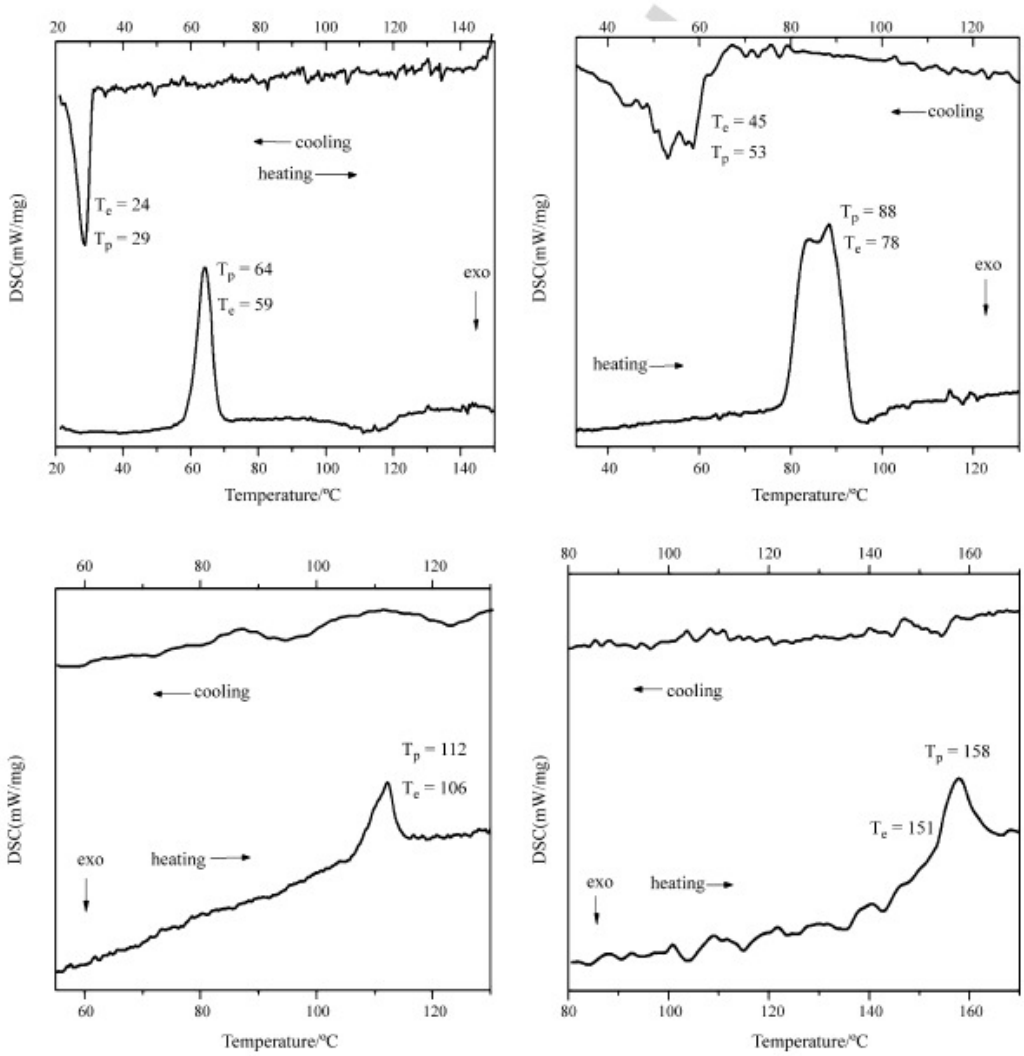

Fig. 9. DSC traces of the ethyl (top left), propyl (top right), pentyl (bottom left) and heptyl (bottom right) compounds $[(R)_4N]_2[WS_4]$.

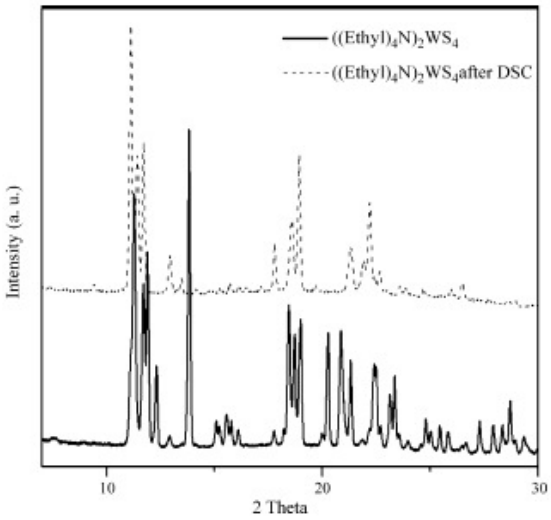

Fig. 10. Powder patterns of tetraethylammonium tetrathiotungstate, before and after the DSC experiment. *Note*: the sample was heated up to 150 °C.

no phase transition is observed for the C4 precursor in contrast to the Mo analogue sample, which showed a transition at 113 °C [25].

In the DSC experiment of the tetrapentyl compound (Fig. 9) an endothermic peak (T_p = 112 °C) occurs but there is no signal in the cooling curve. According to the X-ray powder pattern collected after the treatment a new phase is formed (Fig. 14). Contrary to the Mo analogue [25], the tetrahexyl thiotungstate sample shows no thermal event in the DSC curve up to 150 °C. Finally, the C7 sample behaves similarly to the molybdenum analogue. In the DSC heating curve (Fig. 9) an intense endothermic peak is detected (T_p = 158 °C) but no peak occurs in the cooling curve indicating the irreversibility of this effect. The powder pattern of a sample heated to 150 °C (Fig. 15) shows a broad modulation of the background in the region of the pristine material and several new reflections at higher scattering angles suggesting a partial decomposition. When the sample is heated to 170 °C an amorphous material is obtained and in the XRPD only broad and featureless modulations occur. The product looks like

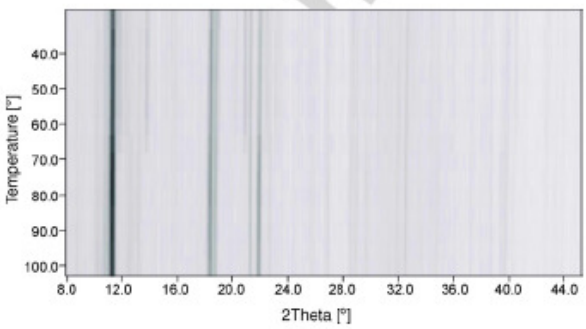

Fig. 11. Powder patterns of the in situ X-ray diffraction experiments of tetraethylammonium tetrathiotungstate.

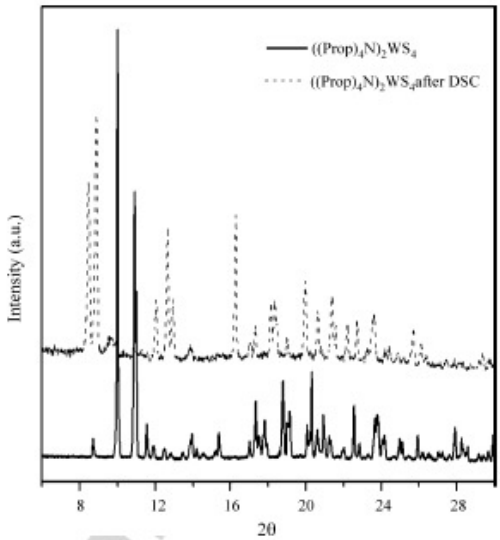

Fig. 12. Powder patterns of tetrapropylammonium tetrathiotungstate, before and after the DSC experiment. *Note*: the sample was heated up to 150 °C.

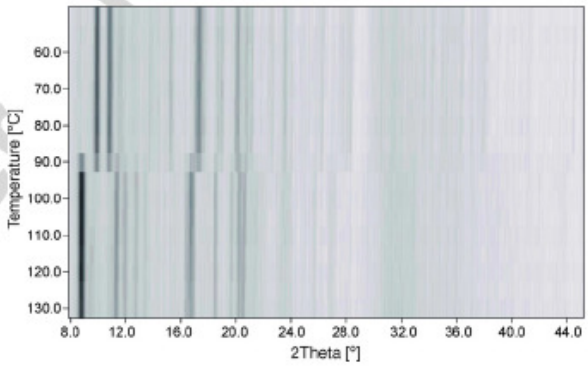

Fig. 13. Powder pattern of the in situ X-ray diffraction experiments of tetrapropylammonium tetrathiotungstate.

a glass and the chemical analysis reveals a loss of about 11 wt% C and 2.2 wt% H. It can be assumed that incongruent melting occurs at the beginning of the decomposition process, in contrast to the Mo analogue, which showed a melting point with no change of the chemical composition [25].

4. Discussion

Our recent study about the thermal decomposition of tetraalkylammonium tetrathiomolybdates revealed an increasing complexity of the thermal reactions with increasing alkyl chain lengths. During the thermal degradation tri-alkylamines and dialkyldisulfides were eliminated and for some samples low-temperature structural phase transitions were observed [25]. The tetraalkylammonium thiotungstates show a similar behaviour suggesting that the decomposition processes are very similar. For all samples the MS data reveal that intact tri-alkylamine and

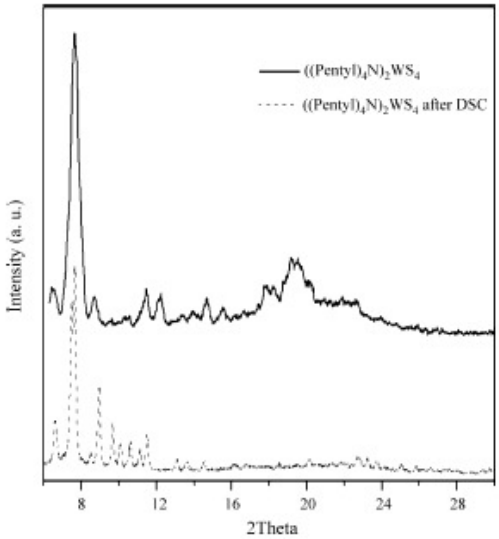

Fig. 14. Powder patterns of tetrapentylammonium tetrathiotungstate before and after the DSC experiment. *Note*: the sample was heated up to 150 °C.

dialkyldisulfide molecules are the main species emitted during thermal decomposition. All experimental MS data display the fragmentation patterns of these molecules as is evidenced by a careful comparison with the data found in the NIST database. The MS traces of the tetrapropyl precursor are shown as an example in Fig. 16. The formation of dialkyldisulfide molecules can be envisaged by the reaction of intermediate formed alkyl radicals with two S atoms from the $(WS_4)^{2-}$ anion. Therefore, a general decomposition pathway can be represented as

$$(R_4N)_2WS_4 \rightarrow 2R_3N + R_2S_2 + WS_{2-n}C_xN_yH_z$$

with values for n, x, y, and z depending on the actual composition of the precursor material (compare Table 1). In order

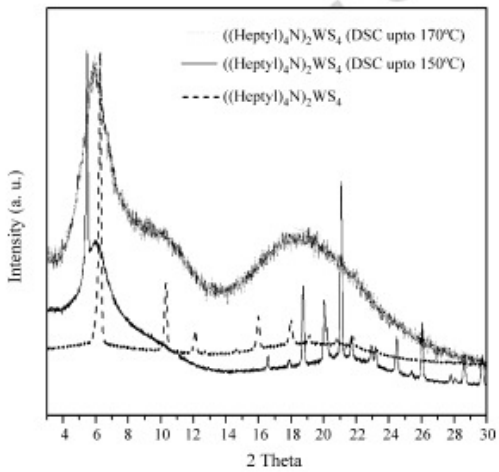

Fig. 15. Powder patterns of tetraheptylammonium tetrathiotungstate before and after DSC experiments up to 150 and 170 °C.

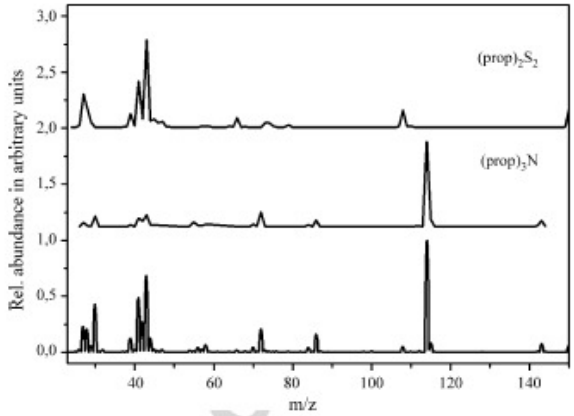

Fig. 16. Mass spectrum of $[(propyl)_4N]_2[WS_4]$ scanned at 183 °C. Note: the top two traces were taken from http://webbook.nist.gov/chemistry.

to explain this reaction a nucleophilic bimolecular substitution (S_N2) mechanism is most likely [25]: a nucleophilic attack from one anionic sulfur atom to the α carbon atom in the ammonium ions gives tri-alkylamine and dialkyldisulfide as products [38].

The XRPD patterns of all decomposition products show a high dispersion of the phases with very low layer stacking and no reflections of crystalline carbon or tungsten carbides are seen indicating that no segregation of C or formation of a carbide occurs in the final product. Fig. 17 shows a comparison of the powder patterns of C5, C6 and C7 decomposition products with that of 2H-WS_2. Amorphous tungsten disulfide (a-WS_2) is formed up to C5 derived materials, which is in agreement with the observation made by Liang et al. [39]. The XRPD of the C6 and C7 decomposition products are typical for highly dispersed small particles with a low layer stacking. In view of results presented by Berhault et al. [40] it can be assumed that S atoms at the edges of WS_2 platelets are replaced by C atoms and $WS_{2-x}C_x$ materials are formed. According to these evidences published in [40] C stabilizes texturally sulfide particles keeping the crystallites smaller and less stacked. Furthermore, all decomposition

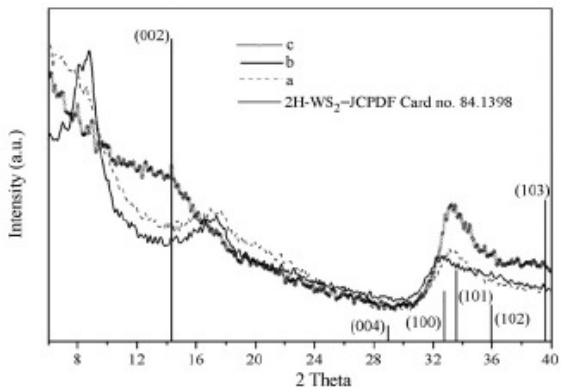

Fig. 17. Powder patterns of $[(R)_4N]_2[WS_4]$ after thermal decomposition up to 350 °C, R = (a) heptyl, (b) hexyl and (c) pentyl. Vertical bars indicate the positions of reflections of crystalline WS_2.

products were characterized with IR spectroscopy and no hints were found for the presence of undestroyed organic molecules, i.e., no signals of C–H or C–N vibrations were seen.

The hexyl and heptyl decomposition products show W/C and W/H ratios larger than the W/S stoichiometric ratio (Table 1). A similar observation was made for the analogous Mo compounds [25], but the carbon content was not as large as in the present decomposition products [25]. Another difference to the Mo samples is the observation that the W based decomposition products are more compact and only the precursor with the longest alkyl chain produces large cavities. The DSC results in combination with in situ X-ray diffraction highlight the complex thermal behaviour of these materials. The tetraethyl and tetrapropyl samples undergo structural phase transitions at low temperatures, which may be due to conformational motion and/or disorder of the alkyl chains. Such a disorder is seen in the crystal structure of the tetrapropyl tetrathiotungstate at room temperature [41]. Similar transitions were reported in the literature for tetraethyl and tetrapropylammonium tetraclorozincates [42]. The results of our study indicate that the two tetraalkylammonium thiotungstates obtained by solvent route are metastable forms that transform into the thermodynamically more stable materials upon heating.

For the tetrabutylammonium compound the most extended decomposition process (110–330 °C) is observed, but no phase transition occurs. For tetrabutylammonium iodide a glass transition was reported at 230 K [43]. The low decomposition temperature may be due to the fact that the material melts just before thermal degradation starts. Similarly for the tetraalkylammonium tetrafluoroborate series with C1–C4, the earliest melting point has been observed for C4 compound [37]. The tetrapentyl sample is irreversibly transformed into a new compound at 112 °C, a different behavior compared with the Mo analogue [25]. No phase transition is observed for the tetrahexyl sample, in contrast to what was found for the analogous Mo sample. The tetrahexyl and tetraheptyl precursors show both weak endothermic peaks at around 160 °C, followed by more complex endothermic events. The corresponding X-ray powder patterns evidence that the products are amorphous immediately after the decomposition process starts. The disorder and motion in crystals and mesophases of tetrahexylammonium iodide was studied based on entropy changes during the phase transition concluding that the mesophase is likely a conformational disordered crystal [44]. The disordered crystals may be quenched to glasses as it has been observed by quenching of the present tetraheptyl compound at 150 °C.

5. Summary

The tetraalkylammonium thiotungstates, $(R_4N)_2WS_4$, with R = methyl to heptyl undergo thermal decomposition reactions very similar to the analogous Mo samples. The elimination of tri-alkylamines and dialkyldisulfides is accompanied by endothermic peaks in DSC and DTA curves. All samples decompose without formation of WS_3 as an intermediate. The composition of the final products is affected by the alkyl chain length: samples from methyl through pentyl yield WS_2, whereas the hexyl and heptyl precursors decompose to carbon supported tungsten sulfides because the carbon content is higher than the sulfur content. Previous studies presented evidences that the surface of the active phase under real hydrotreating conditions presents a carbidic like nature. Therefore, thermal decomposition of starting materials with long alkyl chains offer the possibility to prepare catalysts with a desired structural C content. We note that tetraheptyl thiotungstate was used as starting material for the preparation of active WS_2 catalysts [45]. In this study the precursor was not decomposed prior to the catalytic test but was applied under HDS conditions yielding in situ formed active WS_2 material containing a large amount of carbon. Like for the molybdenum analogues a general decomposition reaction mechanism is proposed following a nucleophilic bimolecular substitution (S_N2) mechanism yielding tri-alkylamines and dialkyldisulfides as eliminated products. The morphology of the final decomposition products shows no tendency to develop porous materials. This observation is in contrast to the findings for the analogous Mo samples. A highly interesting result is that several compounds undergo phase transitions to more stable polymorphs. These new modifications are then reversibly transformed into a new modification at elevated temperatures. X-ray diffraction analyses of the final products demonstrate that amorphous WS_2 is obtained up to the tetrapentyl material, and with C6 and C7 precursors S-poor products are developed which may be better described as carbosulfide phases.

Acknowledgements

The authors thank C. Teske for fruitful discussions. The financial support by the Deutsche Forschungsgemeinschaft DFG (project: BE 1653/11-2) is gratefully acknowledged.

References

[1] R.R. Chianelli, M. Daage, Adv. Catal. 40 (1994) 7.
[2] M. Yamada, Catal. Surv. Jpn. 3 (1999) 3.
[3] D.S. Thakur, B. Delmon, J. Catal. 91 (1985) 308.
[4] M. Breysse, J.L. Portefaix, M. Vrinat, Catal. Today 10 (1991) 489.
[5] F. Luck, Bull. Soc. Chim. Belg. 100 (1991) 781.
[6] B. Delmon, Catal. Lett. 22 (1993) 1.
[7] R.R. Chianelli, T.A. Pecoraro, US Patent 4,508,847 (1985).
[8] M. Zdrazil, Catal. Today 3 (1988) 269.
[9] G. Alonso, M. Del Valle, J. Cruz, A. Licea-Claverie, V. Petranovskii, S. Fuentes, Catal. Lett. 52 (1998) 55.
[10] F. Pedraza, S. Fuentes, Catal. Lett. 65 (2000) 107.
[11] G. Alonso, M. Del Valle, J. Cruz, A. Licea-Claverie, V. Petranovskii, S. Fuentes, Catal. Today 43 (1998) 117.
[12] G. Alonso, V. Petranovskii, M. Del Valle, J. Cruz-Reyes, A. Licea-Claverie, S. Fuentes, Appl. Catal. A: Gen. 197 (2000) 87.
[13] K. Inamura, R. Prins, J. Catal. 147 (1994) 515.
[14] M. Sun, T. Bürgi, R. Cattaneo, R. Prins, J. Catal. 197 (2001) 172.
[15] M. Sun, M.E. Bussel, R. Prins, Appl. Catal. A 216 (2001) 103.
[16] M. Sun, P.J. Kooyman, R. Prins, J. Catal. 206 (2002) 368.
[17] V. Schwartz, M. Sun, R. Prins, J. Phys. Chem. B. 106 (2002) 2597.
[18] G. Alonso, J. Espino, G. Berhault, L. Alvarez, J.L. Rico, Appl. Cat. A 266. (2004) 29.
[19] B.R. Srinivasan, M. Poisot, C. Näther, W. Bensch, Acta Crystallogr. E 60 (2004) i136.
[20] B.R. Srinivasan, S.N. Dhuri, C. Näther, W. Bensch, Acta Cryst. E 58 (2002) m622.

[21] B.R. Srinivasan, S.N. Dhuri, C. Näther, W. Bensch, Monatshefte Chemie 137 (2006) 397.
[22] B.R. Srinivasan, S.N. Dhuri, C. Näther, W. Bensch, Acta Crystallogr. C 59 (2003) m124.
[23] B.R. Srinivasan, S.N. Dhuri, M. Poisot, C. Näther, W. Bensch, Z. Anorg. Allg. Chem. 631 (2005) 1087.
[24] B.R. Srinivasan, S.N. Dhuri, C. Näther, W. Bensch, Acta Crystallogr. E 59 (2003) m681.
[25] M. Poisot, W. Bensch, S. Fuentes, G. Alonso, Thermochim. Acta 444 (2006) 35.
[26] J.W. McDonald, G.D. Friesen, L.D. Rosenhein, W.E. Newton, Inorg. Chim. Acta 72 (1983) 205.
[27] G. Alonso, G. Aguirre, I.A. Rivero, S. Fuentes, Inorg. Chim. Acta 274 (1998) 108.
[28] J. Espino, L. Alvarez, C. Ornelas, J.L. Rico, S. Fuentes, G. Berhault, G. Alonso, Catal. Lett. 90 (2003) 71.
[29] T.P. Prasad, E. Diemann, A. Müller, J. Inorg. Nucl. Chem. 35 (1973) 1895.
[30] A. Müller, E. Diemann, R. Jostes, H. Bögge, Angew. Chem. 93 (1981) 95.
[31] G. Berhault, L.C. Araiza, A.D. Moller, A. Mehta, R.R. Chianelli, Catal. Lett. 78 (2002) 81.
[32] K. Voorhoeve, J. Stuiver, J. Catal. 23 (1971) 228.
[33] M. Del Valle, M. Yanez, M. Avalos, S. Fuentes, in: M. Ocelli, R.R. Chianelli (Eds.), Hydrotreating Technology for Pollution Control, 1996, p. 47.
[34] K. Holmberg, J. Colloid Interf. Sci. 274 (2004) 355.
[35] G. Alonso, G. Berhault, F. Paraguay, E. Rivera, S. Fuentes, R.R. Chianelli, Mater. Res. Bull. 38 (2003) 1045.
[36] G. Alonso, M.H. Siadati, R.R. Chianelli, US Patent Application 20050032636.
[37] G. Zabinska, P. Ferloni, M. Sanesi, Thermochim. Acta 122 (1987) 87.
[38] J. March, Advanced Organic Chemistry: Reactions Mechanism and Structure, Mc Graw-Hill, Japan, 1968.
[39] K.S. Liang, R.R. Chianelli, F.Z. Chien, S.C. Moss, J. Non-Cryst. Solids 79 (1986) 251.
[40] G. Berhault, A. Mehta, A.C. Pavel, J. Yang, L. Rendon, M.J. Yacaman, L.C. Araiza, A.D. Moller, R.R. Chianelli, J. Catal. 198 (2001) 9.
[41] M. Poisot, C. Näther, W. Bensch, Z. Naturforsch 61b (2006) 1.
[42] R. Blachnick, C. Siethoff, Thermochim. Acta 278 (1996) 39.
[43] A. Xenopoulos, A.H. Narten, J. Cheng, B. Wunderlich, J. Non-Cryst. Solids 131 (1991) 113.
[44] J. Cheng, A. Xenopoulos, B. Wunderlich, Mol. Cryst. Liq. Cryst. 220 (1992) 127.
[45] G. Alonso, R.R. Chianelli, J. Catal. 221 (2004) 657.

3.3 Catalytic activity studies

3.3.1 M. Poisot, W. Bensch, S. Fuentes, C. Ornelas and G. Alonso

High Activity Ni/MoS_2 Catalysts obtained from Blends of Alkylthiometallates for the Hydrodesulfurization of Dibenzothiophene, *submitted to Catalysis Letters.*

The controlled decomposition of blends of Ni(diethylenetriamine)$_2$$MoS_4$ and (propyl$_4$N)$_2$$MoS_4$ yields high active nickel promoted molybdenum disulfide catalysts for the hydrodesulfurization (HDS) of dibenzothiophene (DBT). The activity and selectivity for the direct desulfurization (DDS) pathway follows the tendency to higher nickel content as a result of the synergistic effect of nickel and carbon producing single-slabs of nickel promoted molybdenum carbosulfides. The chemical interaction that occurs during the blending procedure cause the redispersion of nickel atoms from one precursor to the surface of the molybdenum-carbonsulfide phase provided by the (propyl$_4$N)$_2$$MoS_4$, in this way the amount of NiMoS active sites increases resulting in an enhancement of the catalytic activity. In comparison, the activity of the catalysts obtained from blends of $(NH_4)_2MoS_4$ and Ni(diethylenetriamine)$_2$$MoS_4$ remains similar to that of the unblended precursors indicating that no good redispersion of the promoter was obtained.

3.3.1

High Activity Ni/MoS_2 Catalysts obtained from Blends of Alkylthiometallates for the Hydrodesulfurization of Dibenzothiophene

M. Poisot[1], W. Bensch [1,*], S. Fuentes[2], C. Ornelas[3] and G. Alonso[3]

[1]*Institut für Anorganische Chemie, University of Kiel, Olshausenstr. 40-60 24118 Kiel, Germany*
[2]*Centro de Ciencias de la Materia Condensada, UNAM, Ensenada, Baja California, C.P.22860 México*
[3]*Centro de Investigación en Materiales Avanzados S. C., Chihuahua, Chih., C.P. 31109 México*

Abstract

An efficient method for improving the catalytic properties of unsupported Ni/MoS_2 catalysts is the blending of thiometallate precursors applying the appropriate precursors and thermal conditions. High active catalysts for the hydrodesulfurization (HDS) of dibenzothiophene (DBT) are prepared by the controlled decomposition of physical mixtures of Ni(diethylentriamine)$_2$$MoS_4$ (II) and (Propyl$_4$N)$_2$$MoS_4$ (III). The catalysts with a higher content of II are very active with a high selectivity for the direct desulfurization pathway (DDS) due to the synergistic effect of nickel and carbon producing single-slabs of nickel promoted molybdenum carbosulfides. The activity enhancement is attributed to an increased number of NiMoS active sites originated by the chemical interaction between precursors II and III occurring during the blending procedure. In addition, the carbon content in the final products is related to the enhancement of the activity and the preference of the DDS pathway. The controlled decomposition of mixtures of II + III yields catalysts which are about twofold more active an industrial NiMo/Al_2O_3 catalyst. This improvement may be attributed to an intense interaction of the precursors during the blending process causing a re-dispersion of nickel atoms from II over the surface of molybdenum-carbosulfide provided by precursor III, increasing the amount of active sites.

The catalysts from blends of $(NH_4)_2MoS_4$ (I) and II behave similarly to the unblended precursors.

Keywords: Thiometallates, Ni/MoS_2 catalysts, HDS of DBT, Ni(diethylenetriamine)$_2$$MoS_4$, $(NH_4)_2MoS_4$, (Propyl$_4$N)$_2$$MoS_4$

1. Introduction

As the supply of low sulfur crude decreases, refineries are processing crude with high sulfur content meanwhile environmental regulation is becoming more and more restrictive for the gas emissions from diesel vehicles (50 wt ppm-S in Europe and Japan in 2005 [1, 2]). Consequently the necessity to develop efficient hydrodesulfurization (HDS) catalysts is evident. The catalysts of choice for HDS of crude oils for many decades have been cobalt and nickel promoted molybdenum sulfides [3, 4]. Recently new technologies for the production of ultra low sulfur diesel (ULSD) have been used in commercial hydrotreaters reaching < 10 ppm sulfur content in the products [5-7]. The actual hydrotreatment (HDT) catalysts are generally based on Mo and W sulphides commonly supported on alumina, and promoted with Co and Ni. Different preparation methods are used to synthesize unsupported HDS catalysts, e. g. comaceration [8], homogeneous sulfide precipitation [9], and thiosalt decomposition [10]. The catalytic properties of MoS2 obtained by these methods are reported to depend strongly on the reacting atmosphere as well as on the heating conditions [8-10]. In others words, the properties depend on the experimental conditions applied during decomposition of precursor thiosalts and large variations in specific surface areas from few to several tenth of square meters per gram have been reported [11-16] The use of thiometallate complexes as precursors for the synthesis of active Co(Ni)MoS phases has provided enabled activity of the catalysts [15, 17-23]. Results like this encouraged us to search for new preparation routes yielding finally high efficient HDS catalysts. In the present work blends of precursors containing only molybdenum ($(NH_4)_2MoS4$ (I) or $(Propyl_4N)_2MoS_4$ (III)) and nickel-molybdenum (Ni(diethylenetriamine)$_2MoS_4$ (II)) were used in order to create functional Ni/MoS_2 catalysts for HDS of dibenzothiophene (DBT).

2. Experimental

Precursor II was prepared by reacting $NiCl_2$ and $(NH_4)_2MoS_4$ (ATM) (molar ratio1:1) in 3 mL diethylenetriamine (100 %) (dien) under solvothermal conditions in a Teflon lined steel autoclave at 120°C for six days. The orange-red powder was obtained in 70% yield. The powder was filtered and washed with ethanol. However, the amount of the products obtained under solvothermal conditions is not enough for the HDS test reactions and a simpler synthesis route was developed. 10 mL aqueous solution of $NiCl_2$ (3.5 mmol) was mixed with dien (100 %, 7 mmol) forming a pink solution. ATM (3.5 mmol) dissolved in the minimum amount of water was added to the Ni-dien solution and immediately the product precipitated with 100% yield.

3. Results

The precursors $(NH_4)_2MoS_4$ (I) and $(Propyl_4N)_2MoS_4$ (III) were synthesized as previously reported in [24]. The blends of the catalyst precursors were manually ground in an agate mortar according to the Ni/Ni + Mo ratios shown in Tables 1 and 2. The mixtures were then decomposed under N_2 atmosphere in a rotating glass tube (300 rpm) adapted for a Gero SR oven with Eurotherm controller. The tube was loaded with 1 to 3.6 g. per batch. The temperature program was selected to obtain a surface-porous material. The blends included in Table 1 were introduced in a preheated oven (T = 285°C) and then heated up to 500°C within 2 h. This temperature was hold for 10 minutes followed by cooling to 400°C within 1 h, and hold at this temperature for other 2 hours. The blends presented in Table 2 were introduced in a less hot preheated oven (T = 100°), then heated up to 325°C within 1.5 h. This temperature was hold for 20 minutes. After cooling down to 250°C within 0.5 hour the reaction products were removed from the oven. The samples were cooled down to room temperature under N_2 flow (0.4 l/min) and stored in this atmosphere. (N_2, Air Liquide 5.0). Chemical elemental analyses were performed with a EURO Vector EURO EA combustion analyzer using zinc sample holders filled with 2-3 mg. The samples were heated to 1000 °C under oxygen atmosphere and the gases were detected by a thermal-conductivity cell. Far Infrared spectra were collected on a Bruker IFS 66 instrument. The samples were prepared in polyethylene matrix. Mid Infrared spectra were recorded on an ATI Mattson Genesis instrument preparing the samples in a KBr matrix. FT-Raman spectroscopy experiments were performed with a Bruker RSA 106 instrument equipped with a Nd/YAG-Laser (1064 nm). X-Ray powder diffraction patterns were recorded on a STOE-Stadi P diffractometer operating with Cu $K\alpha_1$ radiation and a position sensitive detector. A Philips ESEM XL 30 microscope equipped with an EDAX analyzer was used to perform morphological studies and semi-quantitative elemental analyses. Pictures were taken at different areas of the samples applying several magnifications. For DTA-TG experiments the samples were placed in Al_2O_3 crucibles under a dynamic nitrogen atmosphere (flow rate: 75 ml/min., purity 5.0). The curves were measured with a 4 K/min heating rate up to 500°C. The TG curves were corrected for buoyancy and current effects. Specific surface area (SSA) determination was performed with a QUANTACHROM AUTOSORB-1 model by nitrogen adsorption at 77 K using the BET isotherm method. Samples were degassed under flowing argon at 473 K for 2 h before nitrogen adsorption. Mean standard deviation for specific surface area measurements is about 2%. The pore size distribution was obtained from the desorption branch following the BJH method. The HDS of DBT has been extensively studied as a model reaction for hydrodesulfurization of petroleum feedstock [3]. Laboratory studies have been performed in

pressurized flow and batch reactors [15, 19-20, 25-26]. Using batch reactors, useful information such as rate constants and selectivity can be obtained by following the composition of the reaction mixture as a function of time. The reaction was carried out in a Parr model 4522 high-pressure batch reactor. About 1 g of the precursor and 75 ml of a freshly prepared solution of DBT in decaline (5% wt/wt.) were placed in the reactor. The reactor was then purged and pressurized with H_2 to 3.37 MPa and heated up to 623 K at 10 K/min heating rate. After reaching the working temperature, the products were collected for chromatographic analysis every half an hour to determine conversion vs. time dependence. A Perkin Elmer Auto-System XL gas chromatograph equipped with a 9 ft x 1/8 inch packed column OV17 3% was used to analyze the collected samples. The main products obtained by HDS reaction of DBT were biphenyl (BP), cyclohexylbenzene (CHB) and tetrahydrodibenzothiophene (THDBT). The concentration of bicyclohexyl (BCH) was found to be negligible for all experiments. Selectivity was calculated as the mol percentage of the given product in the reaction mixture. The BP was produced through the so-called direct desulfurization pathway (DDS), and CHB and THDBT through the hydrogenation pathway (HYD), both pathways are parallel [27]. The ratio between HYD and DDS can be estimated in terms of the experimental selectivity by means of the (CHB), (THDBT) and (BP) concentrations**.** The selectivity (HYD/DDS) can be approximately calculated by

HYD/DDS= ([CHB] + [THDBT]/[BP]

For each catalyst the rate constant was calculated from DBT conversion as function of time assuming DBT conversion being a pseudo-zero order reaction [9], according to the equation:

$$\mathbf{X_{DBT} = (1 - \eta_{DBT} / \eta_{DBT}) = (\boldsymbol{k} / \eta_{DBT,0}) \boldsymbol{t}}$$

where $\mathbf{X_{DBT}}$ is the fraction of DBT conversion, $\boldsymbol{\eta_{DBT}}$ = moles of DBT, $\boldsymbol{k}$ = pseudo zero order rate constant, $\boldsymbol{t}$ = time in seconds and $\mathbf{(\boldsymbol{k} / \eta_{DBT,0})}$ is the slope. The mean standard deviation for catalytic measurements is about 2.5%.

3. Results

3.1 Catalytic activity and selectivity

Catalysts from blends of ATM (I) and Ni(diethylenetriamine)$_2$MoS$_4$ (II)

The change of the molar concentration of DBT with reaction time (h) for catalysts obtained from I, II and blends of them is presented in Figure 1. The catalyst derived from I shows a decreases in DBT concentration almost linearly confirming that pseudo-zero order kinetics takes place under the experimental conditions used. The slight deviation from linearity

observed at the end of the reaction is attributed to the deactivation of the catalyst by H_2S accumulated in the reactor. Hydrogen sulfide is known to have an inhibiting effect in the HDS of DBT reaction where the order depends on the partial pressure [28-30]. The formation of THDBT is favored at the beginning of the reaction but it declines at the end, showing a behavior like an intermediate compound [3], meanwhile CHB formation suits more a linear fit confirming the known trend of catalysts derived from I for HYD (Figure not shown). The catalytic activity (k) of the samples, in moles of DBT per second and gram of catalyst, as well as the HYD/DDS ratio after 5 hours experiment are reported in Table 1. The MoS_2 catalyst obtained from I shows a low activity ($k = 4.8 \times 10^{-7}$ mol/s·g) and high selectivity for hydrogenation (HYD/DDS = 1.68). Catalysts derived from ATM have been extensively studied and typically used as reference for unsupported catalysts in HDS tests [15, 31-32]. On the other hand the catalytic results for Ni/MoS_2 prepared from II (see Figure 1) exhibit a decay of DBT concentration with time in nearly linear fashion. The concentration of BP through the DDS pathway is largely favored for this catalyst starting from the beginning of the reaction (Figure not shown). The catalysts obtained from blends exhibit a very similar behavior to catalyst II producing mainly BP. For all catalysts from I + II blends an increase of the slope with time is observed at the beginning of the experiment and no deactivation occurs at the end. The initial effect is assigned to a slow process of catalyst activation requiring H_2S generated from the reaction. The catalysts reach then their activated form after two hours of reaction and remained very active up to end of the experiment without deactivation. The latter observation suggests that the H_2S concentration during the last hour of the experiment is relatively low. In contrast to the low activity of the MoS_2 catalyst obtained from I the Ni/MoS_2 material derived by decomposition of II shows a high activity ($k = 6.7 \times 10^{-7}$ mol/s·g) and a high selectivity for desulfurization (HYD/DDS = 0.28). A gradual increase of the activity of the catalysts is found with increasing nickel content (Table 1). The activity of a commercial catalyst ($NiMo/Al_2O_3$) was characterized under the actual experimental conditions for comparison ($k = 12 \times 10^{-7}$ mol/s·g, HYD/DDS = 0.53). The present catalysts prepared by decomposition of I or II or from mixtures of them exhibit lower constant rate values. But the materials derived by decomposition of I and II blends are more selective for DDS than the commercial catalyst and the samples received from I or II (Table 1). The surface area of blended catalysts measured after the catalytic test increases gradually with the amount of precursor II in the initial mixture (Table 1). A similar trend is observed for the pore volumes of the catalysts (Table 1).

Catalysts from blends of Ni(diethylenetriamine)$_2$MoS$_4$ (II) and (Propyl$_4$N)$_2$MoS$_4$ (III)

Figure 2 displays the change of the molar concentration of DBT as function of reaction time for catalysts derived from precursor III and blends of III with II. The numerical results for k and the HYD/DDS ratios are compiled in Table 2. The experiments were run for six hours to compensate the time consumed at the beginning to form the activated catalyst.

The catalytic activity pattern of MoS_2 obtained from IV is similar to that of the material received using I as precursor with a linear decrease of DBT supporting the assumption of pseudo-zero order kinetics for the reaction. This catalyst has a similar activity (4.7 x 10^{-7} mol/s·g) but a higher HYD/DDS selectivity (2.04) compared to the catalyst prepared by thermal decomposition of the precursor I. Such a change of selectivity can be attributed to carbon introduced into the catalyst by the alkyl group in III. It has been reported in literature that carbon influences both the activity and the selectivity in the HDS reaction of DBT [33-35]. All III + II blended catalysts display an increase of the slope with reaction time at the beginning of the test, similarly to the results presented for I + II blends. This behavior is attributed to a slow activation process requiring H_2S generated during the reaction. But materials processed by decomposition of III + II blends present more conversion of DBT after 6 hours than catalysts of I + II blends indicating that they contain more active sites for HDS. All blended catalysts produce increasing amounts of BP and CHB while the concentration of THDBT reach a maximum and decrease again (Figure not shown). An interesting observation are the higher activities (16 - 20 x 10^{-7} mol/s·g) than those obtained from single precursors. Moreover, the catalytic activities are much higher than the activity of the industrial supported catalyst (see above and Table 2). The observed HYD/DDS ratios (0.28 - 0.82) represent a higher selectivity for DDS compared to Ni-Mo/Al_2O_3, and intermediate selectivity compared to data observed for materials from precursors I or III and the promoted sample from precursor II. All synthesized catalysts show mainly BP formation (DDS route). Because the selectivity is linked with the mode of DBT adsorption, the large BP formation indicates that DBT adsorption on the active phase occurs with the DBT molecule standing up in a vertical geometry. Thus, for all catalysts the flat DBT adsorption through the adsorption of π-electrons of DBT molecules favoring the hydrogenation route of the HYD reaction of DBT appeared more difficult than the direct C-S bond cleavage. The surface areas of catalysts derived by thermal decomposition of III + II blends measured after the catalytic test show values ranging from 46 m^2/g (III) to the largest one of 142 m^2/g for C3Mo035. This last sample also presents the highest pore volume. The other catalysts have relatively poor surface areas ranging from 2 to 27 m^2/g (Table 2). These results suggest the effect of carbon support combined to the

synergistic effect of nickel being at the optimum in C3Mo035, as previously observed when tetrabutylammonium thiometallate is used as precursor combined with a cobalt promoter [36].

The most active catalysts were obtained from III + II blends after an activation period at the beginning of the catalytic test. In order to study the chemical composition of the samples the analyses were performed before and after the catalytic test. Moreover, the samples obtained after the catalytic test were heated in an inert atmosphere. These samples were then also analyzed carefully. Far-Infrared spectra, powder X-Ray patterns and scanning electron micrographs were collected with the fresh materials and the catalysts after the HDS of DBT.

3.2 Thermal analysis

After the HDS reaction with DBT the samples were studied by thermal analysis under inert atmosphere up to 500°C. Table 3 lists the mass change of the samples under study. In general the decomposition occurs in a broad single step which is accompanied by a broad endothermic event. The decomposition starts at room temperature and is finished between about 400 and 430°C. Most of the samples exhibit a mass loss of about 11%. The catalysts with a high Ni content show a lower weight decrease than the samples with a low surface area. The latter observation suggests that much more carbon particles cover the sample surface and not just support the structure. The sample C3Mo040 has the smallest pore volume of all blends and the highest carbon content after the catalytic test as well as after the thermal treatment.

3.3. Elemental analysis

The chemical compositions of the catalysts from III + II blends were calculated converting the chemical elemental data to atom percent and considering the atom percent ratio regarding molybdenum, nickel and sulfur obtained by semi-quantitative EDX analyses. In Table 4 the compositions of the samples in the as prepared state and after the catalytic test are summarized. Due to the blending procedure the Ni content of the as prepared samples increases whereas the carbon content significantly decreases and the sulfur content exhibits a moderate decrease. After the HDS reaction with DBT the composition of the catalysts show a remarkable increase of the sulfur content while the carbon content is further reduced. This tendency must be related to the activation time during the early stages of the test reaction. The two materials abbreviated as C3Mo035*act* and C3Mo050*act* in Table 4 showed a good activity and selectivity. For both samples a similar trend of the chemical compositions is observed, i.e., the sulfur content has increased about 2.6 times for the former and 3 times for the latter material.

Simultaneously, the carbon content was reduced by 37.5% and 15% for the two materials respectively. The thermal treatment of the catalysts leads to a further decrease of the sulfur and carbon content with a much more pronounced reduction of the carbon content (41 to 62%) than for sulfur (about 15 to 32%). After the thermal post-treatment, the ratios of Mo:S and Mo:C are around 1:2.6 and 1:0.7, respectively, suggesting that after all these experiments the carbon content remaining in the materials could belong to the final stable catalyst structure.

3.4. X-Ray diffraction

Figure 3 shows the XRD patterns of the catalysts from III + II blends after the HDS reaction while in Figure 4 the patterns of the same catalysts after the thermal post-treatment are displayed. In both patterns the (002) diffraction peak is observed as a broad and weak signal indicating that a poorly crystalline MoS_2 is obtained with a low layer stacking along the *c* direction. The overall features of the patterns are in agreement with those reported for poorly crystalline catalysts [36-37] and the profiles are also similar to those observed for carbon-supported NiMo-sulfide prepared using active carbon and recorded after the catalytic test with DBT [38]. Weak and broad peaks of nickel sulfide are detected beneath two sharp and intense unidentified peaks at around 38° and 44° 2θ. These reflections could be caused by a new form of molybdenum carbide or sulfocarbide since a comparison with the JCPDS data bank provided no match with molybdenum- or sulfocarbides collected in this data base. However, the C3Mo035 sample shows a rather homogeneous dispersion of nickel and the weakest (002) reflection of all catalysts. After the thermal post-treatment the powder pattern evidences a rather crystalline nature of the material (Fig. 4). The (002) peak is clearly more intense than for the other samples and the asymmetric shape on the low angle side may be due to the turbostratic disorder of the MoS_2 layers [39]. The reflections of Ni_3S_2 are still seen in the pattern. The pattern of C3Mo040*act* indicates that the material is nearly amorphous against X-rays with a broad modulation at around 14° 2θ (see Fig. 3). Even after the post-treatment this sample seems to be the material with the lowest crystalline nature (compare Fig. 4). The unidentified reflections (see above) disappeared after the post-treatment and are also not seen in the patterns of the catalysts with larger nickel content than C3Mo040act (compare Fig.'s 3 and 4).

3.5. IR Spectroscopy

In Table 5 the IR data of the catalysts and of the catalysts after the thermal post-treatment are summarized. In general the absorption bands are broad and have a low intensity. For Mo-S

stretching modes two main bands are expected according to the layered nature of the MoS_2 crystallites, i.e., one band along the basal plane (⊥ *c,* 385 cm^{-1}) and another perpendicularly to the basal plane or along the c axis (// *c*, 467 cm^{-1}) [40]. In the IR spectra of all samples just one band at 383 cm^{-1} is registered. This band is asymmetric towards lower wave-numbers being attributed to strongly distorted monolayers of MoS_2 along the basal plane, as already detected by X-ray diffractometry. Moreover it is suggested that the pronounced asymmetry results from the partial incorporation of carbon into the MoS_2 structure, at least in the surface, and from increased bending and folding of the MoS_2 layers [33, 41]. Recently, Raman studies of promoted catalysts obtained by urea-matrix combustion synthesis on alumina support revealed similar distortions of MoS_2 [42]. In the mid-IR region a broad band centered at around 1100 cm^{-1} is observed. This absorption was reported [43] to be accompanied by a weak signal at 830 cm^{-1} and is related to the intermediary products of dimethylsulfide decomposition forming $(C_xS)_n$ polymer species [44]. For our samples we relate this band to the formation of a carbosulfide phase at the edge-planes of MoS_2. Indeed, the group of Berhault have found that the interaction between carbon and sulphur not only favors the formation of surface carbosulfide phases, but also stabilizes texturally the sulfide particles which is reflected in improved catalytic stability and high catalytic performance [40, 45].

The band at around 1630 cm^{-1} may be the vibration of "Ni-Mo-C" entities resulting from the synergistic effect of nickel and carbon in molybdenum disulfide by the substitution of sulfur by carbon in an analogy of the synergistic effect of nickel and molybdenum carbide on alumina observed by IR experiments of adsorbed CO [1] or by pyridine adsorption on $NiMo_2C/Al$ catalysts [46]. This band is not observed for the catalyst obtained from precursor I, and remarkably the intensity of this absorption increases with the nickel content in the III + II catalyst blends. We note that for the most active catalyst (C3MoO35) this absorption occurs at the highest frequency, even after the post-treatment. The highest catalytic activity of NiMoS based catalysts is a result of the synergistic effect. Whether the absorption band at around 1630 cm^{-1} is an indicator for the catalytic activity of a material must be investigated more in detail and efforts are under way in the laboratories.

3.6 Scanning electron microscopy

The catalysts were characterized with scanning electron microscopy with a special focus onto the sample with the best catalytic activity, i.e., C3Mo035. In Fig.'s 5a to c are shown the images of this material before and after the catalytic test as well as after the thermal post-treatment, respectively. The as-prepared sample shows very fine surface porosity while after

the catalytic test a wide variety of pore shapes ranging from very fine to very large pores are seen and also distorted pores occur. The large range of pore sizes is related to the highest surface area measured for the catalyst series. After the thermal treatment the surface looks even more distorted containing some big pores. The other samples in this series have a significantly less pronounced surface porosity.

4. Discussion

The study of the effect of precursor blends onto the HDS activity was carried out following the principles of the method of *in situ* decomposition of thiosalts reported by Chianelli [19] and Alonso *et al*. [22, 25, 34]. Such a method comprises three important steps occurring in the reaction medium just before or at the beginning of the catalytic reaction: a) Decomposition of the precursor; commonly thiomolybdates containing the MoS_4^{2-} ion like ATM, which generates MoS_3 and then MoS_2 by successive fragmentation [10, 47-48]; b) Formation of MoS_2 nanoparticles resulting in a poorly-crystalline structure [37]; c) Activation of MoS_2 by hydrogen/hydrogen sulfide gas mixtures in order to create S^{2-} vacancies, which are the active sites for HDS during the catalytic test [49]. In the present method the first and second steps are already completed by the thermal decomposition of the blends yielding fresh active catalysts.

However, the efficiency of the decomposition process to generate good catalysts depends on the type of the precursor and the chosen conditions [50]. The use of alkyl groups substituting the ammonium cation in ATM has been shown to enhance the catalytic activity of MoS_2 catalysts [15, 19, 48]. Bithiometallates containing Co or Ni as precursors are also used to create very efficient HDS catalysts [51, 52].

The catalysts derived from I + II blends show a moderate activity enhancement up to the (Ni/Ni + Mo) ratio of 0.40. Then the well known synergistic effect of addition of Ni yields an increase of the catalyst activity at the ratio of 0.43. In the same direction the surface area and the pore volume follow this tendency. The selectivity of catalysts obtained by decomposition of I is directed to HYD while the blends and the catalysts obtained from II prefers the DDS path evidencing the nickel influence. These results are comparable to those reported in previous studies [22, 34]. The catalysts derived from decomposition of II and III show an important improvement of the activity by a factor of three compared with the catalyst generated only from II and almost twice the activity of a $NiMo/Al_2O_3$ industrial catalyst. This activity enhancement indicates that a chemical interaction between the precursors causes a better distribution of nickel in III + II blended catalysts, thus increasing the number of NiMoS active sites. The active sites for HDS reactions are recognized to be situated at the edges of

MoS_2 crystallites forming NiMoS sites [53]. Recently, studies with scanning tunneling microscopy of the Co-Mo-S structure of HDS catalysts have shown that in single layer Co-Mo-S nanosheets the Co atoms are preferably located at the S-edge of MoS_2 [54]. Unfortunately, no infrared data were included in this report for comparison with ours. Nevertheless, the results of the different characterizations of the present catalysts highly suggest that the *in-situ* method produces catalysts consisting of a very small number of Ni-Mo-S layers which show the Ni-Mo synergistic on carbosulfide phases during HDS reactions.

The Ni redistribution process among the II and III precursors can take place through two ways, i.e., by the precursor blending or an *in situ* decomposition of the precursors in the reaction media. The first pathway is controlled by the decomposition temperature while the second one is affected by the catalytic test conditions selected. The catalysts from mixtures of III and II precursors were prepared at a relatively low final decomposition temperature yielding materials with modest surface porosity. X-ray diffraction experiments of these samples indicate that no crystalline nickel sulfides are formed but some intense reflections occur which are related to the formation of a kind of hitherto unknown molybdenum carbide. Infrared spectra show a vibration band around 1630 cm^{-1} related to the nickel-molybdenum-carbon interactions, which is also observed in the fresh catalysts. Therefore, it is suggested that Ni was redistributed from precursor II to III during the blending process, which can be viewed as an advantage of the modified *in situ* method. The *in situ* activation can also contribute to improve the activity that is obvious from Figure 2. Most of the II + III blends exhibit an increased slope of DBT conversion vs. time for one or two hours after the reaction starts, indicating that more active sites are also formed during this time period. Besides the nickel redistribution in the catalysts obtained from III + II blends a complementary effect may cause an enhancement of the activity when the optimum distribution of mesopores is reached. These mesopores are provided by the simultaneous decomposition of precursors II and III generating an interconnected mesoporous network. In such optimized pore networks the DBT, BP and CHB molecules may diffuse more rapidly than in pores formed in single precursor catalysts. Confining effects that affect the selectivity of HDS of DBT have been suggested for mesoporous catalysts [11]. However, more studies about the distribution of mesopores are needed in order to support this supposed model.

It is known that the degree of stacking of MoS_2 layers influences the activity/selectivity of unsupported catalysts [55]. Multi-stacking has been related to the high activity of catalysts type II structure on alumina supports because of weak support interactions. However, it is possible to produce catalyst with single-slab type II Co-Mo-S structures [54]. Studies of WS_2

supported on graphite performed by high-angle annular dark-field scanning transmission electron microscopy (HAADF-STEM) imaging revealed that single-slab structures will have the advantage of making more rim sites available for the reaction [56]. For multi-stack structures, only the top layer will expose the rim sites, increasing the rate of the DDS pathway [7]. The results of the present studies show the preference of the DDS pathway and the production of single-slab catalysts consisting of Ni promoted moybdenum carbosulfides.

5. Conclusions

In the present study we demonstrated that the use of thiometallate blends in combination with the *in situ* activation method is a very promising method for the optimization of catalytic properties of Ni promoted molybdenum carbosulfide catalysts. These highly active catalysts are obtained by the thermal decomposition of blends of precursors $(NH_4)_2MoS_4$ (I), Ni(diethylentriamine)$_2MoS_4$ (II), and (Propyl$_4$N)$_2MoS_4$ (III).

The catalysts obtained from blends of precursors II and III exhibit an improved catalytic activity with a high selectivity for the DDS pathway due to the synergistic effect of nickel. The influence of the carbon content is clearly related with the enhancement of the activity and the preference of the DDS pathway, which both may be regarded as an evidence for the production of single-slab structure catalysts. The catalysts produced by controlled decomposition of III + II are threefold and twofold more active than the catalyst produced by decomposition of the pure precursor II and the industrial NiMo/Al_2O_3 catalyst, respectively. Such an improvement is attributed to the interaction of the precursors during the blending process that cause a re-dispersion of nickel atoms from precursor II over the surface of molybdenum carbosulfide provided by precursor III, increasing the amount of active sites. The HYD/DDS selectivity ratios of the catalysts from III + II blends are in-between to that of catalysts from the pure precursors II and III. The catalysts derived from blends of I and II present mainly an activity similar to the unblended precursors.

Acknowledgments

The authors are grateful to E. Flores, F. Ruiz, G. Vilchez for technical assistance. S. Fuentes acknowledges grants from PAPIIT-UNAM IN119602-3 and CONACYT 41331-Y. Financial support by the German Science Foundation (DFG) is gratefully acknowledged by W. Bensch and M. Poisot (Project: DFG BE 1653/11-2).

References

[1] P. Da Costa, J. M. Manoli, C. Potvin,G. D. Mariadassou, Catal. Today, 107 (2005) 520.

[2] N. Koizumi, Y. Urabe, K. Inamura, T. Itoh, M. Yamada, Catal. Today, 106 (2005) 211.

[3] H. Topsoe, B. S. Clausen, F. E. Massoth, in Catalysis-Science and Technology Vol. 11, eds. J.R. Anderson and M. Boudart, Springer Berlin, 1996.

[4] R. Prins, V. H. J. De Beer, G. A. Somorjai, Catal. Rev. Sci. Eng., 31 (1989) 1.

[5] F. L. Plantenga, R. Cerfontain, S. Eijsbouts, F. van Houtert, G. H. Anderson, S. Miseo, S. Soled, K. Riley, K. Fujita, Y. Inoue, Studies in Surface Science and Catalysis (2003), 145 (Science and Technology in Catalysis 2002), 407.

[6] T. Fujikawa, H. Kimura, K. Kiriyama, K. Hagirawa, Catal. Today, 111 (2006) 188.

[7] H. Topsoe, B. Hinnemann, J. K. Norskov, J. V. Lauritsen, F. Besenbacher, P. L. Hansen, G. Hytoft, R. G. Egeberg, K. G. Knudsen, Catal. Today, 107 (2005) 12.

[8] G. Hagenbach, Ph. Courty, B. Delmon, J. Catal. 31 (1973) 264.

[9] R. Candia, B.S. Clausen, H. Topsoe, J. Catal. 77 (1982) 564.

[10] M. Zdrazil, Catal. Today 3 (1988) 269.

[11] R. Frety, M. Breysse, M. Lacroix, M. Vrinat, Bull. Soc. Chim. Belg., 93 (1984) 663.

[12] K. Ramanathan, S. W. Weller, J. Catal., 95 (1985) 249.

[13] D. G. Kalthod, S. W. Weller, J. Catal., 95 (1985) 455.

[14] R. R. Chianelli, M. Daage, M. Ledoux, Adv. Catal., 40 (1994) 177.

[15] G. Alonso, M. Del Valle, J. Cruz-Reyes, V. Petranovskii, A. Licea-Claverie, S. Fuentes, Catal. Today, 43 (1998) 117.

[16] F. Pedraza, S. Fuentes, M. Vrinat, M. Lacroix, Catal.Lett., 62(1999)121.

[17] G. Alonso, R. R. Chianelli, S. Fuentes, US Patent 2005/005945 A1.

[18] A. W. Naumann, A. S. Behan, US Patent 4,243,554 (1981).

[19] R. R. Chianelli, T. A. Pecoraro, U.S. Patent 4,508,847 (1985).

[20] A. J. Jacobson, R. R. Chianelli, T. A. Pecoraro, US Patent 4,650,563 (1987).

[21] G. Alonso, V. Petranovskii, M. Del Valle, J. Cruz- Reyes, A. Licea-Claverie, S. Fuentes, Appl. Catal. A, 197 (2000) 87.

[22] G. Alonso, M. H. Siadati, G. Berhault, A. Aguilar, S. Fuentes, R. R. Chianelli, Appl. Catal. A, 263 (2004) 109.

[23] F. Pedraza, S. Fuentes, Catal. Lett., 65 (2000) 107.

[24] M. Poisot, W. Bensch, S. Fuentes, G. Alonso, Thermochim. Acta, 444 (2006) 35.

[25] G. Alonso, M. Del Valle, J. Cruz, A. Licea-Claverie, V. Petranovskii, S. Fuentes, Catal. Lett., 52, (1998), 55.

[26] D. J. Sajkowski, S. T. Oyama, Appl. Catal. A, 134 (1996) 339.

[27] D. D. Whitehurst, T. Isoda, I. Mochida, Adv. Catal., 42, (1998), 345.

[28] E. Olguin Orozco, M. Vrinat, Appl. Catal. A, 170 (1998) 195.

[29] H. Farag, I, Mochida, K. Sakanishi, Appl. Catal. A, 194 (2000) 147.

[30] B. Vogelaar, N. Kagami, A. D. van Langeveld, S. Eijsbouts, J. A. Moulijn, Prep. Pap.-Am. Chem. Soc., Div. Fuel Chem., 48 (2003) 548.

[31] M. Vrinat, M. Lacroix, M. Breysse, R. Frety, Bull. Soc. Chim. Belg., 93 (1984) 697.

[32] F. Zhang, P.T. Vasudevan, J. Catal., 157(1995) 536.

[33] R. R. Chianelli, G. Berhault, Catal. Today, 53 (1999) 357.

[34] G. Alonso, G. Berhault, A. Aguilar, V. Collins, C. Ornelas, S. Fuentes, R. R. Chianelli, J. Catal., 208 (2002) 359.

[35] E. J. M. Hensen, P. J. Kooyman, Y. van der Meer, A. M. van der Kraan, V. H. J. de Beer, J. A. R. van Veen, R. A. van Santen, J. Catal., 199 (2001) 224.

[36] H. Nava, C. Ornelas, A. Aguilar, G. Berhault, S. Fuentes, G. Alonso, Catal. Lett., 86 (2003) 257.

[37] K. Liang, R. R. Chianelli, F. Z. Chien, S. C. Moss, J. Non-Cryst. Solids, 79 (1986) 251.

[38] M. Kouzu, Y. Kuriki, F. Hamdy, K. Sakanishi, Y. Sugimoto, I. Saito, Appl. Catal. A, 265 (2004) 61.

[39] Modern Powder Diffraction in Reviews in Mineralogy Vol. 20, eds D. L. Bish, J. E. Post, Bookscrafters, Washington D. C. 1989.

[40] G. Berhault, A. Mehta, A. C. Pavel, J. Yang, L. Rendon, M. J. Yacaman, L. Cota Araiza, A. D. Moller, R. R. Chianelli, J. Catal., 198 (2001) 9.

[41] R. R. Chianelli, G. Berhault, P. Santiago, D. Mendoza, A. Espinoza, J. A. Ascencio, M. J. Yacaman, Mater. Tech., 15 (2000) 54.

[42] S. L. Gonzalez-Cortes, S. M. A. Rodulfo-Baechler, T. Xiao, M. L. Green, Catal. Lett., 111 (2006) 1.

[43] C. H. Chang, S. S. Chan, J. Catal., 72 (1981) 139.

[44] B. Krebs, G. Gattow, Z. Anorg. Allg. Chem., 338 (1963) 225.

[45] G. Berhault, L. Cota Araiza, A. Duarte Moller, A. Mehta, R. R. Chianelli, Catal. Lett., 78 (2002) 81.

[46] J. M. Manoli, P. Da Costa, M. Brun, M. Vrinat, F. Mauge, C. Potvin, J. Catal., 221 (2004) 365.

[47] E. Diemman, A. Müller, Coord. Chem. Rev., 10 (1973) 79.

[48] J. Brito, M. Ilija, P. Hernandez, Thermochim. Acta, 256 (1995) 325.

[49] P. Raybaud, J. Hafner, G. Kresse, H. Toulhoat, in Proc. 2nd Int. Symp. on Hydrotreatment and Hydrocraking of Oil Fractions, eds. B. Delmon, G.F. Froment and P. Grange (Elsevier, 1999) 309.

[50] J. V. Lauritsen, M. V. Bollinger, E. Laegsgaard, K. W. Jacobsen, J. K. Norskov, B. S. Clausen, H. Topsoe, F. Besenbacher, J. Catal., 221 (2004) 510.

[51] W. Eltzner, M Breysse, M. Lacroix, M. Vrinat, Polyhedron, 5 (1986) 203.

[52] E. I. Stiefel, W.H. Pan, R. R. Chianelli, T. C. Ho, US pat. 4,581,125 (1986).

[53] H. Topsoe, B.S. Clausen, N.Y. Topsoe, P. Zeuthen, Stud. Surf. Sci. Catal., 53 (1989) 77.

[54] J. V. Lauritsen, S. Helveg, E. Laegsgaard, I. Stensgaard, B. S. Clausen, H. Topsoe, F. Besenbacher, J. Catal., 197 (2001) 1.

[55] M. Daage, R. R. Chianelli, J. Catal., 149 (1994) 414.

[56] A. Carlson, M. Brorson, H. Topsoe, J. Catal., 227 (2004) 530.

[57] O. Monteiro, T. Trindade, Mater. Res. Bull., 39 (2004) 357.

3. Results

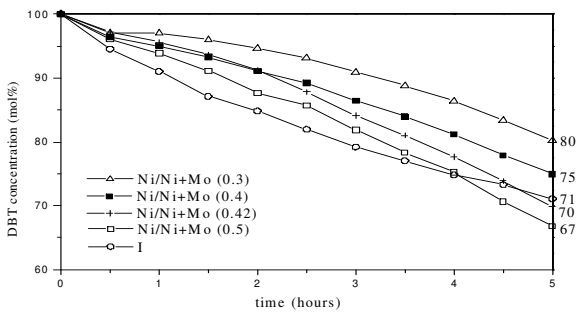

Figure 1 Time dependence of DBT change for catalysts obtained from I+II blends.

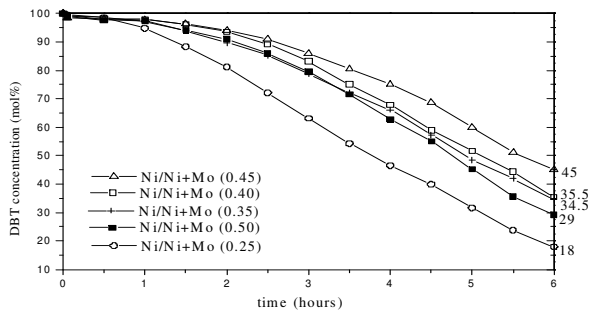

Figure 2 Time dependence of DBT change For catalysts obtained from III+II blends.

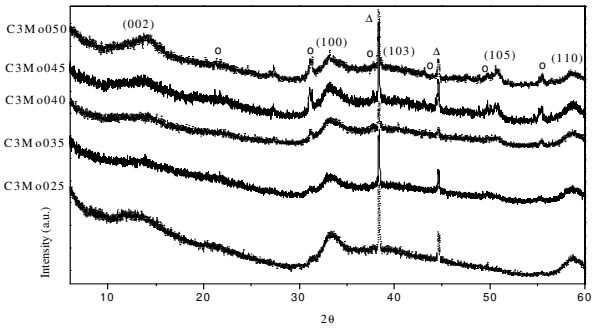

Figure 3 XRD patterns of III+II blends after blends after HDS of DBT.
(hkl) = MoS_2 (JCPDS, 37-1492)
o = Ni_3S_2 (JCPDS, 851802)
Δ = unknown.

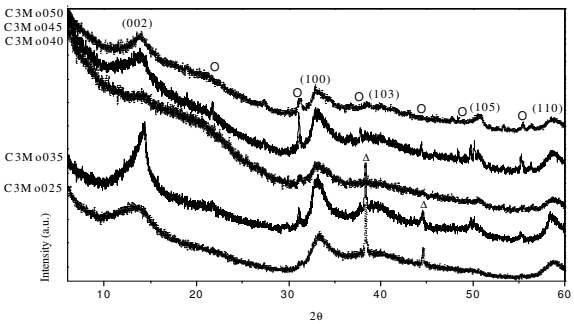

Figure 4 XRD patterns of III+II the HDS reaction and the thermal post- treatment to 500°C.
(hkl) = MoS_2 (JCPDS, 37-1492)
o = Ni_3S_2 (JCPDS, 851802)
Δ = unknown.

a b c

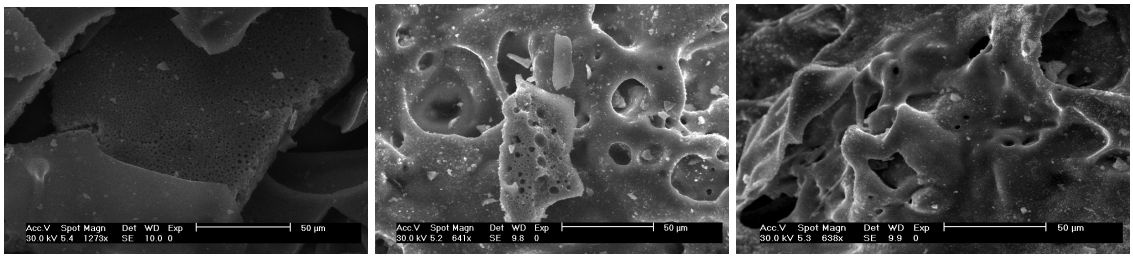

Figure 5 Scanning electron micrographs of the C3Mo035 catalyst, a) fresh; b) after HDS of DBT; c) after the thermal post-treatment to 500°C.

Table 1. Initial rate constants and selectivity, specific surface areas and total pore volume of catalysts obtained from I + II blends.

Catalyst	Ni/ Ni+Mo	k ($1*10^{-7}$) [mol s^{-1} g^{-1}]	HYD /DDS	Surface area (m^2/g)	Pore volume (cm^3/g)
I	-	4.8	1.68	9	0.023
I + II (1:1)	0.3	4.5	0.26	8	0.023
I + II (1:2)	0.4	4.7	0.29	22	0.063
I + II (1:3)	0.428	6.5	0.23	40	0.118
II	0.5	6.7	0.28	43	0.110

Table 2. Initial rate constants and selectivity, specific surface areas and total pore volume of catalysts obtained from III + II blends.

Catalyst	Ni/ Ni+Mo	k ($1*10^{-7}$) [mol s^{-1} g^{-1}]	HYD /DDS	Surface area (m^2/g)	Pore volume (cm^3/g)
III	-	4.7	2.04	46	0.017
C3Mo025	0.25	19	0.82	26	0.014
C3Mo035	0.35	18	0.73	142	0.075
C3Mo040	0.40	19	0.61	2	0.003
C3Mo045	0.45	16	0.60	27	0.016
C3Mo050	0.50	20	0.28	13	0.009

Table 3. Mass loss and chemical composition of catalysts from III + II blends after the thermal post-treatment to 500°C.

Catalyst	+Composition	Mass loss (%)
C3Mo025actTA	$MoS_{2.2}Ni_{0.2}C_{0.7}$	- 11
C3Mo035actTA	$MoS_{2.7}Ni_{0.7}C_{0.7}H_{0.5}$	- 10.6
C3Mo040actTA	$MoS_{2.5}Ni_{0.6}C_{0.8}$	- 12.9
C3Mo045actTA	$MoS_{2.8}Ni_{0.8}C_{0.7}$	- 10.6
C3Mo050actTA	$MoS_{2.7}Ni_{1.3}C_{0.6}$	- 8.7

+Calculated from EDX and CHNS as combination of atom %.

Table 4. Chemical composition of catalyst from III + II blends.

Catalyst	C	H	N	S	*Ni/ Mo	*S/ Mo	S	Mo	Ni	+Composition
			(wt %)					(wt	%)	
C3Mo025	19	2.1	7.2	26.4	0.29	1.55	30.6	58.6	10.8	$MoS_{1.5}Ni_{0.2}C_3N_{0.9}H_4$
C3Mo035	20	2.3	8.9	26.3	0.3	1.18	25	63	12	$MoS_{1.2}Ni_{0.2}C_{2.4}N_{0.9}H_{3.3}$
C3Mo040	19.9	2.4	10.3	26.3	0.38	1.43	27.8	58.3	13.9	$MoS_{1.4}Ni_{0.3}C_{2.8}N_{1.2}H_{4.2}$
C3Mo045	16	1.7	8.9	27.2	0.58	1.42	25.7	54.5	19.8	$MoS_{1.4}Ni_{0.5}C_{2.2}NH_{2.8}$
C3Mo050	15.1	1.7	8.6	27.8	0.53	1.36	25.5	56.2	18.3	$MoS_{1.3}Ni_{0.9}C_{1.9}N_{0.9}H_{2.6}$
C3Mo025act	8.4	1.3	0.4	34.2	0.39	2.7	41.8	46.5	11.7	$MoS_{2.7}Ni_{03}C_{1.7}H_{3.3}$
C3Mo035act	6.7	1.3	0.5	32.2	0.75	3.14	41.5	39.9	18.6	$MoS_{3.2}Ni_{0.7}C_{1.5}H_{4.1}$
C3Mo040act	8.7	1.3	0.4	33.6	0.52	2.5	38.5	46.4	15.1	$MoS_{2.5}Ni_{0.5}C_{1.7}H_{3.1}$
C3Mo045act	6.5	0.9	0.5	34.3	0.93	2.51	34.9	41.4	23.7	$MoS_{2.5}Ni_{0.9}C_{1.2}H_{2.1}$
C3Mo050act	5.4	0.8	0.4	34.9	1.17	3.94	43.1	33.4	23.5	$MoS_{2.6}Ni_{1.4}CH_2$

* Calculated from EDX data as atom %.
+ Calculated from EDX and CHNS as combination of atom %.
act = after catalytic test, actTA = thermal analysis after catalytic test.

Table 5. IR data in cm^{-1} of catalysts obtained from III + II blends

Sample	ν Mo-S(orth c) [40, 57]	ν C_xS_n [45]	ν Ni-Mo-C [46]
C3Mo025act	383	1127	1625
C3Mo035act	382	1082	1633
C3Mo040act	381	1120	1626
C3Mo045act	375	1119	1629
C3Mo050act	382	---	1628
C3Mo025actTA	383	1082	1635
C3Mo035actTA	383	1138	1636
C3Mo040actTA	383	---	1630
C3Mo045actTA	382	1092	1630
C3Mo050actTA	383	1093	1629

4. Conclusions

Several conclusions can be derived from the results obtained in this work.

1. The synthesis of tetraalkylammonium tetrathiomolybdates and tetrathiotungstates $(R_4N)_2MS_4$ (M = Mo, W) via the direct salt substitution approach using $(NH_4)_2MS_4$ as starting materials and a tetraalkylammonium salt yields phase pure products with high yields and crystals are formed which are suitable for the structure determination.
2. The results of the single crystal X-ray work of the tetraalkylammonium precursors demonstrate that the size of the alkyl chain is related to the partial positional disorder of the cations. An interesting observation is that in the compounds with longer alkyl chains the cations show no positional disorder whereas those with shorter alkyl chains display a pronounced disorder.
3. The IR and Raman study of the compounds give evidences for the influence of the alkyl chain size onto the frequency of the main M-S vibrations (M = Mo, W). With increasing alkyl chain length the bands shift gradually to lower energies which may be interpreted in terms of decreasing electropositivity with increasing bulkiness of the alkyl ammonium ion.
4. In the tetraalkylammonium compounds the thiometallate ions are less distorted than in compounds where N-H atoms can form hydrogen bonds to the S atoms of the anion. Therefore, no splitting of the M-S vibrations occurs in the Raman or IR spectra.
5. The thermal behavior of the molybdenum and tungsten containing precursors is very similar. With increasing size of the alkylammonium ion the decomposition mechanism becomes more complex reflecting the strong influence of the alkyl chain length. The mass spectroscopic investigations of the thermal reactions allowed the formulation of a general decomposition route. For all compounds a simultaneous emission of trialkylamines and dialkyldisulfides is observed. In addition, porous MoS_2 products are obtained for precursors with bulky alkylammonium ions. Interestingly, for the tetrathiotungstates such a porous material is observed only for R = heptyl.
6. During the decomposition reactions no sulfur-rich intermediates are formed in contrast to the decomposition of $(NH_4)_2MS_4$ where MS_3 occurs as an intermediate. For R = methyl to pentyl the final decomposition products are nearly stoichiometric disulfides being slight contaminated with C, N, and H. The amount of the contaminants increases with increasing amount of these elements in the starting materials. For R = hexyl and heptyl the final decomposition products have a M:S ratio below 1:2 and very high C and H contents. These products may be better described as carbosulfides where S atoms are partially substituted by C atoms.

4. Conclusions

7. DSC combined with thermodiffractometry revealed that several compounds with small tetraalkylammonium ions undergo structural phase transitions which are in part reversible. For the samples with the larger cations phase transitions are irreversible or glass-like transitions occur before the decomposition starts.
8. The controlled thermal decomposition of mixtures of of Ni(diethylenetriamine)$_2$MoS$_4$ and (propyl$_4$N)$_2$MoS$_4$ yields very active nickel promoted catalysts without an activation step during the HDS of DBT. These catalysts are twofold more active than the commercial alumina supported molybdenum catalyst.
9. A moderate carbon content in the catalysts leads to higher catalytic activity due to the formation of single-slabs of nickel promoted molybdenum carbosulfides enabling the creation of more NiMoS active sites.
10. In the HDS of DBT the nickel promoted catalyst preferred the DDS pathway due to the synergistic effect of the promoter.

5.1 Methods

Several characterisation methods were used in this work to study the features of the materials obtained. The reader is remitted to the extended literature to obtain a proper explanation of the methods used.

5.1.1 Chemical elemental analysis

Chemical elemental analyses were performed on a EURO Vector EURO EA combustion analyzer; using zinc sample holders with 2-3 mg pro sample, heated up to 1000°C under oxygen atmosphere and the gases were then detected by a thermal conductivity system using helium 5.0.

5.1.2 FIR, MIR and FT-Raman spectroscopy [1]

Far Infrared spectra were measured using a Bruker IFS66 instrument, the samples were prepared in a polyethylene matrix. Range 80 - 500 cm^{-1} with precision of 1 cm^{-1}. Medium Infrared spectra were collected with an ATI Mattson Genesis instrument using KBr matrix to prepare the sample. Range 400 – 4000 cm^{-1} with precision of 1 cm^{-1}. FT-Raman spectra were measured with a Bruker RSA 106 spectrometer with laser of Nd/YAG (1064 nm). The precision is 2 cm^{-1}.

5.1.3 X-Ray powder diffraction [2, 3]

X-Ray powder diffraction was performed with a STOE STADI-P instrument (Fig. 5.1) operating with Cu $K\alpha_1$ radiation (1.54056 Å) with a position sensitive detector. The collected data were processed with the STOE WIN "X^{POW}" software.

Fig. 5.1 STOE STADI-P X-Ray diffractometer.

5.1.4 Single crystal diffraction [4, 5]

The diffractometers used are STOE AED II, equipped with Mo Kα radiation (0.71073 Å) and graphic monochromator, and STOE IPDS also equipped with Mo Kα radiation. The programs

used to solve structure are *SHELXS97* and to refine structure are *SHELXL97* [6]. Graphics were done with the Diamond 2.1c [7] software. *XCIF* in *SHELXT* was used to prepare the material for publication. The database of the International Union of Crystallography was consulted as well as the Inorganic Crystal Structure Database: http://icsd-db.uni-kiel.de/icsd/index.php.

5.1.5 Thermogravimetry, differential thermal analysis coupled with mass spectrometry [8-10]

DTA-TG and measurements coupled with Mass Spectrometry (MS) were performed using a NETZSCH STA-409CD device with Skimmer coupling, equipped with a BALZERS quadrupole mass spectrometer QMA 400 (max. 512 amu) (Fig.5.2). For DTA-TG experiments alumina crucibles were used under a dynamic nitrogen atmosphere (flow rate: 75 mL/min., purity 5.0). The TG curve of an empty crucible was measured under the same experimental conditions and the effects of gas flow and buoyancy were corrected automatically with the evaluation software. DTA-TG-MS measurements were performed under a dynamic helium atmosphere (flow rate: 50 mL/min., purity 5.6). The National Institute of Standards and Technology (NIST) (http://webbook.nist.gov/chemistry) data were used for comparison with the spectra obtained in the same way like data from the National Institute of Advanced Industrial Science and Technology (SDBSWeb : http://www.aist.go.jp/RIODB/SDBS/).

Fig. 5.2 NETZSCH STA-409CD DTA-TG-MS.

Fig. 5.3 Oven for diffractometry.

5.1.6 Thermodiffractometry [11]

The collection of powder patterns with a programmed temperature was done with the STOE STADI-P instrument (see above), equipped with a graphite-high-temperature oven (Fig. 5.3). The data were processed with the STOE WIN "X^{POW}" software.

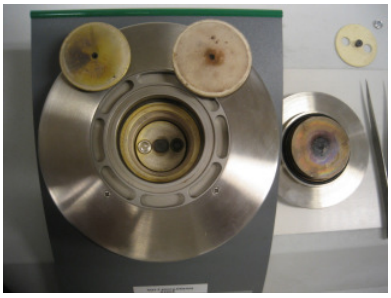

Fig. 5.4 NETZSCH DSC 204 Phoenix.

5.1.7 Differential scanning calorimetry [12]

DSC experiments were performed with a NETZSCH DSC 204 Phoenix device using aluminium crucibles toped with an aluminium lid and pressed. In some cases sealed glass ampoules filled with argon were also used. Protective atmosphere of nitrogen (30 mL/min) was applied, see Fig. 5.4.

5.1.8 Scanning electron microscopy [13]

Imaging of the morphology of the samples and energy dispersive X-ray analysis (EDX) for semiquantitative elemental analysis were performed with a Philips ESEM XL 30 scanning electron microscope equipped with an EDAX analyzer (Fig. 5.5) and operated at 30 kV. The lines of Mo L, S K, Ni K and Co K were considered and the precision is 3%.

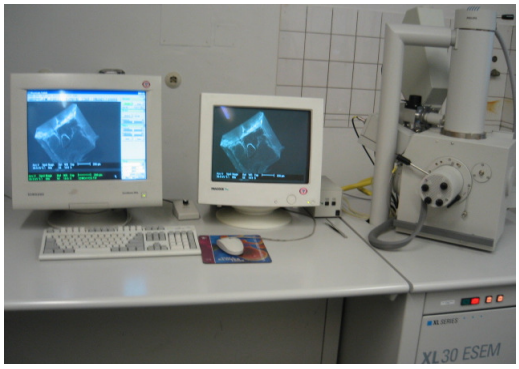

Fig. 5.5 Scanning electron microscope Philips ESEM XL 30.

5.1.9 Catalytic activity test of HDS of DBT [14]

The reaction was carried out in a Parr model 4522 high-pressure batch reactor. About 1 g of the catalyst and 75 ml of a freshly prepared solution of DBT in decaline (5% wt/wt.) were placed in the reactor. The reactor was then purged and pressurized with H_2 to 3.37 MPa and heated up to 623 K at 10 K/min heating rate, see Fig. 5.6. When the working temperature was reached, the evolved gaseous samples were collected for chromatographic analysis every half an hour to determine conversion vs. time dependence. A Perkin Elmer gas chromatograph

model Auto-System XL with a 9 ft long, 1/8 inch packed column containing OV-3 (phenyl-methyl-dimethyl silicone, 10% phenyl) as separating phase was used to analyse the collected gases. These equipments belong to the Center of advanced materials research, CIMAV, in Chihuahua, Mexico.

Fig. 5.6 Reactor Parr model 4522.

Fig. 5.7 Quantachrome AUTOSORB-1.

5.1.10 Surface area and pore size determination [14]

Specific surface area determinations were performed with a Quantachrome AUTOSORB-1 (Fig. 5.7) by nitrogen adsorption at 77K using the BET isotherm. Samples were degassed under flowing Argon at 473 K for 2h before nitrogen adsorption. The pore distribution was obtained from the desorption isotherm following the BJH method. The mean standard deviation for surface area measurements is about 2%. These last two instruments belong to the Center of Advanced Materials Research, CIMAV, in Chihuahua, Mexico.

Fig. 5.8 Sample of promoted/umpromoted MoS_2 catalyst.

5.1.11 Rotating sample oven

The syntheses of the catalysts were carried out placing the samples directly in a rotating glass tube (300 rpm) adapted for a Gero SR oven with an Eurotherm controller under N_2

atmosphere. The catalysts obtained look like the sample shown in Fig. 5.8. The oven can be seen in Fig. 5.9.

Fig. 5.9 Gero SR oven adapted to rotate a sample.

5.2 Chemicals used

Chemical	Purity	Maker
Ammoniac 25% in H_2O	Technical grade	Merck
Ammoniumheptamolybdate · $4H_2O$	p.a.	Merck
Cobalt(II) chloride· $6H_2O$	Reagent grade	Merck
Dibenzothiophene	98%	Aldrich
Diethylenetriamine	97%	Fluka
Decahydronaphthalene (Decalin, cis +trans)	98 %	Aldrich
Ethanol	Technical grade	Merck
Hydrogen	4.5	Praxair
Hydrogen sulfide	2.0	Messer-Griesheim
Nickel bromide hydrate	98%	Aldrich
Nitrogen	ten ppm	Messer-Griesheim
Sodium hydroxide	Reagent grade	Merck
Tetrabutylammonium bromide	≥ 98%	Fluka
Tetraethylammonium bromide	≥ 99%	Fluka
Tetraheptylammonium bromide	≥ 99%	Fluka
Tetrahexylammonium bromide	≥ 99%	Fluka
Tetramethylammonium bromide	> 99%	Fluka
Tetrapentylammonium bromide	≥ 99%	Fluka
Tetrapropylammonium bromide	≥ 98%	Fluka
Tungstic acid	99%	ABCR

5.3 Details of single crystal structures determination

Bis(tetramethylammonium) tetrathiomolybdate

Table 1. Crystal data and structure refinement for bis(tetramethylammonium) tetrathiomolybdate.

Identification code	mp299	
Empirical formula	$C_8H_{24}MoN_2S_4$	
Formula weight	372.47	
Temperature	293(2) K	
Wavelength	0.71073 Å	
Crystal system	Orthorhombic	
Space group	$P2_12_12_1$	
Unit cell dimensions	a = 8.9233(4) Å	α= 90°.
	b = 15.5210(9) Å	β= 90°.
	c = 37.255(3) Å	γ = 90°.
Volume	5159.8(5) $Å^3$	
Z	12	
Density (calculated)	1.438 Mg/m^3	
Absorption coefficient	1.227 mm^{-1}	
F(000)	2304	
Crystal size	0.15 x 0.12 x 0.12 mm^3	
Theta range for data collection	1.71 to 22.34°.	
Index ranges	-9<=h<=9, -16<=k<=16, -39<=l<=39	
Reflections collected	32907	
Independent reflections	6589 [R(int) = 0.0436]	
Completeness to theta = 22.34°	99.3 %	
Refinement method	Full-matrix least-squares on F^2	
Data / restraints / parameters	6589 / 0 / 398	
Goodness-of-fit on F^2	1.083	
Final R indices [I>2sigma(I)]	R1 = 0.0328, wR2 = 0.0817	
R indices (all data)	R1 = 0.0430, wR2 = 0.0865	
Absolute structure parameter	0.0(10)	
Extinction coefficient	0.00091(12)	
Largest diff. peak and hole	0.414 and -0.455 e.$Å^{-3}$	

Table 2. Atomic coordinates (x 10^4) and equivalent isotropic displacement parameters ($Å^2$x 10^3).
U(eq) is defined as one third of the trace of the orthogonalized U_{ij} tensor.

	x	y	z	U(eq)
Mo(1)	7893(1)	8469(1)	5806(1)	33(1)
S(1)	9755(3)	9266(2)	5985(1)	71(1)
S(2)	7875(3)	8435(2)	5225(1)	81(1)
S(3)	8150(2)	7167(1)	6018(1)	66(1)
S(4)	5766(3)	8994(2)	5992(1)	81(1)
Mo(2)	2382(1)	6563(1)	7521(1)	40(1)
S(5)	2375(5)	7878(2)	7318(1)	125(1)
S(6)	4233(3)	5865(2)	7287(1)	81(1)
S(7)	285(3)	5936(2)	7377(1)	85(1)
S(8)	2602(3)	6562(2)	8102(1)	69(1)
Mo(3)	2707(1)	3458(1)	5859(1)	37(1)
S(9)	507(3)	3965(2)	5715(1)	74(1)
S(10)	4467(3)	4274(2)	5636(1)	75(1)
S(11)	2946(2)	2157(2)	5641(1)	65(1)
S(12)	2959(2)	3440(2)	6440(1)	66(1)
N(1)	7387(8)	8415(5)	7152(2)	48(2)
C(1)	7379(12)	8460(7)	7549(3)	94(3)
C(2)	7753(12)	7512(7)	7031(3)	74(6)
C(3)	5790(30)	8703(16)	7051(7)	105(8)
C(4)	8480(20)	9012(11)	6977(5)	60(4)
C(2')	6970(20)	7557(12)	7016(6)	67(5)
C(3')	6480(30)	9043(17)	6987(7)	115(9)

C(4')	9000(20)	8621(15)	7038(6)	98(7)
N(2)	2853(6)	9258(4)	5029(2)	39(2)
C(5)	1850(20)	9231(12)	4708(5)	98(5)
C(6)	2775(18)	10217(10)	5088(5)	76(5)
C(7)	4386(16)	9054(10)	4925(4)	73(4)
C(8)	2319(18)	8582(12)	5292(5)	89(5)
C(5')	1200(30)	8935(16)	4922(7)	79(7)
C(6')	2830(20)	10000(13)	5286(6)	62(6)
C(7')	3670(40)	9330(20)	4685(9)	134(12)
C(8')	3390(40)	8650(20)	5272(10)	135(12)
N(3)	7698(7)	1624(4)	5483(2)	43(2)
C(9)	7233(12)	2506(6)	5381(3)	79(3)
C(10)	6592(12)	996(6)	5311(3)	74(3)
C(11)	7615(12)	1532(7)	5884(3)	85(3)
C(12)	9204(10)	1426(9)	5371(3)	102(4)
N(4)	7733(8)	4258(4)	6638(2)	51(2)
C(13)	9296(10)	3981(8)	6765(3)	97(4)
C(14)	7251(13)	3634(9)	6379(4)	121(5)
C(15)	6735(15)	4327(10)	6929(4)	127(6)
C(16)	7909(16)	5109(7)	6445(5)	136(6)
N(5)	-2220(7)	8372(5)	3829(2)	50(2)
C(17)	-2474(13)	8427(8)	4224(3)	98(4)
C(18)	-680(10)	8648(9)	3731(3)	102(4)
C(19)	-2530(14)	7491(6)	3701(3)	90(4)
C(20)	-3231(12)	8976(7)	3653(3)	83(3)
N(6)	2468(8)	765(4)	6699(2)	48(2)
C(21)	3617(16)	738(10)	6390(4)	132(6)
C(22)	2222(12)	-109(7)	6839(4)	100(4)
C(23)	3135(12)	1364(8)	6978(3)	116(5)
C(24)	1094(10)	1110(7)	6580(3)	88(3)

Table 3. Bond lengths [Å] and angles [°].

Mo(1)-S(2)	2.166(3)	C(1)-N(1)-C(4)	114.2(10)
Mo(1)-S(1)	2.175(2)	C(3')-N(1)-C(2)	129.5(13)
Mo(1)-S(4)	2.178(3)	C(2')-N(1)-C(2)	27.3(8)
Mo(1)-S(3)	2.182(2)	C(1)-N(1)-C(2)	110.2(8)
Mo(2)-S(6)	2.159(3)	C(4)-N(1)-C(2)	107.7(9)
Mo(2)-S(8)	2.172(2)	C(3')-N(1)-C(4')	105.9(16)
Mo(2)-S(7)	2.177(3)	C(2')-N(1)-C(4')	109.2(13)
Mo(2)-S(5)	2.177(3)	C(1)-N(1)-C(4')	105.8(11)
Mo(3)-S(12)	2.177(3)	C(4)-N(1)-C(4')	30.4(10)
Mo(3)-S(9)	2.182(2)	C(2)-N(1)-C(4')	84.7(11)
Mo(3)-S(10)	2.183(2)	C(3')-N(1)-C(3)	32.8(14)
Mo(3)-S(11)	2.186(2)	C(2')-N(1)-C(3)	86.9(12)
N(1)-C(3')	1.41(3)	C(1)-N(1)-C(3)	103.1(12)
N(1)-C(2')	1.47(2)	C(4)-N(1)-C(3)	108.4(13)
N(1)-C(1)	1.479(11)	C(2)-N(1)-C(3)	113.4(11)
N(1)-C(4)	1.495(18)	C(4')-N(1)-C(3)	137.6(14)
N(1)-C(2)	1.508(13)	C(8')-N(2)-C(7')	117(2)
N(1)-C(4')	1.53(2)	C(7)-N(2)-C(7')	47.6(15)
N(1)-C(3)	1.54(2)	C(8')-N(2)-C(5)	135.1(17)
N(2)-C(8')	1.39(3)	C(7)-N(2)-C(5)	110.1(11)
N(2)-C(7)	1.456(15)	C(7')-N(2)-C(5)	66.5(17)
N(2)-C(7')	1.48(3)	C(8')-N(2)-C(6')	96.3(17)
N(2)-C(5)	1.49(2)	C(7)-N(2)-C(6')	110.4(11)
N(2)-C(6')	1.50(2)	C(7')-N(2)-C(6')	120.0(17)
N(2)-C(6)	1.505(17)	C(5)-N(2)-C(6')	121.7(12)

N(2)-C(8)	1.512(19)	C(8')-N(2)-C(6)	126.2(17)
N(2)-C(5')	1.61(2)	C(7)-N(2)-C(6)	107.3(10)
N(3)-C(12)	1.440(11)	C(7')-N(2)-C(6)	94.0(16)
N(3)-C(9)	1.481(11)	C(5)-N(2)-C(6)	96.7(11)
N(3)-C(11)	1.502(12)	C(6')-N(2)-C(6)	31.4(9)
N(3)-C(10)	1.527(11)	C(8')-N(2)-C(8)	38.6(15)
N(4)-C(15)	1.406(12)	C(7)-N(2)-C(8)	108.5(10)
N(4)-C(14)	1.434(12)	C(7')-N(2)-C(8)	140.5(16)
N(4)-C(16)	1.513(12)	C(5)-N(2)-C(8)	108.1(11)
N(4)-C(13)	1.535(11)	C(6')-N(2)-C(8)	96.7(12)
N(5)-C(20)	1.456(12)	C(6)-N(2)-C(8)	125.3(11)
N(5)-C(19)	1.474(12)	C(8')-N(2)-C(5')	105.5(18)
N(5)-C(18)	1.485(11)	C(7)-N(2)-C(5')	136.7(12)
N(5)-C(17)	1.493(12)	C(7')-N(2)-C(5')	105.1(18)
N(6)-C(24)	1.410(11)	C(5)-N(2)-C(5')	40.9(11)
N(6)-C(22)	1.469(11)	C(6')-N(2)-C(5')	112.7(12)
N(6)-C(23)	1.517(12)	C(6)-N(2)-C(5')	107.6(11)
N(6)-C(21)	1.542(12)	C(8)-N(2)-C(5')	69.8(11)
S(2)-Mo(1)-S(1)	108.96(12)	C(12)-N(3)-C(9)	112.6(9)
S(2)-Mo(1)-S(4)	108.65(12)	C(12)-N(3)-C(11)	108.3(8)
S(1)-Mo(1)-S(4)	110.87(12)	C(9)-N(3)-C(11)	109.2(8)
S(2)-Mo(1)-S(3)	109.86(13)	C(12)-N(3)-C(10)	110.2(8)
S(1)-Mo(1)-S(3)	109.64(10)	C(9)-N(3)-C(10)	107.6(7)
S(4)-Mo(1)-S(3)	108.84(11)	C(11)-N(3)-C(10)	108.8(8)
S(6)-Mo(2)-S(8)	109.44(11)	C(15)-N(4)-C(14)	112.4(10)
S(6)-Mo(2)-S(7)	109.53(12)	C(15)-N(4)-C(16)	111.5(10)
S(8)-Mo(2)-S(7)	108.85(11)	C(14)-N(4)-C(16)	107.4(10)
S(6)-Mo(2)-S(5)	109.41(15)	C(15)-N(4)-C(13)	111.0(10)
S(8)-Mo(2)-S(5)	110.29(13)	C(14)-N(4)-C(13)	106.9(8)
S(7)-Mo(2)-S(5)	109.32(15)	C(16)-N(4)-C(13)	107.3(9)
S(12)-Mo(3)-S(9)	110.06(9)	C(20)-N(5)-C(19)	109.6(8)
S(12)-Mo(3)-S(10)	108.18(10)	C(20)-N(5)-C(18)	106.1(9)
S(9)-Mo(3)-S(10)	110.12(12)	C(19)-N(5)-C(18)	111.2(9)
S(12)-Mo(3)-S(11)	110.34(11)	C(20)-N(5)-C(17)	108.1(9)
S(9)-Mo(3)-S(11)	109.22(10)	C(19)-N(5)-C(17)	110.2(8)
S(10)-Mo(3)-S(11)	108.90(11)	C(18)-N(5)-C(17)	111.5(8)
C(3')-N(1)-C(2')	109.2(15)	C(24)-N(6)-C(22)	109.4(8)
C(3')-N(1)-C(1)	113.6(13)	C(24)-N(6)-C(23)	108.9(8)
C(2')-N(1)-C(1)	112.7(10)	C(22)-N(6)-C(23)	112.5(9)
C(3')-N(1)-C(4)	75.9(14)	C(24)-N(6)-C(21)	110.7(9)
C(2')-N(1)-C(4)	125.1(12)	C(22)-N(6)-C(21)	109.8(9)
C(8')-N(2)-C(7)	72.5(15)	C(23)-N(6)-C(21)	105.5(9)

Table 4. Anisotropic displacement parameters ($Å^2 x\ 10^3$).

The anisotropic displacement factor exponent takes the form: $-2\pi^2[\ h^2\ a^{*2}U_{11} + \ldots\ + 2\ h\ k\ a^*\ b^*\ U_{12}]$

	U_{11}	U_{22}	U_{33}	U_{23}	U_{13}	U_{12}
Mo(1)	28(1)	35(1)	35(1)	-3(1)	0(1)	0(1)
S(1)	72(2)	57(1)	84(2)	-9(1)	-23(1)	-24(1)
S(2)	101(2)	104(2)	37(1)	-8(1)	-4(1)	4(2)
S(3)	56(1)	45(1)	98(2)	19(1)	-5(1)	-2(1)
S(4)	53(1)	89(2)	101(2)	-10(2)	21(1)	21(1)
Mo(2)	47(1)	36(1)	37(1)	0(1)	3(1)	5(1)
S(5)	232(4)	45(1)	99(2)	21(1)	2(3)	6(2)
S(6)	72(2)	101(2)	70(2)	-11(1)	21(1)	33(1)
S(7)	53(2)	126(2)	77(2)	-17(2)	-10(1)	-19(1)
S(8)	70(1)	99(2)	39(1)	-4(1)	-1(1)	0(2)
Mo(3)	40(1)	37(1)	35(1)	1(1)	5(1)	0(1)
S(9)	69(2)	94(2)	59(2)	0(1)	0(1)	36(1)
S(10)	79(2)	68(2)	78(2)	6(1)	21(1)	-26(1)
S(11)	71(1)	46(1)	77(2)	-17(1)	-1(1)	2(1)
S(12)	69(1)	91(2)	39(1)	2(1)	0(1)	-2(2)
N(1)	46(3)	54(4)	44(4)	12(3)	4(3)	6(4)
C(1)	127(9)	102(8)	53(7)	-11(6)	-33(7)	1(8)
N(2)	27(3)	41(3)	51(4)	-3(3)	6(3)	0(2)

N(3)	39(3)	45(3)	43(4)	-2(3)	0(3)	3(3)
C(9)	85(7)	61(6)	92(8)	23(5)	-10(6)	-2(5)
C(10)	80(6)	68(6)	76(7)	-17(5)	-16(5)	-25(5)
C(11)	117(7)	80(7)	58(7)	-8(5)	29(6)	10(7)
C(12)	51(5)	145(10)	111(9)	-5(7)	11(5)	16(6)
N(4)	63(4)	37(3)	54(5)	5(3)	16(3)	11(3)
C(13)	46(5)	133(9)	112(9)	13(6)	-21(5)	24(5)
C(14)	130(9)	139(11)	93(9)	-30(7)	-12(7)	-79(8)
C(15)	112(9)	141(10)	128(11)	0(8)	93(9)	37(8)
C(16)	150(13)	69(7)	188(16)	74(9)	25(10)	14(7)
N(5)	48(4)	51(4)	50(4)	4(4)	5(3)	1(4)
C(17)	125(8)	121(10)	47(7)	0(8)	-13(7)	-27(8)
C(18)	48(5)	170(12)	88(7)	6(7)	12(5)	-33(6)
C(19)	110(8)	55(6)	105(10)	-11(6)	19(7)	-6(6)
C(20)	60(6)	84(6)	105(8)	17(6)	-15(5)	16(5)
N(6)	40(3)	48(4)	57(5)	12(3)	-12(3)	-1(3)
C(21)	139(11)	135(10)	122(11)	17(8)	95(9)	43(8)
C(22)	83(8)	80(7)	136(11)	57(7)	3(6)	-9(5)
C(23)	109(8)	158(11)	80(7)	-16(7)	-25(6)	-69(8)
C(24)	57(5)	81(6)	126(9)	-13(6)	-23(5)	2(4)

Table 5. Coordinates of H atoms (x 10^4) and isotropic displacement parameters (Å^2 x 10^3).

	x	y	z	U(eq)
H(1A)	8345	8295	7639	141
H(1B)	6630	8076	7642	141
H(1C)	7158	9038	7623	141
H(1D)	6393	8330	7636	141
H(1E)	7660	9029	7624	141
H(1F)	8080	8050	7644	141
H(2A)	7063	7114	7139	111
H(2B)	8756	7369	7102	111
H(2C)	7672	7478	6774	111
H(3A)	5078	8326	7162	158
H(3B)	5679	8683	6795	158
H(3C)	5633	9282	7134	158
H(4A)	8425	8945	6721	90
H(4B)	9475	8878	7058	90
H(4C)	8240	9596	7040	90
H(2D)	7618	7130	7119	101
H(2E)	7071	7548	6759	101
H(2F)	5951	7434	7080	101
H(3D)	6744	9603	7076	173
H(3E)	5445	8928	7040	173
H(3F)	6626	9025	6732	173
H(4D)	9671	8208	7142	147
H(4E)	9261	9189	7118	147
H(4F)	9073	8595	6781	147
H(5A)	843	9364	4779	147
H(5B)	1880	8666	4604	147
H(5C)	2185	9647	4535	147
H(6A)	1774	10374	5156	114
H(6B)	3040	10509	4870	114
H(6C)	3460	10378	5275	114
H(7A)	4738	9474	4756	110
H(7B)	4413	8493	4817	110
H(7C)	5016	9059	5134	110
H(8A)	1306	8706	5362	134
H(8B)	2952	8586	5500	134
H(8C)	2360	8025	5180	134
H(5D)	776	9321	4749	118
H(5E)	579	8924	5133	118
H(5F)	1258	8366	4822	118
H(6D)	2511	10511	5162	92
H(6E)	3819	10087	5381	92
H(6F)	2150	9877	5478	92

H(7D)	3206	9772	4540	201
H(7E)	3629	8793	4560	201
H(7F)	4691	9485	4731	201
H(8D)	2789	8660	5485	202
H(8E)	4412	8787	5333	202
H(8F)	3353	8088	5166	202
H(9A)	6215	2600	5455	119
H(9B)	7309	2572	5125	119
H(9C)	7873	2918	5497	119
H(10A)	5591	1141	5384	112
H(10B)	6820	420	5388	112
H(10C)	6669	1031	5055	112
H(11A)	6615	1656	5963	128
H(11B)	8302	1927	5994	128
H(11C)	7876	953	5950	128
H(12A)	9452	849	5442	153
H(12B)	9889	1822	5481	153
H(12C)	9275	1475	5114	153
H(13A)	9960	3948	6563	145
H(13B)	9233	3427	6879	145
H(13C)	9674	4396	6934	145
H(14A)	7958	3613	6185	181
H(14B)	6284	3793	6288	181
H(14C)	7190	3078	6491	181
H(15A)	7111	4742	7097	191
H(15B)	6643	3777	7045	191
H(15C)	5771	4509	6843	191
H(16A)	8599	5041	6249	203
H(16B)	8286	5534	6608	203
H(16C)	6954	5291	6353	203
H(17A)	-1818	8032	4345	147
H(17B)	-3497	8282	4277	147
H(17C)	-2272	9003	4305	147
H(18A)	35	8269	3841	152
H(18B)	-514	9226	3814	152
H(18C)	-565	8628	3475	152
H(19A)	-1866	7094	3817	135
H(19B)	-2378	7465	3446	135
H(19C)	-3549	7342	3755	135
H(20A)	-3023	9550	3736	124
H(20B)	-4249	8829	3711	124
H(20C)	-3089	8948	3398	124
H(21A)	4545	504	6477	198
H(21B)	3783	1312	6302	198
H(21C)	3238	383	6200	198
H(22A)	3157	-344	6921	149
H(22B)	1821	-467	6652	149
H(22C)	1527	-87	7036	149
H(23A)	4073	1135	7061	173
H(23B)	2458	1416	7177	173
H(23C)	3297	1922	6873	173
H(24A)	1258	1675	6483	132
H(24B)	409	1146	6778	132
H(24C)	680	744	6398	132

Bis(tetrapropylammonium) tetrathiomolybdate

Table 1. Crystal data and structure refinement for bis(tetrapropylammonium) tetrathiomolybdate.

Identification code	mp300	
Empirical formula	$C_{24}H_{56}MoN_2S_4$	
Formula weight	596.89	
Temperature	293(2) K	
Wavelength	0.71073 Å	
Crystal system	monoclinic	
Space group	C2/c	
Unit cell dimensions	a = 32.334(4) Å	α= 90°.
	b = 13.812(2) Å	β= 109.239(15)°.
	c = 15.017(3) Å	γ = 90°.
Volume	6331.7(18) $Å^3$	
Z	8	
Density (calculated)	1.252 Mg/m^3	
Absorption coefficient	0.692 mm^{-1}	
F(000)	2560	
Crystal size	0.8 x 0.35 x 0.15 mm^3	
Theta range for data collection	2.49 to 28.01°.	
Index ranges	-42<=h<=40, -18<=k<=12, 0<=l<=19	
Reflections collected	14412	
Independent reflections	7657 [R(int) = 0.0395]	
Completeness to theta = 28.01°	99.9 %	
Refinement method	Full-matrix least-squares on F^2	
Data / restraints / parameters	7657 / 0 / 318	
Goodness-of-fit on F^2	0.977	
Final R indices [I>2sigma(I)]	R1 = 0.0305, wR2 = 0.0674	
R indices (all data)	R1 = 0.0753, wR2 = 0.0758	
Extinction coefficient	0.00039(6)	
Largest diff. peak and hole	0.283 and -0.467 e.$Å^{-3}$	

Table 2. Atomic coordinates (x 10^4) and equivalent isotropic displacement parameters ($Å^2$ x 10^3).
U(eq) is defined as one third of the trace of the orthogonalized U_{ij} tensor.

	x	y	z	U(eq)
Mo(1)	3732(1)	7430(1)	4146(1)	36(1)
S(1)	4195(1)	6680(1)	3596(1)	51(1)
S(2)	3165(1)	7934(1)	2983(1)	56(1)
S(3)	3504(1)	6435(1)	5006(1)	61(1)
S(4)	4056(1)	8660(1)	5010(1)	60(1)
N(1)	2550(1)	4890(1)	6034(1)	34(1)
C(1)	2485(1)	5318(2)	5058(1)	35(1)
C(2)	2197(1)	6197(2)	4787(2)	45(1)
C(3)	2179(1)	6536(2)	3813(2)	49(1)
C(4)	2112(1)	4630(2)	6138(2)	42(1)
C(5)	1830(1)	3937(2)	5409(2)	56(1)
C(6)	1418(1)	3706(2)	5627(2)	64(1)
C(7)	2770(1)	5639(2)	6777(1)	41(1)
C(8)	2876(1)	5297(2)	7791(2)	65(1)
C(9)	3095(1)	6085(3)	8459(2)	96(1)
C(10)	2829(1)	3983(2)	6141(2)	42(1)
C(11)	3310(1)	4137(2)	6277(2)	47(1)
C(12)	3515(1)	3196(2)	6119(2)	52(1)
N(2)	5000	9109(2)	2500	36(1)
C(21)	5070(1)	8454(2)	3351(2)	40(1)
C(22)	5116(1)	8970(2)	4275(2)	53(1)
C(23)	5205(1)	8250(2)	5075(2)	58(1)
C(24)	5397(1)	9758(2)	2640(2)	44(1)
C(25)	5823(1)	9242(2)	2777(2)	58(1)
C(26)	6180(1)	9970(2)	2792(2)	75(1)
N(3)	5000	4220(2)	2500	44(1)

C(31)	5224(2)	5056(5)	3192(4)	53(1)
C(32)	5424(2)	4808(5)	4222(4)	72(2)
C(31')	5124(2)	4575(4)	3469(4)	47(1)
C(32')	5486(2)	5321(5)	3731(5)	63(2)
C(33)	5594(1)	5632(2)	4786(2)	83(1)
C(34)	5338(2)	3395(4)	2648(4)	48(1)
C(35)	5771(2)	3621(5)	2500(4)	64(2)
C(34')	5366(2)	3842(4)	2179(4)	56(1)
C(35')	5606(2)	3028(5)	2733(5)	73(2)
C(36)	6025(1)	2754(3)	2540(2)	95(1)

Table 3. Bond lengths [Å] and angles [°].

Mo(1)-S(3)	2.1749(7)	N(1)-C(7)-C(8)	114.92(18)
Mo(1)-S(4)	2.1837(7)	C(9)-C(8)-C(7)	110.3(2)
Mo(1)-S(2)	2.1885(8)	C(11)-C(10)-N(1)	116.46(18)
Mo(1)-S(1)	2.1928(7)	C(12)-C(11)-C(10)	109.94(19)
N(1)-C(7)	1.517(3)	C(21)-N(2)-C(21)#1	106.9(2)
N(1)-C(4)	1.519(3)	C(21)-N(2)-C(24)	110.53(12)
N(1)-C(10)	1.522(3)	C(21)#1-N(2)-C(24)	110.57(12)
N(1)-C(1)	1.529(2)	C(21)-N(2)-C(24)#1	110.57(12)
C(1)-C(2)	1.503(3)	C(21)#1-N(2)-C(24)#1	110.53(12)
C(2)-C(3)	1.519(3)	C(24)-N(2)-C(24)#1	107.8(2)
C(4)-C(5)	1.511(3)	N(2)-C(21)-C(22)	115.40(17)
C(5)-C(6)	1.509(3)	C(23)-C(22)-C(21)	110.6(2)
C(7)-C(8)	1.521(3)	C(25)-C(24)-N(2)	115.63(19)
C(8)-C(9)	1.491(4)	C(24)-C(25)-C(26)	110.1(2)
C(10)-C(11)	1.516(3)	C(31')-N(3)-C(31')#1	140.8(5)
C(11)-C(12)	1.513(3)	C(31')-N(3)-C(34')#1	77.6(3)
N(2)-C(21)	1.521(2)	C(31')#1-N(3)-C(34')#1	116.5(3)
N(2)-C(21)#1	1.521(2)	C(31')-N(3)-C(34')	116.5(3)
N(2)-C(24)	1.521(2)	C(31')#1-N(3)-C(34')	77.6(3)
N(2)-C(24)#1	1.521(2)	C(34')#1-N(3)-C(34')	139.6(5)
C(21)-C(22)	1.523(3)	C(31')-N(3)-C(34)	98.9(3)
C(22)-C(23)	1.512(3)	C(31')#1-N(3)-C(34)	109.9(3)
C(24)-C(25)	1.506(3)	C(34')#1-N(3)-C(34)	106.9(4)
C(25)-C(26)	1.524(3)	C(34')-N(3)-C(34)	36.8(2)
N(3)-C(31')	1.461(5)	C(31')-N(3)-C(34)#1	109.9(3)
N(3)-C(31')#1	1.461(5)	C(31')#1-N(3)-C(34)#1	98.9(3)
N(3)-C(34')#1	1.510(5)	C(34')#1-N(3)-C(34)#1	36.8(2)
N(3)-C(34')	1.510(5)	C(34')-N(3)-C(34)#1	106.9(4)
N(3)-C(34)	1.543(5)	C(34)-N(3)-C(34)#1	84.8(4)
N(3)-C(34)#1	1.543(5)	C(31')-N(3)-C(31)	34.4(2)
N(3)-C(31)	1.563(7)	C(31')#1-N(3)-C(31)	109.3(4)
N(3)-C(31)#1	1.563(7)	C(34')#1-N(3)-C(31)	106.5(3)
C(31)-C(32)	1.506(8)	C(34')-N(3)-C(31)	103.1(3)
C(32)-C(33)	1.417(7)	C(34)-N(3)-C(31)	107.4(3)
C(31')-C(32')	1.512(7)	C(34)#1-N(3)-C(31)	142.4(3)
C(31')-C(34')#1	1.862(7)	C(31')-N(3)-C(31)#1	109.3(4)
C(32')-C(33)	1.566(7)	C(31')#1-N(3)-C(31)#1	34.4(2)
C(34)-C(35)	1.521(8)	C(34')#1-N(3)-C(31)#1	103.1(3)
C(35)-C(36)	1.442(7)	C(34')-N(3)-C(31)#1	106.5(3)
C(34')-C(35')	1.460(9)	C(34)-N(3)-C(31)#1	142.4(3)
C(34')-C(31')#1	1.862(7)	C(34)#1-N(3)-C(31)#1	107.4(3)
C(35')-C(36)	1.526(7)	C(31)-N(3)-C(31)#1	84.8(5)
S(3)-Mo(1)-S(4)	109.19(3)	C(6)-C(5)-C(4)	109.9(2)
S(3)-Mo(1)-S(2)	108.34(3)	C(33)-C(32)-C(31)	112.4(6)
S(4)-Mo(1)-S(2)	109.76(3)	N(3)-C(31')-C(32')	115.0(5)
S(3)-Mo(1)-S(1)	109.48(3)	N(3)-C(31')-C(34')#1	52.4(2)
S(4)-Mo(1)-S(1)	109.79(3)	C(32')-C(31')-C(34')#1	163.6(6)

S(2)-Mo(1)-S(1)	110.25(3)	C(31')-C(32')-C(33)	110.1(5)
C(7)-N(1)-C(4)	108.23(16)	C(32)-C(33)-C(32')	42.5(3)
C(7)-N(1)-C(10)	111.46(16)	C(35)-C(34)-N(3)	118.0(5)
C(4)-N(1)-C(10)	109.61(16)	C(36)-C(35)-C(34)	111.3(6)
C(7)-N(1)-C(1)	108.92(15)	C(35')-C(34')-N(3)	114.1(6)
C(4)-N(1)-C(1)	110.67(16)	C(35')-C(34')-C(31')#1	156.5(6)
C(10)-N(1)-C(1)	107.96(15)	N(3)-C(34')-C(31')#1	50.0(2)
C(2)-C(1)-N(1)	116.65(16)	C(34')-C(35')-C(36)	114.9(6)
C(1)-C(2)-C(3)	109.47(18)	C(35)-C(36)-C(35')	43.2(3)
C(5)-C(4)-N(1)	115.73(17)		

Symmetry transformations used to generate equivalent atoms:
#1 -x+1, y, -z+1/2

Table 4. Anisotropic displacement parameters ($Å^2 x 10^3$).
The anisotropic displacement factor exponent takes the form: $-2\pi^2[h^2 a^{*2}U_{11} + ... + 2 h k a^* b^* U_{12}]$

	U_{11}	U_{22}	U_{33}	U_{23}	U_{13}	U_{12}
Mo(1)	35(1)	39(1)	38(1)	-6(1)	15(1)	-5(1)
S(1)	47(1)	56(1)	56(1)	-5(1)	23(1)	6(1)
S(2)	52(1)	67(1)	47(1)	-9(1)	12(1)	16(1)
S(3)	58(1)	67(1)	65(1)	9(1)	28(1)	-17(1)
S(4)	61(1)	57(1)	66(1)	-24(1)	26(1)	-20(1)
N(1)	43(1)	30(1)	32(1)	0(1)	16(1)	-4(1)
C(1)	38(1)	38(1)	33(1)	-2(1)	16(1)	-5(1)
C(2)	48(1)	46(1)	41(1)	2(1)	16(1)	6(1)
C(3)	49(1)	50(1)	47(1)	11(1)	12(1)	1(1)
C(4)	48(1)	42(1)	45(1)	-2(1)	27(1)	-8(1)
C(5)	52(2)	60(2)	64(2)	-15(1)	29(1)	-20(1)
C(6)	54(2)	58(2)	91(2)	-9(2)	39(2)	-13(1)
C(7)	50(1)	36(1)	35(1)	-6(1)	13(1)	-7(1)
C(8)	94(2)	62(2)	35(1)	-2(1)	15(1)	-13(2)
C(9)	130(3)	107(3)	43(2)	-21(2)	17(2)	-50(2)
C(10)	52(1)	33(1)	42(1)	4(1)	17(1)	2(1)
C(11)	45(1)	42(1)	49(1)	2(1)	11(1)	-1(1)
C(12)	55(1)	55(2)	49(1)	4(1)	23(1)	7(1)
N(2)	41(1)	30(1)	40(1)	0	17(1)	0
C(21)	41(1)	37(1)	43(1)	5(1)	13(1)	1(1)
C(22)	65(2)	53(2)	41(1)	1(1)	18(1)	-1(1)
C(23)	57(2)	70(2)	45(1)	10(1)	12(1)	-2(1)
C(24)	53(1)	37(1)	44(1)	-4(1)	19(1)	-11(1)
C(25)	49(1)	60(2)	68(2)	-11(1)	22(1)	-13(1)
C(26)	63(2)	86(2)	85(2)	-18(2)	37(2)	-29(2)
N(3)	46(2)	41(2)	50(2)	0	25(1)	0
C(31)	55(3)	54(4)	55(3)	-4(3)	26(3)	0(3)
C(32)	70(4)	76(4)	63(4)	-4(4)	13(3)	6(3)
C(31')	51(3)	47(3)	49(3)	-6(3)	24(3)	-4(2)
C(32')	69(4)	65(4)	53(4)	-12(3)	18(3)	-17(3)
C(33)	101(3)	91(2)	63(2)	-22(2)	34(2)	-20(2)
C(34)	50(3)	46(3)	52(3)	1(2)	20(3)	16(3)
C(35)	53(3)	81(4)	62(4)	9(3)	24(3)	10(3)
C(34')	54(3)	60(4)	60(4)	-8(3)	26(3)	-5(3)
C(35')	57(4)	81(5)	73(4)	-10(4)	11(3)	10(4)
C(36)	60(2)	139(3)	82(2)	-32(2)	17(2)	33(2)

Table 5. Coordinates of H atoms ($x 10^4$) and isotropic displacement parameters ($Å^2 x 10^3$).

	x	y	z	U(eq)
H(1A)	2771	5484	5024	42
H(1B)	2363	4818	4592	42
H(2A)	2312	6709	5243	53
H(2B)	1904	6040	4784	53
H(3A)	1996	7100	3641	74
H(3B)	2061	6030	3363	74
H(3C)	2469	6693	3820	74

H(4A)	2166	4347	6757	50
H(4B)	1947	5222	6113	50
H(5A)	1755	4226	4787	68
H(5B)	1992	3345	5410	68
H(6A)	1243	3259	5167	96
H(6B)	1255	4290	5610	96
H(6C)	1494	3421	6244	96
H(7A)	2580	6201	6683	49
H(7B)	3040	5843	6684	49
H(8A)	2608	5107	7901	78
H(8B)	3067	4736	7898	78
H(9A)	3167	5855	9095	145
H(9B)	2901	6630	8368	145
H(9C)	3358	6278	8342	145
H(10A)	2807	3618	6676	50
H(10B)	2705	3585	5584	50
H(11A)	3341	4622	5836	56
H(11B)	3460	4370	6912	56
H(12A)	3819	3301	6199	78
H(12B)	3367	2967	5491	78
H(12C)	3490	2722	6566	78
H(21A)	5331	8070	3435	48
H(21B)	4824	8009	3215	48
H(22A)	5355	9432	4412	63
H(22B)	4849	9324	4216	63
H(23A)	5232	8588	5650	87
H(23B)	5473	7910	5142	87
H(23C)	4968	7796	4941	87
H(24A)	5338	10179	2095	53
H(24B)	5431	10167	3185	53
H(25A)	5788	8783	2269	70
H(25B)	5908	8886	3367	70
H(26A)	6450	9634	2878	112
H(26B)	6217	10418	3301	112
H(26C)	6096	10317	2205	112
H(31A)	5453	5329	2982	63
H(31B)	5008	5559	3135	63
H(32A)	5204	4506	4438	86
H(32B)	5658	4343	4299	86
H(31C)	5216	4028	3894	57
H(31D)	4868	4854	3568	57
H(32C)	5396	5884	3326	75
H(32D)	5747	5053	3638	75
H(33A)	5715	5440	5435	125
H(33B)	5363	6092	4717	125
H(33C)	5819	5922	4587	125
H(34A)	5403	3155	3287	58
H(34B)	5200	2870	2226	58
H(35A)	5714	3929	1891	77
H(35B)	5937	4070	2982	77
H(34C)	5244	3642	1525	68
H(34D)	5570	4365	2210	68
H(35C)	5414	2469	2609	87
H(35D)	5679	3185	3397	87
H(36A)	6295	2917	2438	143
H(36B)	5862	2310	2061	143
H(36C)	6088	2458	3149	143

Bis(tetrabutylammonium) tetrathiomolybdate

Table 1. Crystal data and structure refinement for bis(tetrabutylammonium) tetrathiomolybdate.

Identification code	mp332	
Empirical formula	$C_{32}H_{72}MoN_2S_4$	
Formula weight	709.10	
Temperature	293(2) K	
Wavelength	0.71073 Å	
Crystal system	orthorhombic	
Space group	Fdd2	
Unit cell dimensions	a = 28.9142(18) Å	α= 90°.
	b = 35.7811(10) Å	β= 90°.
	c = 15.6774(17) Å	γ = 90°.
Volume	16220(2) $Å^3$	
Z	16	
Density (calculated)	1.162 Mg/m^3	
Absorption coefficient	0.550 mm^{-1}	
F(000)	6144	
Crystal size	0.6 x 0.8 x 0.6 mm^3	
Theta range for data collection	2.26 to 28.06°.	
Index ranges	-38<=h<=38, -42<=k<=47, -20<=l<=20	
Reflections collected	30857	
Independent reflections	9645 [R(int) = 0.0987]	
Completeness to theta = 28.06°	99.6 %	
Refinement method	Full-matrix least-squares on F^2	
Data / restraints / parameters	9645 / 1 / 353	
Goodness-of-fit on F^2	0.994	
Final R indices [I>2sigma(I)]	R1 = 0.0502, wR2 = 0.0913	
R indices (all data)	R1 = 0.0942, wR2 = 0.1064	
Absolute structure parameter	-0.08(4)	
Extinction coefficient	0.000225(15)	
Largest diff. peak and hole	0.488 and -0.800 e.$Å^{-3}$	

Table 2. Atomic coordinates (x 10^4) and equivalent isotropic displacement parameters ($Å^2$ x 10^3).
U(eq) is defined as one third of the trace of the orthogonalized U_{ij} tensor.

	x	y	z	U(eq)
Mo(1)	-1545(1)	-9560(1)	7107(1)	25(1)
S(1)	-1242(1)	-9003(1)	7142(1)	58(1)
S(2)	-2290(1)	-9529(1)	6815(1)	35(1)
S(3)	-1191(1)	-9899(1)	6146(1)	45(1)
S(4)	-1440(1)	-9818(1)	8363(1)	33(1)
N(1)	-2821(1)	-9557(1)	9493(2)	26(1)
C(22)	-4960(2)	-9199(2)	11533(4)	50(2)
C(5)	-3345(2)	-9561(2)	9371(3)	32(1)
C(8)	-4230(2)	-9955(2)	8666(5)	66(2)
C(23)	-5020(3)	-9439(2)	10731(4)	66(2)
C(7)	-4041(2)	-9581(2)	8426(4)	54(2)
C(1)	-2733(2)	-9558(2)	10447(3)	30(1)
C(12)	-2061(2)	-10625(2)	9558(5)	43(1)
C(15)	-2526(2)	-8520(2)	8975(4)	41(1)
C(13)	-2604(2)	-9218(1)	9069(3)	30(1)
C(2)	-2231(2)	-9534(2)	10716(3)	46(2)
C(10)	-2816(2)	-10275(1)	9340(4)	35(1)
C(6)	-3512(2)	-9551(2)	8452(3)	41(1)
C(14)	-2766(2)	-8843(1)	9414(4)	40(1)
C(9)	-2606(2)	-9903(2)	9082(3)	30(1)
C(3)	-2192(2)	-9464(2)	11670(4)	46(2)
C(11)	-2507(2)	-10597(2)	9046(4)	45(1)
C(24)	-5033(4)	-9216(3)	9930(5)	103(4)

N(2)	-4695(1)	-9246(1)	13102(3)	27(1)
C(21)	-4897(2)	-9437(2)	12320(3)	39(1)
C(25)	-4267(2)	-9013(2)	12881(3)	31(1)
C(26)	-3884(2)	-9227(2)	12428(4)	44(1)
C(30)	-4330(2)	-9439(1)	14528(4)	37(1)
C(27)	-3497(2)	-8952(2)	12193(5)	54(2)
C(33)	-5038(2)	-8970(1)	13494(3)	30(1)
C(34)	-5452(2)	-9134(2)	13956(3)	30(1)
C(29)	-4569(2)	-9558(2)	13721(3)	32(1)
C(28)	-3616(3)	-8696(3)	11471(5)	73(2)
C(32)	-4010(3)	-9677(2)	15933(4)	61(2)
C(35)	-5759(2)	-8815(2)	14273(4)	35(1)
C(31)	-4292(2)	-9769(2)	15143(4)	50(2)
C(4)	-1708(2)	-9420(3)	11997(5)	75(2)
C(36)	-6173(2)	-8952(2)	14770(4)	53(2)
C(16)	-2688(2)	-8139(2)	9324(5)	64(2)

Table 3. Bond lengths [Å] and angles [°].

Mo(1)-S(1)	2.1791(14)	S(1)-Mo(1)-S(2)	110.58(6)
Mo(1)-S(3)	2.1897(14)	S(3)-Mo(1)-S(2)	110.05(5)
Mo(1)-S(4)	2.1949(13)	S(4)-Mo(1)-S(2)	110.11(5)
Mo(1)-S(2)	2.2050(12)	C(1)-N(1)-C(13)	111.4(4)
N(1)-C(1)	1.516(6)	C(1)-N(1)-C(5)	106.8(3)
N(1)-C(13)	1.518(6)	C(13)-N(1)-C(5)	111.3(4)
N(1)-C(5)	1.529(5)	C(1)-N(1)-C(9)	110.2(4)
N(1)-C(9)	1.529(6)	C(13)-N(1)-C(9)	107.1(3)
C(22)-C(21)	1.512(8)	C(5)-N(1)-C(9)	110.1(4)
C(22)-C(23)	1.531(9)	C(21)-C(22)-C(23)	111.6(6)
C(5)-C(6)	1.520(7)	C(6)-C(5)-N(1)	115.7(4)
C(8)-C(7)	1.493(10)	C(24)-C(23)-C(22)	113.3(7)
C(23)-C(24)	1.488(11)	C(8)-C(7)-C(6)	115.0(6)
C(7)-C(6)	1.532(8)	C(2)-C(1)-N(1)	115.8(4)
C(1)-C(2)	1.516(7)	C(14)-C(15)-C(16)	112.0(5)
C(12)-C(11)	1.522(8)	N(1)-C(13)-C(14)	114.9(4)
C(15)-C(14)	1.516(8)	C(1)-C(2)-C(3)	110.7(4)
C(15)-C(16)	1.542(8)	C(9)-C(10)-C(11)	110.3(4)
C(13)-C(14)	1.520(7)	C(5)-C(6)-C(7)	109.9(5)
C(2)-C(3)	1.521(7)	C(15)-C(14)-C(13)	111.7(4)
C(10)-C(9)	1.520(7)	C(10)-C(9)-N(1)	115.8(4)
C(10)-C(11)	1.528(7)	C(4)-C(3)-C(2)	114.9(5)
C(3)-C(4)	1.500(8)	C(12)-C(11)-C(10)	112.8(5)
N(2)-C(21)	1.521(6)	C(21)-N(2)-C(29)	105.9(4)
N(2)-C(29)	1.524(6)	C(21)-N(2)-C(33)	111.4(4)
N(2)-C(33)	1.529(6)	C(29)-N(2)-C(33)	112.0(4)
N(2)-C(25)	1.533(6)	C(21)-N(2)-C(25)	112.0(4)
C(25)-C(26)	1.522(7)	C(29)-N(2)-C(25)	110.5(4)
C(26)-C(27)	1.534(8)	C(33)-N(2)-C(25)	105.2(4)
C(30)-C(29)	1.504(7)	C(22)-C(21)-N(2)	116.8(4)
C(30)-C(31)	1.527(8)	C(26)-C(25)-N(2)	114.7(4)
C(27)-C(28)	1.496(10)	C(25)-C(26)-C(27)	108.6(5)
C(33)-C(34)	1.520(7)	C(29)-C(30)-C(31)	110.2(5)
C(34)-C(35)	1.531(7)	C(28)-C(27)-C(26)	113.9(6)
C(32)-C(31)	1.519(10)	C(34)-C(33)-N(2)	116.8(4)
C(35)-C(36)	1.509(8)	C(33)-C(34)-C(35)	108.8(4)
S(1)-Mo(1)-S(3)	109.58(8)	C(30)-C(29)-N(2)	116.0(4)
S(1)-Mo(1)-S(4)	107.85(6)	C(36)-C(35)-C(34)	112.6(5)
S(3)-Mo(1)-S(4)	108.62(6)	C(32)-C(31)-C(30)	112.7(6)

Table 4. Anisotropic displacement parameters ($Å^2 \times 10^3$).
The anisotropic displacement factor exponent takes the form: $-2\pi^2[\, h^2 a^{*2} U_{11} + \ldots + 2\, h\, k\, a^*\, b^*\, U_{12} \,]$

	U_{11}	U_{22}	U_{33}	U_{23}	U_{13}	U_{12}
Mo(1)	28(1)	23(1)	24(1)	0(1)	-3(1)	-1(1)
S(1)	80(1)	31(1)	62(1)	16(1)	-34(1)	-21(1)

S(2)	30(1)	44(1)	32(1)	-2(1)	-5(1)	8(1)
S(3)	32(1)	65(1)	37(1)	-16(1)	6(1)	3(1)
S(4)	34(1)	34(1)	31(1)	8(1)	-3(1)	3(1)
N(1)	26(2)	31(2)	20(2)	3(2)	3(2)	1(2)
C(22)	58(4)	49(4)	42(3)	-10(3)	-1(3)	6(3)
C(5)	31(3)	34(3)	30(2)	3(2)	3(2)	-1(2)
C(8)	50(4)	80(6)	69(5)	6(4)	-11(3)	-23(4)
C(23)	67(4)	82(6)	50(4)	-20(4)	4(3)	-27(4)
C(7)	33(3)	79(5)	49(4)	1(3)	-10(3)	5(3)
C(1)	31(2)	36(3)	22(2)	3(2)	6(2)	-5(2)
C(12)	38(3)	36(3)	55(3)	9(3)	-1(3)	5(2)
C(15)	39(3)	34(3)	50(3)	5(3)	1(3)	-3(2)
C(13)	35(3)	29(3)	26(2)	6(2)	9(2)	0(2)
C(2)	30(3)	79(5)	29(3)	-5(3)	-3(2)	-1(3)
C(10)	34(3)	30(3)	41(3)	1(2)	-4(2)	1(2)
C(6)	38(3)	52(3)	33(3)	11(3)	0(2)	0(3)
C(14)	49(3)	29(3)	42(3)	3(2)	12(2)	2(2)
C(9)	29(2)	35(3)	25(2)	-1(2)	3(2)	0(2)
C(3)	46(3)	60(4)	32(3)	0(3)	-6(2)	-4(3)
C(11)	48(3)	32(3)	54(4)	-9(3)	0(3)	5(3)
C(24)	126(8)	140(9)	43(4)	-12(5)	-9(5)	61(7)
N(2)	29(2)	21(2)	33(2)	-2(2)	4(2)	-1(2)
C(21)	45(3)	34(3)	40(3)	-10(2)	2(2)	-9(2)
C(25)	31(3)	25(3)	38(3)	1(2)	10(2)	-5(2)
C(26)	42(3)	33(3)	55(3)	-3(3)	13(3)	8(2)
C(30)	34(3)	34(3)	43(3)	7(3)	1(3)	6(2)
C(27)	34(3)	71(4)	55(4)	9(4)	11(3)	3(3)
C(33)	31(3)	26(3)	32(3)	-4(2)	5(2)	5(2)
C(34)	28(2)	30(3)	32(3)	-3(2)	-4(2)	0(2)
C(29)	34(3)	21(2)	41(3)	3(2)	5(2)	0(2)
C(28)	61(4)	92(6)	65(5)	30(4)	17(4)	-17(4)
C(32)	61(4)	77(5)	45(3)	19(3)	9(3)	27(4)
C(35)	30(2)	38(3)	38(3)	-12(3)	0(2)	4(2)
C(31)	58(4)	46(4)	45(4)	12(3)	18(3)	11(3)
C(4)	60(4)	114(7)	50(5)	-13(5)	-17(4)	3(4)
C(36)	40(3)	61(4)	59(4)	-26(4)	14(3)	-3(3)
C(16)	62(4)	34(3)	95(6)	12(4)	8(4)	4(3)

Table 5. Coordinates of H atoms (x 10^4) and isotropic displacement parameters (Å^2 x 10^3).

	x	y	z	U(eq)
H(22A)	-4693	-9038	11463	60
H(22B)	-5230	-9041	11605	60
H(5A)	-3468	-9784	9640	38
H(5B)	-3475	-9347	9668	38
H(8A)	-4561	-9950	8620	99
H(8B)	-4144	-10012	9242	99
H(8C)	-4108	-10142	8289	99
H(23A)	-4767	-9616	10699	80
H(23B)	-5306	-9580	10780	80
H(7A)	-4169	-9395	8808	65
H(7B)	-4144	-9521	7853	65
H(1A)	-2898	-9348	10697	36
H(1B)	-2865	-9785	10684	36
H(12A)	-1880	-10831	9349	65
H(12B)	-2133	-10666	10149	65
H(12C)	-1888	-10398	9499	65
H(15A)	-2588	-8531	8367	49
H(15B)	-2195	-8543	9056	49
H(13A)	-2671	-9227	8463	36
H(13B)	-2271	-9233	9135	36
H(2A)	-2080	-9333	10408	56
H(2B)	-2075	-9766	10574	56
H(10A)	-3120	-10301	9085	42
H(10B)	-2851	-10284	9955	42
H(6A)	-3376	-9757	8136	49

H(6B)	-3415	-9319	8185	49
H(14A)	-3098	-8821	9332	48
H(14B)	-2705	-8832	10022	48
H(9A)	-2631	-9878	8467	36
H(9B)	-2279	-9907	9222	36
H(3A)	-2365	-9239	11807	55
H(3B)	-2337	-9670	11970	55
H(11A)	-2676	-10830	9099	54
H(11B)	-2431	-10562	8449	54
H(24A)	-5072	-9380	9452	154
H(24B)	-4748	-9080	9870	154
H(24C)	-5286	-9043	9952	154
H(21A)	-4699	-9646	12173	47
H(21B)	-5196	-9540	12476	47
H(25A)	-4362	-8806	12521	38
H(25B)	-4142	-8908	13404	38
H(26A)	-4004	-9344	11917	52
H(26B)	-3764	-9421	12799	52
H(30A)	-4503	-9239	14795	45
H(30B)	-4023	-9346	14395	45
H(27A)	-3423	-8802	12691	64
H(27B)	-3222	-9093	12042	64
H(33A)	-4870	-8812	13893	36
H(33B)	-5152	-8809	13042	36
H(34A)	-5349	-9284	14436	36
H(34B)	-5626	-9294	13573	36
H(29A)	-4850	-9690	13874	38
H(29B)	-4370	-9734	13425	38
H(28A)	-3362	-8531	11362	109
H(28B)	-3885	-8552	11618	109
H(28C)	-3679	-8842	10969	109
H(32A)	-3999	-9892	16299	92
H(32B)	-4152	-9473	16231	92
H(32C)	-3702	-9608	15768	92
H(35A)	-5578	-8651	14633	42
H(35B)	-5866	-8671	13787	42
H(31A)	-4600	-9845	15314	60
H(31B)	-4149	-9978	14849	60
H(4A)	-1715	-9376	12601	112
H(4B)	-1563	-9211	11718	112
H(4C)	-1535	-9643	11880	112
H(36A)	-6352	-8742	14960	80
H(36B)	-6070	-9093	15255	80
H(36C)	-6360	-9108	14410	80
H(16A)	-2531	-7942	9027	96
H(16B)	-2619	-8124	9922	96
H(16C)	-3016	-8114	9240	96

Bis(tetramethylammonium) tetrathiotungstate

Table 1. Crystal data and structure refinement for bis(tetramethylammonium) tetrathiotungstate.

Identification code	pw100_1	
Empirical formula	$((CH_3)_4N)_2WS_4$	
Formula weight	460.38	
Temperature	293(2) K	
Wavelength	0.71073 Å	
Crystal system	orthorhombic	
Space group	$P2_12_12_1$	
Unit cell dimensions	a = 8.9433(4) Å	α= 90°.
	b = 15.5658(9) Å	β= 90°.
	c = 37.279(2) Å	γ = 90°.
Volume	5189.7(5) $Å^3$	
Z	12	
Density (calculated)	1.768 Mg/m^3	
Absorption coefficient	7.139 mm^{-1}	
F(000)	2688	
Crystal size	0.7 x 0.12 x 0.30 mm^3	
Theta range for data collection	1.70 to 22.37°.	
Index ranges	-9<=h<=9, -16<=k<=16, -39<=l<=39	
Reflections collected	26540	
Independent reflections	6609 [R(int) = 0.0884]	
Completeness to theta = 22.37°	98.8 %	
Refinement method	Full-matrix least-squares on F^2	
Data / restraints / parameters	6609 / 21 / 364	
Goodness-of-fit on F^2	1.169	
Final R indices [I>2sigma(I)]	R1 = 0.0567, wR2 = 0.1402	
R indices (all data)	R1 = 0.0706, wR2 = 0.1483	
Absolute structure parameter	0.0(3)	
Extinction coefficient	0.00037(5)	
Largest diff. peak and hole	1.664 and -2.224 e.$Å^{-3}$	

Table 2. Atomic coordinates (x 10^4) and equivalent isotropic displacement parameters ($Å^2$ x 10^3).
U(eq) is defined as one third of the trace of the orthogonalized U_{ij} tensor.

	x	y	z	U(eq)
W(1)	2121(1)	1537(1)	4193(1)	35(1)
S(1)	228(10)	755(5)	4016(3)	73(2)
S(2)	2157(10)	1566(7)	4773(2)	84(3)
S(3)	1858(10)	2848(5)	3984(3)	73(2)
S(4)	4271(12)	1026(7)	4008(3)	92(3)
W(2)	-2384(1)	3428(1)	2478(1)	41(1)
S(5)	-2361(14)	2123(6)	2679(3)	106(4)
S(6)	-4227(10)	4128(7)	2709(3)	86(3)
S(7)	-384(7)	4018(7)	2619(3)	89(3)
S(8)	-2576(9)	3440(7)	1896(2)	72(2)
W(3)	7294(1)	6538(1)	4141(1)	40(1)
S(9)	9510(13)	6010(7)	4293(2)	95(3)
S(10)	5521(10)	5722(6)	4369(3)	75(2)
S(11)	7031(10)	7845(5)	4355(3)	74(3)
S(12)	7024(8)	6553(7)	3559(2)	68(2)
N(1)	2623(19)	1590(16)	2856(5)	43(5)
C(1)	2560(30)	1580(30)	2453(8)	90(12)
C(2)	2150(70)	2410(40)	2968(17)	66(17)
C(3)	4300(80)	1290(50)	2899(19)	90(20)
C(4)	1470(60)	970(30)	3033(13)	48(12)
C(2')	3120(60)	2480(40)	2973(16)	56(14)
C(3')	3800(70)	910(40)	2973(16)	65(16)
C(4')	890(60)	1420(40)	2992(16)	72(16)
N(2)	-2810(20)	733(13)	4973(6)	55(7)
C(5)	-2510(50)	1420(30)	4693(10)	125(15)
C(6)	-2040(80)	720(50)	5336(12)	120(20)

C(7)	-4410(40)	940(30)	5074(13)	65(13)
C(8)	-2820(80)	-30(30)	4722(17)	110(20)
C(6')	-1220(50)	990(60)	5070(20)	100(30)
C(7')	-3970(70)	810(50)	5271(17)	80(20)
C(8')	-2700(90)	-240(20)	4950(20)	70(20)
N(3)	2250(20)	8379(14)	4517(5)	41(5)
C(9)	2830(40)	7508(18)	4623(11)	91(13)
C(10)	3420(30)	8960(20)	4711(7)	71(9)
C(11)	2400(40)	8520(30)	4108(9)	92(11)
C(12)	830(40)	8640(30)	4589(11)	108(13)
N(4)	2250(20)	5720(13)	3363(6)	41(5)
C(13)	800(50)	6010(30)	3260(12)	117(15)
C(14)	2740(40)	6360(30)	3634(11)	116(14)
C(15)	3280(50)	5720(30)	3076(10)	106(12)
C(16)	2090(40)	4890(20)	3523(10)	82(10)
N(5)	12250(30)	1599(18)	6165(6)	61(7)
C(17)	12420(50)	1590(30)	5776(7)	112(14)
C(18)	12520(30)	2514(19)	6306(9)	70(9)
C(19)	13250(50)	1030(20)	6321(11)	112(15)
C(20)	10670(40)	1450(30)	6304(9)	91(11)
N(6)	7490(30)	9214(14)	3300(6)	58(6)
C(21)	6290(40)	9350(30)	3591(12)	129(17)
C(22)	7720(60)	9980(30)	3032(14)	52(13)
C(23)	7010(70)	8390(50)	3059(17)	85(19)
C(24)	9030(50)	8870(30)	3401(13)	39(11)
C(22')	7770(60)	10200(30)	3235(15)	51(13)
C(23')	6550(50)	8800(30)	3032(11)	45(11)
C(24')	8470(90)			

Table 3. Bond lengths [Å] and angles [°].

W(1)-S(2)	2.162(8)	C(2)-N(1)-C(3)	122(4)
W(1)-S(1)	2.187(8)	C(1)-N(1)-C(3)	98(3)
W(1)-S(4)	2.192(10)	C(2')-N(1)-C(3)	88(4)
W(1)-S(3)	2.196(8)	C(3')-N(1)-C(3)	29(3)
W(2)-S(7)	2.079(7)	C(4)-N(1)-C(3)	114(4)
W(2)-S(6)	2.155(8)	C(2)-N(1)-C(4')	77(3)
W(2)-S(5)	2.165(9)	C(1)-N(1)-C(4')	106(3)
W(2)-S(8)	2.176(7)	C(2')-N(1)-C(4')	109(3)
W(3)-S(12)	2.182(8)	C(3')-N(1)-C(4')	116(4)
W(3)-S(11)	2.199(8)	C(4)-N(1)-C(4')	32(2)
W(3)-S(10)	2.202(9)	C(3)-N(1)-C(4')	144(4)
W(3)-S(9)	2.219(10)	C(8)-N(2)-C(6)	123(4)
N(1)-C(2)	1.41(7)	C(8)-N(2)-C(5)	97(4)
N(1)-C(1)	1.50(3)	C(6)-N(2)-C(5)	123(4)
N(1)-C(2')	1.52(6)	C(8)-N(2)-C(8')	35(3)
N(1)-C(3')	1.56(6)	C(6)-N(2)-C(8')	91(4)
N(1)-C(4)	1.56(5)	C(5)-N(2)-C(8')	130(4)
N(1)-C(3)	1.58(7)	C(8)-N(2)-C(6')	111(4)
N(1)-C(4')	1.65(6)	C(6)-N(2)-C(6')	50(4)
N(2)-C(8)	1.52(2)	C(5)-N(2)-C(6')	80(4)
N(2)-C(6)	1.52(2)	C(8')-N(2)-C(6')	103(5)
N(2)-C(5)	1.52(2)	C(8)-N(2)-C(7)	108(3)
N(2)-C(8')	1.52(3)	C(6)-N(2)-C(7)	102(3)
N(2)-C(6')	1.52(3)	C(5)-N(2)-C(7)	101(3)
N(2)-C(7)	1.52(2)	C(8')-N(2)-C(7)	107(4)

N(2)-C(7')	1.52(3)	C(6')-N(2)-C(7)	140(4)
C(5)-C(6')	1.95(9)	C(8)-N(2)-C(7')	121(4)
N(3)-C(12)	1.36(4)	C(6)-N(2)-C(7')	70(4)
N(3)-C(9)	1.51(3)	C(5)-N(2)-C(7')	124(4)
N(3)-C(11)	1.55(4)	C(8')-N(2)-C(7')	100(4)
N(3)-C(10)	1.56(3)	C(6')-N(2)-C(7')	116(5)
N(4)-C(15)	1.41(4)	C(7)-N(2)-C(7')	33(3)
N(4)-C(13)	1.43(4)	N(2)-C(5)-C(6')	50(2)
N(4)-C(16)	1.44(4)	N(2)-C(6')-C(5)	50(2)
N(4)-C(14)	1.49(4)	C(12)-N(3)-C(9)	123(3)
N(5)-C(19)	1.39(4)	C(12)-N(3)-C(11)	104(2)
N(5)-C(17)	1.46(3)	C(9)-N(3)-C(11)	111(2)
N(5)-C(20)	1.52(4)	C(12)-N(3)-C(10)	112(3)
N(5)-C(18)	1.54(4)	C(9)-N(3)-C(10)	99(2)
N(6)-C(24')	1.32(7)	C(11)-N(3)-C(10)	109(2)
N(6)-C(23')	1.46(5)	C(15)-N(4)-C(13)	113(3)
N(6)-C(24)	1.52(5)	C(15)-N(4)-C(16)	112(3)
N(6)-C(21)	1.54(4)	C(13)-N(4)-C(16)	108(3)
N(6)-C(22)	1.57(5)	C(15)-N(4)-C(14)	109(3)
N(6)-C(22')	1.57(5)	C(13)-N(4)-C(14)	104(3)
N(6)-C(23)	1.62(7)	C(16)-N(4)-C(14)	111(3)
C(21)-C(24')	2.02(8)	C(19)-N(5)-C(17)	110(3)
S(2)-W(1)-S(1)	109.0(4)	C(19)-N(5)-C(20)	111(3)
S(2)-W(1)-S(4)	108.0(4)	C(17)-N(5)-C(20)	116(3)
S(1)-W(1)-S(4)	112.5(4)	C(19)-N(5)-C(18)	110(3)
S(2)-W(1)-S(3)	109.6(4)	C(17)-N(5)-C(18)	110(3)
S(1)-W(1)-S(3)	109.1(3)	C(20)-N(5)-C(18)	100(3)
S(4)-W(1)-S(3)	108.6(4)	C(24')-N(6)-C(23')	140(4)
S(7)-W(2)-S(6)	109.5(4)	C(24')-N(6)-C(24)	31(3)
S(7)-W(2)-S(5)	108.6(4)	C(23')-N(6)-C(24)	123(3)
S(6)-W(2)-S(5)	110.1(4)	C(24')-N(6)-C(21)	90(4)
S(7)-W(2)-S(8)	108.5(4)	C(23')-N(6)-C(21)	98(3)
S(6)-W(2)-S(8)	109.5(4)	C(24)-N(6)-C(21)	120(3)
S(5)-W(2)-S(8)	110.7(4)	C(24')-N(6)-C(22)	123(4)
S(12)-W(3)-S(11)	109.8(4)	C(23')-N(6)-C(22)	88(3)
S(12)-W(3)-S(10)	108.1(3)	C(24)-N(6)-C(22)	108(3)
S(11)-W(3)-S(10)	108.4(4)	C(21)-N(6)-C(22)	116(3)

Table 4. Anisotropic displacement parameters ($Å^2 \times 10^3$).

The anisotropic displacement factor exponent takes the form: $-2\pi^2[h^2 a^{*2} U_{11} + \ldots + 2 h k a^* b^* U_{12}]$

	U_{11}	U_{22}	U_{33}	U_{23}	U_{13}	U_{12}
W(1)	35(1)	36(1)	35(1)	-3(1)	0(1)	3(1)
S(1)	91(6)	52(4)	77(5)	-10(4)	-41(5)	-17(4)
S(2)	107(6)	106(7)	39(4)	-12(4)	-8(4)	7(7)
S(3)	79(5)	44(4)	96(6)	15(4)	-15(5)	-1(4)
S(4)	88(6)	93(7)	94(7)	-2(6)	35(6)	0(6)
W(2)	51(1)	36(1)	37(1)	0(1)	4(1)	4(1)
S(5)	158(10)	55(5)	104(8)	20(5)	3(7)	10(6)
S(6)	83(6)	99(7)	76(6)	-13(5)	25(4)	50(5)
S(7)	17(3)	146(9)	105(7)	1(6)	-3(4)	-34(4)
S(8)	72(4)	100(6)	42(4)	-5(4)	-3(3)	-5(6)
W(3)	46(1)	38(1)	36(1)	1(1)	5(1)	2(1)
S(9)	139(8)	93(7)	52(5)	13(5)	-3(5)	46(7)
S(10)	71(5)	71(5)	82(6)	10(4)	4(4)	-18(4)
S(11)	100(6)	43(4)	80(6)	-18(4)	-12(5)	12(5)
S(12)	71(4)	93(6)	41(4)	-4(4)	-2(3)	-1(6)
N(1)	26(8)	55(13)	47(12)	10(11)	17(8)	0(12)
C(1)	70(19)	130(30)	70(20)	-10(20)	-28(19)	0(30)
N(2)	64(14)	42(12)	58(15)	-20(11)	24(12)	-4(12)
N(3)	44(11)	44(12)	34(11)	-3(9)	-18(8)	3(12)
C(9)	70(20)	48(18)	150(40)	6(19)	-20(20)	30(17)
C(10)	71(19)	100(20)	46(15)	-25(14)	2(14)	-36(18)
C(11)	120(20)	80(20)	80(30)	-11(18)	50(20)	20(20)
N(4)	25(9)	42(12)	55(14)	9(10)	19(9)	12(9)
N(5)	70(15)	56(15)	56(15)	-1(13)	27(11)	-6(17)

C(17)	220(40)	100(30)	20(17)	0(16)	-10(20)	-30(30)
C(18)	59(18)	59(19)	90(20)	-23(16)	-16(18)	12(16)
C(19)	160(40)	70(20)	110(30)	-13(19)	-50(30)	10(30)
N(6)	87(17)	42(13)	46(14)	-5(10)	-13(13)	-11(13)
C(21)	60(20)	140(40)	190(40)	-10(30)	70(20)	30(20)

Table 5. Coordinates of H atoms ($\times 10^4$) and isotropic displacement parameters ($Å^2 \times 10^3$)

	x	y	z	U(eq)
H(1A)	2180	2117	2368	135
H(1B)	1906	1122	2376	135
H(1C)	3541	1483	2358	135
H(1D)	2181	2114	2364	135
H(1E)	3541	1479	2359	135
H(1F)	1905	1120	2379	135
H(2A)	2189	2447	3225	100
H(2B)	1150	2516	2887	100
H(2C)	2807	2842	2868	100
H(3A)	4413	720	2800	134
H(3B)	4560	1275	3149	134
H(3C)	4950	1677	2775	134
H(4A)	1718	388	2973	72
H(4B)	485	1101	2946	72
H(4C)	1496	1041	3288	72
H(2D)	3160	2508	3230	84
H(2E)	2422	2902	2886	84
H(2F)	4095	2601	2876	84
H(3D)	3481	349	2894	97
H(3E)	3884	910	3230	97
H(3F)	4748	1042	2868	97
H(4D)	572	860	2918	108
H(4E)	242	1847	2890	108
H(4F)	850	1459	3249	108
H(5A)	-1972	1169	4495	188
H(5B)	-1918	1870	4796	188
H(5C)	-3439	1648	4609	188
H(5D)	-1972	1168	4495	188
H(5E)	-1918	1870	4796	188
H(5F)	-3439	1648	4609	188
H(6A)	-2148	1267	5449	184
H(6B)	-1002	588	5306	184
H(6C)	-2499	284	5484	184
H(7A)	-5019	954	4862	97
H(7B)	-4450	1492	5190	97
H(7C)	-4786	509	5235	97
H(8A)	-3395	105	4512	166
H(8B)	-3261	-516	4842	166
H(8C)	-1815	-170	4653	166
H(6D)	-903	659	5279	149
H(6E)	-1190	1588	5132	149
H(6F)	-560	875	4877	149
H(7D)	-3943	308	5418	118
H(7E)	-4943	875	5166	118
H(7F)	-3747	1309	5415	118
H(8D)	-2939	-491	5175	109
H(8E)	-1708	-401	4877	109
H(8F)	-3401	-442	4769	109
H(9A)	3853	7453	4546	136
H(9B)	2238	7069	4512	136
H(9C)	2783	7448	4879	136
H(10A)	4410	8794	4636	106
H(10B)	3336	8879	4966	106
H(10C)	3248	9547	4652	106
H(11A)	3407	8397	4036	139
H(11B)	2154	9101	4050	139
H(11C)	1727	8136	3984	139
H(12A)	132	8248	4480	162

H(12B)	675	9205	4495	162
H(12C)	674	8645	4844	162
H(13A)	200	6101	3470	176
H(13B)	330	5586	3110	176
H(13C)	884	6540	3129	176
H(14A)	2026	6377	3826	173
H(14B)	2799	6918	3524	173
H(14C)	3701	6203	3726	173
H(15A)	3269	6271	2961	159
H(15B)	3003	5284	2906	159
H(15C)	4264	5603	3166	159
H(16A)	1495	4931	3737	123
H(16B)	3062	4664	3585	123
H(16C)	1614	4504	3357	123
H(17A)	11720	1979	5669	168
H(17B)	12231	1016	5688	168
H(17C)	13419	1754	5714	168
H(18A)	11809	2900	6200	105
H(18B)	13513	2692	6245	105
H(18C)	12401	2520	6562	105
H(19A)	13139	1048	6577	167
H(19B)	14248	1188	6256	167
H(19C)	13043	458	6237	167
H(20A)	10000	1855	6195	137
H(20B)	10655	1524	6560	137
H(20C)	10359	876	6245	137
H(21A)	5622	8865	3593	193
H(21B)	5737	9862	3541	193
H(21C)	6763	9398	3822	193
H(21D)	5622	8865	3593	193
H(21E)	5738	9862	3541	193
H(21F)	6763	9398	3822	193
H(22A)	8502	9842	2866	79
H(22B)	7976	10489	3163	79
H(22C)	6804	10077	2902	79
H(23A)	7736	8300	2875	128
H(23B)	6048	8499	2952	128
H(23C)	6947	7892	3209	128
H(24A)	9654	8849	3192	59
H(24B)	8932	8304	3500	59
H(24C)	9480	9243	3576	59
H(22D)	7045	10415	3067	77
H(22E)	8756	10285	3140	77
H(22F)	7673	10505	3458	77
H(23D)	5911	9222	2923	68
H(23E)	5947	8368	3145	68
H(23F)	7166	8540	2851	68
H(24D)	8755	9529	3678	140
H(24E)	9342	8767	3442	140
H(24F)	8035	8615	3715	140

Bis(tetraethylammonium) tetrathiotungstate

Table 1. Crystal data and structure refinement for bis(tetraethylammonium) tetrathiotungstate.

Identification code	pw200	
Empirical formula	$C_{16}H_{40}N_2S_4W$	
Formula weight	572.59	
Temperature	293(2) K	
Wavelength	0.71073 Å	
Crystal system	Monoclinic	
Space group	$P2_1/n$	
Unit cell dimensions	a = 16.6695(12) Å	α= 90°.
	b = 9.3415(6) Å	β= 117.185(8)°.
	c = 16.9965(13) Å	γ = 90°.
Volume	2354.3(3) $Å^3$	
Z	4	
Density (calculated)	1.615 Mg/m^3	
Absorption coefficient	5.263 mm^{-1}	
F(000)	1152	
Crystal size	15 x 24 x 30 mm^3	
Theta range for data collection	2.32 to 28.04°.	
Index ranges	-22<=h<=22, -12<=k<=11, -22<=l<=22	
Reflections collected	22222	
Independent reflections	5644 [R(int) = 0.0410]	
Completeness to theta = 28.04°	98.9 %	
Refinement method	Full-matrix least-squares on F^2	
Data / restraints / parameters	5644 / 0 / 225	
Goodness-of-fit on F^2	1.034	
Final R indices [I>2sigma(I)]	R1 = 0.0294, wR2 = 0.0694	
R indices (all data)	R1 = 0.0459, wR2 = 0.0744	
Extinction coefficient	0.0090(3)	
Largest diff. peak and hole	1.067 and -1.047 e.$Å^{-3}$	

Table 2. Atomic coordinates (x 10^4) and equivalent isotropic displacement parameters ($Å^2$ x 10^3).
U(eq) is defined as one third of the trace of the orthogonalized U_{ij} tensor.

	x	y	z	U(eq)
W(1)	7421(1)	2412(1)	5097(1)	29(1)
S(1)	6598(1)	2264(2)	5804(1)	49(1)
S(2)	6616(1)	3356(2)	3791(1)	53(1)
S(3)	7859(1)	279(1)	4912(1)	55(1)
S(4)	8602(1)	3741(2)	5865(1)	64(1)
N(1)	6344(2)	7378(3)	6254(2)	31(1)
C(1)	5663(4)	6284(6)	6238(4)	44(1)
C(1')	6557(16)	6720(30)	7139(16)	45(5)
C(2)	5810(4)	5801(8)	7148(4)	75(2)
C(3)	6418(4)	8636(6)	6830(4)	45(1)
C(3')	5489(15)	8320(20)	5970(15)	40(5)
C(4)	5521(4)	9396(6)	6600(4)	60(1)
C(5)	6045(4)	7912(7)	5311(4)	44(1)
C(5')	6157(18)	6260(30)	5552(16)	50(6)
C(6)	6032(5)	6811(9)	4671(4)	83(2)
C(7)	7262(4)	6627(7)	6625(5)	48(1)
C(7')	7125(15)	8350(20)	6382(15)	41(5)
C(8)	7998(4)	7504(7)	6592(6)	76(2)
N(2)	9118(2)	2447(3)	3228(2)	31(1)
C(11)	8100(3)	2262(6)	2755(3)	48(1)
C(12)	7698(4)	2018(7)	1761(4)	60(1)
C(13)	9417(3)	3645(5)	2818(3)	39(1)
C(14)	8966(4)	5071(5)	2752(4)	56(1)
C(15)	9348(3)	2773(5)	4182(3)	43(1)
C(16)	10350(4)	2980(7)	4797(3)	60(1)
C(17)	9590(3)	1098(5)	3152(3)	42(1)
C(18)	9428(5)	-241(6)	3569(4)	64(2)

Table 3. Bond lengths [Å] and angles [°].

W(1)-S(4)	2.1846(12)	C(1')-N(1)-C(1)	64.9(10)
W(1)-S(2)	2.1867(12)	C(7')-N(1)-C(1)	171.6(9)
W(1)-S(3)	2.1933(12)	C(3)-N(1)-C(5)	108.6(4)
W(1)-S(1)	2.2030(12)	C(5')-N(1)-C(5)	63.0(10)
N(1)-C(3)	1.498(6)	C(1')-N(1)-C(5)	173.3(10)
N(1)-C(5')	1.51(3)	C(7')-N(1)-C(5)	78.7(9)
N(1)-C(1')	1.51(2)	C(1)-N(1)-C(5)	108.5(4)
N(1)-C(7')	1.52(2)	C(3)-N(1)-C(7)	108.8(4)
N(1)-C(1)	1.519(6)	C(5')-N(1)-C(7)	79.3(10)
N(1)-C(5)	1.527(6)	C(1')-N(1)-C(7)	70.5(10)
N(1)-C(7)	1.533(7)	C(7')-N(1)-C(7)	65.4(9)
N(1)-C(3')	1.55(2)	C(1)-N(1)-C(7)	107.2(4)
C(1)-C(2)	1.520(8)	C(5)-N(1)-C(7)	111.6(4)
C(1')-C(2)	1.52(2)	C(3)-N(1)-C(3')	63.2(9)
C(3)-C(4)	1.536(8)	C(5')-N(1)-C(3')	108.5(13)
C(3')-C(4)	1.45(2)	C(1')-N(1)-C(3')	107.7(13)
C(5)-C(6)	1.490(9)	C(7')-N(1)-C(3')	108.4(12)
C(5')-C(6)	1.50(3)	C(1)-N(1)-C(3')	78.5(9)
C(7)-C(8)	1.497(8)	C(5)-N(1)-C(3')	71.1(9)
C(7')-C(8)	1.55(2)	C(7)-N(1)-C(3')	171.8(9)
N(2)-C(15)	1.517(5)	N(1)-C(1)-C(2)	114.3(5)
N(2)-C(13)	1.518(5)	N(1)-C(1')-C(2)	114.9(15)
N(2)-C(11)	1.519(5)	C(1')-C(2)-C(1)	64.7(9)
N(2)-C(17)	1.521(5)	N(1)-C(3)-C(4)	114.6(4)
C(11)-C(12)	1.524(7)	C(4)-C(3')-N(1)	116.3(14)
C(13)-C(14)	1.508(7)	C(3')-C(4)-C(3)	64.6(9)
C(15)-C(16)	1.525(7)	C(6)-C(5)-N(1)	115.4(5)
C(17)-C(18)	1.521(7)	C(6)-C(5')-N(1)	115.7(17)
S(4)-W(1)-S(2)	110.21(6)	C(5)-C(6)-C(5')	64.0(10)
S(4)-W(1)-S(3)	109.52(6)	C(8)-C(7)-N(1)	114.5(5)
S(2)-W(1)-S(3)	108.12(5)	N(1)-C(7')-C(8)	112.7(14)
S(4)-W(1)-S(1)	109.00(5)	C(7)-C(8)-C(7')	65.6(9)
S(2)-W(1)-S(1)	109.40(5)	C(15)-N(2)-C(13)	111.5(3)
S(3)-W(1)-S(1)	110.59(5)	C(15)-N(2)-C(11)	105.3(3)
C(3)-N(1)-C(5')	170.5(10)	C(13)-N(2)-C(11)	111.2(3)
C(3)-N(1)-C(1')	76.0(10)	C(15)-N(2)-C(17)	111.7(3)
C(5')-N(1)-C(1')	111.9(14)	C(13)-N(2)-C(17)	106.3(3)
C(3)-N(1)-C(7')	68.3(9)	C(11)-N(2)-C(17)	110.9(3)
C(5')-N(1)-C(7')	112.4(14)	N(2)-C(11)-C(12)	115.0(4)
C(1')-N(1)-C(7')	107.8(13)	C(14)-C(13)-N(2)	115.4(4)
C(3)-N(1)-C(1)	112.1(4)	N(2)-C(15)-C(16)	114.8(4)
C(5')-N(1)-C(1)	68.7(11)	C(18)-C(17)-N(2)	115.6(4)

Table 4. Anisotropic displacement parameters ($Å^2 \times 10^3$).

The anisotropic displacement factor exponent takes the form: $-2\pi^2[h^2 a^{*2} U_{11} + ... + 2 h k a^* b^* U_{12}]$

	U_{11}	U_{22}	U_{33}	U_{23}	U_{13}	U_{12}
W(1)	33(1)	29(1)	31(1)	0(1)	19(1)	-3(1)
S(1)	48(1)	68(1)	46(1)	2(1)	34(1)	-6(1)
S(2)	62(1)	59(1)	42(1)	18(1)	27(1)	18(1)
S(3)	71(1)	34(1)	73(1)	5(1)	43(1)	11(1)
S(4)	62(1)	78(1)	62(1)	-28(1)	35(1)	-42(1)
N(1)	31(2)	30(2)	34(2)	3(1)	15(1)	-3(1)
C(1)	40(3)	41(3)	51(3)	3(2)	22(3)	-9(2)
C(2)	57(3)	82(5)	86(4)	43(4)	32(3)	-5(3)
C(3)	47(3)	41(3)	46(3)	-7(2)	20(3)	-4(2)
C(4)	74(4)	50(3)	74(4)	-3(3)	49(3)	14(3)
C(5)	52(3)	50(3)	34(3)	9(2)	22(2)	3(3)
C(6)	110(6)	104(6)	52(3)	-23(3)	51(4)	-13(4)
C(7)	42(3)	43(3)	63(4)	9(3)	28(3)	5(2)
C(8)	39(3)	72(4)	121(6)	12(4)	41(3)	0(3)
N(2)	29(2)	35(2)	34(2)	-1(1)	19(1)	-2(1)
C(11)	31(2)	66(3)	51(3)	3(2)	23(2)	-3(2)
C(12)	47(3)	74(4)	47(3)	3(3)	10(2)	-9(3)
C(13)	42(2)	43(3)	42(2)	7(2)	27(2)	0(2)
C(14)	63(3)	40(3)	67(3)	6(2)	31(3)	4(2)

C(15)	55(3)	44(3)	36(2)	-5(2)	27(2)	-2(2)
C(16)	65(3)	63(3)	37(2)	-7(2)	10(2)	-14(3)
C(17)	43(2)	39(2)	48(3)	-2(2)	25(2)	4(2)
C(18)	96(5)	38(3)	55(3)	4(2)	33(3)	2(3)

Table 5. Coordinates of H atoms (x 10^4) and isotropic displacement parameters (Å^2 x 10^3).

	x	y	z	U(eq)
H(1A)	5688	5452	5909	52
H(1B)	5064	6690	5925	52
H(1C)	6695	7478	7569	55
H(1D)	7094	6132	7325	55
H(2A)	5357	5112	7086	113
H(2B)	5769	6612	7475	113
H(2C)	6396	5373	7459	113
H(2D)	5714	4980	6776	113
H(2E)	5264	6351	6934	113
H(2F)	5979	5491	7742	113
H(3A)	6832	9324	6787	54
H(3B)	6675	8315	7439	54
H(3C)	5370	8792	5421	48
H(3D)	4982	7687	5849	48
H(4A)	5625	10184	6998	90
H(4B)	5110	8733	6656	90
H(4C)	5267	9745	6004	90
H(4D)	5974	10093	6677	90
H(4E)	5666	8949	7158	90
H(4F)	4944	9858	6381	90
H(5A)	5444	8313	5091	53
H(5B)	6445	8680	5330	53
H(5C)	6653	5582	5772	60
H(5D)	5618	5740	5460	60
H(6A)	5838	7243	4101	125
H(6B)	5622	6058	4629	125
H(6C)	6626	6422	4872	125
H(6D)	5476	7336	4391	125
H(6E)	6013	6020	4303	125
H(6F)	6525	7429	4758	125
H(7A)	7442	6363	7235	58
H(7B)	7195	5751	6294	58
H(7C)	7239	9007	6861	49
H(7D)	6959	8904	5848	49
H(8A)	8548	6961	6833	114
H(8B)	8084	8362	6933	114
H(8C)	7834	7752	5990	114
H(8D)	8262	7178	7194	114
H(8E)	8417	8116	6511	114
H(8F)	7857	6696	6203	114
H(11A)	7825	3109	2858	57
H(11B)	7942	1455	3016	57
H(12A)	7056	1912	1517	91
H(12B)	7951	1165	1649	91
H(12C)	7834	2822	1490	91
H(13A)	10063	3770	3165	47
H(13B)	9303	3353	2229	47
H(14A)	9196	5758	2486	85
H(14B)	9088	5390	3333	85
H(14C)	8327	4972	2395	85
H(15A)	9127	1996	4409	51
H(15B)	9030	3636	4195	51
H(16A)	10436	3184	5383	90
H(16B)	10574	3763	4588	90
H(16C)	10671	2122	4805	90
H(17A)	9395	909	2530	51
H(17B)	10234	1281	3425	51
H(18A)	9753	-1029	3490	96
H(18B)	8795	-458	3291	96
H(18C)	9633	-80	4189	96

Bis(tetrapropylammonium) tetrathiotungstate

Table 1. Crystal data and structure refinement for bis(tetrapropylammonium) tetrathiotungstate.

Identification code	pw300	
Empirical formula	$C_{24}H_{56}N_2S_4W$	
Formula weight	684.80	
Temperature	293(2) K	
Wavelength	0.71073 Å	
Crystal system	monoclinic	
Space group	C2/c	
Unit cell dimensions	a = 32.440(2) Å	a= 90°.
	b = 13.8453(6) Å	b= 109.191(7)°.
	c = 15.0563(10) Å	g = 90°.
Volume	6386.7(7) $Å^3$	
Z	8	
Density (calculated)	1.424 Mg/m^3	
Absorption coefficient	3.893 mm^{-1}	
F(000)	2816	
Crystal size	0.5 x 0.5 x 0.25 mm^3	
Theta range for data collection	2.48 to 28.04°.	
Index ranges	-42<=h<=42, -16<=k<=17, -18<=l<=19	
Reflections collected	30476	
Independent reflections	7615 [R(int) = 0.0534]	
Completeness to theta = 28.04°	98.4 %	
Refinement method	Full-matrix least-squares on F^2	
Data / restraints / parameters	7615 / 0 / 318	
Goodness-of-fit on F^2	1.034	
Final R indices [I>2sigma(I)]	R1 = 0.0300, wR2 = 0.0610	
R indices (all data)	R1 = 0.0486, wR2 = 0.0664	
Extinction coefficient	0.00069(4)	
Largest diff. peak and hole	0.526 and -0.708 e.$Å^{-3}$	

Table 2. Atomic coordinates (x 10^4) and equivalent isotropic displacement parameters ($Å^2$ x 10^3).
U(eq) is defined as one third of the trace of the orthogonalized U_{ij} tensor.

	x	y	z	U(eq)
W(1)	3732(1)	7429(1)	4145(1)	37(1)
S(1)	4194(1)	6679(1)	3594(1)	52(1)
S(2)	3164(1)	7934(1)	2979(1)	56(1)
S(3)	3503(1)	6434(1)	5006(1)	63(1)
S(4)	4056(1)	8661(1)	5009(1)	61(1)
N(1)	2550(1)	4887(2)	6029(2)	35(1)
C(1)	2487(1)	5319(3)	5061(3)	37(1)
C(2)	2196(1)	6197(3)	4786(3)	45(1)
C(3)	2177(1)	6533(3)	3812(3)	50(1)
C(4)	2112(1)	4628(3)	6140(3)	44(1)
C(5)	1833(2)	3936(4)	5417(3)	59(1)
C(6)	1417(2)	3711(4)	5636(4)	65(1)
C(7)	2772(1)	5633(3)	6776(3)	43(1)
C(8)	2881(2)	5288(4)	7792(3)	66(1)
C(9)	3095(3)	6079(5)	8459(4)	100(2)
C(10)	2830(1)	3978(3)	6141(3)	42(1)
C(11)	3310(1)	4142(3)	6273(3)	48(1)
C(12)	3513(2)	3194(3)	6112(3)	53(1)
N(2)	5000	9107(3)	2500	38(1)
C(21)	5069(1)	8462(3)	3354(3)	40(1)
C(22)	5114(2)	8972(3)	4270(3)	54(1)
C(23)	5206(2)	8247(4)	5072(3)	60(1)
C(24)	5395(1)	9761(3)	2641(3)	46(1)
C(25)	5825(1)	9247(4)	2787(4)	59(1)

C(26)	6177(2)	9966(4)	2788(4)	80(2)
N(3)	5000	4222(3)	2500	46(1)
C(31)	5228(3)	5063(8)	3197(7)	51(2)
C(32)	5420(4)	4812(9)	4219(8)	71(3)
C(31')	5127(3)	4574(7)	3475(6)	50(2)
C(32')	5487(3)	5337(8)	3732(7)	61(2)
C(33)	5592(2)	5638(5)	4782(4)	86(2)
C(34)	5345(3)	3395(7)	2658(6)	49(2)
C(35)	5764(3)	3630(9)	2494(7)	65(3)
C(34')	5366(3)	3844(8)	2198(8)	58(2)
C(35')	5614(4)	3006(10)	2734(10)	85(4)
C(36)	6022(2)	2760(6)	2538(4)	97(2)

Table 3. Bond lengths [Å] and angles [°].

W(1)-S(3)	2.1836(11)	C(4)-C(5)-C(6)	109.7(4)
W(1)-S(4)	2.1918(11)	N(1)-C(7)-C(8)	115.2(3)
W(1)-S(1)	2.1979(10)	C(9)-C(8)-C(7)	110.4(4)
W(1)-S(2)	2.2001(11)	C(11)-C(10)-N(1)	115.9(3)
N(1)-C(7)	1.522(4)	C(10)-C(11)-C(12)	109.1(3)
N(1)-C(1)	1.525(4)	C(21)-N(2)-C(21)#1	108.1(4)
N(1)-C(4)	1.529(4)	C(21)-N(2)-C(24)#1	110.5(2)
N(1)-C(10)	1.529(5)	C(21)#1-N(2)-C(24)#1	110.3(2)
C(1)-C(2)	1.511(5)	C(21)-N(2)-C(24)	110.3(2)
C(2)-C(3)	1.520(5)	C(21)#1-N(2)-C(24)	110.5(2)
C(4)-C(5)	1.507(6)	C(24)#1-N(2)-C(24)	107.2(4)
C(5)-C(6)	1.525(6)	C(22)-C(21)-N(2)	116.1(3)
C(7)-C(8)	1.529(6)	C(21)-C(22)-C(23)	110.5(4)
C(8)-C(9)	1.493(7)	C(25)-C(24)-N(2)	115.6(3)
C(10)-C(11)	1.519(5)	C(26)-C(25)-C(24)	110.5(4)
C(11)-C(12)	1.523(6)	C(31')-N(3)-C(31')#1	141.2(9)
N(2)-C(21)	1.520(4)	C(31')-N(3)-C(34')#1	78.7(6)
N(2)-C(21)#1	1.520(4)	C(31')#1-N(3)-C(34')#1	115.3(5)
N(2)-C(24)#1	1.526(4)	C(31')-N(3)-C(34')	115.3(5)
N(2)-C(24)	1.526(4)	C(31')#1-N(3)-C(34')	78.7(6)
C(21)-C(22)	1.513(6)	C(34')#1-N(3)-C(34')	139.1(10)
C(22)-C(23)	1.522(6)	C(31')-N(3)-C(34)#1	110.3(5)
C(24)-C(25)	1.517(6)	C(31')#1-N(3)-C(34)#1	98.0(5)
C(25)-C(26)	1.514(6)	C(34')#1-N(3)-C(34)#1	36.0(5)
N(3)-C(31')	1.471(9)	C(34')-N(3)-C(34)#1	107.3(7)
N(3)-C(31')#1	1.471(9)	C(31')-N(3)-C(34)	98.0(5)
N(3)-C(34')#1	1.499(9)	C(31')#1-N(3)-C(34)	110.3(5)
N(3)-C(34')	1.499(9)	C(34')#1-N(3)-C(34)	107.3(7)
N(3)-C(34)#1	1.564(10)	C(34')-N(3)-C(34)	36.0(5)
N(3)-C(34)	1.564(10)	C(34)#1-N(3)-C(34)	85.9(7)
N(3)-C(31)	1.580(10)	C(31')-N(3)-C(31)	34.5(4)
N(3)-C(31)#1	1.580(10)	C(31')#1-N(3)-C(31)	109.5(7)
C(31)-C(32)	1.499(14)	C(34')#1-N(3)-C(31)	107.5(6)
C(32)-C(33)	1.424(12)	C(34')-N(3)-C(31)	102.4(5)
C(31')-C(32')	1.528(12)	C(34)#1-N(3)-C(31)	142.7(5)
C(31')-C(34')#1	1.883(13)	C(34)-N(3)-C(31)	106.5(5)
C(32')-C(33)	1.561(11)	C(31')-N(3)-C(31)#1	109.5(7)
C(34)-C(35)	1.496(14)	C(31')#1-N(3)-C(31)#1	34.5(4)
C(35)-C(36)	1.455(12)	C(34')#1-N(3)-C(31)#1	102.4(5)
C(34')-C(35')	1.488(16)	C(34')-N(3)-C(31)#1	107.5(6)
C(34')-C(31')#1	1.883(13)	C(34)#1-N(3)-C(31)#1	106.5(5)
C(35')-C(36)	1.486(13)	C(34)-N(3)-C(31)#1	142.7(5)
S(3)-W(1)-S(4)	109.17(5)	C(31)-N(3)-C(31)#1	84.9(8)
S(3)-W(1)-S(1)	109.48(5)	C(32)-C(31)-N(3)	117.1(9)
S(4)-W(1)-S(1)	109.79(4)	C(33)-C(32)-C(31)	111.9(10)
S(3)-W(1)-S(2)	108.30(5)	N(3)-C(31')-C(32')	115.0(8)
S(4)-W(1)-S(2)	109.83(5)	N(3)-C(31')-C(34')#1	51.3(4)
S(1)-W(1)-S(2)	110.24(4)	C(32')-C(31')-C(34')#1	162.2(9)
C(7)-N(1)-C(1)	108.8(3)	C(31')-C(32')-C(33)	109.6(8)
C(7)-N(1)-C(4)	108.0(3)	C(32)-C(33)-C(32')	43.1(6)

C(1)-N(1)-C(4)	111.0(3)	C(35)-C(34)-N(3)	117.4(8)
C(7)-N(1)-C(10)	111.0(3)	C(36)-C(35)-C(34)	110.6(10)
C(1)-N(1)-C(10)	108.4(3)	C(35')-C(34')-N(3)	116.6(10)
C(4)-N(1)-C(10)	109.6(3)	C(35')-C(34')-C(31')#1	157.3(10)
C(2)-C(1)-N(1)	117.0(3)	N(3)-C(34')-C(31')#1	50.0(4)
C(1)-C(2)-C(3)	109.5(3)	C(36)-C(35')-C(34')	115.3(12)
C(5)-C(4)-N(1)	115.4(3)	C(35)-C(36)-C(35')	44.3(6)

Symmetry transformations used to generate equivalent atoms:
#1 -x+1, y, -z+1/2

Table 4. Anisotropic displacement parameters ($Å^2 \times 10^3$).
The anisotropic displacement factor exponent takes the form: $-2\pi^2[h^2 a^{*2} U11 + ... + 2 h k a^* b^* U12]$

	U11	U22	U33	U23	U13	U12
W(1)	35(1)	38(1)	39(1)	-6(1)	15(1)	-6(1)
S(1)	46(1)	55(1)	59(1)	-6(1)	24(1)	7(1)
S(2)	51(1)	68(1)	46(1)	-8(1)	10(1)	17(1)
S(3)	58(1)	67(1)	69(1)	11(1)	29(1)	-18(1)
S(4)	62(1)	56(1)	67(1)	-26(1)	25(1)	-21(1)
N(1)	40(2)	30(2)	36(2)	-2(1)	16(1)	-5(1)
C(1)	41(2)	38(2)	35(2)	2(1)	17(1)	-3(2)
C(2)	49(2)	42(2)	45(2)	4(2)	15(2)	6(2)
C(3)	47(2)	52(3)	49(2)	11(2)	12(2)	1(2)
C(4)	52(2)	41(2)	47(2)	-3(2)	30(2)	-9(2)
C(5)	53(3)	62(3)	68(3)	-17(2)	29(2)	-18(2)
C(6)	52(3)	61(3)	93(4)	-9(2)	39(3)	-14(2)
C(7)	53(2)	36(2)	40(2)	-5(2)	15(2)	-8(2)
C(8)	96(4)	61(3)	37(2)	-3(2)	16(2)	-14(3)
C(9)	139(6)	107(5)	40(3)	-16(3)	10(3)	-47(4)
C(10)	51(2)	32(2)	44(2)	2(2)	17(2)	2(2)
C(11)	44(2)	44(2)	51(2)	3(2)	10(2)	0(2)
C(12)	56(2)	51(3)	52(2)	1(2)	20(2)	10(2)
N(2)	43(2)	30(2)	42(2)	0	17(2)	0
C(21)	37(2)	37(2)	47(2)	6(2)	15(2)	0(2)
C(22)	63(3)	56(3)	44(2)	3(2)	20(2)	-1(2)
C(23)	52(2)	78(3)	46(2)	13(2)	11(2)	-1(2)
C(24)	54(2)	39(2)	44(2)	-4(2)	18(2)	-11(2)
C(25)	44(2)	62(3)	76(3)	-11(2)	25(2)	-12(2)
C(26)	65(3)	91(4)	94(4)	-21(3)	40(3)	-31(3)
N(3)	48(3)	42(3)	55(3)	0	27(2)	0
C(31)	53(5)	51(6)	58(5)	-8(4)	28(5)	0(4)
C(32)	63(6)	83(8)	64(6)	-18(6)	17(5)	-1(5)
C(31')	53(5)	53(6)	50(5)	-5(4)	25(4)	-10(4)
C(32')	57(6)	74(7)	53(5)	-16(5)	19(5)	-26(5)
C(33)	106(5)	93(5)	62(3)	-21(3)	32(3)	-20(4)
C(34)	65(6)	35(5)	47(5)	4(4)	20(4)	5(4)
C(35)	63(6)	79(8)	58(6)	14(5)	28(5)	23(5)
C(34')	41(5)	65(7)	68(6)	-10(5)	19(4)	2(4)
C(35')	68(7)	80(9)	102(9)	-1(7)	23(7)	31(7)
C(36)	63(3)	142(6)	81(4)	-27(4)	17(3)	30(4)

Table 5. Coordinates of H atoms ($\times 10^4$) and isotropic displacement parameters ($Å^2 \times 10^3$).

	x	y	z	U(eq)
H(1A)	2772	5489	5031	44
H(1B)	2368	4821	4595	44
H(2A)	2310	6711	5238	54
H(2B)	1905	6039	4785	54
H(3A)	1995	7095	3640	76
H(3B)	2059	6027	3365	76
H(3C)	2466	6689	3816	76
H(4A)	2166	4348	6758	52

H(4B)	1947	5219	6114	52
H(5A)	1994	3344	5423	70
H(5B)	1760	4220	4795	70
H(6A)	1241	3265	5178	97
H(6B)	1255	4297	5616	97
H(6C)	1491	3430	6251	97
H(7A)	2583	6193	6686	52
H(7B)	3039	5839	6679	52
H(8A)	2616	5088	7904	79
H(8B)	3075	4736	7898	79
H(9A)	3167	5849	9094	150
H(9B)	2899	6617	8367	150
H(9C)	3357	6278	8345	150
H(10A)	2810	3619	6678	51
H(10B)	2707	3577	5588	51
H(11A)	3459	4376	6904	57
H(11B)	3339	4625	5829	57
H(12A)	3815	3295	6192	79
H(12B)	3364	2968	5486	79
H(12C)	3486	2723	6558	79
H(21A)	4826	8017	3220	48
H(21B)	5331	8081	3441	48
H(22A)	4847	9319	4213	65
H(22B)	5350	9437	4406	65
H(23A)	5233	8581	5647	90
H(23B)	5474	7912	5135	90
H(23C)	4971	7791	4940	90
H(24A)	5337	10179	2096	55
H(24B)	5426	10171	3182	55
H(25A)	5911	8903	3380	71
H(25B)	5791	8780	2288	71
H(26A)	6446	9630	2874	120
H(26B)	6216	10419	3291	120
H(26C)	6092	10305	2199	120
H(31A)	5458	5328	2992	62
H(31B)	5014	5572	3136	62
H(32A)	5197	4518	4429	85
H(32B)	5652	4342	4300	85
H(31C)	5223	4028	3896	60
H(31D)	4871	4843	3581	60
H(32C)	5393	5898	3330	73
H(32D)	5748	5079	3637	73
H(33A)	5712	5448	5429	129
H(33B)	5362	6099	4714	129
H(33C)	5816	5925	4582	129
H(34A)	5415	3169	3300	58
H(34B)	5209	2862	2248	58
H(35A)	5703	3930	1882	78
H(35B)	5930	4086	2967	78
H(34C)	5247	3660	1542	70
H(34D)	5571	4367	2241	70
H(35C)	5688	3141	3401	101
H(35D)	5425	2445	2596	101
H(36A)	6290	2924	2435	145
H(36B)	5860	2315	2061	145
H(36C)	6085	2466	3145	145

Bis(diethylenetriamine)cobalt(II) tetrathiomolybdate(VI) oxotrithiamolybdate(IV)

Table 1. Crystal data and structure refinement for bis(diethylenetriamine)cobalt(II) tetrathiomolybdate(VI) oxotrithiamolybdate(IV).

Identification code	p1050a	
Empirical formula	$C_8H_{26}CoMoN_6O_{0.50}S_{3.50}$	
Formula weight	481.43	
Temperature	293(2) K	
Wavelength	0.71073 Å	
Crystal system	monoclinic	
Space group	$P2_1/n$	
Unit cell dimensions	a = 7.4164(5) Å	α= 90°.
	b = 15.9171(11) Å	β= 93.063(9)°.
	c = 15.4070(12) Å	γ = 90°.
Volume	1816.2(2) $Å^3$	
Z	4	
Density (calculated)	1.761 mg/m^3	
Absorption coefficient	2.007 mm^{-1}	
F(000)	980	
Crystal size	0.27 x 0.28 x 0.28 mm^3	
Theta range for data collection	2.56 to 25.68°.	
Index ranges	-8<=h<=8, -19<=k<=19, -18<=l<=18	
Reflections collected	11766	
Independent reflections	3269 [R(int) = 0.0475]	
Completeness to theta = 25.68°	95.0 %	
Refinement method	Full-matrix least-squares on F^2	
Data / restraints / parameters	3269 / 0 / 191	
Goodness-of-fit on F^2	1.024	
Final R indices [I>2sigma(I)]	R1 = 0.0408, wR2 = 0.0905	
R indices (all data)	R1 = 0.0628, wR2 = 0.0985	
Extinction coefficient	0.0022(6)	
Largest diff. peak and hole	0.551 and -0.601 e.$Å^{-3}$	

Table 2. Atomic coordinates (x 10^4) and equivalent isotropic displacement parameters ($Å^2$ x 10^3). U(eq) is defined as one third of the trace of the orthogonalized U_{ij} tensor.

	x	y	z	U(eq)
Mo(1)	6041(1)	3919(1)	7007(1)	42(1)
S(1)	5524(2)	3873(1)	8401(1)	52(1)
S(2)	3463(2)	3850(1)	6258(1)	57(1)
S(3)	7703(3)	2854(1)	6633(1)	72(1)
S(4)	7172(9)	5013(4)	6591(4)	55(1)
O(1)	7200(30)	4902(11)	6917(9)	68(5)
Co(1)	2224(1)	6320(1)	7433(1)	33(1)
N(1)	1203(6)	5070(3)	7743(3)	44(1)
C(1)	644(9)	5033(4)	8646(4)	56(2)
C(2)	19(9)	5897(4)	8936(4)	61(2)
N(2)	1289(6)	6570(3)	8715(2)	43(1)
C(3)	2877(8)	6695(4)	9322(3)	55(2)
C(4)	4408(8)	6096(4)	9153(3)	55(2)
N(3)	4732(6)	6078(3)	8217(2)	41(1)
N(11)	-308(6)	6593(3)	6700(3)	50(1)
C(11)	-24(9)	6554(4)	5760(3)	62(2)
C(12)	1432(9)	5930(4)	5574(3)	61(2)
N(12)	3083(7)	6055(3)	6149(2)	46(1)
C(13)	4338(10)	6720(4)	5890(4)	67(2)
C(14)	3953(12)	7563(4)	6228(4)	79(2)
N(13)	3297(6)	7559(3)	7104(3)	45(1)

Table 3. Bond lengths [Å] and angles [°].

Mo(1)-O(1)	1.796(17)	H(1N)-N(1)-H(2N)	108.0
Mo(1)-S(4)	2.050(6)	N(1)-C(1)-C(2)	110.3(4)
Mo(1)-S(2)	2.1826(16)	N(1)-C(1)-H(1A)	109.6
Mo(1)-S(3)	2.1908(16)	C(2)-C(1)-H(1A)	109.6
Mo(1)-S(1)	2.2041(14)	N(1)-C(1)-H(1B)	109.6
Co(1)-N(12)	2.152(4)	C(2)-C(1)-H(1B)	109.6
Co(1)-N(2)	2.164(4)	H(1A)-C(1)-H(1B)	108.1
Co(1)-N(11)	2.182(4)	N(2)-C(2)-C(1)	112.3(5)
Co(1)-N(1)	2.191(4)	N(2)-C(2)-H(2A)	109.2
Co(1)-N(13)	2.196(4)	C(1)-C(2)-H(2A)	109.2
Co(1)-N(3)	2.197(4)	N(2)-C(2)-H(2B)	109.2
N(1)-C(1)	1.474(7)	C(1)-C(2)-H(2B)	109.2
N(1)-H(1N)	0.9000	H(2A)-C(2)-H(2B)	107.9
N(1)-H(2N)	0.9000	C(3)-N(2)-C(2)	116.6(4)
C(1)-C(2)	1.524(8)	C(3)-N(2)-Co(1)	108.6(3)
C(1)-H(1A)	0.9700	C(2)-N(2)-Co(1)	108.4(3)
C(1)-H(1B)	0.9700	C(3)-N(2)-H(3N)	107.6
C(2)-N(2)	1.479(7)	C(2)-N(2)-H(3N)	107.6
C(2)-H(2A)	0.9700	Co(1)-N(2)-H(3N)	107.6
C(2)-H(2B)	0.9700	N(2)-C(3)-C(4)	112.7(4)
N(2)-C(3)	1.478(7)	N(2)-C(3)-H(3A)	109.1
N(2)-H(3N)	0.9100	C(4)-C(3)-H(3A)	109.1
C(3)-C(4)	1.516(8)	N(2)-C(3)-H(3B)	109.1
C(3)-H(3A)	0.9700	C(4)-C(3)-H(3B)	109.1
C(3)-H(3B)	0.9700	H(3A)-C(3)-H(3B)	107.8
C(4)-N(3)	1.474(6)	N(3)-C(4)-C(3)	110.1(4)
C(4)-H(4A)	0.9700	N(3)-C(4)-H(4A)	109.6
C(4)-H(4B)	0.9700	C(3)-C(4)-H(4A)	109.6
N(3)-H(4N)	0.9000	N(3)-C(4)-H(4B)	109.6
N(3)-H(5N)	0.9000	C(3)-C(4)-H(4B)	109.6
N(11)-C(11)	1.476(7)	H(4A)-C(4)-H(4B)	108.2
N(11)-H(6N)	0.9000	C(4)-N(3)-Co(1)	110.9(3)
N(11)-H(7N)	0.9000	C(4)-N(3)-H(4N)	109.5
C(11)-C(12)	1.506(9)	Co(1)-N(3)-H(4N)	109.5
C(11)-H(11A)	0.9700	C(4)-N(3)-H(5N)	109.5
C(11)-H(11B)	0.9700	Co(1)-N(3)-H(5N)	109.5
C(12)-N(12)	1.486(7)	H(4N)-N(3)-H(5N)	108.1
C(12)-H(12A)	0.9700	C(11)-N(11)-Co(1)	109.6(3)
C(12)-H(12B)	0.9700	C(11)-N(11)-H(6N)	109.7
N(12)-C(13)	1.478(7)	Co(1)-N(11)-H(6N)	109.7
N(12)-H(8N)	0.9100	C(11)-N(11)-H(7N)	109.7
C(13)-C(14)	1.473(9)	Co(1)-N(11)-H(7N)	109.7
C(13)-H(13A)	0.9700	H(6N)-N(11)-H(7N)	108.2
C(13)-H(13B)	0.9700	N(11)-C(11)-C(12)	110.9(4)
C(14)-N(13)	1.459(7)	N(11)-C(11)-H(11A)	109.5
C(14)-H(14A)	0.9700	C(12)-C(11)-H(11A)	109.5
C(14)-H(14B)	0.9700	N(11)-C(11)-H(11B)	109.5
N(13)-H(9N)	0.9000	C(12)-C(11)-H(11B)	109.5
N(13)-H(10N)	0.9000	H(11A)-C(11)-H(11B)	108.1
O(1)-Mo(1)-S(4)	14.0(5)	N(12)-C(12)-C(11)	112.0(4)
O(1)-Mo(1)-S(2)	114.5(5)	N(12)-C(12)-H(12A)	109.2
S(4)-Mo(1)-S(2)	103.84(19)	C(11)-C(12)-H(12A)	109.2
O(1)-Mo(1)-S(3)	112.0(7)	N(12)-C(12)-H(12B)	109.2
S(4)-Mo(1)-S(3)	109.2(2)	C(11)-C(12)-H(12B)	109.2
S(2)-Mo(1)-S(3)	108.11(7)	H(12A)-C(12)-H(12B)	107.9
O(1)-Mo(1)-S(1)	102.3(5)	C(13)-N(12)-C(12)	116.5(5)
S(4)-Mo(1)-S(1)	115.37(18)	C(13)-N(12)-Co(1)	109.2(3)
S(2)-Mo(1)-S(1)	108.71(6)	C(12)-N(12)-Co(1)	107.4(3)
S(3)-Mo(1)-S(1)	111.11(6)	C(13)-N(12)-H(8N)	107.8
N(12)-Co(1)-N(2)	178.43(18)	C(12)-N(12)-H(8N)	107.8
N(12)-Co(1)-N(11)	81.49(17)	Co(1)-N(12)-H(8N)	107.8
N(2)-Co(1)-N(11)	97.29(17)	C(14)-C(13)-N(12)	114.9(5)
N(12)-Co(1)-N(1)	98.35(16)	C(14)-C(13)-H(13A)	108.6
N(2)-Co(1)-N(1)	80.64(16)	N(12)-C(13)-H(13A)	108.6
N(11)-Co(1)-N(1)	89.79(18)	C(14)-C(13)-H(13B)	108.6
N(12)-Co(1)-N(13)	80.48(16)	N(12)-C(13)-H(13B)	108.6
N(2)-Co(1)-N(13)	100.55(16)	H(13A)-C(13)-H(13B)	107.5

N(11)-Co(1)-N(13)	90.77(18)	N(13)-C(14)-C(13)	113.7(5)
N(1)-Co(1)-N(13)	178.61(17)	N(13)-C(14)-H(14A)	108.8
N(12)-Co(1)-N(3)	100.80(17)	C(13)-C(14)-H(14A)	108.8
N(2)-Co(1)-N(3)	80.43(16)	N(13)-C(14)-H(14B)	108.8
N(11)-Co(1)-N(3)	177.54(16)	C(13)-C(14)-H(14B)	108.8
N(1)-Co(1)-N(3)	90.75(16)	H(14A)-C(14)-H(14B)	107.7
N(13)-Co(1)-N(3)	88.74(16)	C(14)-N(13)-Co(1)	111.2(3)
C(1)-N(1)-Co(1)	111.1(3)	C(14)-N(13)-H(9N)	109.4
C(1)-N(1)-H(1N)	109.4	Co(1)-N(13)-H(9N)	109.4
Co(1)-N(1)-H(1N)	109.4	C(14)-N(13)-H(10N)	109.4
C(1)-N(1)-H(2N)	109.4	Co(1)-N(13)-H(10N)	109.4
Co(1)-N(1)-H(2N)	109.4	H(9N)-N(13)-H(10N)	108.0

Table 4. Anisotropic displacement parameters ($Å^2 x 10^3$).

The anisotropic displacement factor exponent takes the form: $-2\pi^2[h^2 a^{*2} U_{11} + ... + 2 h k a^* b^* U_{12}]$

	U_{11}	U_{22}	U_{33}	U_{23}	U_{13}	U_{12}
Mo(1)	45(1)	45(1)	35(1)	9(1)	6(1)	7(1)
S(1)	72(1)	53(1)	31(1)	1(1)	-2(1)	-8(1)
S(2)	65(1)	63(1)	41(1)	-7(1)	-9(1)	18(1)
S(3)	71(1)	73(1)	71(1)	9(1)	10(1)	37(1)
S(4)	50(2)	43(2)	72(3)	7(2)	5(2)	-13(2)
O(1)	78(8)	50(6)	74(10)	27(7)	-2(8)	-24(5)
Co(1)	40(1)	39(1)	21(1)	1(1)	-1(1)	1(1)
N(1)	43(3)	45(2)	45(2)	-1(2)	1(2)	1(2)
C(1)	64(4)	55(3)	48(3)	15(3)	4(3)	-16(3)
C(2)	61(5)	79(4)	46(3)	4(3)	24(3)	-1(3)
N(2)	49(3)	53(2)	27(2)	1(2)	2(2)	8(2)
C(3)	70(4)	69(4)	26(2)	-11(2)	-6(2)	1(3)
C(4)	54(4)	71(4)	37(3)	4(3)	-18(2)	-3(3)
N(3)	44(3)	44(2)	34(2)	-3(2)	-6(2)	-4(2)
N(11)	55(3)	52(3)	42(2)	-2(2)	-6(2)	12(2)
C(11)	68(5)	75(4)	41(3)	8(3)	-20(3)	7(3)
C(12)	80(5)	77(4)	26(2)	-11(2)	-8(3)	2(3)
N(12)	62(3)	46(2)	31(2)	2(2)	9(2)	8(2)
C(13)	80(5)	73(4)	51(3)	-3(3)	33(3)	-3(3)
C(14)	107(7)	69(4)	65(4)	-9(3)	41(4)	-31(4)
N(13)	51(3)	45(2)	39(2)	5(2)	5(2)	5(2)

Table 5. Coordinates of H atoms ($x 10^4$) and isotropic displacement parameters ($Å^2 x 10^3$).

	x	y	z	U(eq)
H(1N)	255	4944	7377	53
H(2N)	2071	4685	7669	53
H(1A)	1649	4847	9026	67
H(1B)	-332	4632	8687	67
H(2A)	-1160	6015	8660	73
H(2B)	-103	5891	9559	73
H(3N)	661	7061	8687	52
H(3A)	2516	6616	9913	66
H(3B)	3303	7268	9270	66
H(4A)	5496	6275	9478	66
H(4B)	4104	5536	9347	66
H(4N)	5174	5572	8077	49
H(5N)	5559	6469	8099	49
H(6N)	-1153	6217	6836	60
H(7N)	-700	7108	6840	60
H(11A)	316	7105	5556	74
H(11B)	-1142	6392	5449	74
H(12A)	977	5365	5654	74
H(12B)	1739	5985	4973	74
H(8N)	3702	5561	6173	55
H(13A)	5554	6562	6089	81
H(13B)	4304	6746	5261	81

H(14A)	5047	7897	6228	95
H(14B)	3058	7832	5839	95
H(9N)	2423	7948	7141	54
H(10N)	4206	7695	7488	54

5.4 Literature

[1] K. Nakamoto, Infrared and Raman Spectra of Inorganic and Coordination Compounds, John Wiley, New York 1986.

[2] H. P. Klug, L. E. Alexander, X-ray diffraction procedures: for polycrystalline and amorphous materials, Wiley, New York 1974.

[3] C. Giacovazzo, Fundamentals of crystallography, Oxford Univ Press, Oxford 2002.

[4] W. Massa, Crystal Structure Determination, Springer, Berlin 2000.

[5] J. P. Glusker, M. Lewis, M. Rossi, Crystal Structure Analysis for Chemists and Biologists, VCH, New York 1994.

[6] G. M. Sheldrick, SHELXS97 and SHELXL97. University of Göttingen, Germany 1997.

[7] Diamond, Crystal Impact, Bonn, Germany

[8] W. F. Hemminger, H. K. Cammenga, Methoden der Thermischen Analyse, Springer, Berlin 1989.

[9] R. F. Speyer, Thermal Analysis of Materials, Dekker, New York 1994

[10] D. Giron, J. Therm. Anal. Cal., 64 (2001) 37.

[11] International Confederation of Thermal Analysis and Calorimetry (ICTAC), nomenclature 2005. http://www.ictac.org

[12] G. W. H. Höhne, W. F. Hemminger, H. J. Flammersheim, Differential Scanning Calorimetry, Springer, Berlin 2003.

[13] J. Goldstein, Scanning Electron Microscopy and X-ray microanalysis, Kluwer Academic/Plenum Publ, New York 2003.

[14] H. Topsoe, F. E. Massouth, B. S. Clausen, Hydrotreating Catalysis, in J. R. Anderson, M. Boudart (Eds.), Catalysis-Science and Technology, Vol. 11, Springer, Berlin 1996.

[15] K. S. W. Sing, Colloids Surf., A, 241 (2004) 3.

Acknowledgements

The present work was performed in the Institute for Inorganic Chemistry, in the Christian-Albrechts-University of Kiel. By this way is my pleasure to acknowledge every person who was very helpful in any situation during this work development.

First of all, I thank Prof. Dr. Wolfgang Bensch for the opportunity of working on this very interesting topic, for helpful suggestions and all his support during the work.

About PD Dr. Christian Näther I thank him all his cooperativeness on every crystallographic problem and question, as well as Ms. Inke Jeß for the endless patient and effort to look for suitable crystals.

To the whole working group I would like to thank all the help and support they gave me and the nice moments we shared together. In particular I thank my office partners: Dr. Angela Puls, Nicole Pienack, Nergis Sükür and Beatrix Seidlhofer for the nice teamwork atmosphere.

To Mrs. Uschi Cornelissen and Mrs. Stefanie Pehlke I thank for the spectroscopic studies and CHNS-analysis performed. To Dr. Christoph Teske I thank for the rich discussions about thermal analysis methods and all the help in measurements.

For the administrative aspects I especially thank to Dr. Herbert Pausch and the secretaries Mrs. Ute Sobotta, Mrs. Cornelia Schilz and Mrs. Britta Bahn.

For the help finding literature I thank the members of the library: Mrs. Nikola Schmitz and Mrs. Kirstin Stark.

For all the help about hard work I thank the members of the workshop: Mr. Stephan Göttsche, Mr. Wesing and Mr. Ralph Suren.

Finally, but not at the end I thank Mr. Puddig and Mr. A. Slifirski for all helpfulness.